UNSATURATED Pt PINCER COMPLEXES AND ATTEMPTS TOWARD THE ISOLATION OF A METHANE σ-COMPLEX

A Dissertation

by

JESSICA CARMAN DEMOTT

Submitted to the Office of Graduate and Professional Studies of
Texas A&M University
in partial fulfillment of the requirements for the degree of

DOCTOR OF PHILOSOPHY

Chair of Committee,	Oleg V. Ozerov
Committee Members,	Kevin Burgess
	Mark T. Holtzapple
	Matthew Sheldon
Head of Department,	François Gabbaï

December 2015

Major Subject: Chemistry

ABSTRACT

Alkane σ-complexes have been identified as key intermediates in C-H bond activation and subsequent functionalization of alkanes. Methane and larger saturated alkanes, however, are sterically and electronically disinclined to bind to transition metals. In particular, a thermodynamically stable methane σ-complex intermediate has not been attained or structurally characterized. This research aimed to make progress toward the development and isolation of stable organometallic methane σ-complexes.

16-electron d^8 Pt(II) complexes are typically stable square planar, 4-coordinate species that require ligand dissociation in order to provide an open coordination site for methane. Accessing stable three coordinate Pt(II) species, however, is a challenge. Novel Pt silylene pincer ligand scaffolds, however, were found to undergo a net 1,2-migration of R from Pt to Si, yielding highly unsaturated Pt cations with weakly coordinating carborane anions. Apparent protodesilylation of mesitylene resulted in two Pt cationic units linked together by a siloxane bridge where unsaturation at the Pt centers was retained.

Attempts to isolate unsaturated three-coordinate Pt species with bis(phosphine)diarylamido-based (PNP) pincer ligands were frustrated by rapid C-H activation of various arene reaction solvents. When dichloromethane was used as a solvent, formation of the paramagnetic species $[(PNP)PtCl]^+$ was observed. This is consistent with the radical abstraction of a chlorine atom and oxidation of the ligand, demonstrating the system's potential for metalloradical behavior. Overall, the suspected

(PNP)Pt^+ intermediate is a highly reactive species that exhibits both strongly electrophilic and metalloradical behavior.

Exploring alternative pincer ligand scaffolds for generating stable methane σ-complexes lead us to the use of carbazole pincer ligands that have lower oxidation potentials, a less basic central nitrogen, and a new steric profile. In contrast to previously synthesized Pt triflate complexes, facile displacement of triflate by water was observed for a Pt complex of a bis(imino)carbazolyl (NNN) pincer ligand containing mesityl sidearms. The steric bulk projected by the mesityl groups of the NNN ligand may favor the coordination of smaller ligands such as water. Unexpectedly facile cyclometallation of the mesityl sidearm was also observed.

DEDICATION

To Mom and Dad

ACKNOWLEDGEMENTS

First and foremost I would like to thank my advisor, Dr. Oleg V. Ozerov. It has been a long path and certainly an impossible one without you. Thank you for your contagious curiosity, your inspiration, and your challenges. I've deeply appreciated the opportunities you've built for me over the last several years.

Thank you to my committee members: Dr. Kevin Burgess, Dr. Mark Holtzapple, Dr. Matthew Sheldon, and Dr. Hong-Cai Zhou for their support and guidance. I would also like to acknowledge the various funding sources that supported this work: US National Science Foundation, the Welch Foundation, IPMI, and BASF.

I would like to thank all the members of the Ozerov group (past, present, and honorary) that have made this journey all the more interesting, fun, and endurable: Sam Timpa, Jillian Davidson, Chun-I Lee, Loren Press, Billy McCulloch, Chandra Palit, Chris Pell, Wei-Chun Shih, John Dekarske, Linda Redd, Rita Silbernagel, Alex Kosanovich, Patrick Hubbard, Qingheng Lai, Soomin Park, Rafael Huacuja, Rodrigo Ramirez, Jose Veleta, Chelsea Mandell, Yanjun Zhu, Weixing Gu, Justin Walensky, Dan Smith, Dave Herbert, Jia Zhou, Samantha Yreugas, Claudia Fafard, Sophia Koziatek, Sylvain Gatard, Wei Weng, and Lei Fan.

I would like to thank Dr. Joanna Goodey-Pellois for all the mentorship over the last five years. Thank you to the Chemistry Department, PLU, WISE, and GSAC for support, inspiration, and patience. I deeply appreciated the help from Philip Wymola and Melvin Williams for supplies for the troops; Greg Wylie and Steve Silber for NMR

support; Dr. Nattamai Bhuvanesh for X-ray solutions; Prof. Dmitry G. Gusev and Panida Surawatanawong for computational contributions; Yohannes Rezenom and Vanessa Santiago for Mass Spec; Ron Carter and Curtis Lee for lab repairs; and of course the Graduate Advising and Business offices: Sandy Manning, Valerie McLaughlin, Crystal King, Simon North, and François Gabbaï.

I would like to thank all of my family for selflessly supporting this journey, often from behind the scenes and without acknowledgement. I'd like to thank all the women in the family who stepped in as mom. Thank you for the love, the insanity, the memories, and the wisdom: Melissa, Vanessa, Aunt Betty, Grandma Carmen, Aunt Doreen, Aunt Edie, Holly, Heather, Aunt Linda, Jennifer, Shannon, Elizabeth, Amanda, Janet, Jill and Christina Brammell. Thank you to Morgan MacInnis. Special thanks to my mom for her creativity, artistic nature, and bravery and special thanks to my dad for introducing me to Einstein.

TABLE OF CONTENTS

Page

LIST OF FIGURES

Page

LIST OF TABLES

Page

LIST OF CHARTS

Page

I. INTRODUCTION

1.1 Overview

1.1.1 Industrial Uses of Methane

Methane is the smallest and most abundant alkane, making up about 95 percent of natural gas. As a cheap, abundant resource methane has mainly been exploited as a fuel, and in recent years natural gas has been gaining significant market share relative to coal and oil.[1] With the increase in accessible natural gas reserves, specifically the shale gas boom in the United States, making methane commercially viable as a C_1 chemical feedstock is an attractive industrial target.[2]

In addition to its use in the electricity and heat sectors, one of the only industrial uses for methane is its conversion in the presence of H_2O to form carbon monoxide, carbon dioxide, and hydrogen. This product mixture is also known as synthesis gas or syngas (Scheme 1.1).[3]

$$CH_4 + H_2O \longrightarrow \underset{\text{Syngas}}{CO + 3H_2} \qquad \Delta_r H = 206\ \text{kJ/mol}$$

Scheme 1.1 Steam-reforming reaction for methane to syngas.

Methane is the leading source of hydrogen gas for processes including the Haber-Bosch synthesis of ammonia, which provides over 109 million metric tons of ammonia per year.[4] This also means the use of hydrogen as a fuel source is still significantly linked

to methane and syngas production. The produced syngas can also be funneled into the Fischer-Tropsch reaction for the production of diesel fuel or for the synthesis of methanol (Figure 1.2).[2]

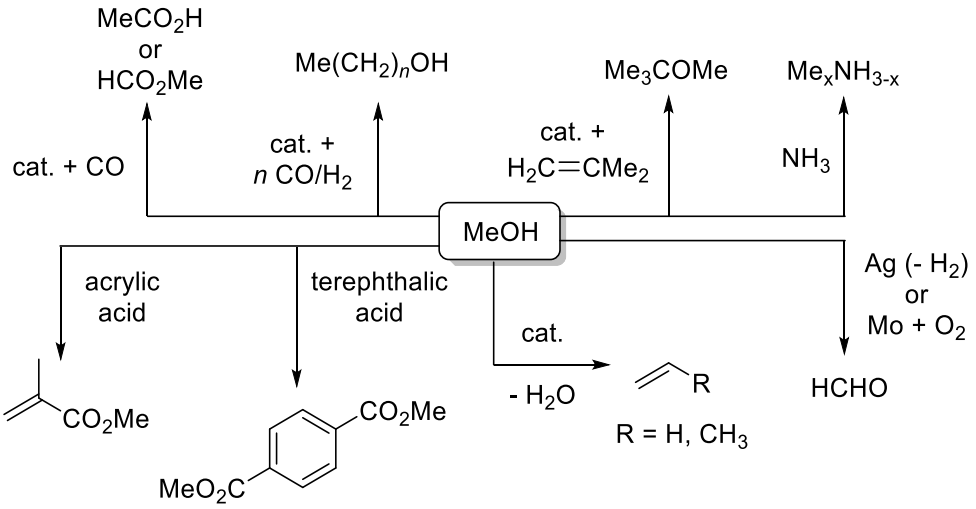

Figure 1.1 Applications of methanol.[5]

Methanol is an extremely important starting material for a wide variety of commodity chemicals (Figure 1.1).[5] Most of the methanol produced is derived from natural gas.[5] Direct conversion of methane into methanol, however, is not an industrially applied strategy. Methane is an inert starting material. With C-H bond dissociation energies of 105 kcal/mol,[6] its resistance to reactivity is a key reason for its accumulation and abundance today.

Prevention of over-oxidation of methane beyond the methanol oxidation state is challenging. Reaction of methane with O_2 first results in the formation of methanol.

However, methanol is more reactive than methane and rapidly undergoes complete oxidation to CO_2 and H_2O. Using lower temperature conditions to slow the oxidation process decreases overall methane conversion and still suffers from poor selectivity.[7] For example, one of the most selective catalysts for the partial oxidation of methane uses Fe-sodalite at 435 °C but with a selectivity as high as 25% and methane conversion of only 5.8%.[8] More recently, transition metal zeolites have been used to achieve higher selectivities (<85%) at lower temperatures but studies are on-going to improve catalyst turnover.[9]

Industrially, methanol is produced indirectly from methane in two steps (Figure 1.2).[3] First, methane is reacted with steam over a heterogeneous nickel catalyst to form syngas (H_2, CO). This process is typically conducted at 800–900 °C and at pressures between 1.5 – 4.5 MPa, depending on the cracking techniques used. This process results in an excess of H_2 relative to the amount of H_2 needed for methanol production. With the addition of CO_2, either upstream or downstream in the steam reformer, the excess H_2 can be converted further to CO and H_2O and the concentrations of H_2, CO_2, and CO can be adjusted to optimize the stoichiometry needed for methanol production. In the second step, syngas is then reacted over heterogeneous Cu-ZnO-Al_2O_3 or Cu-ZnO-Cr_2O_3 catalysts at temperatures between 200–300 °C and at pressures between 5–10 MPa.[5]

Fischer-Tropsch Reaction

$$(2n + 1)\,H_2 + n\,CO \xrightarrow{\text{heterogeneous catalyst}} C_nH_{(2n+2)} + n\,H_2O$$

Methane to Methanol Reactions

$$CH_4 + H_2O \longrightarrow CO + 3\,H_2 \qquad \Delta_rH = 206\ \text{kJ/mol}$$

$$CO + H_2O \longrightarrow CO_2 + H_2 \qquad \Delta_rH = -41\ \text{kJ/mol}$$

$$2\,H_2 + CO \longrightarrow CH_3OH \qquad \Delta_rH = -92\ \text{kJ/mol}$$

Figure 1.2 Fischer-Tropsch reaction for synthesis of heavier alkanes from syngas and conversion of methane to methanol via syngas.

The industrial production of methanol from methane can perhaps be considered a solved problem.[10] However, the current process is energy intensive and indirect. The development of a process for the selective and direct conversion of methane into other value-added chemicals such as ethane, ethylene, aromatics, and other oxygenates is still a significant focus of fundamental research, and the extension of such a process to an industrial scale has remained a Holy Grail of catalysis.[11-13] Homogeneous catalysis is a widely studied area of research, and its application for increasing the selectivity of industrial processes is well known.[14] Currently, however, no homogeneous catalysts are available industrially for the selective catalytic conversion of methane.

1.1.2 Platinum-Catalyzed Oxidation of Methane: The Shilov System

The direct, homogeneous catalytic conversion of methane has been demonstrated on a small scale. In 1972, Shilov and co-workers reported that a catalytic amount of either

$(H_2O)_2Pt(II)Cl_2$ or $[(H_2O)PtCl_3]^-$ in aqueous solution was able to oxidize methane to methanol or chloromethane in the presence of a Pt(IV) oxidant.[15-17] The overall reaction is shown in Equation 1.

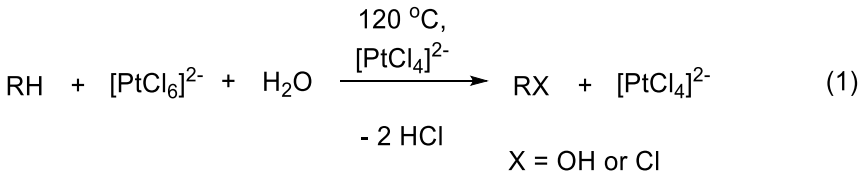

(1)

While the Shilov system is not practical on an industrial scale due to low turnover and the cost of stoichiometric Pt as an oxidant, it is nonetheless a seminal work in alkane C-H activation. The reaction can be thought to proceed via three major steps (Scheme 1.2). The first step is the activation of an alkane by $Pt(II)Cl_2$ to give a Pt(II)-alkyl with concomitant loss of HCl. Oxidation of the Pt(II) alkyl species by $[Pt(IV)Cl_6]^{2-}$ gives a Pt(IV)-alkyl species. Nucleophilic attack by Cl^- or HO^- produces the oxidized alkane and regenerates the Pt(II) starting material.

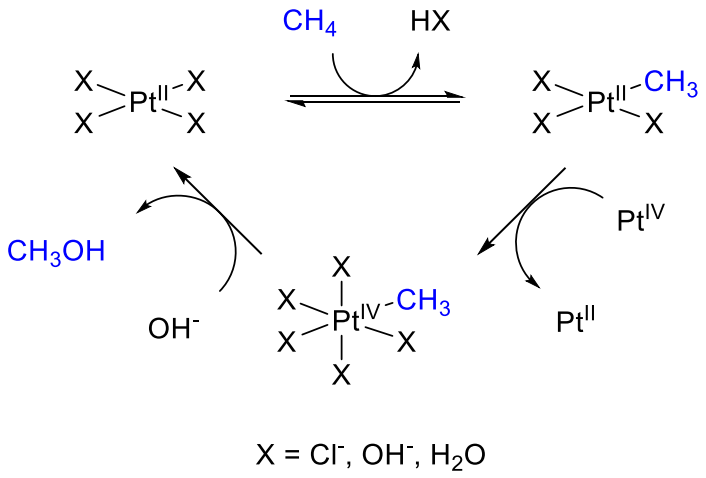

Scheme 1.2 Shilov system for the catalytic oxidation of methane.

Extensive mechanistic studies on the Shilov system have confirmed that the first step is reversible, and in the absence of the $[Pt(IV)Cl_6]^{2-}$ as oxidant only H/D exchange between the alkane and water is observed. While the oxidation step is known to involve electron transfer and not alkyl transfer from the Pt(II)-alkyl species to the stoichiometric Pt(IV) oxidant, limited success has been achieved replacing the cost-prohibitive $[PtCl_6]^{2-}$ oxidant with other potential oxidants. Utilization of $Cu(II)Cl_2/O_2$ as oxidant resulted in increased turnover numbers in comparison to the Shilov system, but oxidation of the Pt catalyst to Pt(IV) eventually shuts down further reactivity. The third and final step of the reaction is known to involve outer-sphere attack of the nucleophile on the alkyl group of the Pt(IV)-alkyl species to regenerate the Pt(II) catalyst concurrent with release of oxidized alkane.[18]

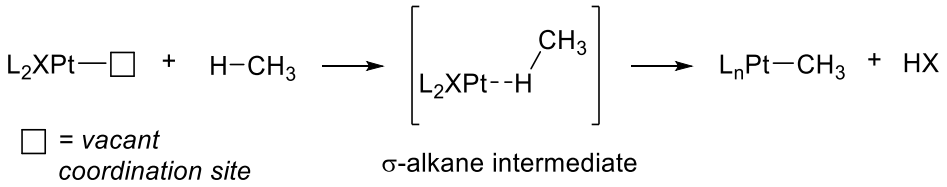

Scheme 1.3 Proposed σ-alkane complex as an intermediate in C-H activation of methane in the Shilov system.

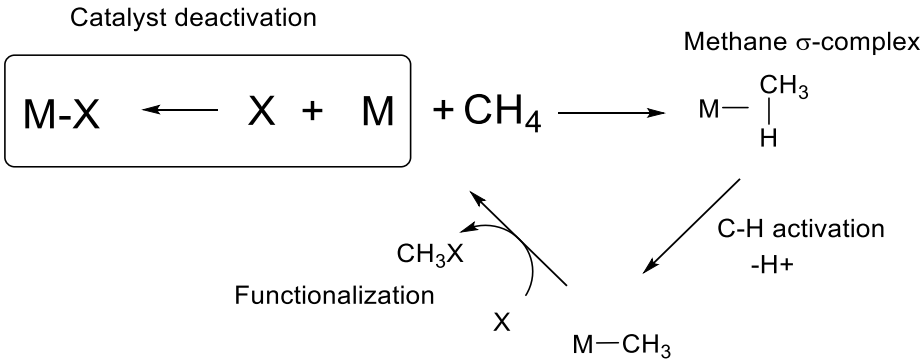

Scheme 1.4 Catalytic cycle for methane activation and functionalization, as well as competition between methane and reagents for unsaturated metal center.

Investigation of the first mechanistic step by Bercaw and co-workers has shown that the C-H activation of methane in the Shilov system involves the rate-determining coordination of methane to Pt and formation of a methane σ-complex (Scheme 1.3).[18] In the Shilov system, water (which is the source of the hydroxo groups for conversion to methanol) can easily outcompete methane to bind to any open coordination sites at the Pt center and displacement of an aquo ligand by methane is easily the slowest step of the catalytic cycle (Scheme 1.4). Improving the binding affinity of methane to transition metal catalysts relative to other substrates would have the potential to increase the rate of

methane conversion as well as the selectivity. As such, a better understanding of how to improve the coordination chemistry between methane and transition metals is of value.

1.1.3 Improved Catalysts for Platinum-Catalyzed Methane Conversion

Work by Periana and colleagues at the Catalytica company has resulted in significant improvements to the homogeneous Pt-catalyzed conversion of methane. They found that the use of sulfuric acid and Hg(II) salts allowed them to convert methane into methylbisulfate in 43% yield.[19] Building off of this work, the use of the homogeneous catalyst dichloro[η^2-(2,2'-bipyrimidyl)]platinum(II) ((bpym)$PtCl_2$) improved the overall yield to 72% (Schemes 1.5 and 1.6).[20] Methylbisulfate can be considered a protected form of methanol, and the use of acidic solvents helps prevent the catalyst from binding the product instead of methane. Downstream reaction of methylbisulfate with water can be used to generate methanol and sulfuric acid (which can then be recycled back into the reaction medium).

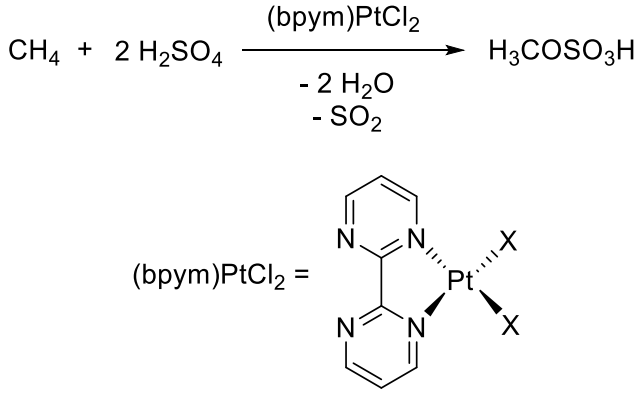

Scheme 1.5 Conversion of methane to methylbisulfate using (bpym)$PtCl_2$ catalyst.

More recently, Periana and co-workers demonstrated the use of lead and thallium salts for the conversion of methane to methyltrifluoroacetate, with yields of 76% and 74%, respectively.[21] In contrast to the Pt-based systems where methane coordination is the rate determining step, methane coordination to Pb or Tl is believed to be faster relative to rate determining electrophilic C-H activation of methane at Pt. The group also showed that cationic complexes of Au(I) or Au(III) catalytically convert methane to methanol in strong acid solvent. A Se(VI) oxidant is required to oxidize stoichiometrically generated Au(0) back to cationic Au, thus making the system catalytic. Synthetic limitations have obviated detailed kinetic studies of this system.[22]

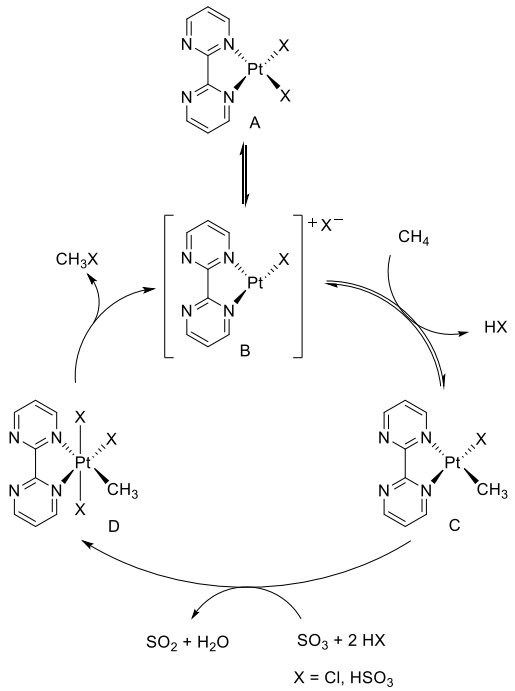

Scheme 1.6 Proposed catalytic cycle for the conversion of methane to methylbisulfate using (bpym)$PtCl_2$ catalyst.

1.2 Coordination of C-H σ-Bonds to Transition Metals

1.2.1 Impetus for Improving the Understanding of Alkane σ-Complexes

C-H bonds are ubiquitous, and attempts to directly functionalize C-H bonds using transition metal catalysts is a prominent and active research topic in organic and organometallic chemistry.[11,23,24] However, C-H bonds are also relatively inert; C(sp^3)-H bonds have a bond strength of 104 kcal/mol. This makes the direct conversion of C-H bonds into more valuable functional groups challenging but numerous examples of direct C-H functionalization involve activation of a C-H bond by a transition metal have been reported.[12,17,18,25-27] Alkane coordination to a transition metal is often thought to be an intermediate step in C-H functionalization reactions (Figure 1.3).[28-33] However, due to the difficulty in binding alkanes to transition metals, most transformations of C(sp^3)-H bonds require substrates that contain donating groups that readily coordinate to the transition metal[34-37] and thus facilitate a formally intramolecular C-H activation, which limits the substrate scope. A better understanding of the synthesis and properties of alkane σ-complexes has the potential to obviate the need for a coordinating group and expand the substrate scope of direct C-H functionalization reactions.[28,30]

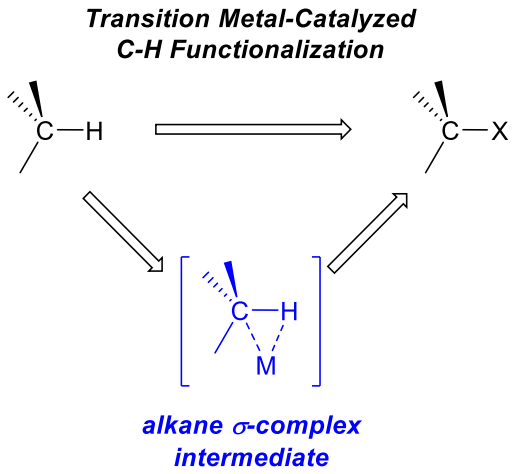

Figure 1.3 Diagram emphasizing the role of alkane σ-complexes in the direct functionalization of C-H bonds.

1.2.2 E-H Bonds as Ligands for Transition Metals

Although it was not always known that a σ-bond could act as a ligand for a transition metal,[33,38,39] E-H σ-bonds are now firmly established as ligands in organometallic chemistry. Generally speaking, E-H σ-bonds coordinate to a transition metal in a synergistic fashion, analogous to the Dewar-Chatt-Duncanson model that is commonly used to explain the binding of olefins and alkynes to transition metals (Figure 1.4).[40]

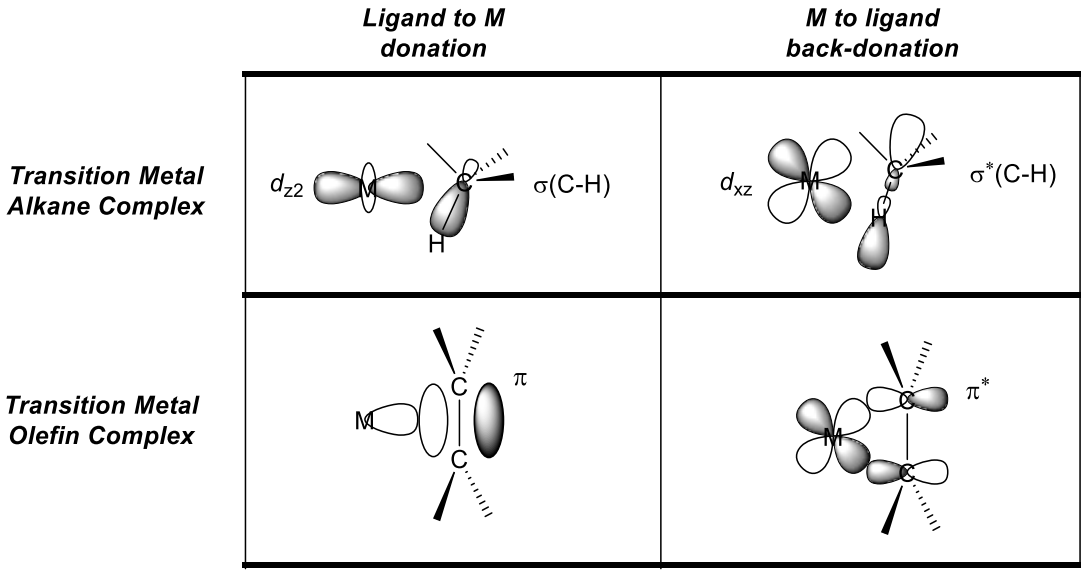

Figure 1.4 Comparison of Dewar-Chatt-Duncanson model of transition metal olefin bonding interactions (bottom) adapted for transition metal alkane σ-complexes (right).

The E-H σ-bonding orbital provides the electron density for donation to an unfilled transition metal orbital. A filled transition metal orbital of π-symmetry can then back donate electron density to the σ*-antibonding orbital of the E-H bond. The back-donation is an important component of the bonding interaction, and without it E-H σ-adducts to transition metals would be much less stable. Examples of E-H σ-bonds interacting with main group elements are much less common[41] since the main group element does not have filled orbitals of appropriate symmetry to back-donate to the E-H σ*-antibonding orbital.[28,33,40] On the other hand, if the degree of back-bonding is too strong, the σ*-antibonding orbital will become populated and oxidative addition of the E-H bond will occur (Figure 1.5). This adds to the challenge in isolating and studying E-H σ-complexes, as a balance must be achieved such that back-donation reinforces binding of the E-H σ-

bond without being so strong as to break it completely. This can be accomplished by tuning the ancillary ligands on the transition metal.

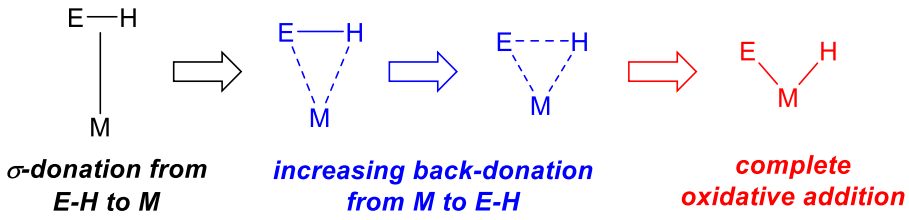

Figure 1.5 Spectrum of E-H σ-bond interactions with a transition metal from weakest interaction (far left) to complete back-donation and oxidative addition of the E-H bond (far right).

While examples of proper alkane σ-complexes – that is, the intermolecular interaction between an alkane σ-bond and a transition metal – are rare, adducts B-H and Si-H σ-bonds to transition metals are significantly more common. Silanes were the first species identified to form σ-adducts with transition metals, although they were recognized only as H-bridged Si-M bonds and not as σ-complexes at the time of their discovery.[42-44] Si-H σ-bonds are better donors than H_2 or C-H σ-bonds. The Si-H bond is also longer and weaker than H-H and C-H σ-bonds, and the σ* orbital is therefore lower in energy. While this facilitates back-donation from a transition metal to the Si-H bond, it also makes Si-H bonds more prone to oxidative addition than for other E-H bonds (Figure 1.6).[45]

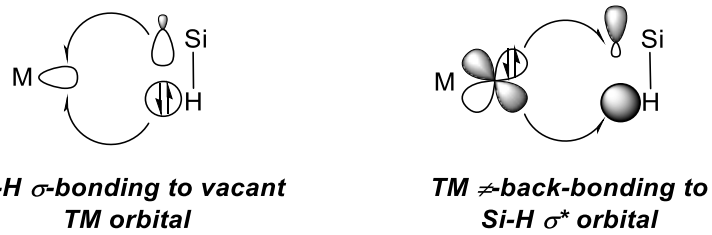

Figure 1.6 Molecular orbital diagram of the donation and back-donation involved in the binding of a Si-H σ-bond to a transition metal.

One early example of a B-H σ-bond binding to a transition metal was reported by Hartwig and co-workers in 1996,[46,47] when they reported the isolation and characterization of $Cp_2Ti(HBcat)_2$ (HBcat = catechol borane, $HB(O_2C_6H_4)$). The X-ray diffraction study revealed that the Ti-B bond lengths (2.335(5) Å) were significantly longer than what would be expected for a metallocene boryl species. Additionally, the B atom was found to lay in the plane containing Ti and the two oxygens of the catechol substituent, contrary to what would be expected for a Lewis acid/base complex. Calculations gave insight into the bonding between the borane ligands and Ti. A partial molecular orbital picture (Figure 1.7) shows that the B-H σ-bond donates to the LUMO of Cp_2Ti to form a bonding interaction as has been described for E-H σ-complexes. However, the key difference between B-H σ-complexes and other E-H σ-complexes lies in the back-donation. While the filled transition metal d-obital must back-donate into the σ*-antibonding orbital in σ-silane and σ-alkane adducts, boranes have an empty p-orbital that can potentially receive electron density from the filled metal orbital. Calculations for $Cp_2Ti(HBcat)_2$ suggest that the Cp_2Ti HOMO back-donates into the lower energy empty p-orbital of the HBcat

ligands.[46-49] The geometry at B is also explained in terms of back-bonding as the planarity allows the best overlap between the Cp_2Ti HOMO and the B p-orbital. The back-donation to the B p-orbital results in stronger adducts relative to E = H, C, or Si.[48,50,51] Calculations on the mono borane adduct $Cp_2Ti(HBcat)(PMe_3)$ describe a similar bonding picture, with back-donation to the borane p-orbital.[49,52]

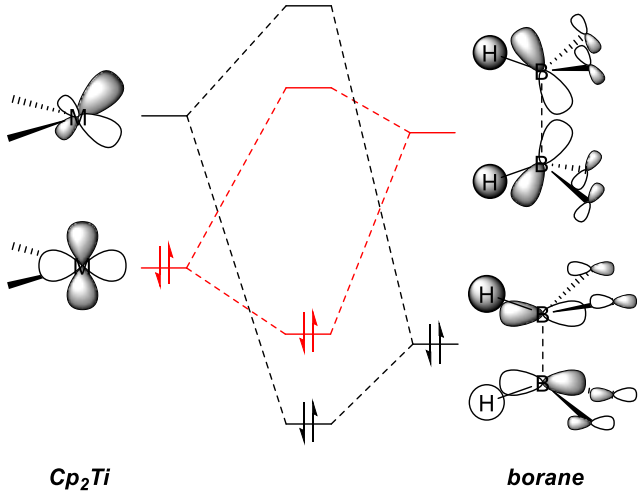

Figure 1.7 Partial molecular orbital diagram for $Cp_2Ti(HBcat)_2$. Back-donation from Cp_2Ti to $(HBcat)_2$ is depicted in red.

1.2.2.1 Dihydrogen

The discovery that H_2 could bond to an unsaturated transition metal was a breakthrough in organometallic chemistry.[39,40,53] While the H-H bond is similar in strength to an alkane C-H bond (104 kcal/mol and 100–105 kcal/mol, respectively),[54] examples of H_2 binding to transition metals vastly outnumbered reported alkane σ-complexes for a

number of reasons.[38] One obvious advantage that dihydrogen has over other E-H groups for binding to transition metals is its relatively small size; dihydrogen has effectively no steric hindrance when binding to transition metals. In addition, the σ-bonding and σ*-antibonding orbitals of H_2 are symmetrical about the H-H bond (Figure 1.8). As such, orbital overlap for dihydrogen complexes is much more efficient than for other E-H σ-complexes for both the σ-bonding and π-backbonding components of the interaction.

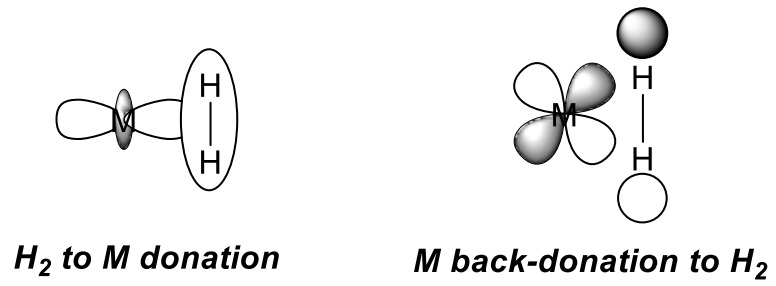

Figure 1.8 Orbital interactions in the coordination of dihydrogen to a transition metal.

The multitude of reports of dihydrogen complexes has provided a large characterization data pool, and the dihydrogen-transition-metal interaction is the most studied of all the E-H σ-complexes. While X-ray diffraction techniques are limited in characterizing H_2 complexes due to the weak diffraction of an H atom relative to a heavy metal, NMR spectroscopy is frequently used to determine the nature of the interaction between H_2 and a transition metal. The two most commonly utilized NMR spectroscopic techniques are measurement of the minimum T_1 relaxation time (T_{1min}) and the $J_{H\text{-}D}$ coupling constant. The T_1 relaxation time is a measure of the time it takes for the nuclear

spins to relax after a magnetic field pulse has been applied. In the presence of adjacent nuclei, this relaxation rate is faster, and as the H-H bond weakens (lengthens), the effect of one H on the relaxation rate of the other H decreases resulting in a longer T_1 relaxation time. To measure the $J_{H\text{-}D}$ coupling constant one must first synthesize the transition metal H-D isotopologue. As the H-H bond is weakened, the coupling constant decreases. Ranges for both the T_{1min} and the $J_{H\text{-}D}$ have been firmly established for dihydrogen complexes.[33] Typical ranges for dihydrogen, stretched dihydrogen, and dihydride complexes are given in Table 1.1.

Table 1.1 Representative characterization parameters for dihydrogen, stretched dihydrogen, and dihydride transition metal complexes. [a] $J_{H\text{-}D}$ values are approximately 1/6.5 the magnitude of $J_{H\text{-}H}$.[33,55,56]

Type	d (H-H) (Å)	$J_{H\text{-}H}$ or $J_{H\text{-}D}$[a]	$T_{1(min)}$
Free dihydrogen	0.74	43 Hz ($J_{H\text{-}D}$)	
Dihydrogen	0.8 – 1.0	32 Hz ($J_{H\text{-}D}$)[57]	< 20 ms
		33.5 Hz ($J_{H\text{-}D}$)[39]	
Stretched dihydrogen	1.0 – 1.5	21 Hz ($J_{H\text{-}D}$)[58]	20 ms – 100 ms
Dihydride	> 1.5	0–20 Hz	> 100 ms

The strength of the σ-donating and π-accepting properties of H_2 are important factors in discussing its bonding. Measuring the IR stretching frequency (ν) of a CO ligand *trans* to a ligand L can give an estimation of the strength of p-acceptor of L since both ligands are competing for electron density from the same orbital on the metal (Figure 1.9).

Better π-accepting L ligands results in less electron density to back-donate to the CO antibonding orbital. This is manifested in a larger value of ν_{CO}. Examination of ν_{CO} for the CO ligand *trans* to L in the complex $W(CO)_5(L)$ revealed that H_2 was comparable to N_2 and C_2H_4 in its π-accepting capacity. The compounds **101**, **102**, and **103** (Figure 1.9) were consistent with this observed trend. Table 1.2 lists ν_{CO} for compounds with varying L ligands (dppe = $Ph_2PC_2H_4PPh_2$). The varying donicity of L has an effect on the value of ν_{CO}, as it affects the electron density at the metal. Nonetheless, a trend emerged that could be roughly correlated to the π-accepting ability of L. The strongest π-acceptor, SO_2, gives the largest values for ν_{CO} for all three complexes. The weakest π-acceptors in the series are the alkylamines and they give the lowest values of ν_{CO}. As can be seen, H_2 is a comparably strong π-acceptor, while CH_4 is a weak π-acceptor.

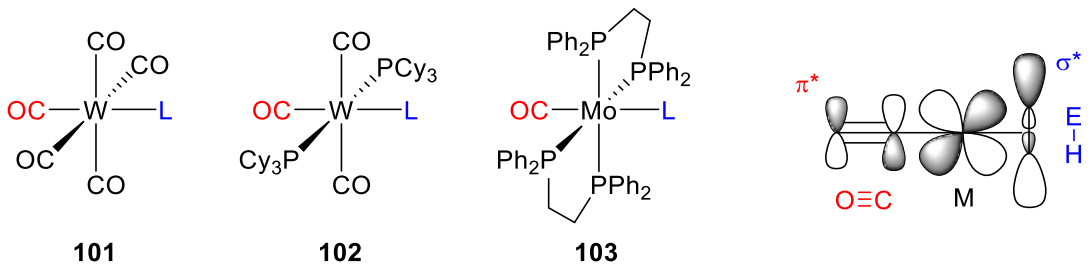

Figure 1.9 Complexes **101**, **102**, and **103** (left) and the competition between CO and L for the filled M orbital. Table 1.2 shows the change of the CO stretching frequency for the CO colored red as the ligand L changes.

Table 1.2 CO stretches for the CO ligand *trans* to L for the complexes shown.

L	$W(CO)_5(L)$ (101)	$W(CO)_3(PCy_3)_2(L)$ (102)	$Mo(CO)(dppe)_2(L)$ (103)
SO_2	2002	1873	1901
H_2	1971	1843	1815
C_2H_4	1973	1834	1813
N_2	1961	1835	1809
Argon/agostic[a]	1932	1797	1723
CH_4	1926	-	-
Pyridine	1921	1757	1718
NR_3	1919[b]	1788[c]	1723[b]

[a] L = argon (matrix) for $W(CO)_5(L)$; agostic C-H for others, [b] $NR_3 = NEt_2H$, [c] $NR_3 = NH_2Bu$

1.2.2.2 Agostic Complexes

The coordination of alkanes to transition metals through a C-H σ-bond has been observed only rarely.[30,59] Other E-H bonds have become established as ligands for transition metals, and the synergistic bonding mode described above also applies for the binding of a C-H σ-bond to a metal (Figure 1.10). However, alkane C-H σ-bonds are both sterically and electronically disinclined to act as ligands for transition metals. While silanes and boranes also have sterics working against them, the polarization of the Si-H and B-H bond helps overcome this hindrance because of the smaller HOMO-LUMO gap (Figure 1.6 and 1.7). Conversely for H_2, although it is similar in bond strength to C-H σ-bonds the lack of steric hindrance allows H_2 access to a transition metal affording efficient orbital overlap.

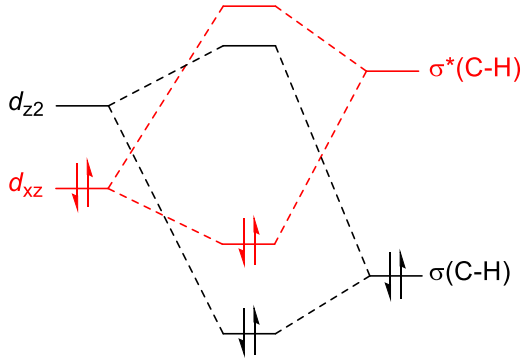

Figure 1.10 Partial molecular orbital picture for the bonding in a transition metal alkane σ-complex. σ-bonding framework in black, σ-back-donation from M to C-H σ* in red.

While examples of intermolecular alkane σ-complexes are limited, there are myriad examples of intramolecular M-H-C interactions throughout the literature. The most common type of metal C-H σ-complexes are agostic complexes.[60] The term "agostic" is reserved for intramolecular situations in which a hydrogen atom is covalently bonded to both a carbon atom and a transition metal atom in a 3-center-2-electron arrangement (Figure 1.11). This can be denoted as an η^2-C-H binding mode characterized by short M-H distances (~1.8–2.3 Å) and small M-H-C bond angles (~90–140°). Agostic interactions provide a reasonable model for understanding interactions of C-H σ-bonds with transition metals. Indeed, experimental evidence for complexes containing agostic interactions[60,61] was part of the original argument for the existence of alkane σ-complexes as intermediates in C-H bond activation.[31-33]

The structural characterization of $(Me_2PCH_2CH_2PMe_2)TiEtCl_3$ is cited as an important example of the affinity of C-H σ-bonds for metal centers.[62,63] The Ti(IV), d^0

metal center has empty d-orbitals available for accepting electron density. The ligands about the Ti center are small and would not sterically inhibit the approach of a C-H group from the ethyl ligand nor would the adjacent ligands force the ethyl group into the empty coordination site. ^{1}H and ^{13}C NMR spectroscopy and neutron diffraction studies of $(Me_2PCH_2CH_2PMe_2)TiEtCl_3$ demonstrated the formation of an agostic interaction. The Ti-H distance was found to be 2.9 Å and an acute Ti-C-C angle of 85.9(6)° was observed for the ethyl substituent as opposed to the expected 109° for the substituents about an uncoordinated C_{sp3} group (Figure 1.11). This is evidence of an electronic proclivity for the formation of an agostic interaction in order to stabilize an unsaturated transition metal. It should be noted that this case only demonstrates the forward electron donation from the C-H σ-bond. The strength of the η^2-C-H interaction with non-d^0 transition metal centers can be enchanced by back-donation into the C-H σ* orbital as discussed in Section 1.2.2.

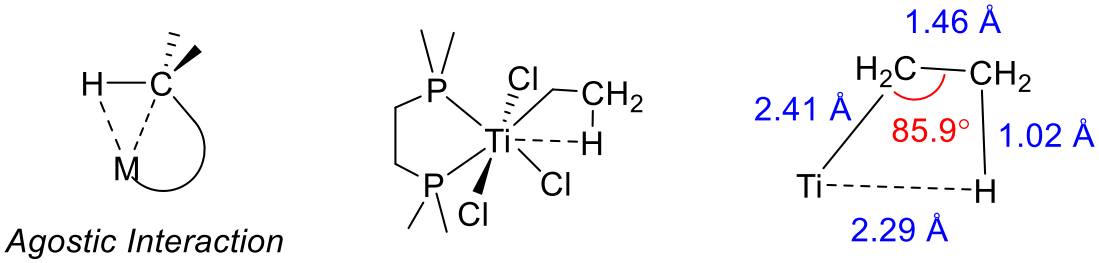

Figure 1.11 General depiction of an agostic interaction with metal M (left), and (η^2-$Me_2PCH_2CH_2PMe2)TiEtCl_3$ featuring an agostic interaction between the Ti center and the β-H of the ethyl ligand.

An agostic interaction involves the donation of electron density from the C-H σ-bond to a metal center that has ≤ 16 electrons. This forward donation can be supplemented by back-donation from filled metal d-orbitals to the σ* orbital of the C-H bond. Distinct from *intramolecular* agostic interactions, alkane σ-complexes also possess this covalent 3-center-2-electron bonding between a transition metal and C-H σ-bond, but the complex is instead *intermolecular*. In addition to paying a smaller entropic penalty and being positioned within the coordination sphere of a metal center, intramolecular alkyl C-H bonds compared to free alkanes may already be slightly polarized relative to a free alkane molecule. This polarization results in a smaller HOMO-LUMO gap thus making intramolecular C-H bonds primed for a stronger interaction with a metal center.

1.2.2.3 Additional Evidence for the Intermediacy of Alkane σ-Complexes

In addition to the observation of numerous agostic complexes, H-D scrambling experiments and the observation of inverse kinetic isotope effects for C-H reductive elimination suggest the intermediacy of alkane σ-complexes in C-H activation.[18,28,64,65]

A key H-D scrambling experiment was reported by Bergman and co-workers in 1986 in which they examined the oxidative addition and reductive elimination of cyclohexane to Cp^*IrPMe_3 (Figure 1.13).[64] If there was not an alkane σ-complex intermediate, deuterium would be observed at the α, β, χ, and δ positions since complete alkane dissociation would take place and re-activation of the cyclohexane ring could occur at any of the C-H bonds. Monitoring the deuterium incorporation, however, demonstrated that deuterium was only incorporated into the α–cyclohexyl position. This supports the

presence of a relative stable alkane σ-complex intermediate that then gets reactivated at the same position. Additionally, thermolysis of a mixture of Cp*IrPMe$_3$(C_6D_{11})D and Cp*IrPMe$_3$(C_6H_{11})H resulted in no H/D exchange. The fact that only d^0 or d^{12} cyclohexanes were produced indicated the RE was intramolecular.

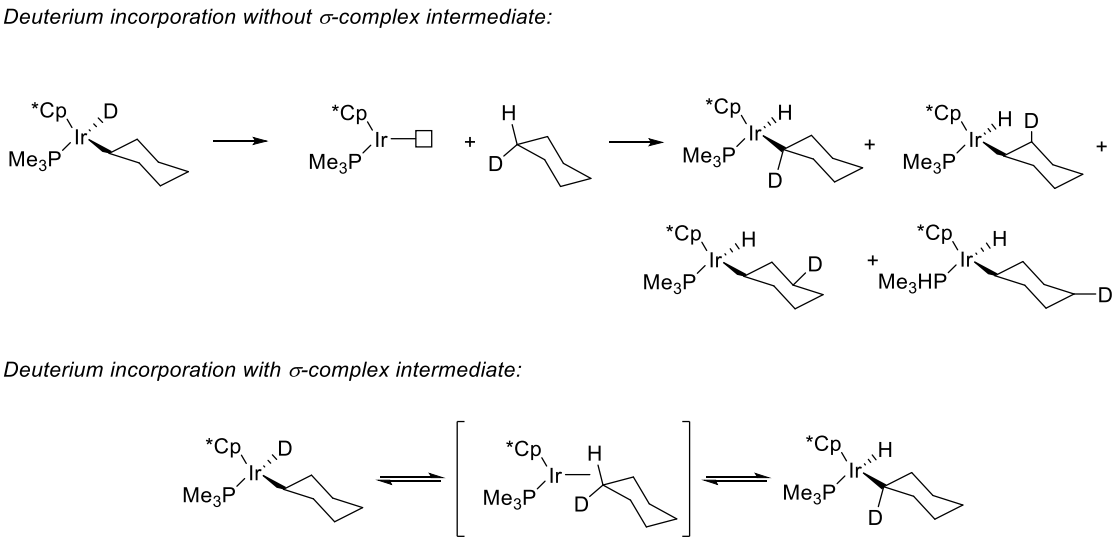

Figure 1.12 Expected deuterium incorporation for pathway without σ-complex intermediate and for a pathway with σ-complex intermediate.

An inverse KIE was also observed for the reductive elimination of cyclohexane in this system. In fact, an inverse kinetic isotope effect ($k^H/k^D < 1$) has been observed for several reactions involving the reductive elimination of a C-H(D) bond and this observation has been associated with a mechanism involving the presence of an unobserved alkane σ-complex intermediate (Figure 1.14).[65]

Generally speaking, for C-H reductive elimination not involving an alkane σ-complex intermediate, the KIE is expected to be greater than one where M-H bond cleavage is faster than M-D bond cleavage. For reactions involving an alkane σ-complex intermediate, an inverse KIE is observed because of the equilibrium between the metal(hydrido)(alkyl) and the alkane σ-complex (Figure 1.14).

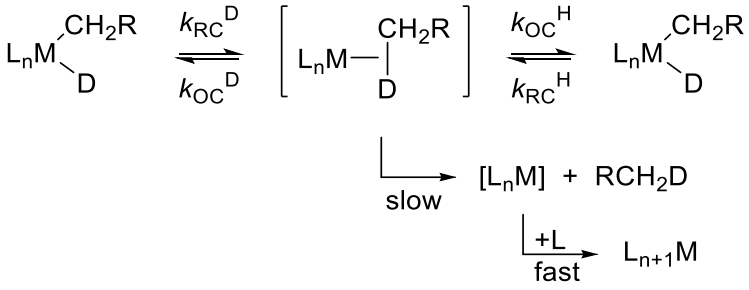

Figure 1.13 Mechanism for C-H and C-D reductive elimination.

This equilibrium depends on the rates of reductive coupling for C-H versus C-D to form the alkane σ-complex and the reverse oxidative cleavage of the alkane σ-complex to reform the M-hydrido or deuterio alkyl species. Thus, the equilibrium KIE for this process is equal to KIE_{RC}/KIE_{OC} which can also be written as $(k_{RC}^{H}/k_{RC}^{D})/(k_{OC}^{H}/k_{OC}^{D})$.[65] The denominator in this equation is always greater than one since C-H cleavage is faster than C-D cleavage ($k_{OC}^{H}/k_{OC}^{D} > 1$). The denominator is also greater in magnitude relative to the numerator (which can be less than or greater than one depending on the reaction coordinate (Figure 1.15). This results in an equilibrium KIE < 1 also known as an inverse KIE.[65]

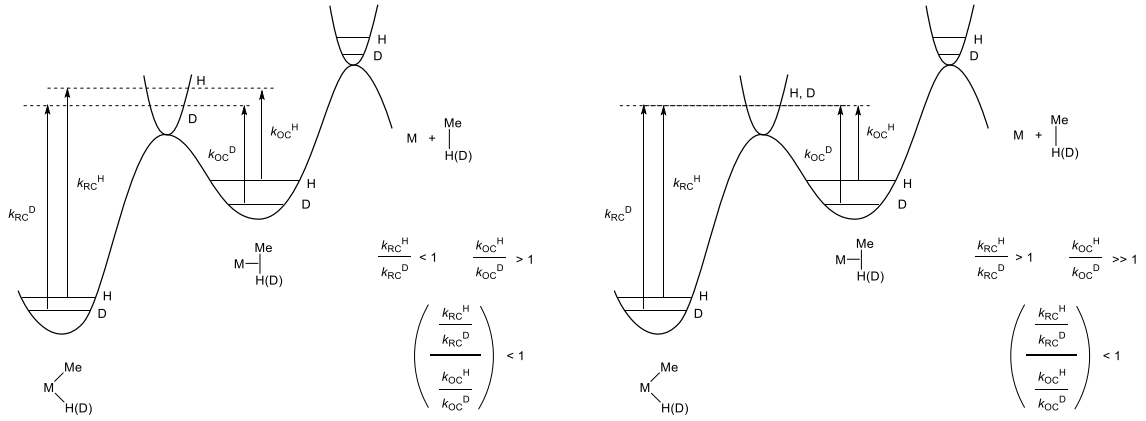

Figure 1.14[a] Reaction coordinates for reductive elimination of C-H and C-D bonds.[65]

1.3 Transition Metal σ-Alkane Complexes in the Literature

1.3.1 Observation of Alkane σ-Complexes in Matrices

The first experimental evidence for alkane σ-complexes was reported in the 1960s.[66,67] Upon photolysis of $M(CO)_6$ species at 77 K to generate an unsaturated 16 electron complex with loss of CO, coordination of alkane solvents was indirectly observed. Monitoring changes in the CO stretching frequencies by infrared spectroscopy, subtle differences were observed depending on the alkane solvent matrix that was present. In this way, σ-complexes of methane, cyclohexane and other alkanes have been examined by UV-vis spectroscopy and time-resolved IR spectroscopy.[66-74] At the femtosecond time scale, the formation of the pentacarbonyl species could be detected prior to the formation of the alkane complex. For methane in particular, photolysis of $M(CO)_6$ in a methane matrix resulted in $(CO)_5(CH_4)$ (**104,** Figure 1.7).[68,69,75]

---

[a] Adapted with permission from Jones, W.D. *Acc. Chem. Res.* **2003**, *36*, 140. Copyright 2003 American Chemical Society.

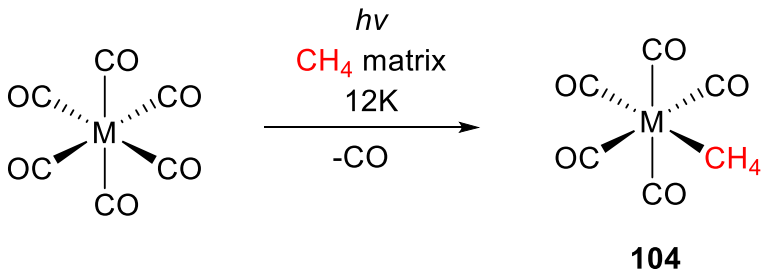

104

Scheme 1.7 Matrix isolation of methane σ-complex.

1.3.2 Transition Metal σ-Alkane Complexes Characterized in Solution

The synthesis of longer lived alkane adducts has allowed for the use of NMR spectroscopy to interrogate alkane binding more directly. Ball and co-workers have performed work on a series of rhenium alkane complexes of the type Cp'Re(CO)$_2$L (Cp' = cyclopentadienyl, *iso*-propylcyclopentadienyl, or 1,2-di-*tert*-butylcyclopentadienyl; L = CO, PF_3, or N_2) and these species remain the most extensively studied alkane complexes (Figure 1.16).[76-81] Photo-induced CO dissociation to open a vacant coordination site for alkane binding occurred with relative ease for different ancillary ligands, thus allowing the researchers to probe alkane binding under subtly different steric and electronic environments.

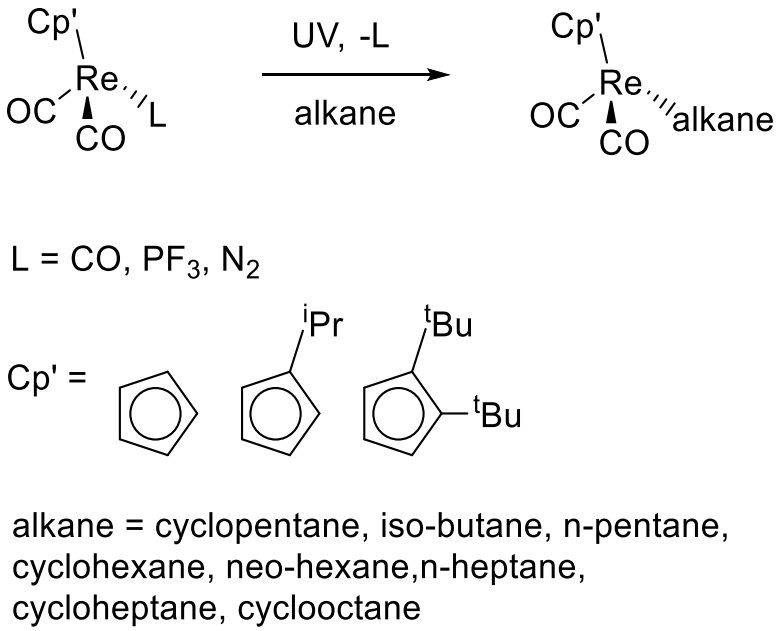

Figure 1.15 Re alkane complexes characterized by NMR spectroscopy.

Ball and co-workers reported the first observation of an η^2-C-H σ-interaction with a transition metal in 1998 using low-temperature NMR spectroscopy.[80] Motivated by earlier IR studies demonstrating [$CpRe(CO)_2$(*n*-heptane)] (Cp = cyclopentadienyl) as having a significantly long life time,[82] the group set out to generate [$CpRe(CO)_2$(cyclopentane)] (**105**).[80] Photo-induced CO dissociation from $CpRe(CO)_3$ in neat cyclopentane solvent at temperatures below 193 K generated a species with signals in the ^{1}H NMR spectrum at 4.92 (s) and –2.32 ppm in a 5:2 ratio. The signal at 4.92 ppm is assigned to the Cp ligand, which is shifted from 5.23 ppm in the starting complex. The signal at –2.32 ppm is shifted upfield of the signal for free cyclopentane (1.4 ppm) and is assigned to the methylene group bound to Re (Figure 1.17).

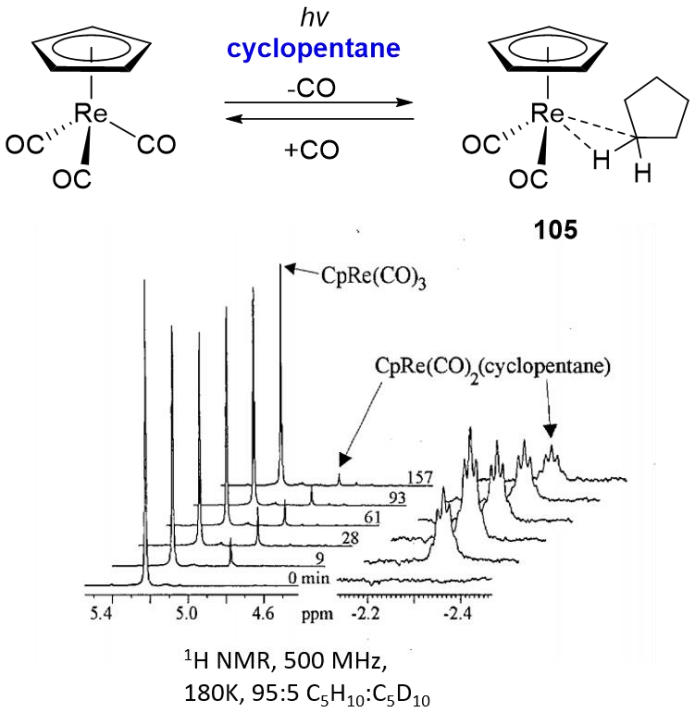

Figure 1.16 First alkane complex characterized in the solution state by NMR spectroscopy.[b,80]

The ^{13}C NMR spectrum features a signal at –31.2 ppm (t, J_{CH} = 112.9 Hz) that was assigned to the C of the Re-bound methylene group. The value of J_{CH} for the alkane ligand is reduced compared to that of the free cyclopentane (J_{CH} = 129.4 Hz), providing further evidence for alkane coordination. Generally speaking, compared to free alkane, the C-H coupling constants for an alkane ligand in an alkane σ-complex are reduced due to the removal of electron density from the C-H bond and reduction of bond order upon coordination to a transition metal. The upfield shift of the chemical resonance (degree of

[b] Reprinted with permission from Geftakis, S.; Ball, G. E. *J. Am. Chem. Soc.* **1998**, *120*, 9953. Copyright 1998 American Chemical Society.

shielding) and J_{CH} is dependent on the number of C-H bonds and the fraction of time those C-H bonds interact with the metal center. The greater the effective depopulation of the electron density from the C-H σ-bond, the smaller the J_{CH} and the greater the shielding. For example, this is seen in the greater upfield chemical shifts for methylene C-H bonds relative to methyl C-H bonds.

Interrogation of n-pentane complexes revealed binding preference for methylene C-H bonds over methyl C-H bonds.[76,77] Methylene C-H bonds are weaker than methyl C-H bonds resulting in C-H σ-bond orbitals that are slightly higher in energy. This difference in energy is enough to make methylene C-H bonds preferential donors to Re. NMR spectroscopic studies by Ball and co-workers are consistent with this notion, and a preference for binding to the methylene groups on pentane was observed for (^{i}PrCp)Re(CO)$_2$(pentane) (^{i}PrCp = η^5-*iso*-propylcyclopentadienyl). This is also consistent with the preference for cycloalkane binding over linear alkane binding.[81] The subtle differences in bond strength between axial versus equatorial C-H bonds in cyclohexane were reflected in preferred binding of the slightly weaker axial C-H bond of cyclohexane to Re compared to the equatorial C-H bond. Using a partially deuterated n-pentane, preference for C-H bonds over C-D bonds was observed.[83]

To date, a wide range of Re(alkane) complexes have been examined in the literature. Following the use of CpRe(CO)$_2$ fragment to support alkane complexes in solution, Perutz and co-workers employed a TpRe(CO)$_2$ (Tp = tris(pyrazol-1-yl)borate) complex to characterize a cyclopentane adduct at 190 K (Figure 1.18).[84] Rhenium complexes with KpRe(CO)$_2$ (Kp = cyclopentadienyltris(diethylphosphito)cobaltate(III))

fragment have also been reported (Figure 1.18).[85] For all the reported rhenium alkane complexes the ^{1}H NMR chemical shift range for the alkane ligand hydrogens is –8.3 ppm to –1.1 ppm.

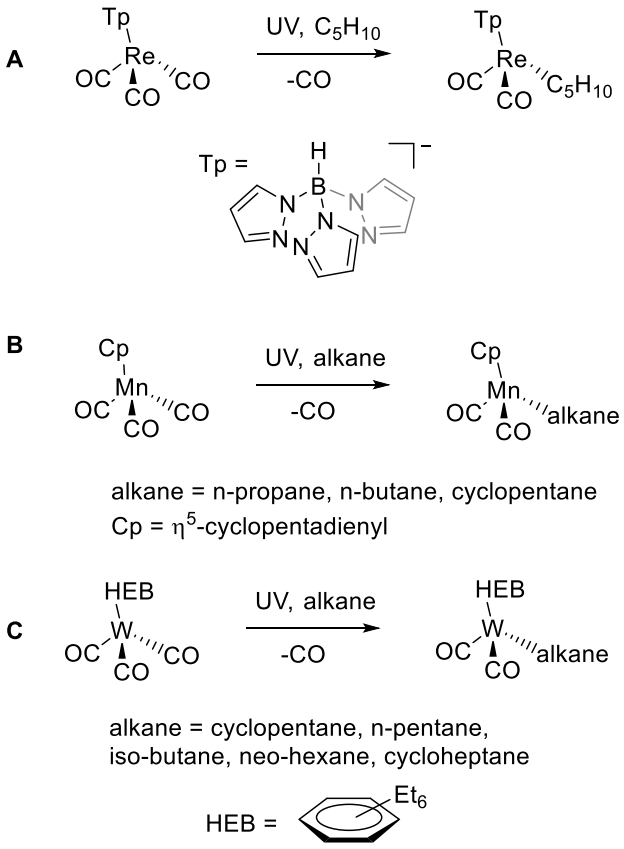

Figure 1.17 Re, Mn, and W alkane complexes characterized by NMR spectroscopy.

In addition to Re, alkane complexes have also been reported for tungsten and manganese (Figure 1.18).[86,87] In 2011, Perutz and coworkers reported propane, butane, and cyclopentane adducts of a $CpMn(CO)_2$ fragment.[86] The ^{1}H NMR chemical shift for bound C-H groups ranged from –8.7 ppm to –5.9 ppm and the Mn complexes maintained

a preference for binding cycloalkane over the linear alkanes. In 2012, Ball and co-workers reported a series of tungsten alkane complexes. In contrast to the $CpRe(CO)_2$ complexes, the $(HEB)W(CO)_2$(pentane) complex did not appear to have a strong preference for methylene C-H bonds versus methyl C-H bonds.[87] Rh complexes of methane[88] and ethane[89] have also been characterized by NMR spectroscopy and will be discussed further in Section 1.3.4.

1.3.3 Transition Metal σ-Alkane Complexes Characterized in the Solid-State

Compared to solution-state examples, the solid-state characterization of alkane σ-complexes is even less common, and therefore structural details of metal-alkane interactions is limited. Only a handful of examples of crystallographically characterized mononuclear transition metal alkane σ-complexes have been reported (Figure 1.19).[90-92] In general, these species possess a cavity in the crystal lattice that allows for an alkane molecule to fit within the coordinate sphere of the transition metal center.

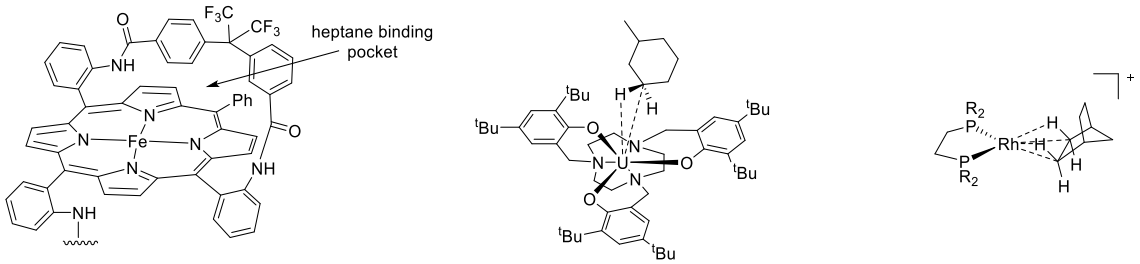

Figure 1.18 Alkane σ-complexes characterized in the solid state.

1.3.3.1 First Solid State σ-Complexes and the Role of Secondary Ligand Stabilization

In 1997, Reed and co-workers reported the first crystallographically characterized transition metal alkane σ-complex.[90] They used a porphyrin ligand which possessed a molecular chain above and below the porphyrin plane to sterically exclude larger ligands and solvent molecules from the axial coordination sites at iron. Following ligation of the porphyrin ligand to an iron center and recrystallization by heptane diffusion into a fluorobenzene solution, crystals of **106** were obtained. X-ray diffraction studies showed that heptane was incorporated into a hydrophobic cavity formed between two adjacent molecules and within the o-amindophenyl linkages tethered above and below the porphyrin planes.

Examining the structure, it was revealed that the iron center was displaced slightly above the porphyrin plane towards the heptane ligand indicating that an interaction between iron and heptane existed and the alkane did not merely co-crystallize with the ligand. Both the iron center and n-heptane are disordered but the iron-carbon distances for the closest n-heptane carbon atoms are 2.52 and 2.83 Å. This is within van der Waals radii of Fe and C and these distances fall within the range of previously reported iron-carbon agostic interactions (2.5 and 3.0 Å).

Binding energies were calculated for methane, ethane, propane and butane and found to be 10.5, 14.1, 16.7, and 16.3 kcal/mol, respectively. The increase in hydrophobic interactions between the longer chain alkanes and the porphyrin ligand were suggested to be the source of increased stabilization. Reed's example provided the first structural

snapshot of an intermolecular interaction between an alkane and transition metal center. It also suggested this interaction could be stabilized by increased hydrophobic interactions between the alkane and ligand platform.

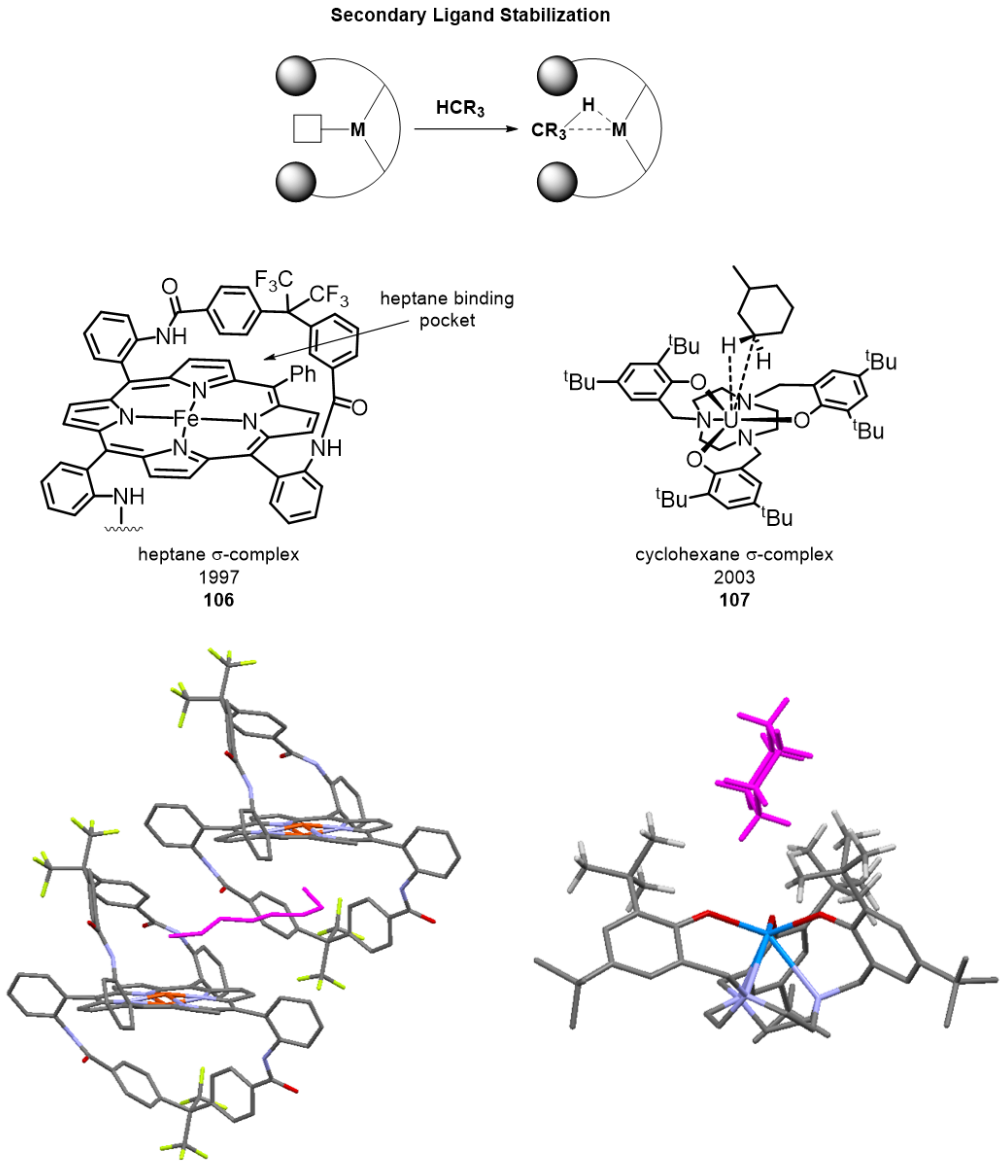

Figure 1.19 Secondary ligand stabilization for formation of **106** and **107** and crystal structures.[90,91]

Following Reed's report, Meyer and co-workers reported a series of uranium alkane σ-complexes.[93] A macrocyclic polyamine ligand with *tert*-butyl substituted aryloxide pendant arms was designed to serve as a bulky ligand platform to facilitate the formation of sterically protected unsaturated uranium complexes.[94] Formation of the six-coordinate U(III) complex **108** was achieved upon reaction of the ligand with $[U(N(SiMe_3)_2)_3]$ (Figure 1.21). Complex **108** could be characterized in solution, but attempts to structurally characterize the unsaturated uranium complex were unsuccessful. Recrystallization of the complex from acetonitrile lead to the formation of 7-coordinate complex with MeCN bound axially.[91] The structure of this complex revealed the cavity created about the open coordination site by the ligand's pendant *tert*-butyl groups leaves a single axial coordination site available. Interestingly, recrystallization of the unsaturated U complex from pentane containing a trace amount of cyclohexane resulted in the formation of a U(cyclohexane) σ-complex.[91] When 50 equivalents of methyl cyclopentane, methylcyclohexane, or neo-hexane were added to a solution of **108** in pentane, high-quality X-ray diffraction data was obtained for the respective U-alkane σ-complex.

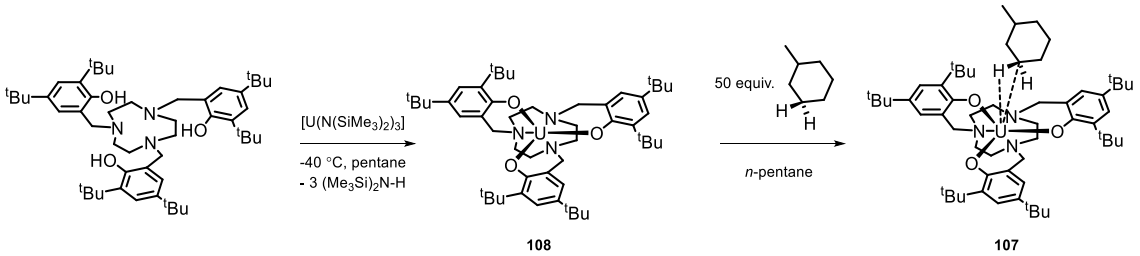

Figure 1.20 Synthesis of unsaturated U complex (**108**) and methylcyclohexane σ-complex, **107**.

The preference for **108** to bind cycloalkane over n-pentane is consistent with results described by Ball and co-workers (*vide supra*). Additionally, a competition experiment between cyclopentane and neohexane resulted in the formation of X-ray quality crystals that confirmed the preference for neohexane coordination to **108**. Overall, **108** showed a relative preference of the order neo-hexane>cyclopentane>n-pentane. Of all the complexes, neo-hexane had the closest approaching alkane carbon with a U···C distance of 3.73 Å. This is within the sum of the van der Waals radii of U and C, but is greater than the sum of the U-H-C covalent radii and C-U distances in related U(III) agostic examples. The alkane ligand and the *tert*-butyl groups of the ancillary ligand (2.12 and 2.71 Å) are also in close contact suggesting that the interaction of U with the alkane is reinforced by the hydrophobic interactions between the alkane and the ancillary ligand. Interestingly, the analogous ligand featuring adamantyl groups in place of *tert*-butyl groups does not allow for the formation of alkane adducts with U. The tert-butyl substituted ligand creates a shallower binding pocket than the adamantyl derivative which likely facilitates interaction between the U center and an alkane.

The Reed and Meyer examples were the result of fortuitous incorporation of an alkane into a hydrophobic binding pocket at the metal center (Figure 1.20). As a model for the importance of this secondary ligand stabilization, calculations suggest that an increase in the number of hydrophobic interactions can increase the binding energy of the alkane by more than 50% going from methane to propane or butane.[90] This additional stabilization can help offset the entropic penalty for σ-complex formation with intermolecular species.

1.3.3.2 Solid-state Synthesis of a Rhodium bis-σ-Alkane Complex

While the Reed and Meyer examples were likely serendipitous discoveries, Weller and co-workers were the first to successfully employ a deliberate strategy for generating and crystallographically characterizing alkane σ-complexes. In 2012 they showed that (dibpe)Rh cation (dibpe = bis(di-iso-butylphosphinoethane) supported a bis-σ-alkane interaction with norbornane serving as the bis-σ-alkane ligand (Figure 1.22). Addition of H_2 to the olefinic complex [(dtbpe)Rh(nbd)][$BArF_{24}$] (nbd = norbornadiene; $BArF_{24}$ = (3,5-$(CF_3)_2C_6H_3)_4B$), **109** resulted in the hydrogenation of the norbornadiene ligand to give **110**.[92] The conversion of **109** to **110** was monitored by solid-state ^{31}P NMR spectroscopy. Following hydrogenation, crystallinity was maintained and the solid state structure of **109** was found to possess two C-H interactions. A significant 90° twist of the norbornadiene fragment occurred in the hydrogenation to better orient the two C-H σ-bonds for coordination to the Rh center (Figure 1.23). The minimum rhodium-carbon

distances of 2.49 and 2.48 Å are within the sums of the van der Waals and covalent radii of Rh-HC, consistent with an interaction between Rh and the alkane.

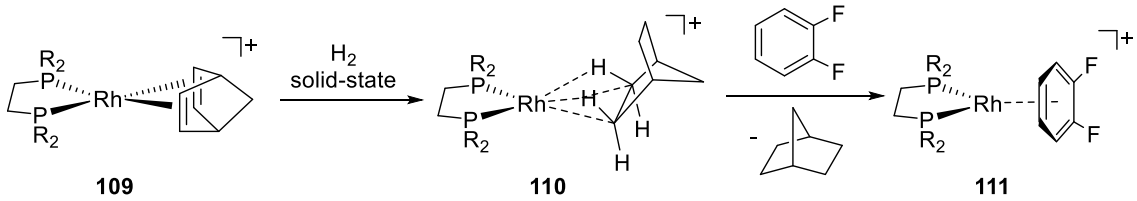

Figure 1.21 Synthesis of Rh-norbornane σ-complex **110** by solid-state hydrogenation of **109**.

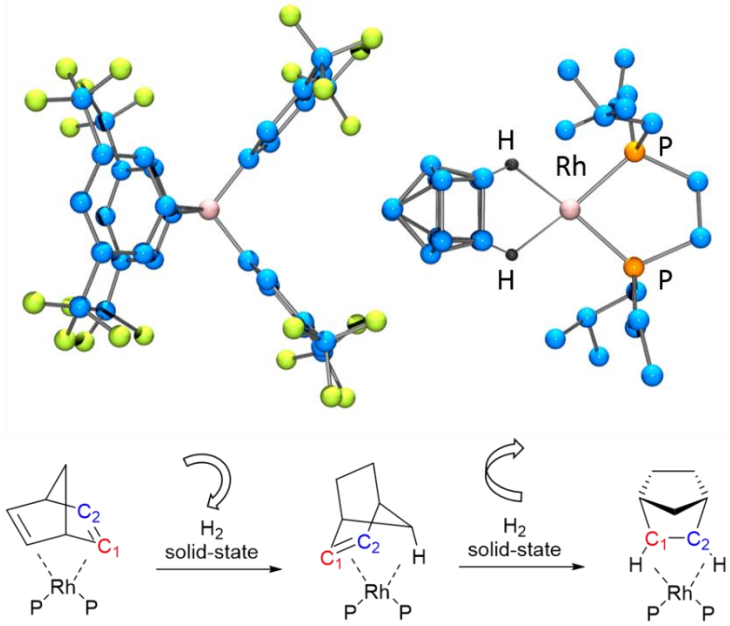

Figure 1.22[c] Crystal structure for **110** and rotation of norbornadiene during hydrogenation to form σ-complex.[92]

[c] Bottom scheme adapted from Pike, S. D.; Thompson, A. K.; Algarra, A. G.; Apperley, D. C.; Macgregor, S. A.; Weller, A. S. *Science* **2012**, *337*, 1648. Reprinted with permission from AAAS.

Computational studies of **110** suggest the major interaction between the alkane and metal center is the result of donation from the C-H bonds to Rh (20.3 kcal/mol), reinforced by π-back donation from Rh to the σ* orbital of C-H (8.9 kcal/mol). Reactivity within a crystallographic cavity formed by the tetraarylborate anion (Figure 1.23) is believed to be a significant reason why the alkane complex could be observed. This strategy circumvented the need to find a solvent or anion that would not displace the alkane from the metal center.

Over time, the single crystals were found to decompose into the previously reported solvent-coordinated complex, **111** with loss of crystallinity (Figure 1.22). Attempts to characterize the alkane complex in solution were also unsuccessful. Upon dissolving crystals of **110**, free norbornane was observed and the Rh fragment ultimately converts to the anion coordinated complex, **111**. Weller and co-workers have extended this solvent-less strategy to three other phosphine-chelated Rh species.[59] $[(R_2P(CH_2)_nPR_2)Rh(\eta^2,\eta^2\text{–}C_7H_{12})][BArF_{24}]$; R = Cy, n = 2, **112**; R = ^{i}Pr, n = 2, **113**; n = 3, **114**). For the cyclohexyl substituted phosphine species **112**, solid state ^{1}H NMR spectroscopy was used to identify the chemical shift for the coordinated C-H signal at approximately –2 ppm.

1.3.3.3 Coordination of Alkanes to Multi-Nuclear Metal Systems

In addition to studies of mononuclear alkane σ-complexes, two other examples of metal-alkane interactions have been reported in the solid state although they are not considered alkane σ-complexes. Long and co-workers used neutron powder diffraction

data to characterize the coordination of deuterated ethane and propane to iron-carboxylate based metal organic frameworks (MOFs).[95] Following stoichiometric dosing, they reported the adsorption sites for alkane coordination were at exposed Fe^{2+} cation centers with Fe-C distances of 3.08 Å for ethane and 2.90 Å for propane. In the context of MOF chemistry, alkane binding, and methane[96] in particular, is described as an ion-induced dipole interaction rather than a covalent σ-complex. A similar type of electrostatic interaction is observed in alkane interactions with potassium such as pentane coordination to potassium cations in the complex **115** (Figure 1.24).[97]

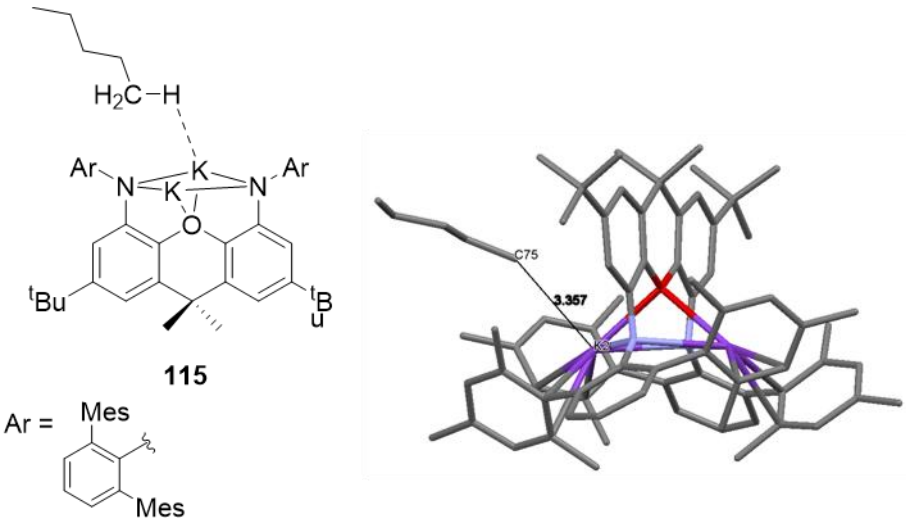

Figure 1.23 Pentane coordination to K^+ in **115** complex and crystal structure.

1.3.4 Direct Observation of a Rhodium σ-Methane and σ-Ethane Complexes

Brookhart and co-workers have extensively studied the interactions of alkanes with Rh and Ir complexes of the PONOP ligand (PONOP = 2,6-(^{t}Bu$_2$PO)$_2$C$_5$H$_3$N). The *tert*-butyl groups on the phosphine donors of the PONOP pincer ligand provide steric protection to the Rh center, and the pyridine donor exhibits only a weak *trans* influence. In 2009, the group was able to isolate [(PONOP)Rh(CH$_4$)][BArF$_{24}$], **116** (BArF$_{24}$ = (3,5-(CF$_3$)$_2$C$_6$H$_3$)$_4$B), and this compound was characterized by NMR spectroscopy in CDCl$_2$F at 163 K. Complex **116** was synthesized by utilizing the protonation strategy outlined in Scheme 1.8.[88] Upon protonation of (PONOP)RhMe, methane was effectively "trapped" within the coordination sphere of Rh, but only at low temperatures where dissociation and oxidative addition of methane are non-competitive pathways.

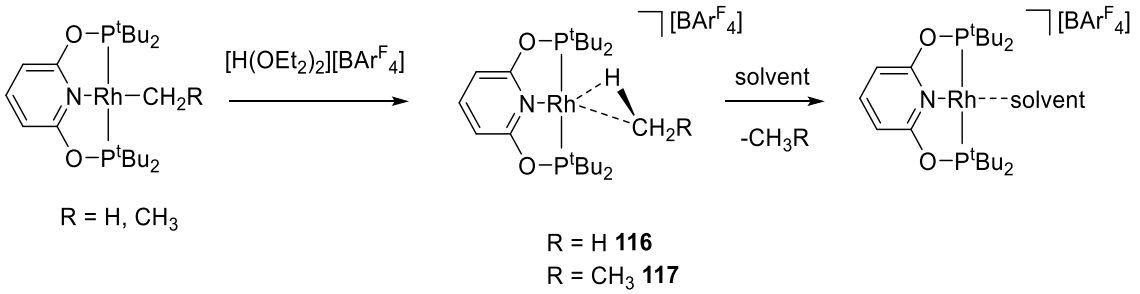

Scheme 1.8 Formation of Rh methane and ethane σ-complexes.

^{1}H and ^{13}C NMR spectroscopic studies of **116** and the ^{13}C isotopologue **116**-^{13}CH$_4$, which was synthesized to help enhance NMR spectra, were performed. The ^{1}H-coupled ^{13}C NMR spectrum of **116**-^{13}CH$_4$ exhibited a quintet at –41.7 ppm, which is significantly

upfield shifted from the Rh-Me signal in **116** (–21.8 ppm). The value of J_{CH} for **116**-$^{13}CH_4$ of 124 Hz is close to free methane in $CDCl_2F$ (125 Hz), but is much larger than that seen for the fluxional $[(PONOP)Ir(H)(Me)]^+$, which has a J_{CH} of 93 Hz and is shown to have rapid exchange of the hydride and methyl hydrogens. The ^1H NMR spectrum was consistent with a molecule of C_{2v} symmetry and featured a doublet at –0.86 ppm (J_{RhH} = 6.3 Hz) that was assigned to the hydrogens of the methane ligand. Computational experiments predicted an σ^2-*C,H* binding mode similar to what has been reported by Ball and co-workers for larger alkanes. The assignment of this binding mode as opposed to an σ^2-*H,H* binding mode is based on the optimized geometry that predicts one of the Rh-H interactions to be shorter than the rest.

In 2013, Brookhart and co-workers also reported the protonation of (PONOP)Rh-ethyl to form an ethane σ-complex (**117**).[89] Analogous to the methane σ-complex, ethane was generated within the coordination sphere of Rh by protonation of Rh-Et using $[H(OEt_2)_2][BArF_{24}]$ at –143 °C in a $CDCl_2F/CD_2Cl_2$ solvent mixture. The ethane was determined to adopt an η^2-C-H binding mode, binding with rapid exchange between the three C-H groups of the bound methyl. The ethane σ-complex **117** was found to be less stable, with a lower barrier for ethane loss ($\Delta G^‡$ = 10.9(2) kcal/mol) compared to methane loss ($\Delta G^‡$ = 14.5(4) kcal/mol). The destabilization of the ethane complex is believed to be due to the steric strain imposed by the *tert*-butyl groups of the phosphine arms which make a comparatively accommodating binding pocket for the smaller methane molecule. Compared to the J_{CH} values for Re-alkane σ-complexes such as pentane (see Section

1.3.2),[d] the changes in J_{CH} values for the Rh-methane σ-complex (J_{CH} = 124 Hz versus 125 Hz for free methane) and the Rh-ethane σ-complex (124 Hz versus 128 Hz for free ethane) are minimal.

A room-temperature stable methane σ-complex is an attractive target for the isolation and structural characterization of these usually transient species. Computational studies related to the use of the PONOP ligand have demonstrated that a room-temperature stable σ-complex may be obtainable if competing decomposition pathways are eliminated. A $\Delta G°_{298}$ of –7.8 kcal/mol was calculated as the binding affinity of methane for the unsaturated (PONOP)Rh^+ fragment. Additionally, the ground state for the Rh-methane complex is predicted to be 8 kcal/mol below the ground state for alkyl hydride complex, (PONOP)Rh(H)Me. A Pd(II)-methane complex was predicted to have a methane binding free energy of –12.7 kcal/mol.[98] An even greater methane binding affinity was predicted for the analogous Pt(II) complex, with a calculated $\Delta G°_{298}$ of –18.1 kcal/mol. These studies suggests that Pt may be the best choice of transition metal for isolating a room temperature stable methane σ-complex.

1.4 Isolation of Unsaturated Pt Complexes and the Role of *Trans*-Influence

Pincer complexes of Rh, Pd, and Pt often bias reactivity to occur at the site *trans* to the pincer ligand central donor. This reactive site is therefore highly sensitive to the

[d] 1- J_{CH} = 117 Hz versus 124.7 Hz for 1-CH of free pentane and 3-pentane σ-complex: J_{CH} = 109 Hz versus 123 pentane σ-complex:.2 Hz for 3-CH of free pentane.[81]

electronics of the central donor. Additionally, the reactive site is also greatly affected by the sterics of the flanking neutral donor substituents. This preorganization of the reactive site allows for complete steric and electronic tunability by careful choice of the central and flanking donor atoms. Thus, being able to synthetically access ligands with a range of central donors is required in order to explore the effect of tuning the labilization induced by the central atom.

Stable square planar, four-coordinate species are typical for 16-electron d^8 Pt(II) complexes. Ligand dissociation to form three-coordinate 14-electron Pt(II) intermediates is believed to be a key step in several Pt-based reactions, including the Shilov chemistry and other C-H activation processes. For T-shape geometry, two ligands are *trans* to one another and a third ligand is *trans* to an open coordination site. The *trans*-influence of the species in this third coordination site influences the stability of the T-shaped complex as well as the lability of the ligand that dissociates from the four-coordinate species. The dissociating ligand is typically a weakly coordinating species, an agostic interaction, counteranion, or a solvent molecule (Figure 1.25).[99]

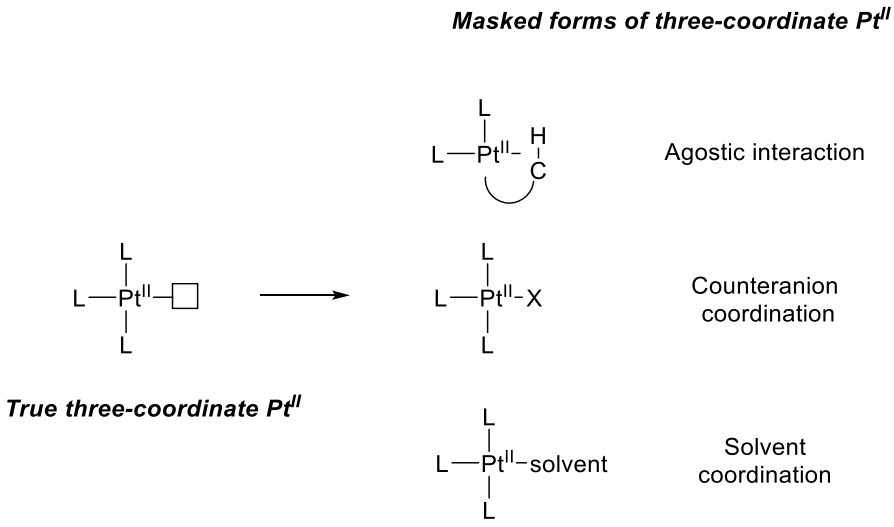

Figure 1.24 Depiction of true unsaturated three-coordinate Pt species, masked three-coordinate Pt species, and forms of masked Pt species.

True T-shaped species are rare in the literature and require steric protection of the open coordination site to avoid intra- or inter-molecular interactions. The first examples of crystallographically characterized three coordinate Pt species were reported by Brauncshweig and co-workers in 2005 when they synthesized a series of Pt complexes of the type $[(PCy_3)_2Pt\text{-}B(R)R'][BArF_{20}]$ (Figure 1.26).[100,101] NHC ligated Pt centers have also been used to isolate true T-shaped species with methyl, benzyl, and aryl groups *trans* to the open coordination site. [102-105]

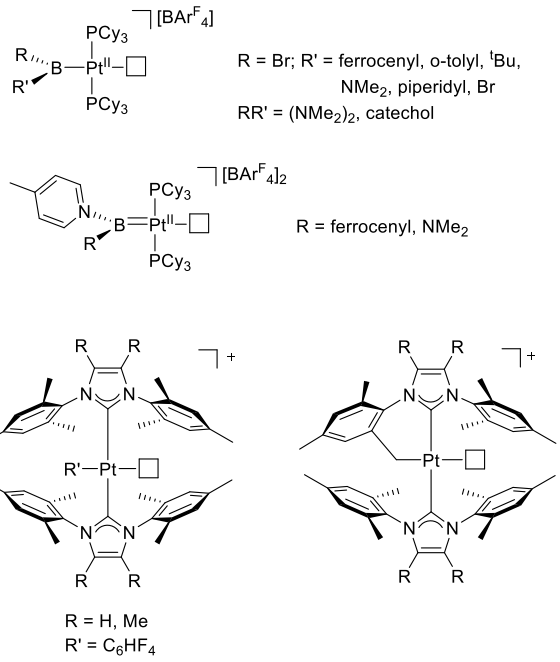

Figure 1.25 Examples of crystallographically characterized true three-coordinate Pt species.

The use of strong *trans* influence ligands has allowed for the formation of stable unsaturated transition metal complexes. The use of weaker *trans* influence ligands as central donors, may reduce the stability of truly unsaturated metal centers. Numerous examples of masked three-coordinate species have been reported which use weaker *trans*-influence ligands but still behave as three-coordinate species in a kinetic sense. Lledos and co-workers[99] used the term "masked" three-coordinate species to identify Pt species having a weakly coordinating species in the 4th coordination site but that could still behave as "operationally unsaturated" species (Figure 1.25). In the context of the synthesis of a Pt-methane σ-complex it is expected that a weak *trans*-influence ligand will promote methane binding by disfavoring a three-coordinate species.

II. SILYL-SILYLENE INTERPLAY IN CATIONIC PSiP PINCER COMPLEXES OF PLATINUM*

2.1 Introduction

The proliferation of pincer-style ligands has led to a number of discoveries in fundamental reactivity of transition metals and their catalytic applications. The success of pincer ligands is due in part to the feasibility of incorporating different combinations of donor atoms into these tridentate, meridionally-binding frameworks.[106-108] Among the many options, incorporation of silylene donors (R_2Si) remains uncommon. Recent work by Hartwig and Driess explored N-heterocyclic silylenes as side arms (**A**, Chart 2.1),[109-111] while appearance of silylene in a central donor position of a pincer has only been documented in a 1993 report by Zybill *et al.* (**B**, Chart 2.1).[112] We were especially interested in accessing a silylene housed within a structure where it is connected to phosphine side arms by *ortho*-arylene linkers. This connectivity provides for a very robust framework prearranged for meridional binding to averagely sized transition metals. Topologically similar ligands with central C,[113] N,[114] O,[115] P,[116] Sb,[117] as well as silyl[118-121] donors have been broadly explored. Recent work by Whited *et al.* implicated a silylene intermediate in some reactions of (PSiP)Rh complexes, but silylene was not directly observed (**C**, Chart 2.1).[122]

---

* Portions of this chapter are reprinted with permission from "Silyl-Silylene Interplay in Cationic PSiP Pincer Complexes of Platinum" by DeMott, J. C.; Gu, W.; McCulloch, B. J.; Herbert, D. E.; Goshert, M. D.; Walensky, J. R.; Zhou, J.; Ozerov, O. V., *Organometallics*, **2015**. Copyright 2015 American Chemical Society.

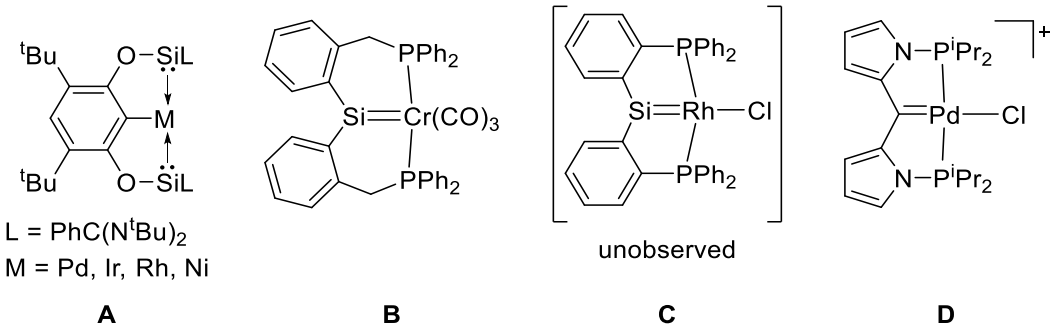

Chart 2.1 Pincer complexes incorporating silylene donors.

Our group previously reported syntheses of carbene/bis(phosphine) complexes of Pd that were synthesized by a combination of C-H activation at Pd^{II} followed by hydride abstraction (**D**, Chart 2.1).[123] Taking note of the existence of ($PSi^{H}P$)PtCl (**202**), we surmised[118] that hydride abstraction[124,125] from the HSi-Pt group could provide access to cationic silylene/bis(phosphine) complexes of Pt. Herein we report that while our efforts were successful, the silylene complexes proved to be rather unstable and displayed behavior indicative of substantial silylium character of these species.

2.2 Results and Discussion

2.2.1 Synthesis of Neutral Pt Complexes

Metallation of $PSi^{H2}P$ (**201**) with $Pt(COD)Cl_2$ in the presence of 2,6-lutidine produced a mixture of **202** and ($PSi^{Cl}P$)PtCl, but it was possible to isolate pure **202** in 85% yield after recrystallization. Milstein's synthesis of **202** using $(Me_2S)_2Pt(Me)Cl$ gave 62% yield following chromatographic purification.[118] Simple salt metathesis reactions allowed replacement of chloride in **202** with other anionic ligands to give **203**–**206** (Scheme 2.1).

Compounds **202**–**206** were characterized by multi-nuclear NMR spectroscopy and **202** by a solid-state diffraction study. The presence of a central silyl donor with an sp^3-hybridized Si atom carrying a hydrogen was evident from the NMR data: the ^{29}Si NMR resonances ranged from –1.5 ppm to 43.1 ppm ($J_{Pt\text{-}Si}$ = 608 to 1192 Hz), while in the ^{1}H NMR spectrum, a signal showing coupling to ^{29}Si ($^{1}J_{Si\text{-}H}$ between 166–193 Hz) and ^{195}Pt ($^{2}J_{Pt\text{-}H}$ between 20–60 Hz) was observed in the 5.5 to 6.5 ppm range.

2.2.2 Synthesis of Cationic Pt Complexes

Hydride abstraction reactions from the central Si-H were carried out by treatment of **202**–**206** with Ph_3C^+ salts of $[HCB_{11}Cl_{11}]^-$ or $[EtCB_{11}Cl_{11}]^-$ anions[126,127] in C_6H_5F (Scheme 2.2). The two different weakly coordinating carborane anions can be viewed as equivalent in their coordinating ability, and simply offered a way to alter solubility and crystallinity of the salts of cations of interest. Abstraction of the hydride proceeded rapidly in all cases and resulted in the formation of Ph_3CH. In the reaction of **202**, immediate formation of the major Pt-containing product was evident. The NMR spectroscopic data (^{29}Si NMR, δ 32.7 ppm) were inconsistent with the silylene formulation, for which chemical shifts of >200 ppm are expected.[124,128-132] Instead, the NMR data pointed to an isomeric structure **208** and were corroborated an XRD structural study (Figure 2.1). Isomerization of the putative **202a** into **202b** can be viewed as a net migration of chloride from Pt to Si. Similarly, abstraction of hydride from **203** and **205** led to **203b** and **205b** (^{29}Si NMR, δ 50.1 and 20.7 ppm, respectively). On the other hand, abstraction of hydride from **206** proceeded to **206b** via an intermediate (**206a**) that appeared to be associated

with the development and then disappearance of the red color. **206a** was observed by ^{31}P NMR spectroscopy in C_6H_5F at 65.5 ppm (J_{Pt-P} = 2828 Hz) but it was not long-lived enough to isolate or collect ^{29}Si NMR data. We surmised that a bulkier aryl may retard the rate of migration and prepared the mesityl derivative **207** via reaction of **202** with Mes_2Mg. Treatment of **207** with $Ph_3C[HCB_{11}Cl_{11}]$ resulted in the development of a deep red color presumed to correspond to the proposed silylene species **207a**. At room temperature, this species was observed as a broad resonance at 69.2 ppm in the ^{31}P NMR spectrum. This signal became sharper at 243 K and the coupling to ^{195}Pt (J_{Pt-P} = 2526 Hz) was further resolved. The diagnostic[124,128-132] silylene downfield signal at 323.1 ppm (J_{Pt-Si} of 879 Hz) was observed in the ^{29}Si NMR spectrum.

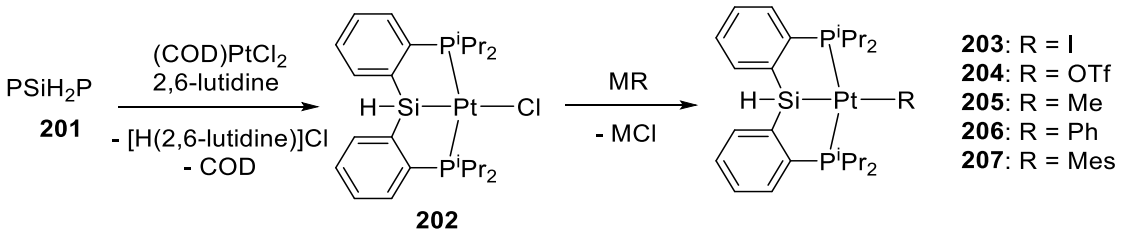

Scheme 2.1 Synthesis of (PSi^HP)PtR compounds.

2.2.3 Isomerization of Silylene Complex

In solution at ambient temperature, the silylene complex **207a** did undergo isomerization to its silyl isomer **207b**, whose structure was confirmed by a single crystal XRD study. Loss of the silylene character in **207b** arising from formal migration of

mesityl from Pt to Si was apparent from ^{29}Si NMR data, with a new signal observed at 6.84 ppm ($J_{Pt\text{-}Si}$ =1267 Hz). The rate of isomerization of **207a** to **207b** proved to be poorly reproducible: it had been observed to take place over 16 h or after as little as 30 min at ambient temperature. It is possible that the rate of isomerization is affected by the presence of varying amounts of impurities. Unfortunately, this ultimately prevented us from obtaining X-ray quality crystals or consistently pure batches of **207a** in the solid form (Figure 2.2).

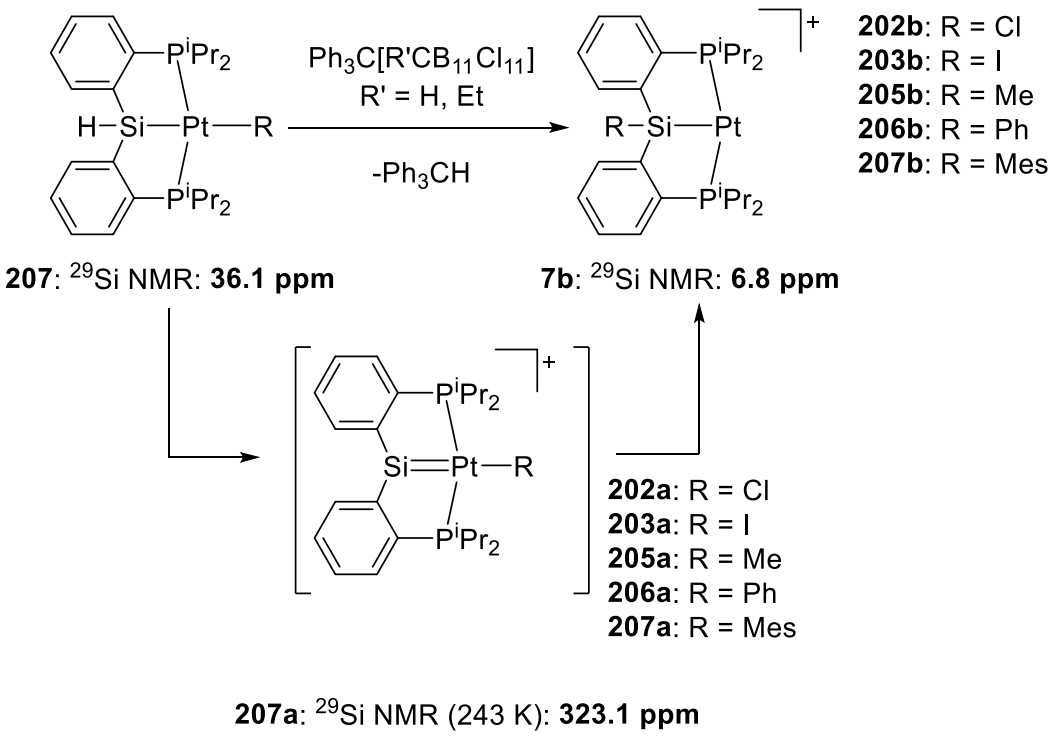

Scheme 2.2 Abstraction reactions of (PSi^{H}P)PtR.

2.2.4 DFT Calculations[e]

DFT calculations were used to examine the isomerization of cations of **202a‘**, **205a‘**, and **206a‘** into **202b‘**, **205b‘**, and **206b‘** (where ‘ indicates gas phase cation, Table 1). In accord with the experiment, the migration of Cl/Me/Ph from Pt to Si was calculated to be favorable by –18.2 kcal/mol, –34.5 kcal/mol, and –31.4 kcal/mol, respectively. Relative energies for the isomers **208a‘/208b‘** and **209a‘/209b‘** involving -SPh and -TePh substituents were also calculated, under the notion that migration of the softer Lewis bases thiolate or tellurolate from soft Pt to hard Si may be less favorable. The computed reaction free energies were less negative (–20.1 kcal/mol and –11.3 kcal/mol, respectively), but because the isomerization was still predicted to be favorable, synthesis of **208** and **209** was not attempted. The calculated barriers of 50–55 kcal/mol for the concerted intramolecular migration of the Cl/Me/Ph ligands from **202‘**/**205‘**/**206‘** are inconsistent with experimental observations. Ostensibly, another mechanism must be operative, although we cannot rule out that the computations do not capture the energetics of the system correctly, especially in the absence of anions and solvent.

[e] Dr. Jia Zhou, Dr. Justin Walensky, and Mitchell Goshert conducted computational work.

Table 2.1 Calculated energies for silylene to silyl isomerization.

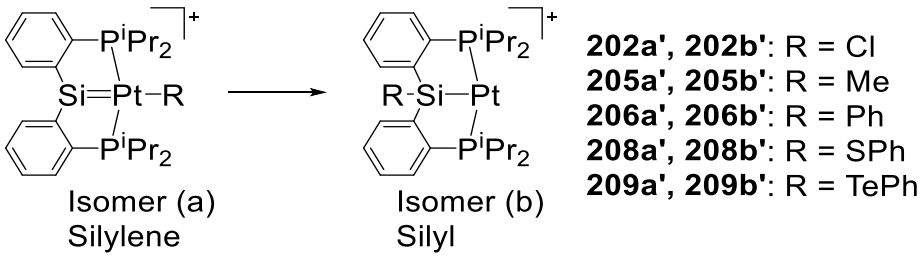

	202a‘/202b‘	205a‘/205b‘	206a‘/206b‘	208a‘/208b‘	209a‘/209b‘
$\Delta G^{\ddagger a}$	+49.6	+50.2	+55.2	+27.6	+23.2
$\Delta G_{rxn}{}^{a}$	–18.2	–34.5	–31.4	–20.1	–11.3

[a]Gas phase calculations for cationic species without $[HCB_{11}Cl_{11}]^-$ (denoted with ‘) were performed at the B3LYP level. Calculated energies are given in kcal/mol.

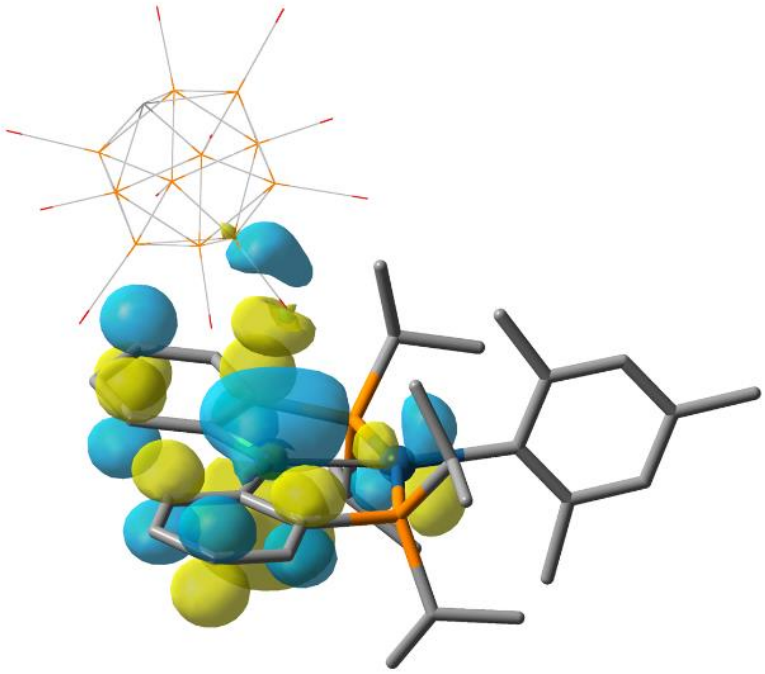

Figure 2.1 Depiction of the LUMO (isovalue = 0.03) of structure **207a** with $[HCB_{11}Cl_{11}]^-$, calculated by M06/SDD/6-31G(d). Hydrogen atoms are omitted for clarity.

The ^{29}Si NMR chemical shifts for **207a** and **206b** (including a $[HCB_{11}Cl_{11}]^-$ anion in the gas phase) were calculated to be 302.8 and 53.5 ppm. While these do not reproduce the experimental values (323 ppm for **207a** and 33.0 ppm for **206b**) precisely, they are consistent with the highly downfield chemical shift for the silylene species. The calculated Pt-Si distances in the silylene complexes are only marginally (0.02–0.08 Å) shorter than in their silyl isomers. Calculations indicate that the LUMO of **207a** (Figure 2.1) is primarily based on the Si p-orbital, with some delocalization into the aromatic rings and only a modest contribution from a d-orbital of Pt. Thus, although the Si center in **207a** is planar (i.e., sp^2-hybridized), the modest extent of π-bonding between Pt and Si suggests that **207a** may be analyzed as a platinyl-substituted silylium cation.[124,132,133] On the other hand, any shortening of the Si-Pt bond in **207a** vs **207b** owing to the increase in the Pt-Si bond order should be attenuated since the silyl Si is *trans* to an empty site, while the silylene Si is not. Not surprisingly, the difference between the Pt-Si bond lengths in silylene vs silyl is greatest in **202b**, where chloride is a weaker *trans*-influence ligand than alkyls or aryls. This analysis also explains why the $^1J_{Pt\text{-}Si}$ coupling constant in **207a** (879 Hz) is actually smaller than that in its **207b** isomer (1267 Hz) and is closer to the neutral **207** complex (608 Hz).

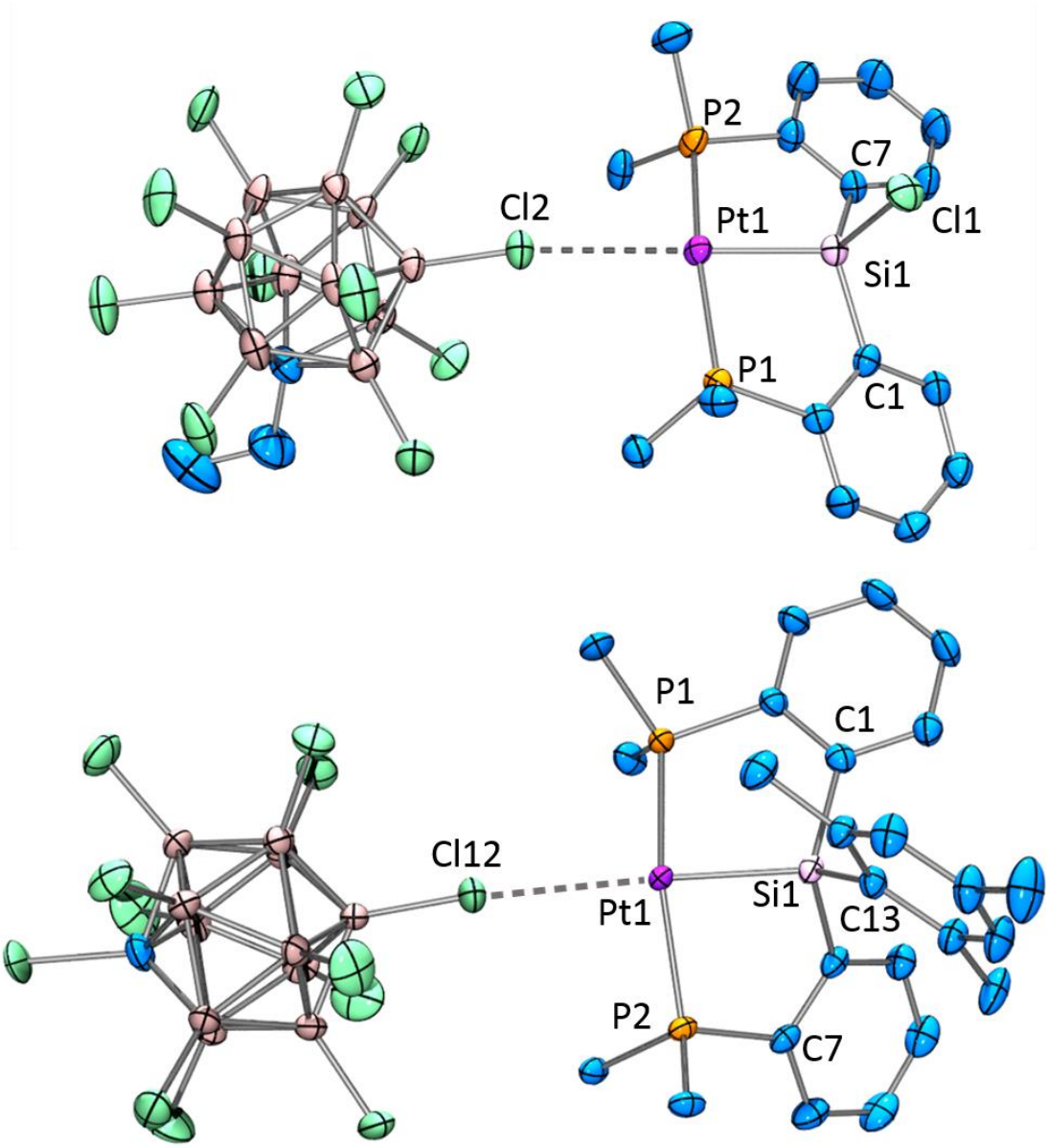

Figure 2.2 ORTEP drawings (50% probability ellipsoids) of **202b** (top) and **207b** (bottom). Omitted for clarity: H atoms, methyl groups of isopropyl. Selected distance (Å) and angles (deg) follow: For **202b**: Pt1-Si1, 2.2452(12); Si1-Cl1, 2.0785(15); Pt1-Cl2, 2.9206(13); P1-Pt1-P2, 163.30(4); Cl2-Pt1-Si1, 177.38(3). For **207b**: Pt1-Si1, 2.2756(10); Si1-C13, 1.901(4); Pt1-Cl12, 2.902(1); P1-Pt1-P2, 153.99(4); Si1-Pt1-Cl12, 167.62(4).

2.2.5 Hydrolysis of Silylene

We observed that solutions of **207b** upon standing for 26 h evolved to generate a new product **210**, resonating at 85.6 ppm in the ^{31}P NMR spectrum. An XRD study on a single crystal surprisingly revealed that **210** is a product of apparent protodesilylation of mesitylene[134] resulting in two Pt cationic units linked together by a siloxane bridge (Scheme 2.3, Figure 2.3). Dissolution of crystals from the same batch gave the same ^{31}P NMR resonance at 85.6 ppm and the formulation of the solid was supported by elemental analysis. The siloxane bridged PSiP ligand has been previously described by Milstein,[118] but in a saturated complex (Scheme 2.3) in which the Si-O bond had been formed by Si-H oxidation. Tilley's disiloxane, also a saturated system, was derived from a silylene complex by apparent addition of O-H across the Si=Ir bond.[130] In contrast, **207b** reacts by protolysis and with retention of unsaturation at Pt.

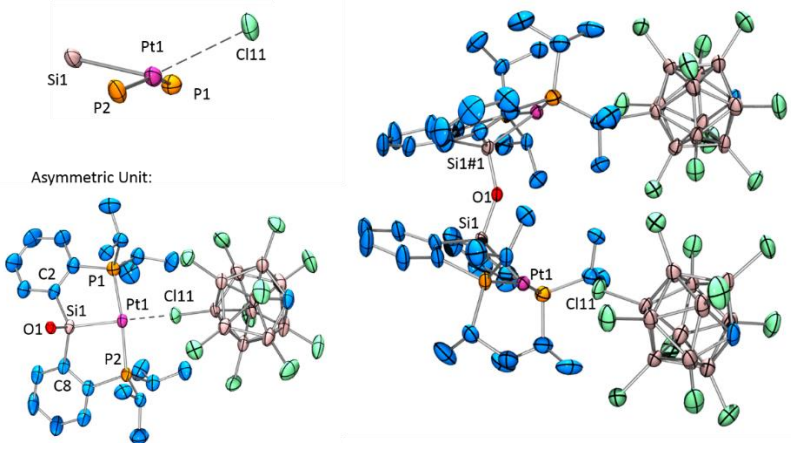

Figure 2.3 ORTEP drawing (50% probability ellipsoids) of **210.** Omitted for clarity: H atoms, ortho-difluorobenzene. Selected distance (Å) and angles (deg) follow: Pt1-Si1, 2.2499(18); Si1-O1, 1.639(2); Pt1-Cl11, 2.8753(16); O1-Si#1, 1.639(2); P1-Pt1-P2, 162.88(7); Si1-Pt1-Cl11, 141.97(6); O1-Si1-Pt1, 113.91(19); Si1-O1-Si1#1, 149.8(4).

In the structures of each of the complexes **202b**, **207b**, and **210**, one of the chlorines of the carborane anion approached the Pt center *trans* to the silyl donor. While the Si-Pt-Cl angles varied from ca. 142° to ca. 178°, the Pt···Cl distances were quite similar at ca. 2.9 Å.[f135] They are much longer than the distances between Pt and the anionic Cl ligand in **202** (2.4524(14) Å) or $PSi^{Me}P$-Pt-Cl (2.437(2) Å),[119] but they are also considerably longer than the previously reported Pt-Cl distances in Pt(II) dichloromethane complexes (2.49 to 2.62 Å)[136,137] or in the $AlCl_4$ adduct of $[PSi^{Me}P\text{-}Pt]^+$ (2.5640(9) Å).[g120] The X-ray structures of **202b**, **207b**, and **210** are also in good agreement with the calculated anion-free structures, as can be illustrated by the similarity of calculated and XRD values for the Pt-Si distance (2.284 Å for **202b'** vs 2.2452(12) Å for **202b**). All in all, the Pt···Cl distance in **202b**, **207b**, and **210** is likely indicative of a close cation-anion approach rather than a proper dative Cl→Pt bond, and is reflective of the stabilization of the empty site at Pt(II) by a strongly trans-influencing silyl ligand and the steric clash between the bulky carborane and the $PSi^{X}P$ ligand. The various degrees of weak stabilization of empty sites in otherwise three-coordinate Pt(II) complexes have recently been reviewed.[99]

[f] This distance is similar to intramolecular Pt···Cl-R contact in a recently reported Pt(IV) complex.[135]

[g] Cationic silyl complexes $[(PSi^{OH}P)Pt][B(C_6F_5)_4]$ and $[(^{Cy}De^{Me}P)Pt][MeB(C_6F_5)_3]$ were reported by Milstein and Turculet, respectively, but only observed in solution.[118,120]

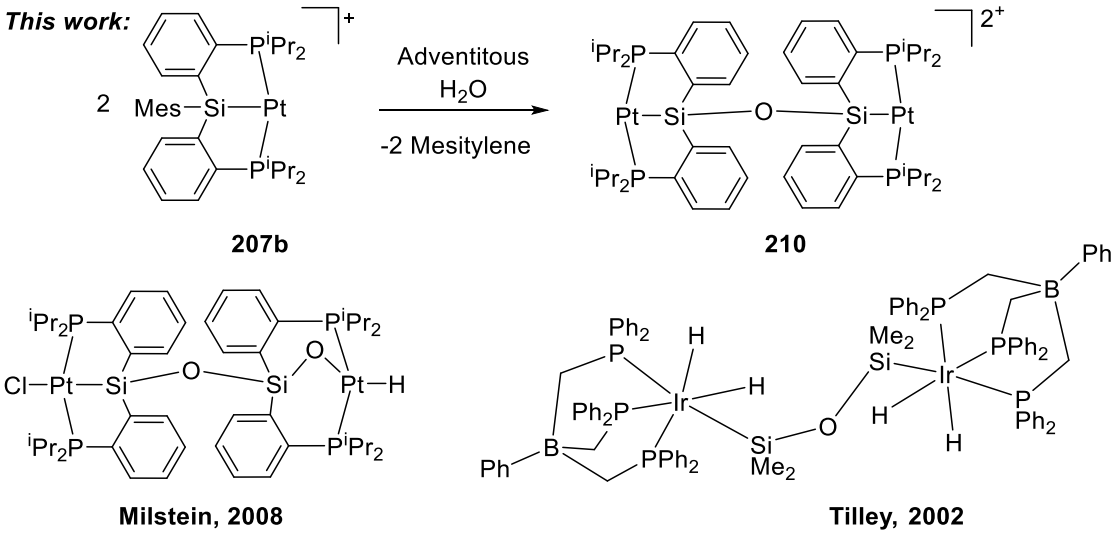

Figure 2.4 Formation of **210** and literature precedent.

2.3 Conclusions

In summary, we have been able to access a silylene-containing pincer ligand in the coordination sphere of Pt. The silylene has proven to be an observable but short-lived species that isomerizes by abstraction of anionic ligand from the position *trans* to it. DFT analysis suggests that the cationic silylene complex has only a modest degree of π-bonding with Pt and may be viewed as a silylium cation with a platinyl substituent. From this perspective, it is not surprising that it readily engages in abstraction of anionic ligands. The products of such abstraction are effectively three-coordinate cationic Pt complexes with only distant approach of the carborane anion to a position *trans* to the silyl donor. One of these complexes underwent an unexpected apparent hydrolysis by adventitious water with preservation of the highly unsaturated character at Pt.

2.4 Experimental

2.4.1 General Considerations

Unless specified otherwise, all reactions and manipulations were carried out under an argon atmosphere using glovebox or Schlenk line techniques. Dry, oxygen-free solvents were employed. Toluene, pentane, diethyl ether and C_6D_6 were dried over NaK /Ph_2CO/18-crown-6, distilled and stored over molecular sieves in an Ar-filled glove box. Fluorobenzene and C_6D_5Br were dried over CaH_2, distilled and stored over molecular sieves in an Ar-filled glove box. $Si(OEt)_4$ and 2,6-lutidine were fractionally distilled prior to use. $Ph_3C[HCB_{11}Cl_{11}]$[138] and $(COD)PtCl_2$[139]were prepared according to published procedures. All other chemicals were used as received from commercial vendors unless otherwise noted. Synthesis and characterization of complexes was conducted in collaboration with Dr. Weixing Gu. Dr. Jia Zhou, Dr. Justin Walensky, and Mitchell Goshert conducted computational work and X-ray data solutions were determined by Billy McCulloch and Dr. Dave Herbert.

NMR spectra were recorded on a Varian iNova 300 spectrometer (^{1}H NMR, 299.951 MHz, ^{13}C NMR, 75.413 MHz, ^{31}P NMR, 121.425 MHz), a Varian iNova 400 spectrometer (^{31}P NMR, 161.737 MHz, ^{13}C NMR, 100.467 MHz, ^{29}Si NMR, 79.380 MHz, ^{195}Pt, 85.891 MHz) and a Varian iNova 500 spectrometer (^{1}H NMR, 499.678 MHz, ^{13}C NMR, 125.688 MHz, ^{31}P NMR, 202.277 MHz) in noted solvents. Chemical shifts are given in δ (ppm). ^{29}Si NMR spectra were referenced externally with $SiMe_4$ at δ 0. ^{31}P NMR spectra were referenced externally with 85% phosphoric acid at δ 0. ^{195}Pt NMR spectra were referenced externally with K_2PtCl_4 aqueous solution at δ –1620. ^{1}H NMR

and ^{13}C NMR spectra were referenced using the solvent signals. Elemental analyses were performed by CALI, Inc. (Parsippany, NJ).

2.4.2 Synthesis and Characterization of Ligand and Pt Complexes

2.4.2.1 Synthesis of Ligand

Diisopropyl(2-bromophenyl)phosphine. Diisopropyl(2-bromophenyl) phosphine was synthesized based on a modified procedure.[140] 1,2-dibromobenzene (4.93 g, 0.0209 mol) was weighed in a 20-dram vial in argon-filled glovebox then transferred to a 100-mL Schlenk flask. Et_2O (30 mL) and 30 mL of THF were added. *Note: Maintaining 1:1 ratio of Et_2O:THF as solvent appeared to be necessary for temperature maintenance and may be important for the success of the reaction*. The flask was placed under Ar on a Schlenk line and placed into an EtOH/N_2(l) cooling bath between –110 °C and –120 °C. *Note: Temperatures were maintained below –110 °C to avoid decomposition of the lithiated bromobenzene. The decomposition is believed to be associated with a color change to a red solution and suspected benzyne formation.* n-BuLi (8.4 mL of 2.5 M soln in hexanes at RT, 0.021 mol) was added via syringe dropwise over 15 min. *Note: Slow dropwise addition also seems to be important. Fast addition of n-BuLi may lead to increasing the reaction mixture's temperature above –100 °C, resulting in decomposition of the lithiated bromobenzene.* The mixture remained a clear, off-white solution until about 40 min when a significant amount of white precipitate was observed. *The total reaction time should not exceed 45 min from the beginning of n-BuLi addition.* Approximately 5 minutes after observing the white precipitate formation, ClP^iPr_2 (3.3 mL, 0.021 mol) was

added dropwise over 15 min. Slow addition is necessary for this step as well. The solution became bright orange and was allowed to warm to RT over the course of 1.5–2 h. As the reaction mixture approached RT, the solution became a paler yellow with white precipitate. Volatiles were then removed under vacuum yielding an oily residue in addition to a white precipitate. The flask was brought into the glovebox and ~25 mL of pentane was added and 3.5 g silica gel were added. The mixture was left to stir for 1 h, and was then filtered over Celite. The Celite plug was washed with pentane. Pentane was removed under vacuum leaving a clear oil. The crude oil contained 89% desired product, 8% n-Bu$P^{i}Pr_2$ and less than 3% of other uncharacterized impurities. The oil from this reaction was combined with a second batch of crude product from a parallel reaction (starting from 5.68 g of dibromobenzene) and purified by distillation to give an overall yield of 7.7 g (63%) of a clear, colorless oil. Product was greater than 98% pure by $^{31}P\{^{1}H\}$. ^{1}H NMR (299.9 MHz, C_6D_6): δ 7.45 (dd, $J_{H\text{-}H}$ = 7 Hz, $J_{H\text{-}H}$ = 2 Hz, 1H, Ar-*H*), 7.10 (dt, $J_{H\text{-}H}$ = 7 Hz, $J_{H\text{-}H}$ = 2 Hz,1, Ar-*H*), 6.91 (td, $J_{H\text{-}H}$ = 7 Hz, $J_{H\text{-}H}$ = 2 Hz, 1H, Ar-*H*), 6.70 (td, $J_{H\text{-}H}$ = 7 Hz, $J_{P\text{-}H}$ = 2 Hz, 1H, Ar-*H*), 1.88 (m, 2H, C*H*Me_2), 1.10 (dd, $J_{P\text{-}H}$ = 14 Hz, $J_{H\text{-}H}$ = 7 Hz, 6H, CH*Me*$_2$), 0.86 (dd, $J_{P\text{-}H}$ = 14 Hz, $J_{H\text{-}H}$ = 7 Hz, 6H, CH*Me*$_2$). $^{31}P\{^{1}H\}$ NMR (C_6D_6): δ 8.2 (s).

PSi^{H2}P (201). To a cold solution of diisopropyl(2-bromophenyl)phosphine (4.85 g, 17.77 mmol) in diethyl ether (100 mL) was slowly added a solution of n-BuLi (7.8 mL, 2.5 M in hexanes, 19.50 mmol). The reaction mixture was stirred at room temperature for 2 h. It was then cooleded to –30 °C and slowly added to a cold solution of $Si(OEt)_4$ (1.68 g, 8.01 mmol) in diethyl ether (25 mL). The reaction mixtures was stirred at room

temperature for 12 h before a solution of $LiAlH_4$ (14.8 mL, 2.4 M in THF, 35.54 mmol) was slowly added. The resulting pale yellow suspension was stirred at room temperature for 6 h. After removal of all volatiles, the residue was redissolved in 100 mL pentane and stirred with silica gel for 1 h. The reaction mixture was passed through a short plug of Celite. (**Caution:** *The solid waste from the filtration was transfered to a Schlenk flask and quenched by acetone under Ar.*) After removal of all volatiles, a pale yellow oil was obtained. This oil was mixed with 1 mL pentane and placed in a freezer at –30 ^{o}C overnight. A white solid was obtained and washed with pentane (3 × 1 mL) to give the final product. (The final product was stored in the freezer) Yield: 2.6 g (79%). $^{31}P\{^{1}H\}$ NMR (121.425 MHz, C_6D_6): δ 2.5 (s). ^{1}H NMR (299.958 MHz, C_6D_6, Figure 2.5): δ 7.86 (dt, $J_{H\text{-}H}$ = 7 Hz, $J_{P\text{-}H}$ = 2 Hz, 2H, Ar-*H*), 7.33 (dt, $J_{H\text{-}H}$ = 7 Hz, $J_{P\text{-}H}$ = 2 Hz, 2H, Ar-*H*), 7.17–7.11 (m, 4H, Ar-*H*), 5.89 (t, $J_{P\text{-}H}$ = 9 Hz, $J_{Si\text{-}H}$ = 204 Hz, 2H, Si-*H*), 1.92 (m, 4H, C*H*Me$_2$), 1.06 (dd, $J_{P\text{-}H}$ = 14 Hz, $J_{H\text{-}H}$ = 7 Hz, 12H, CH*Me*$_2$), 0.85 (dd, $J_{P\text{-}H}$ = 14 Hz, $J_{H\text{-}H}$ = 7 Hz, 12H, CH*Me*$_2$). $^{13}C\{^{1}H\}$ NMR (125.581 MHz, C_6D_6): δ 144.4 (d, $J_{P\text{-}C}$ = 15 Hz), 144.1 (dd, $J_{P\text{-}C}$ = 46 Hz, $J_{P\text{-}C}$ = 4 Hz), 138.9 (dd, $J_{P\text{-}C}$ = 15 Hz, $J_{P\text{-}C}$ = 3 Hz), 131.8 (d, $J_{P\text{-}C}$ = 3 Hz), 129.3 (s), 128.3 (m), 25.1 (d, $J_{P\text{-}C}$ = 14 Hz, *C*HMe$_2$), 20.3 (d, $J_{P\text{-}C}$ = 18 Hz, *C*HMe$_2$), 20.0 (d, $J_{P\text{-}C}$ = 11 Hz, CH*Me*$_2$). ^{29}Si NMR (79.380 MHz, C_6D_6): δ –39.6 (tt, $J_{Si\text{-}H}$ = 204 Hz, $J_{Si\text{-}P}$ = 22 Hz).

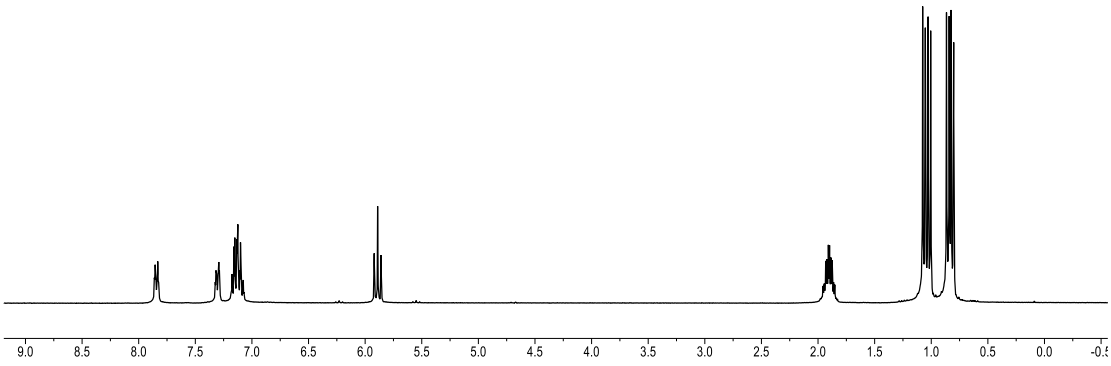

Figure 2.5 ^{1}H NMR spectrum of **201** in C_6D_6 at 23 °C measured on a 300-MHz Varian iNova.

2.4.2.2 Synthesis of Neutral Pt Complexes

(PSi^{H}P)PtCl (202).[h] To a solution of Pt(COD)Cl_2 (1.80 g, 4.76 mmol) and 2,6-lutidine (0.56 mL, 4.81 mmol) in toluene (30 mL) was added a solution of **201** (1.94 g, 4.67 mmol) in 10 mL toluene. The resulting white suspension was stirred at room temperature for 3 h, then the reaction mixtures was filtered through a short plug of Celite. After removal of all volatiles, the product was purified by recrystallization from a toluene/pentane solution at –30 ^{o}C. X-ray quality crystals were obtained by slow diffusion of pentane to a saturated toluene solution of **202**. Yield: 2.6 g (85%). $^{31}P\{^{1}H\}$ NMR (121.425 MHz, C_6D_6): δ 68.1 (s, J_{Pt-P} = 2887 Hz). ^{1}H NMR (299.958 MHz, C_6D_6, Figure 2.6): δ 8.05 (d, J_{H-H} = 7 Hz, 2H, Ar-*H*), 7.31 (m, 2H, Ar-*H*), 7.21 (t, J_{H-H} = 7 Hz, 2H, Ar-*H*), 7.11 (t, J_{H-H} = 7 Hz, 2H, Ar-*H*), 5.74 (s, J_{Pt-H} = 39 Hz, J_{Si-H} = 182 Hz, 1H, Si-*H*), 3.39

[h] Synthesis and characterization of complexes was conducted by Dr. Weixing Gu.

(m, 2H, C*H*Me$_2$), 2.46 (m, 2H, C*H*Me$_2$), 1.41 (m, 12H, CH*Me*$_2$), 1.10 (dvt, $J_{P\text{-}H}$ = 7 Hz, $J_{H\text{-}H}$ = 7 Hz, 6H, CH*Me*$_2$), 0.93 (dvt, $J_{P\text{-}H}$ = 7 Hz, $J_{H\text{-}H}$ = 7 Hz, 6H, CH*Me*$_2$). $^{13}C\{^1H\}$ NMR (100.467 MHz, C_6D_6): δ 151.4 (t, $J_{P\text{-}C}$ = 21 Hz), 141.6 (t, $J_{P\text{-}C}$ = 26 Hz), 134.1 (m), 131.1 (br m, $J_{Pt\text{-}C}$ = 44 Hz), 130.7 (br m), 128.9 (t, $J_{P\text{-}C}$ = 4 Hz), 27.7 (t, $J_{P\text{-}C}$ = 14 Hz, *C*HMe$_2$), 25.9 (t, $J_{P\text{-}C}$ = 14 Hz, *C*HMe$_2$), 19.2 (t, $J_{P\text{-}C}$ = 2 Hz, CH*Me*$_2$), 19.0 (br m, $J_{Pt\text{-}C}$ = 20 Hz, CH*Me*$_2$), 18.6 (br, CH*Me*$_2$), 18.2 (br m, $J_{Pt\text{-}C}$ = 22 Hz, CH*Me*$_2$). $^{195}Pt\{^1H\}$ NMR (85.891 MHz, C_6D_6): δ –5051.4 (t, $J_{Pt\text{-}P}$ = 2885 Hz). ^{29}Si NMR (79.380 MHz, C_6D_6): δ 11.7 (d, $J_{Si\text{-}H}$ = 180 Hz, $J_{Pt\text{-}Si}$ = 1192 Hz). Elem. An. Found (Calculated) for $C_{24}H_{37}ClP_2SiPt$: C, 44.64 (44.61); H, 5.82 (5.77)%.

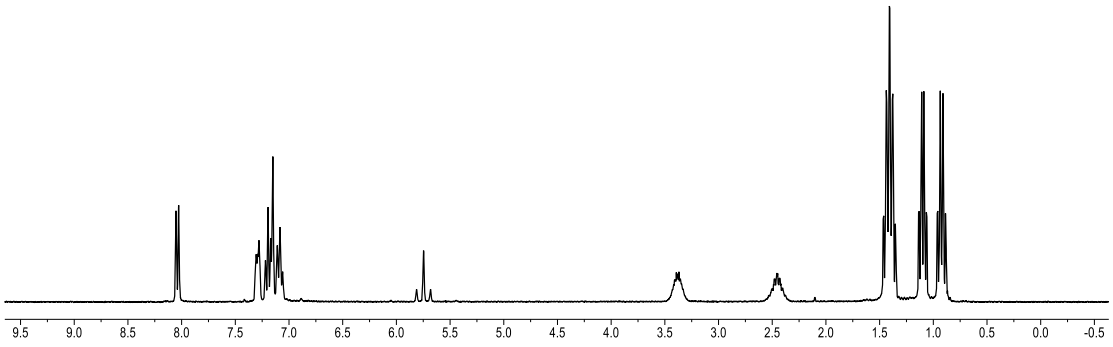

Figure 2.6 ^{1}H NMR spectrum of **202** in C_6D_6 at 23 °C measured on a 300-MHz Varian iNova.

(PSi^{H}P)PtI (203).[i] Iodotrimethylsilane (17.5 μL, 0.12 mmol) was added to a solution of **202** (53 mg, 0.08 mmol) in 2 mL toluene (30 mL). The reaction mixture was

[i] Synthesis and characterization of complexes was conducted by Dr. Weixing Gu.

stirred at room temperature for 1 h before all volatiles were removed under vacuum. The residue was redissolved in 2 mL toluene, mixed with a second portion of iodotrimethylsilane (17.5 μL, 0.12 mmol), and stirred at room temperature for 1 h. After removal of all volatiles, the product was recrystallized from a toluene/pentane solution at –30 ºC and dried under vaccuum. Yield: 36 mg (61%). $^{31}P\{^{1}H\}$ NMR (121.425 MHz, C_6D_6): δ 67.9 (s, $J_{Pt\text{-}P}$ = 2846 Hz). ^{1}H NMR (299.958 MHz, C_6D_6, Figure 2.7): δ 8.03 (d, $J_{H\text{-}H}$ = 7 Hz, 2H, Ar-*H*), 7.35 (m, 2H, Ar-*H*), 7.21 (dt, $J_{H\text{-}H}$ = 7 Hz, $J_{P\text{-}H}$ = 1 Hz, 2H, Ar-*H*), 7.09 (t, $J_{H\text{-}H}$ = 7 Hz, 2H, Ar-*H*), 5.73 (s, $J_{Pt\text{-}H}$ = 41 Hz, $J_{Si\text{-}H}$ = 184 Hz, 1H, Si-*H*), 3.51 (m, 2H, C*H*Me$_2$), 2.66 (m, 2H, C*H*Me$_2$), 1.49 (dvt, $J_{P\text{-}H}$ = 7 Hz, $J_{H\text{-}H}$ = 7 Hz, 6H, CH*Me*$_2$), 1.27 (dvt, $J_{P\text{-}H}$ = 7 Hz, $J_{H\text{-}H}$ = 7 Hz, 6H, CH*Me*$_2$), 1.02 (dvt, $J_{P\text{-}H}$ = 7 Hz, $J_{H\text{-}H}$ = 7 Hz, 6H, CH*Me*$_2$), 0.93 (dvt, $J_{P\text{-}H}$ = 7 Hz, $J_{H\text{-}H}$ = 7 Hz, 6H, CH*Me*$_2$). $^{13}C\{^{1}H\}$ NMR (100.467 MHz, C_6D_6): δ 151.3 (t, $J_{P\text{-}C}$ = 21 Hz), 141.6 (t, $J_{P\text{-}C}$ = 25 Hz), 133.9 (m), 131.3 (br m, $J_{Pt\text{-}C}$ = 43 Hz), 130.6 (br m), 129.0 (t, $J_{P\text{-}C}$ = 4 Hz), 28.6 (t, $J_{P\text{-}C}$ = 14 Hz, *C*HMe$_2$), 28.2 (t, $J_{P\text{-}C}$ = 14 Hz, *C*HMe$_2$), 20.2 (m, CH*Me*$_2$), 19.0 (m, CH*Me*$_2$), 18.8 (br, CH*Me*$_2$), 18.4 (m, $J_{Pt\text{-}C}$ = 24 Hz, CH*Me*$_2$). $^{195}Pt\{^{1}H\}$ NMR (85.891 MHz, C_6D_6): δ –5284.9 (t, $J_{Pt\text{-}P}$ = 2845 Hz). ^{29}Si NMR (79.380 MHz, C_6D_6): δ 19.6 (d, $J_{Si\text{-}H}$ = 183 Hz, $J_{Pt\text{-}Si}$ = 1160 Hz).

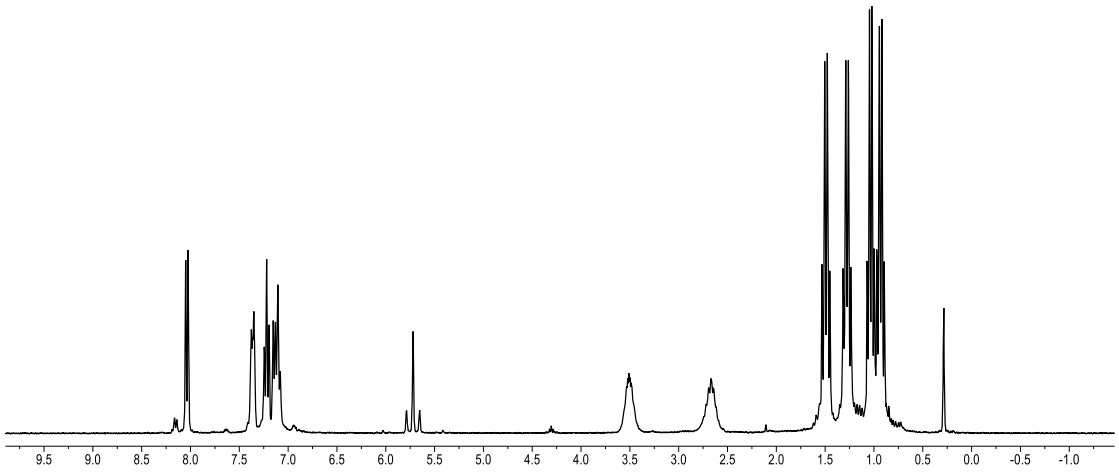

Figure 2.7 ^{1}H NMR spectrum of **203** in C_6D_6 at 23 °C measured on a 300-MHz Varian iNova.

(PSi^{H}P)PtOTf (204).[j] To a solution of **202** (27 mg, 0.04 mmol) in 0.5 mL C_6D_6 was slowly added Me_3SiOTf (75 µL, 0.41 mmol). The reaction mixture was left to stir at room temperature for 1 h. After all volatiles were removed under vacuum, another portion of C_6D_6 (0.5 mL) and Me_3SiOTf (75 µL) was added. The mixture was left at room temperature for 1 h. After removal of all volatiles, the product was washed with cold pentane and dried under vacuum at 80 ºC for 3 h. Yield: 22 mg (71%). $^{31}P\{^{1}H\}$ NMR (121.425 MHz, C_6D_6): δ 72.9 (s, J_{Pt-P} = 2941 Hz). ^{1}H NMR (299.958 MHz, C_6D_6): δ 7.87 (d, J_{H-H} = 7 Hz, 2H, Ar-*H*), 7.20–7.09 (m, 6H, Ar-*H*), 5.53 (s, J_{Pt-H} = 60 Hz, J_{Si-H} = 193 Hz, 1H, Si-*H*), 3.05–2.80 (m, 4H, C*H*Me$_2$), 1.47 (dvt, J_{P-H} = 7 Hz, J_{H-H} = 7 Hz, 6H, CH*Me*$_2$), 1.22 (dvt, J_{P-H} = 7 Hz, J_{H-H} = 7 Hz, 6H, CH*Me*$_2$), 0.96–0.81 (m, 12H, CH*Me*$_2$),. ^{19}F NMR

[j] Synthesis and characterization of complexes was conducted by Dr. Weixing Gu.

(282.211 MHz, C_6D_6): δ –77.7 (s). $^{195}Pt\{^1H\}$ NMR (85.891 MHz, C_6D_6): δ –5056.6 (t, J_{Pt-P} = 2941 Hz). ^{29}Si NMR (79.380 MHz, C_6D_6): δ –1.5 (d, J_{Si-H} = 193 Hz).

(PSi^{H}P)PtMe (205).[k] To a solution of **202** (76 mg, 0.12 mmol) in 2 mL toluene was slowly added MeLi (80 μL, 1.6 M in diethyl ether, 0.13 mmol). The reaction mixture was stirred at room temperature for 1 h and then filtered through a short plug of Celite. After removal of all volatiles, the product was recrystallized from a toluene/pentane solution at –30 ^oC and dried under vaccuum. Yield: 52 mg (71%). $^{31}P\{^1H\}$ NMR (121.425 MHz, C_6D_6): δ 67.1 (s, J_{Pt-P} = 2863 Hz). ^1H NMR (299.958 MHz, C_6D_6, Figure 2.8): δ 8.27 (d, J_{H-H} = 7 Hz, 2H, Ar-*H*), 7.42 (m, 2H, Ar-*H*), 7.25 (t, J_{H-H} = 7 Hz, 2H, Ar-*H*), 7.14 (t, J_{H-H} = 7 Hz, 2H, Ar-*H*), 6.36 (s, J_{Pt-H} = 21 Hz, J_{Si-H} = 166 Hz, 1H, Si-*H*), 2.95 (m, 2H, C*H*Me$_2$), 2.46 (m, 2H, C*H*Me$_2$), 1.32 (t, J_{P-H} = 5 Hz, 3H, Pt*Me*), 1.18 (m, 12H, CH*Me*$_2$), 0.99 (m, 12H, CH*Me*$_2$). $^{13}C\{^1H\}$ NMR (100.467 MHz, C_6D_6): δ 154.8 (t, J_{P-C} = 21 Hz), 144.8 (t, J_{P-C} = 26 Hz), 135.0 (t, J_{P-C} = 10 Hz), 130.8 (br m, J_{Pt-C} = 30 Hz), 129.8 (br m), 128.1 (br m), 28.2 (t, J_{P-C} = 14 Hz, *C*HMe$_2$), 25.7 (t, J_{P-C} = 14 Hz, *C*HMe$_2$), 19.6 (m, CH*Me*$_2$), 19.2 (m, CH*Me*$_2$), 18.4 (m, CH*Me*$_2$), 18.3 (m, CH*Me*$_2$), –3.7 (t, J_{P-C} = 8 Hz, J_{Pt-C} = 505 Hz, Pt*Me*). $^{195}Pt\{^1H\}$ NMR (85.891 MHz, C_6D_6): δ –4935.5 (t, J_{Pt-P} = 2862 Hz). ^{29}Si NMR (79.380 MHz, C_6D_6): δ 43.1 (d, J_{Si-H} = 166 Hz, J_{Pt-Si} = 660 Hz).

[k] Synthesis and characterization of complexes was conducted by Dr. Weixing Gu.

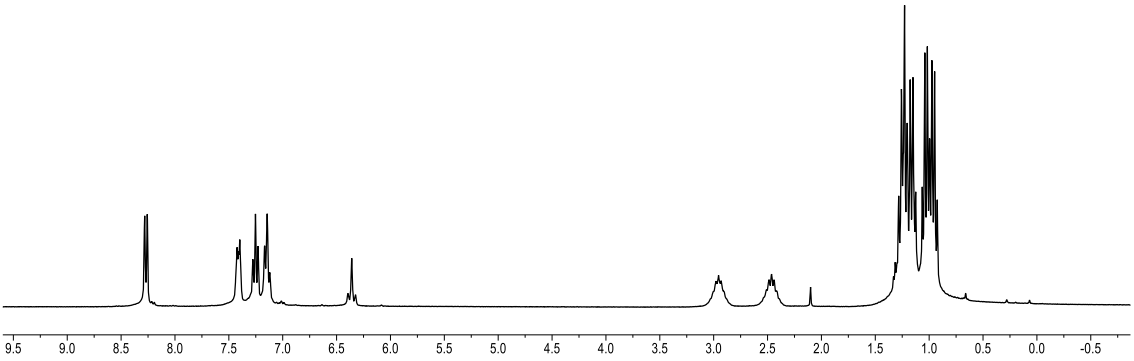

Figure 2.8 ^{1}H NMR spectrum of **205** in C_6D_6 at 23 °C measured on a 300-MHz Varian iNova.

(PSi^{H}P)PtPh (206).[1] To a solution of **202** (102 mg, 0.16 mmol) in 2 mL toluene was slowly added PhLi (90 µL, 1.8 M in dibutyl ether, 0.16 mmol). The reaction mixture was stirred at room temperature for 3 h and then filtered through a short plug of Celite. After removal of all volatiles, the product was recrystallized from a toluene/pentane solution at –30 ^{o}C and dried under vaccuum at 80 ^{o}C for 12 h. Yield: 80 mg (73%). ^{31}P{^{1}H} NMR (121.425 MHz, C_6D_6): δ 64.9 (s, J_{Pt-P} = 2848 Hz). ^{1}H NMR (499.678 MHz, C_6D_6, Figure 2.9): δ 8.26 (d, J_{H-H} = 7 Hz, 2H, Ar-*H*), 7.88 (d, J_{H-H} = 7 Hz, J_{Pt-H} = 40 Hz, 2H, Ar-*H*), 7.44 (t, J_{H-H} = 7 Hz, 2H, Ar-*H*), 7.34 (m, 2H, Ar-*H*), 7.25 (t, J_{H-H} = 7 Hz, 2H, Ar-*H*), 7.14 (m, 3H, Ar-*H*), 6.47 (s, J_{Pt-H} = 20 Hz, J_{Si-H} = 167 Hz, 1H, Si-*H*), 2.88 (m, 2H, C*H*Me$_2$), 2.40 (m, 2H, C*H*Me$_2$), 1.08 (dvt, J_{P-H} = 7 Hz, J_{H-H} = 7 Hz, 6H, CH*Me*$_2$), 0.99 (m, 12H, CH*Me*$_2$), 0.88 (dvt, J_{P-H} = 7 Hz, J_{H-H} = 7 Hz, 6H, CH*Me*$_2$). ^{13}C{^{1}H} NMR (100.467 MHz,

[1] Synthesis and characterization of complexes was conducted by Dr. Weixing Gu.

C_6D_6): δ 174.6 (t, $J_{P\text{-}C}$ = 10 Hz, $J_{Pt\text{-}C}$ = 690 Hz, Pt*Ph*), 154.3 (t, $J_{P\text{-}C}$ = 21 Hz), 143.8 (t, $J_{P\text{-}C}$ = 26 Hz), 141.1 (br m), 134.8 (br m, $J_{Pt\text{-}C}$ = 150 Hz, Pt*Ph*), 131.0 (m), 130.1 (m), 129.9 (m), 122.2 (m, Pt*Ph*), 122.0 (m, Pt*Ph*), 28.0 (t, $J_{P\text{-}C}$ = 14 Hz, *C*HMe$_2$), 24.3 (m, *C*HMe$_2$), 19.2 (m, CH*Me*$_2$), 18.8 (m, CH*Me*$_2$), 18.0 (m, CH*Me*$_2$), 17.6 (m, CH*Me*$_2$). ^{195}Pt{^{1}H} NMR (85.891 MHz, C_6D_6): δ –5024.6 (t, $J_{Pt\text{-}P}$ = 2846 Hz). ^{29}Si NMR (79.380 MHz, C_6D_6): δ 34.5 (d, $J_{Si\text{-}H}$ = 166 Hz, $J_{Pt\text{-}Si}$ = 632 Hz).

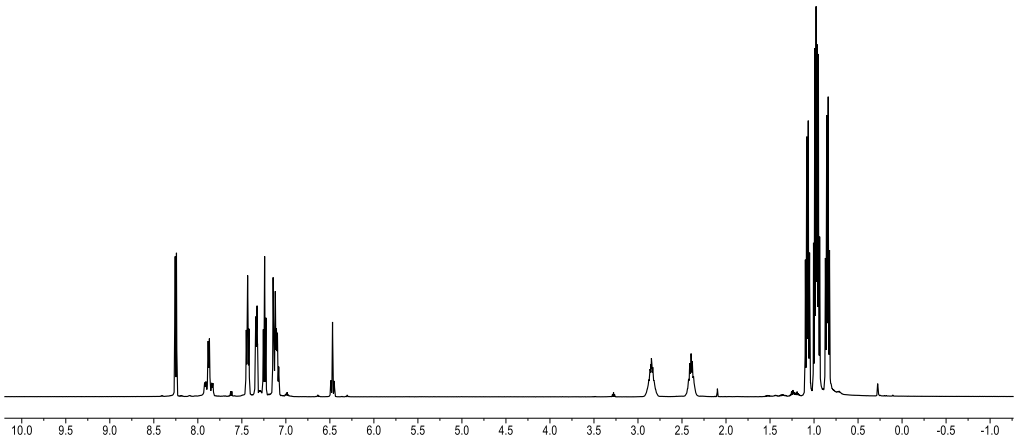

Figure 2.9 ^{1}H NMR spectrum of **206** in C_6D_6 at 23 °C measured on a 500-MHz Varian iNova.

Mes$_2$Mg•1.4THF•1.4Dioxane. This procedure is a modification of the previously reported synthesis of Mes$_2$Mg•2THF.[141] MesMgBr (4.0 mL of 1.0 M soln in diethyl ether, 4.0 mmol) was transferred to a 50-mL culture tube containing 10 mL of THF. Approximately 10 mL of 1,4-dioxane was added immediately forming a white precipitate. The mixture was stirred until it was a homogeneous suspension and then filtered over

Celite. 5 mL of dioxane was added to the filtrate and this solution was filtered over Celite. The volatiles were reduced and the solution was transferred to a 15 mL culture tube, 5 mL of dioxane was added, and the solution was centrifuged. The supernatant was then filtered through a pad of Celite giving a clear, yellow solution. Volatiles were removed yielding a pale yellow solid. The composition of the solid, including the presence of 1.4 equivalents of both THF and dioxane, was determined by ^{1}H NMR. Yield: 503 mg, 52%. ^{1}H NMR (300 MHz, toluene-d_8): δ 6.87 (s, 2H, Mes-*H*), 3.53 (m, 2H, THF-OCH_2), 3.32 (s, 8H, dioxane), 2.36 (s, 6H, ortho-CH_3), 2.29 (s, 3H, *para*-CH_3), 1.14 (m, 4H, THF-CH_2).

(PSi^{H}P)PtMes (207). To a solution of **202** (366 mg, 0.566 mmol) in approx. 40 mL toluene was added **Mes$_2$Mg•1.4THF•1.4Dioxane** (503 mg, 1.03 mmol). The reaction mixture was stirred at 90 °C for 12 h and then filtered through Celite and silica gel. After removal of all volatiles, the product was recrystallized from a toluene/pentane solution at –30 °C. Crystals were washed with cold pentane (3 × 5 mL) and dried under vaccuum. Yield: 159 mg (40%). X-ray quality crystals were obtained by slow diffusion of pentane to a saturated toluene solution of **207**. ^{31}P{^{1}H} NMR (121.425 MHz, C_6D_6): δ 63.0 (s, J_{Pt-P} = 2861 Hz). ^{1}H NMR (499.678 MHz, C_6D_6, Figure 2.10, see Table 2.2 for NMR data comparison): δ 8.23 (d, J_{H-H} = 7 Hz, 2H, Ar-*H*), 7.28–7.22 (m, 4H, Ar-*H*), 7.15–7.07 (m, 4H, Ar-*H*), 6.37 (s, J_{Pt-H} = 22 Hz, J_{Si-H} = 168 Hz, 1H, Si-*H*), 2.76 (s, 3H, Ar-*Me*), 2.74 (m, 2H, C*H*Me$_2$), 2.49 (s, 3H, Ar-*Me*), 2.45 (m, 2H, C*H*Me$_2$), 2.40 (s, 3H, Ar-*Me*), 1.11–0.93 (m, 18H, CH*Me*$_2$), 0.80 (dvt, J_{P-H} = 7 Hz, J_{H-H} = 7 Hz, 6H, CH*Me*$_2$). ^{13}C{^{1}H} NMR (125.662 MHz, C_6D_6): δ 163.7 (m, Pt-*Ar*), 153.2 (t, J_{P-C} = 20 Hz), 145.3 (m), 144.9 (s, J_{Pt-C} = 26 Hz), 143.6 (t, J_{P-C} = 26 Hz, J_{Pt-C} = 26 Hz), 134.7 (t, J_{P-C} = 10 Hz), 131.7 (s), 130.7

(s, J_{Pt-C} = 30 Hz), 130.0 (s), 128.3 (m), 29.1 (m, Ar-*Me*), 29.0 (m, Ar-*Me*), 26.2 (m, J_{Pt-C} = 54 Hz, *C*HMe$_2$), 24.1 (m, J_{P-C} = 16 Hz, *C*HMe$_2$), 21.3 (s, Ar-*Me*), 19.0 (m, CH*Me*$_2$), 18.4 (m, J_{Pt-C} = 21 Hz, CH*Me*$_2$), 17.8 (m, J_{Pt-C} = 17 Hz, CH*Me*$_2$), 17.6 (m, CH*Me*$_2$). ^{195}Pt{^{1}H} NMR (85.891 MHz, C_6D_6): δ –4934.8 (t, J_{Pt-P} = 2864 Hz). ^{29}Si NMR (79.380 MHz, C_6D_6): δ 36.1 (d, J_{Si-H} = 170 Hz, J_{Pt-Si} = 608 Hz). Elem. An. Found (Calculated) for $C_{30}H_{48}P_2SiPt$: C, 54.38 (54.31); H, 6.68 (6.63)%.

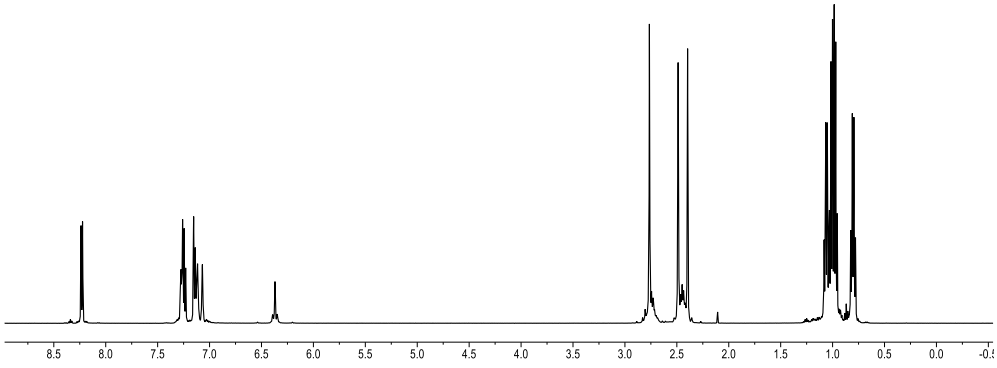

Figure 2.10 ^{1}H NMR spectrum of **207** in C_6D_6 at 23 °C measured on a 500-MHz Varian iNova.

Table 2.2 Summary of selected NMR data for PSi^{H}PPt-X species in C_6D_6.

Compound	^{31}P (J_{Pt-P})	^{29}Si(J_{Si-H}, J_{Pt-Si})	^{195}Pt	^{1}H(Si-*H*, J_{Pt-H})
(PSi^{H}P)PtCl (**202**)	68.1 (2887 Hz)	11.7 (180 Hz, 1192 Hz)	–5051	5.74 (39 Hz)
(PSi^{H}P)PtI (**203**)	67.9 (2846 Hz)	19.6 (183 Hz, 1160 Hz)	–5285	5.73 (41 Hz)
(PSi^{H}P)PtOTf (**204**)	72.9 (2941 Hz)	–1.5 (193 Hz)	–5057	5.53 (60 Hz)
(PSi^{H}P)PtMe (**205**)	67.1 (2863 Hz)	43.1 (166 Hz, 660 Hz)	–4936	6.36 (21 Hz)
(PSi^{H}P)PtPh (**206**)	64.9 (2848 Hz)	34.5 (166 Hz, 632 Hz)	–5025	6.47 (20 Hz)
(PSi^{H}P)PtMes (**207**)	63.0 (2861 Hz)	36.1 (170 Hz, 608 Hz)	–4935	6.37 (22 Hz)

2.4.2.3 Synthesis of Cationic Pt Complexes

[(PSi^{Cl}P)Pt][HCB$_{11}$Cl$_{11}$] (202b). To a solution of **202** (67 mg, 0.10 mmol) in 0.5 mL fluorobenzene was slowly added $Ph_3C[HCB_{11}Cl_{11}]$ (78 mg, 0.10 mmol). The resulting yellow solution was stirred for 1 h at room temperature and then filtered through a short plug of Celite. After removal of all volatiles, the pale yellow product was washed with pentane three times and dried under vacuum for 0.5 h. Yield: 95 mg (79 %). Addition of PMe_3 to a solution of **202b** in fluorobenzene results in the disappearance of the signal at 81.7 ppm by $^{31}P\{^1H\}$ NMR (see Figure 2.11) and the appearance of a new signal corresponding to a PMe_3 adduct of **202b** (Figure 2.12). The signal at 71 ppm remains unchanged. $^{31}P\{^1H\}$ NMR (161.737 MHz, 295 K, C_6H_5F): δ 81.7 (s, $J_{Pt\text{-}P}$ = 2910 Hz). $^{195}Pt\{^1H\}$ NMR (85.891 MHz, 295 K, C_6H_5F, Figure 2.13): δ –5011 (t, $J_{Pt\text{-}P}$ = 2959 Hz). ^{29}Si NMR (79.380 MHz, 295 K, C_6H_5F, Figure 2.14): δ 30.6 (s, $J_{Pt\text{-}Si}$ = 1651 Hz).

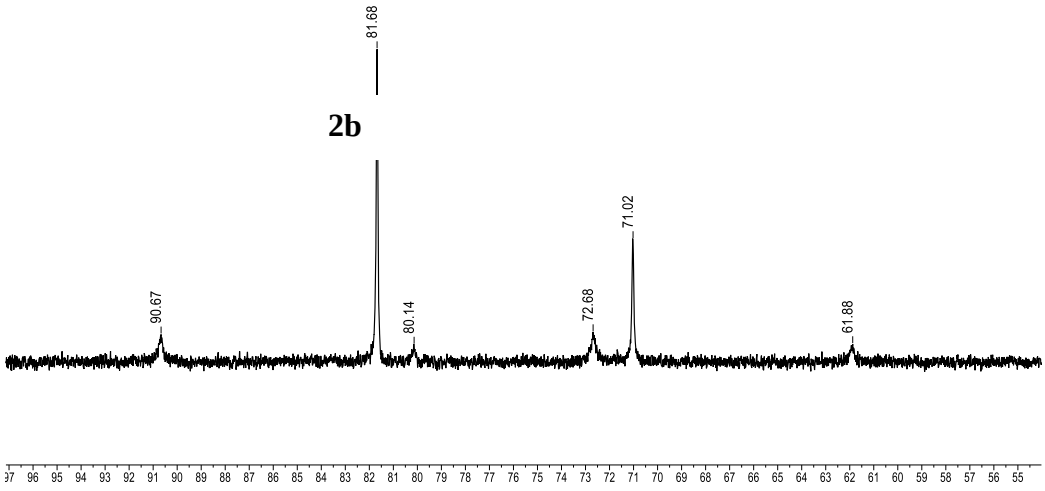

Figure 2.11 $^{31}P\{^1H\}$ NMR spectrum of **202b** in C_6H_5F at 23 °C measured on a 400-MHz Varian iNova.

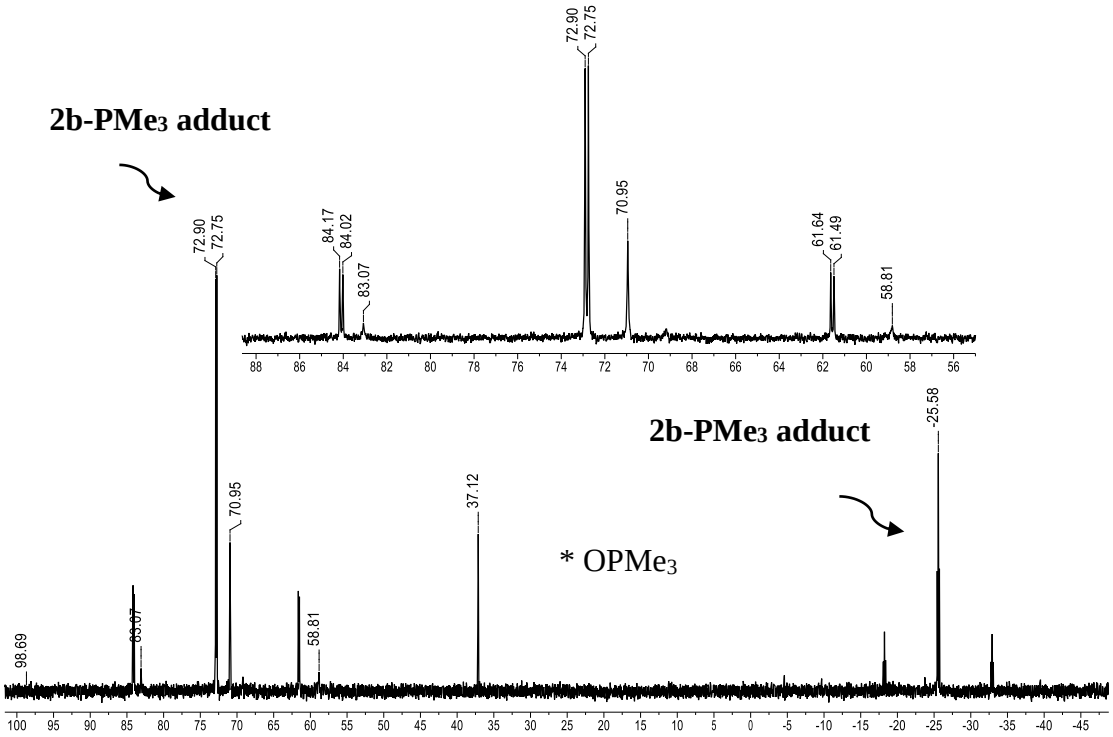

Figure 2.12 $^{31}P\{^{1}H\}$ NMR spectrum of **202b** and addition of one equivalent of PMe_3 in C_6H_5F at 23 °C measured on a 400-MHz Varian iNova.

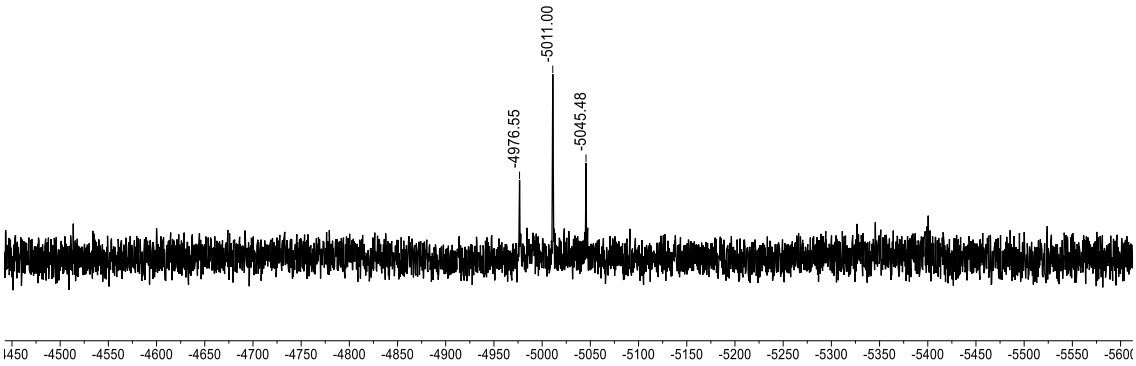

Figure 2.13 $^{195}Pt\{^{1}H\}$ NMR spectrum of **202b** in C_6H_5F at 23 °C measured on a 400-MHz Varian iNova.

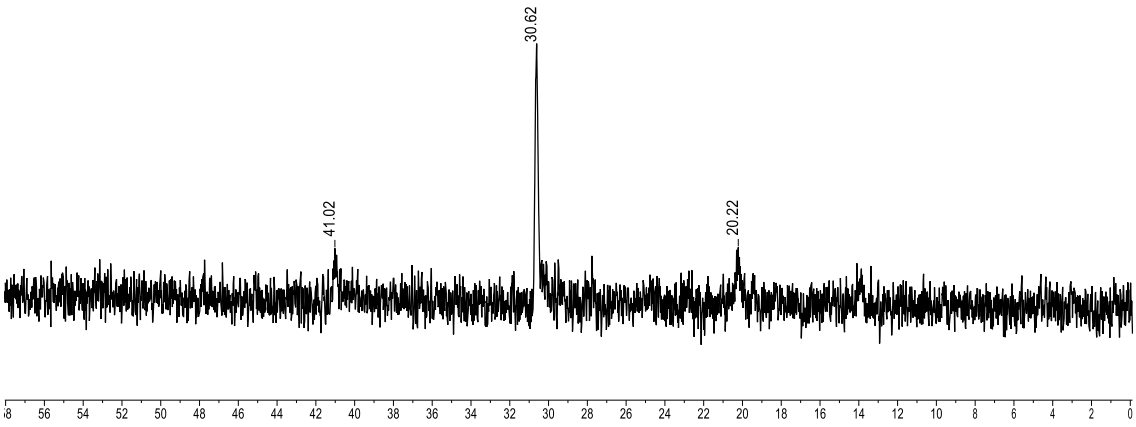

Figure 2.14 ^{29}Si NMR spectrum of **202b** in C_6H_5F at 23 °C measured on a 400-MHz Varian iNova.

[(PSi^{Cl}P)Pt][EtCB$_{11}$Cl$_{11}$] (202b-[EtCB$_{11}$Cl$_{11}$]). $Ph_3C[EtCB_{11}Cl_{11}]$[126] (58 mg, 0.073 mmol) and **202** (47 mg, 0.073 mmol) were transferred as solids to a J. Young NMR tube. Addition of 0.6 mL of fluorobenzene resulted in a yellow solution with a small amount of undissolved solid. NMR of the reaction mixture after 15 min at RT showed two signals by $^{31}P\{^1H\}$ NMR (C_6H_5F): 82.2 (J_{Pt-P} = 2904 Hz) and 71.7 (J_{Pt-P} = 2944 Hz). After two days at RT, no change in product ratio was observed by $^{31}P\{^1H\}$ NMR. After an additional 24 h at RT, there was a significant amount of crystalline precipitate in the NMR tube. X-ray quality crystals were isolated and analyzed by X-ray diffraction. The remaining crystals were washed with pentane, dried under vacuum, and collected as a yellow solid (61 mg, 70% yield). $^{31}P\{^1H\}$ NMR (121.425 MHz, 295 K, $C_6H_4F_2$, Figure 2.15): δ 82.2 (s, J_{Pt-P} = 2904 Hz). $^{195}Pt\{^1H\}$ NMR (85.891 MHz, 295 K, $C_6H_4F_2$, Figure 2.16): δ –4944 (t, J_{Pt-P} = 2880 Hz). Elem. An. Found (Calculated) for $C_{27}H_{41}P_2SiPtB_{11}Cl_{11}$: C, 27.24 (27.14); H, 3.56 (3.46)%.

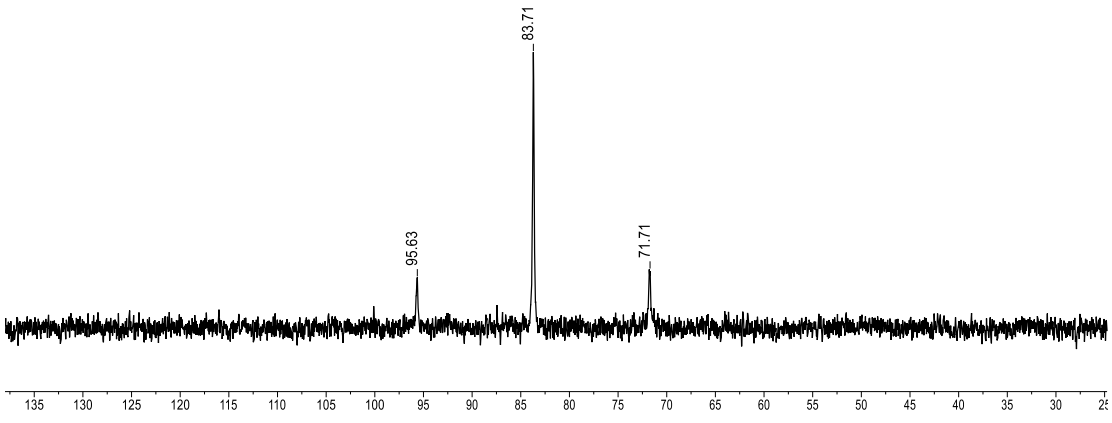

Figure 2.15 $^{31}P\{^1H\}$ NMR spectrum of **202b-[EtCB$_{11}$Cl$_{11}$]** in $C_6H_4F_2$ at 23 °C measured on a 300-MHz Varian iNova.

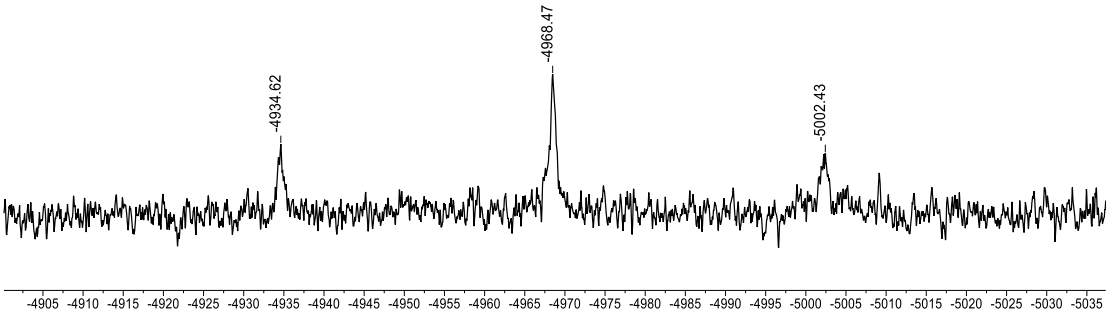

Figure 2.16 $^{195}Pt\{^{1}H\}$ NMR spectrum of **202b-[EtCB$_{11}$Cl$_{11}$]** in $C_6H_4F_2$ at 23 °C measured on a 400-MHz Varian iNova.

[(PSi^{i}P)Pt][HCB$_{11}$Cl$_{11}$] (203b).[m] To a solution of **203** (20 mg, 0.027 mmol) in 0.3 mL fluorobenzene was slowly added $Ph_3C[HCB_{11}Cl_{11}]$ (21 mg, 0.027 mmol). The resulting yellow solution was stirred at room temperature for 1 h. $^{31}P\{^{1}H\}$ NMR (121.425 MHz, 295 K, C_6H_5F, Figure 2.18): δ 69.3 (s, J_{Pt-P} = 2837 Hz). ^{29}Si NMR (79.380 MHz, 295 K, C_6H_5F, Figure 2.17): δ 50.1 (s).

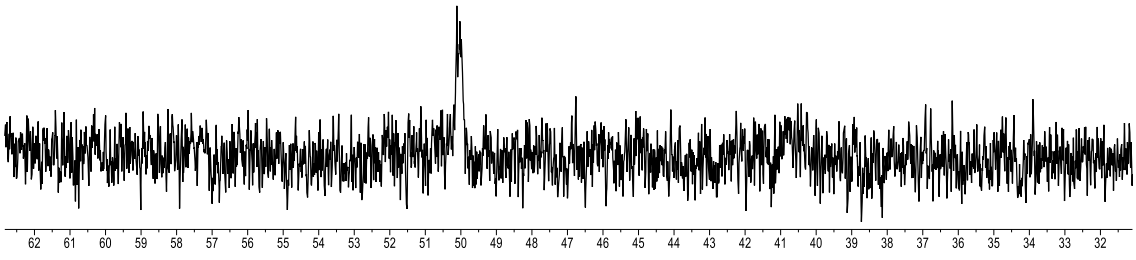

Figure 2.17 ^{29}Si NMR spectrum of **203b** in C_6H_5F at 23 °C measured on a 400-MHz Varian iNova.

[m] Synthesis and characterization of complexes was conducted by Dr. Weixing Gu.

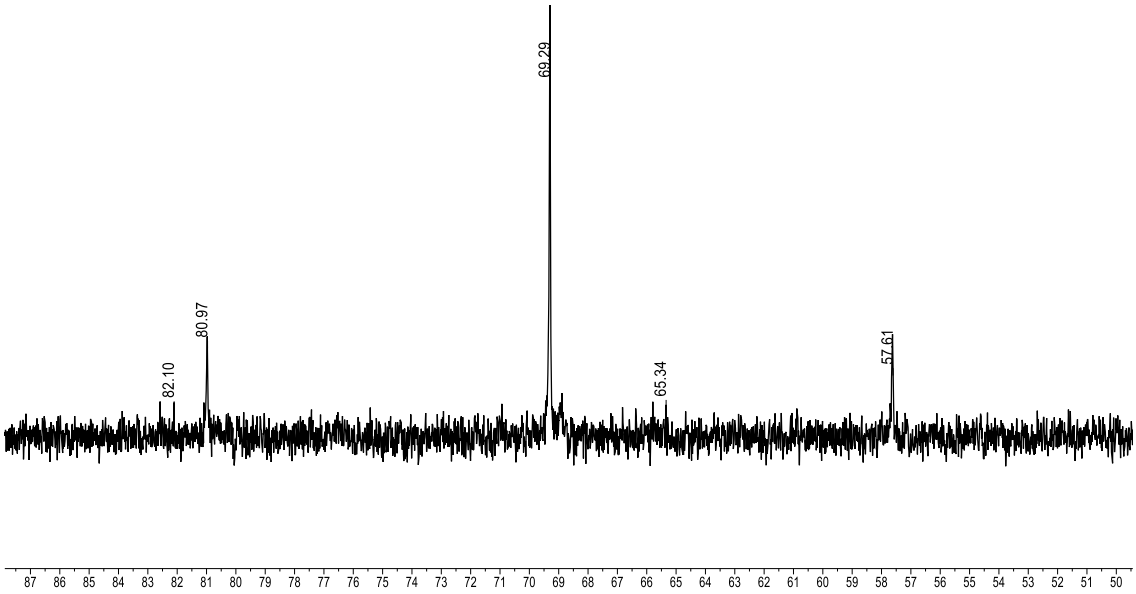

Figure 2.18 $^{31}P\{^{1}H\}$ NMR spectrum of **203b** in C_6H_5F at 23 °C measured on a 300-MHz Varian iNova.

[(PSi^{Me}P)Pt][HCB$_{11}$Cl$_{11}$] (205b).[n] To a solution of **205** (45 mg, 0.074 mmol) in 0.5 mL fluorobenzene was slowly added $Ph_3C[HCB_{11}Cl_{11}]$ (56 mg, 0.704 mmol). The resulting yellow solution was stirred at room temperature for 2 h and then filtered through a short plug of Celite. After removal of all volatiles, the yellow product was washed with pentane three times and dried under vacuum for 3 h. Yield: 76 mg (74%). $^{31}P\{^{1}H\}$ NMR (121.425 MHz, 295 K, C_6H_5F, Figure 2.19): δ 80.8 (s, J_{Pt-P} = 2980 Hz). ^{29}Si NMR (79.380 MHz, 295 K, C_6H_5F, Figure 2.20): δ 20.7 (s).

[n] Synthesis and characterization of complexes was conducted by Dr. Weixing Gu.

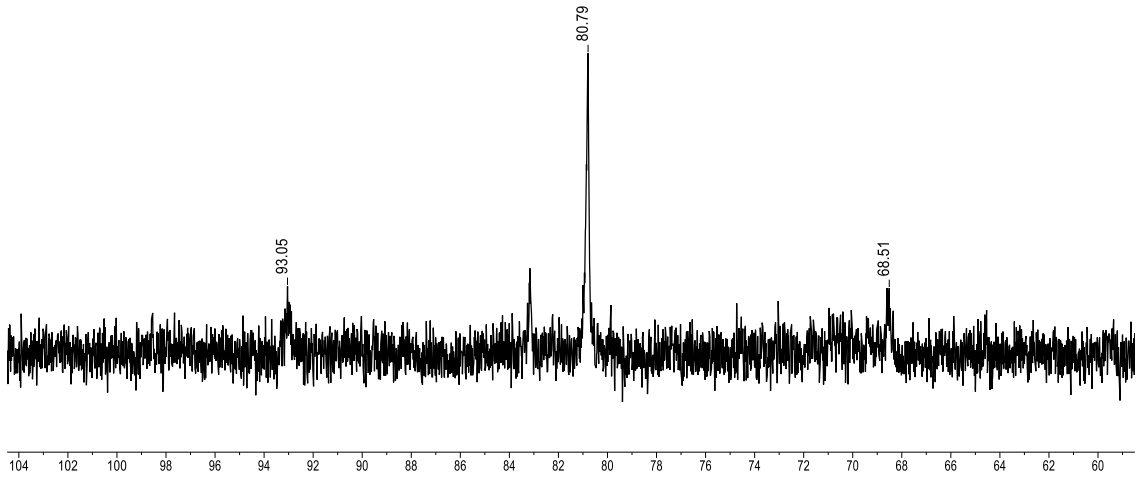

Figure 2.19 $^{31}P\{^{1}H\}$ NMR spectrum of **205b** in C_6H_5F at 23 °C measured on a 300-MHz Varian iNova.

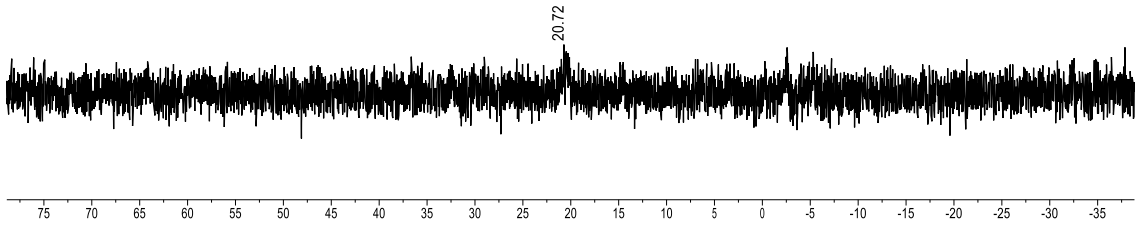

Figure 2.20 ^{29}Si NMR spectrum of **205b** in C_6H_5F at 23 °C measured on a 400-MHz Varian iNova.

[(PSi^{Ph}P)Pt][HCB$_{11}$Cl$_{11}$] (206b).[o] $Ph_3C[HCB_{11}Cl_{11}]$ (50 mg, 0.065 mmol) was slowly added to a solution of **206** (45 mg, 0.065 mmol) in 0.5 mL fluorobenzene. The resulting deep red solution was stirred at room temperature for 2 h. $^{31}P\{^1H\}$ NMR (121.425 MHz, 295 K, C_6H_5F): δ 65.5 (s, J_{Pt-P} = 2828 Hz, [**(P$_2$Si=)PtPh][HCB$_{11}$Cl$_{11}$]**, **206a**), 71.0 (s, J_{Pt-P} = 2942 Hz, **206b**, Figure 2.21). The mixture slowly became a pale yellow solution. $^{31}P\{^1H\}$ NMR (121.425 MHz, 295 K, C_6H_5F): δ 71.1 (s, J_{Pt-P} = 2942 Hz). ^{29}Si NMR (79.380 MHz, 295 K, C_6H_5F, Figure 2.22): δ 33.0 (s).

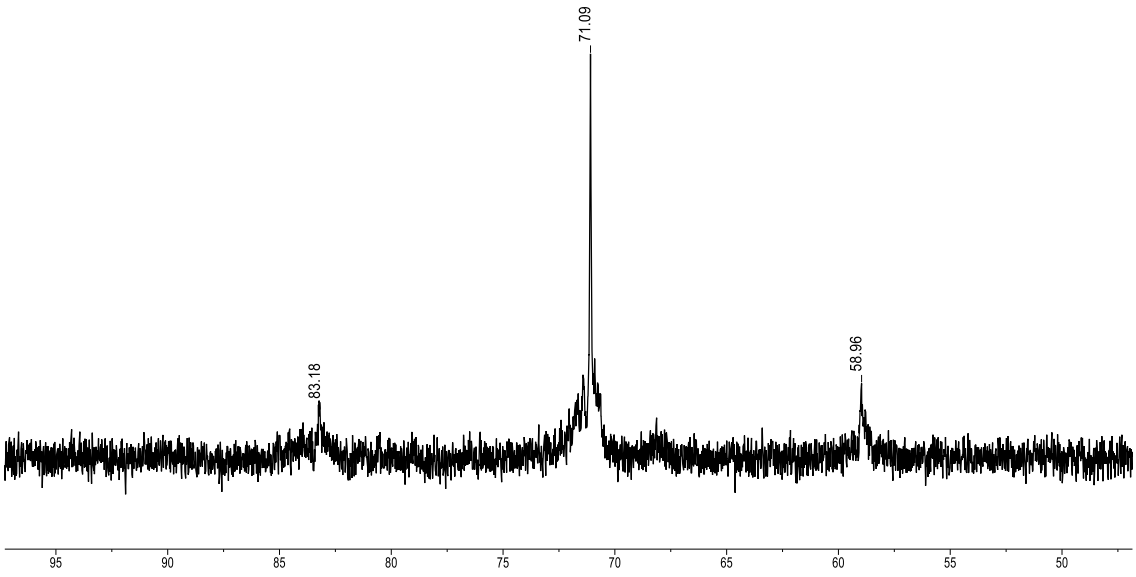

Figure 2.21 $^{31}P\{^1H\}$ NMR spectrum of **206b** in C_6H_5F at 23 °C measured on a 300-MHz Varian iNova.

[o] Synthesis and characterization of complexes was conducted by Dr. Weixing Gu.

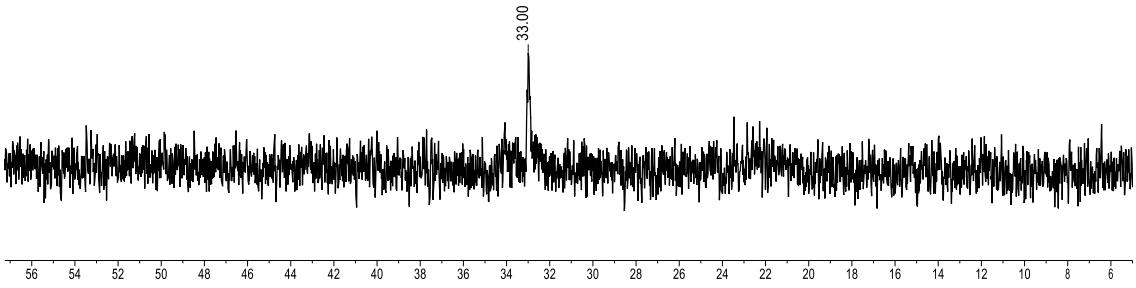

Figure 2.22 ^{29}Si NMR spectrum of **206b** in C_6H_5F at 23 °C measured on a 400-MHz Varian iNova.

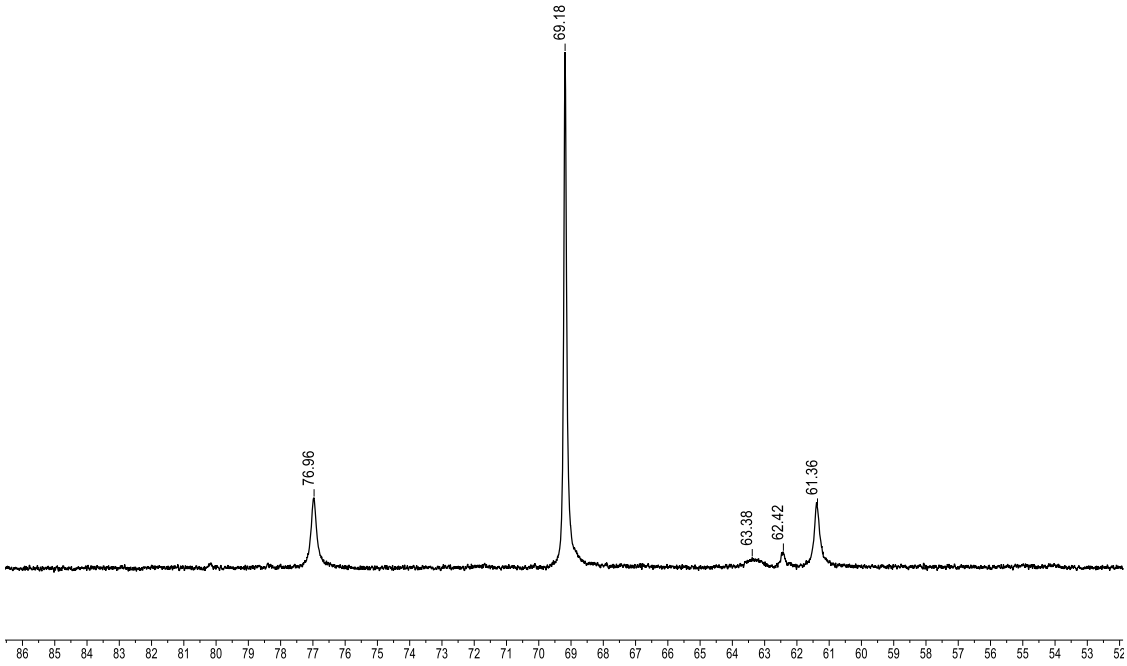

Figure 2.23 $^{31}P\{^1H\}$ NMR spectrum of **207a** in C_6H_5F at –30 °C measured on a 400-MHz Varian iNova.

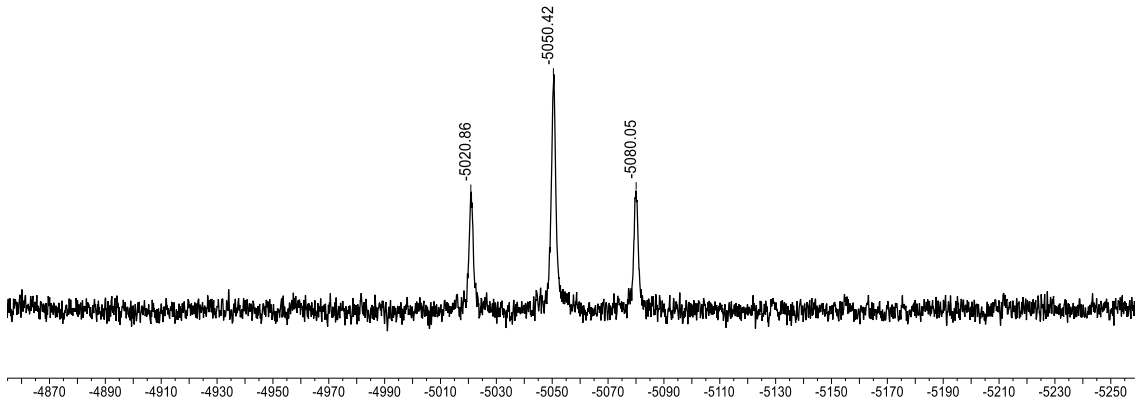

Figure 2.24 $^{195}Pt\{^{1}H\}$ NMR spectrum of **207a** in C_6H_5F at –30 °C measured on a 400-MHz Varian iNova.

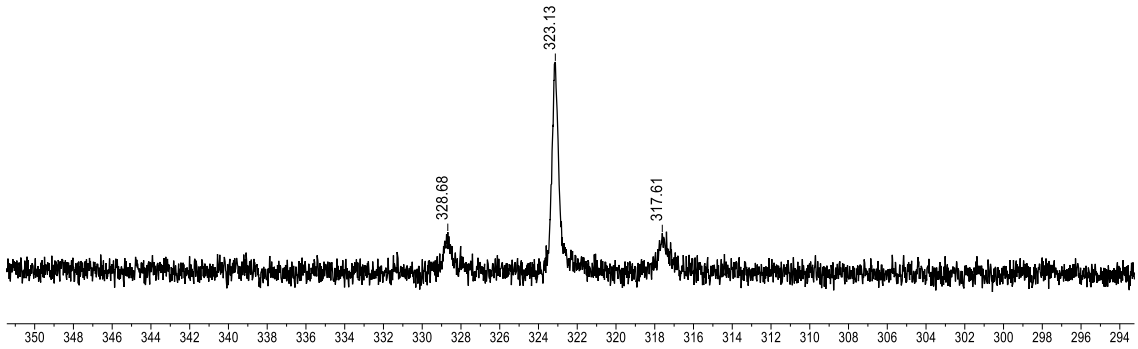

Figure 2.25 ^{29}Si NMR spectrum of **207a** in C_6H_5F at –30 °C measured on a 400-MHz Varian iNova.

[(P$_2$Si=)PtMes][HCB$_{11}$Cl$_{11}$] (207a) Isomerization to Form [(PSi^{Mes}P)Pt][HCB$_{11}$Cl$_{11}$] (207b). $Ph_3C[HCB_{11}Cl_{11}]$ (16 mg, 0.021 mmol) was reacted with **207** (15 mg, 0.021 mmol in 0.7 mL in C_6H_5F) forming a deep red solution. A broad signal at 69.2 ppm corresponding to **207a** was observed by $^{31}P\{^{1}H\}$ NMR along with an unidentified signal at 81.8 ppm (Figure 2.26, also see Figures 2.23-2.25). After 16 h at RT, the red solution of **207a** became a pale yellow and a new signal was observed by

$^{31}P\{^{1}H\}$ NMR (C_6H_5F) at 79.2 ppm, $J_{Pt\text{-}P}$ = 3115 Hz corresponding to **207b** (Figure 2.26). Layering this yellow NMR solution with pentane yielded crystalline material suitable for X-ray diffraction studies. NMR characterization for **207b**: $^{31}P\{^{1}H\}$ NMR (202.3 MHz, 295 K, C_6H_5F): 79.2 ppm ($J_{Pt\text{-}P}$ = 3115 Hz). $^{195}Pt\{^{1}H\}$ NMR (85.891 MHz, 295 K, C_6H_5F, Figure 2.27): δ –4860.1 (t, $J_{Pt\text{-}P}$ = 3126 Hz). ^{29}Si NMR (79.380 MHz, 295 K, C_6H_5F, Figure 2.28): δ 6.84 (s, $J_{Pt\text{-}Si}$ = 1267 Hz). Elem. An. Found (Calculated) for $C_{34}H_{48}B_{11}Cl_{11}P_2PtSi$: C, 32.67 (32.65); H, 3.96 (3.87)%.

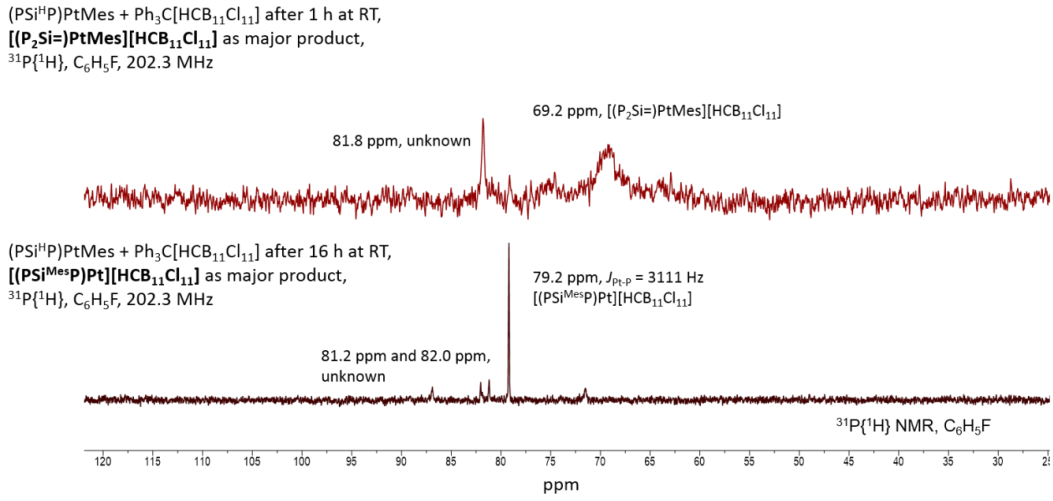

Figure 2.26 Stack plot of $^{31}P\{^{1}H\}$ NMR spectra for decomposition of **207a** to **207b** in C_6H_5F at 23 °C.

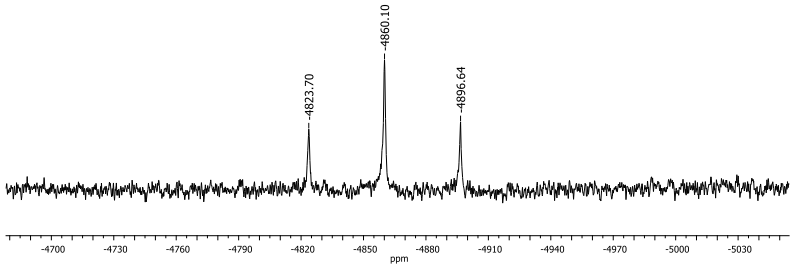

Figure 2.27 $^{195}Pt\{^{1}H\}$ NMR spectrum of **207b** in C_6H_5F at RT measured on a 400-MHz Varian iNova.

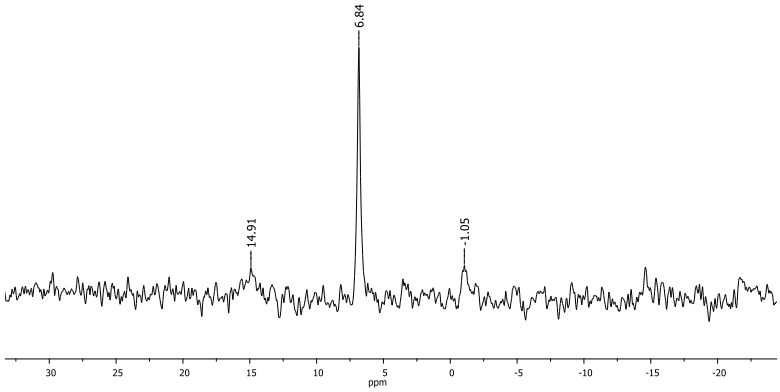

Figure 2.28 ^{29}Si NMR spectrum of **207b** in C_6H_5F at RT measured on a 400-MHz Varian iNova.

Hydrolysis of [(PSi^{Mes}P)Pt][HCB$_{11}$Cl$_{11}$] in C$_6$H$_4$F$_2$ at 23 °C. 207 (74 mg, 0.10 mmol in 0.7 mL in orthodifluorobenzene (ODFB)) was reacted with $Ph_3C[HCB_{11}Cl_{11}]$ (78 mg, 0.10 mmol) forming a deep red solution. After 2 h at RT, the red solution became pale yellow and a new signal was observed by $^{31}P\{^{1}H\}$ NMR at 78.6 ppm, $J_{Pt\text{-}P}$ = 3113 Hz, showing conversion of **207a** to **207b** (Figure 2.29). Further conversion of this product was observed after 26 h at RT. Accompanying the disappearance of the signal for **207b**, a new signal was observed by $^{31}P\{^{1}H\}$ NMR at 85.6 ppm, $J_{Pt\text{-}P}$ = 3020 Hz. After 50 h at RT, the

product at 85.6 ppm remained the major species present. X-ray quality crystals were grown from this NMR solution in ODFB layered with pentane. X-ray diffraction studies indicated the formation of **[O[(PSiP)Pt]$_2$]•2[HCB$_{11}$Cl$_{11}$] (210)**. This product is believed to have formed due to the presence of adventitious water and the subsequent hydrolysis of **207b.** Free mesitylene was observed by ^{1}H NMR. The remainder of the crystals were washed with pentane and dried under vacuum. NMR analysis of the crystals used for the X-ray diffraction studies was consistent with the signal at 85.6 ppm belonging to **210**. See Table 2.3 for NMR data comparison for all cationic Pt species. NMR characterization for **210**: ^{31}P{^{1}H} NMR (202.3 MHz, 295 K, $C_6H_4F_2$): 85.6 ppm ($J_{Pt\text{-}P}$ = 3020 Hz). Elem. An. Found (Calculated) for $C_{50}H_{74}B_{22}Cl_{22}OP_4Pt_2Si_2$: C, 26.26 (26.35); H, 3.03 (3.27)%.

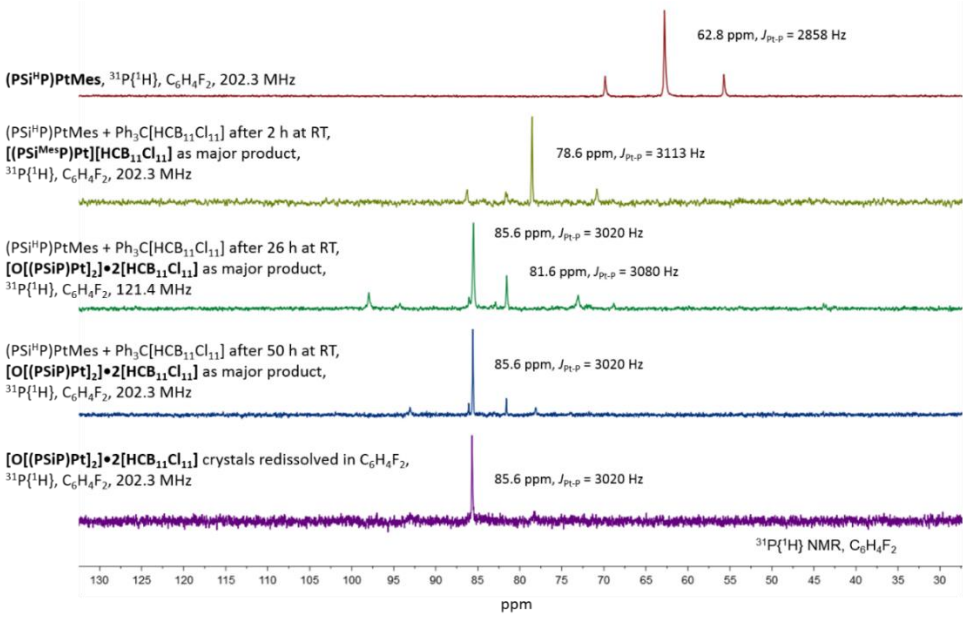

Figure 2.29 Stack plot of ^{31}P{^{1}H} NMR spectra for hydrolysis of **207b** to form **210** in $C_6H_4F_2$ at 23 °C.

Table 2.3 Summary of NMR data table for cationic silyl PSiXPPt and silylene species.

Compound (X=)	^{31}P (J_{Pt-P})	^{29}Si(J_{Si-Pt})	^{195}Pt
Cl (**202b**)[a]	81.7 (2910 Hz)	30.6 (1651 Hz)	–5011
Cl (**202b-[EtCB$_{11}$Cl$_{11}$]**)[b]	82.2 (2904 Hz)		–4944
I (**203b**)[a]	69.3 (2837 Hz)	50.1	
Me (**205b**)[a]	80.8 (2980 Hz)	20.7	
Ph-silylene (**206a**) [a]	65.5 (2828 Hz)		
Ph (**206b**)[a]	71.1 (2942 Hz)	33.0	
Mes-silylene (**207a**)[c]	69.2 (2526 Hz)	323.1 (879 Hz)	–5050
Mes (**207b**)[a]	79.2 (3115 Hz)	6.84 (1267 Hz)	–4860
-O- (**210**)[b]	85.6 (3020 Hz)		

[a]NMR in C_6H_5F at 296 K. [b]NMR in $C_6H_4F_2$ at 296 K. [c]NMR in C_6H_5F at 243 K.

2.4.3 X-Ray Structural Determination Details

2.4.3.1 X-Ray Data Collection, Solution, and Refinement for 202[p]

A colorless block of suitable size and quality (0.2 × 0.2 × 0.1 mm) was selected from a representative sample of crystals of the same habit using an optical microscope, mounted onto a nylon loop and placed in a cold stream of nitrogen (110 K). Low-temperature X-ray data were obtained on a Bruker APEXII CCD based diffractometer (Mo sealed X-ray tube, K_α = 0.71073 Å). All diffractometer manipulations, including data collection, integration and scaling were carried out using the Bruker APEXII software.[142] An absorption correction was applied using SADABS.[143] The space group was determined on the basis of systematic absences and intensity statistics. The structure was first solved in the triclinic *P*-1 space group to produce an adequate model, and then re-solved in the monoclinic space group $P2_1/c$ by direct methods using XS[144] (incorporated in TL) and refined by full-matrix least squares on F^2. No obvious missed symmetry was subsequently reported by PLATON.[145] All non-hydrogen atoms were refined with anisotropic thermal parameters. Hydrogen atoms were placed in idealized positions and refined using riding model with the exception of the hydrogen bound to silicon, which was located from the difference map. The structure was refined (weighted least squares refinement on F^2) to convergence (see Figure 2.30 for ORTEP drawing of **202**).

[p] Solution and refinement were conducted by Dr. David E. Herbert and Billy J. McCulloch.

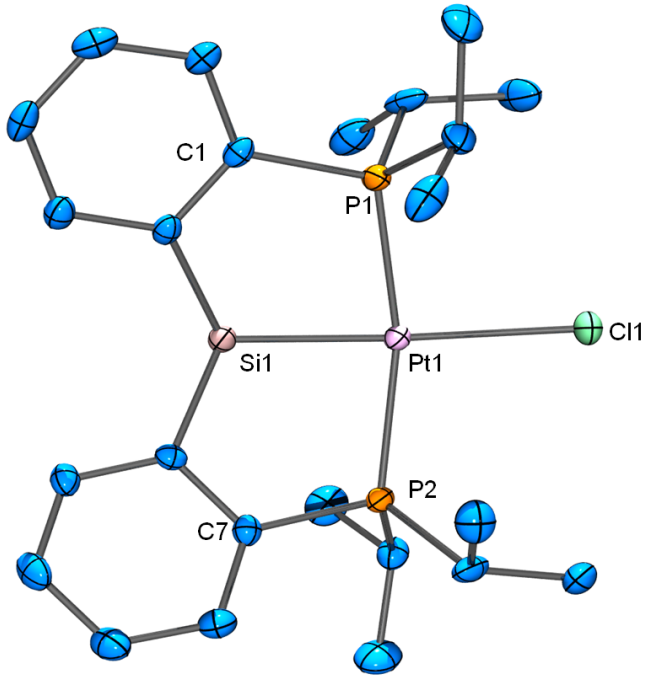

Figure 2.30 ORTEP drawing (50% probability ellipsoids) of **202**. Omitted for clarity: H atoms. Selected distance (Å) and angles (deg) follow: Pt1-Si1, 2.2759 (14); Pt1-P1, 2.2965 (14); Pt1-P2: 2.2960 (15); Pt1-Cl1, 2.4524 (14); P1-Pt1-Si1, 84.05 (5); P2-Pt1-Si1, 84.40 (5); P1-Pt1-P2, 162.40 (4); C1-Si1-Pt1, 108.11 (13); C1-Si1-C7, 114.79 (17); C7-Si1-Pt1, 107.80 (13); Cl1-Pt1-Si1, 177.13 (3); Cl1-Pt-P2, 93.11 (5); Cl1-Pt-P1, 98.69 (5).

2.4.3.2 X-Ray Data Collection, Solution, and Refinement for 207[q]

A colorless block of suitable size and quality (0.17 × 0.12 × 0.10 mm) was mounted onto a nylon loop and placed in a cold stream of nitrogen (110 K). Low-temperature X-ray data were obtained on a Bruker APEXII CCD based diffractometer (Mo sealed X-ray tube, K_α = 0.71073 Å). All diffractometer manipulations, including data collection,

[q] Solution and refinement was conducted by Dr. David E. Herbert.

integration and scaling were carried out using the Bruker APEXII software.[142] An absorption correction was applied using SADABS.[143] The space group was determined on the basis of systematic absences and intensity statistics. The structure was first solved in the orthorhombic $P2_12_12_1$ space group by direct methods using XS[144] (incorporated in SHELXTL) and refined by full-matrix least squares on F^2. No obvious missed symmetry was subsequently reported by PLATON.[145] All non-hydrogen atoms were refined with anisotropic thermal parameters. Hydrogen atoms were placed in idealized positions and refined using riding model with the exception of the hydrogen bound to silicon, which was located from the difference map. The structure was refined (weighted least squares refinement on F^2) to convergence (see Figure 2.31 for ORTEP drawing of **207**).

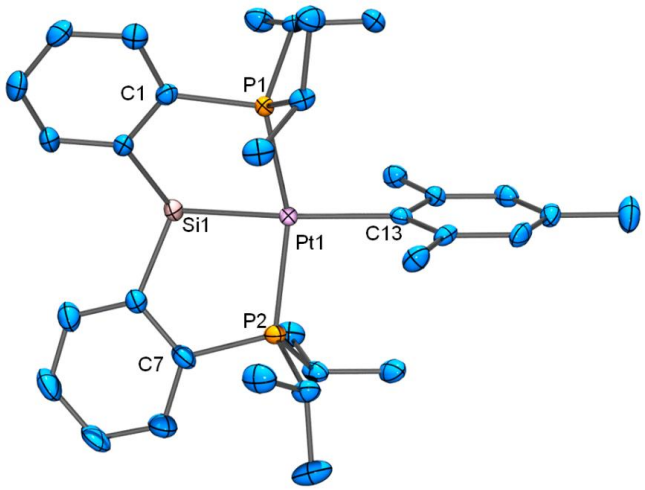

Figure 2.31 ORTEP drawing (50% probability ellipsoids) of **207**. Omitted for clarity: H atoms. Selected distance (Å) and angles (deg) follow: Pt1-Si1, 2.3123 (9); Pt1-P1, 2.2845 (7); Pt1-P2: 2.2876 (7); Pt1-C13, 2.154 (3); P1-Pt1-Si1, 83.66 (3); P2-Pt1-Si1, 83.20 (3); P1-Pt1-P2, 156.52 (3); C1-Si1-Pt1, 108.6 (1); C1-Si1-C7, 116.1 (1); C7-Si1-Pt1, 110.4(1); C13-Pt1-Si1, 168.02 (8); C13-Pt-P2, 99.48 (8); C13-Pt-P1, 97.40 (8).

2.4.3.3 X-Ray Data Collection, Solution, and Refinement for 202b-[$EtCB_{11}Cl_{11}$][r]

A yellow, multi-faceted block of suitable size (0.24 × 0.18 × 0.05 mm) was selected from a representative sample of crystals of the same habit using an optical microscope and mounted onto a nylon loop. Low temperature (110 K) X-ray data were obtained on a Bruker APEXII CCD based diffractometer (Mo sealed X-ray tube, K_α = 0.71073 Å). All diffractometer manipulations, including data collection, integration and scaling were carried out using the Bruker APEXII software.[142] An absorption correction was applied using SADABS.[143] The space group was determined on the basis of systematic absences and intensity statistics and the structure was solved by direct methods and refined by full-matrix least squares on F^2. The structure was solved in the monoclinic $P2_1/c$ space group using XS[144] (incorporated in SHELXTL). No missed symmetry was reported by PLATON.[145] All non-hydrogen atoms were refined with anisotropic thermal parameters. Hydrogen atoms were placed in idealized positions and refined using riding model. The structure was refined (weighted least squares refinement on F^2) and the final least-squares refinement converged to R_1 = 0.0273 ($I > 2\sigma$, 7372 data) and wR_2 = 0.0601 (F^2, 8226 data, 496 parameters, 0 restraints).

2.4.3.4 X-Ray Data Collection, Solution, and Refinement for 207b[s]

Crystals of **207b** were grown from a fluorobenzene layered with pentane. A yellow block of suitable size and quality (0.22 × 0.10 × 0.05 mm) was selected from a

[r] Solution and refinement was conducted by Billy J. McCulloch.
[s] Solution and refinement was conducted by Billy J. McCulloch.

representative sample of crystals of the same habit using an optical microscope, mounted onto a nylon loop, and placed in a cold stream of nitrogen (150 K). Low-temperature X-ray data were obtained on a Bruker APEXII CCD based diffractometer (Mo sealed X-ray tube, K_α = 0.71073 Å). All diffractometer manipulations, including data collection, integration, and scaling were carried out using the Bruker APEX2 software.[142] An absorption correction was applied using SADABS.[143] The space group was determined on the basis of systematic absences and intensity statistics. The structure was solved by direct methods in the triclinic P1 space group using XS (incorporated in SHELXTL).[144] All non-hydrogen atoms were refined with anisotropic thermal parameters. Hydrogen atoms bound to carbon were placed in idealized positions and refined using a riding model. The structure was brought to convergence by weighted full-matrix least-squares refinement on $|F|^2$ using SHELXL.[144] A check for missed symmetry was run using the ADDSYM program within PLATON,[145] revealing no apparent higher symmetry.

The carborane anion is partially disordered, predominantly coordinated to platinum through the *para* chlorine (80%), but also through a chlorine on the *meta* belt (20%). While it was possible to model the disorder as two discrete carborane molecules through the use of elaborate restraints, a simplified model was chosen which partitions the electron density of a single chlorine atom over two sites (Cl4 and Cl1 as the major and minor components, respectively). Due to this incomplete modeling of the carborane disorder, the difference map reveals peaks and holes near the chlorine atoms (highest peak 2.15 e^- $Å^{-3}$ was found 1.08 Å from Cl2, deepest hole –1.05 e^- $Å^{-3}$ was found 0.62 Å from Cl5). The disorder of the carborane cage also appears to influence an apparent

fluorobenzene solvent molecule occupying a nearby special position, causing severe disorder and partial occupancy which was satisfactorily modeled using PLATON's SQUEEZE functionality – void volume was found to be 161 $Å^3$ containing 40 e^-, versus expected 50 e^- for C_6H_5F, an occupancy ratio mirroring that of the disorder ratio for the carborane.

2.4.3.5 X-Ray Data Collection, Solution, and Refinement for 210[t]

Crystals were grown from a solution of ortho-difluorobenzene (ODFB) layered with pentane. A colorless sheet of suitable size and quality (0.18 × 0.12 × 0.02 mm) was selected from a representative sample of crystals of the same habit using an optical microscope, mounted onto a nylon loop, and placed in a cold stream of nitrogen (110 K). Low-temperature X-ray data were obtained on a Bruker APEXII CCD based diffractometer (Mo sealed X-ray tube, K_α = 0.71073 Å). All diffractometer manipulations, including data collection, integration, and scaling were carried out using the Bruker APEX2 software.[142] An absorption correction was applied using SADABS.[143] The space group was determined on the basis of systematic absences and intensity statistics. The structure was solved by direct methods in the monoclinic C2/c space group using SHELXS.[144] All non-hydrogen atoms were refined with anisotropic thermal parameters. Hydrogen atoms bound to carbon were placed in idealized positions and refined using a riding model. Solvent ODFB molecules were modeled with similarity restraints. The

[t] Solution and refinement was conducted by Billy J. McCulloch.

solvent ODFB molecule located at an inversion center was further restrained with rigid bond restraints and symmetry-generated near neighbor atoms (<0.9 Å) restrained to share Uij components. The structure was brought to convergence by weighted full-matrix least-squares refinement on |F|2. PLATON's ADDSYM and NEWSYM features were used to check the space group assignment.[145] Structure manipulations were performed with the aid of shelXle.[146]

2.4.4 Computational Details[u]

2.4.4.1 Gas-phase Calculations for Cations 202a′/202b′, 205a′/205b′, 206a/206b′, 208a′/208b′, 209a′/209b′

These cations were examined using the Gaussian09 suite of software[147] at the B3LYP[148] (Becke-3[149] exchange and Lee-Yang-Parr[150] correlation functional) level. Full geometry optimizations were performed and stationary points were determined to be global minima using analytical frequency calculations with the Stuttgart/Dresden triple-ζ quality basis set[151] and the corresponding effective core potential (ECP) for platinum (See Tables 2.4–2.6 and Figures 2.32–2.37). The Pople double-ζ quality basis set, 6-31G(d,p),[152,153] was used for all remaining atoms.

[u] Calculations performed by Dr. Justin R. Walensky, Mitchell D. Goshert, and Dr. Jia Zhou.

2.4.4.2 Gas-phase Calculations on 206b and 207a

All computations were carried out with the Gaussian09 program.[147] All of the geometries were fully optimized by M06 functional.[154] The Stuttgart basis set and the associated effective core potential (ECP) was used for Pt atoms, and an all-electron 6-31G(d) basis set was used for the other atoms. Based on the optimized structures, B3LYP/SDD/6-311+G(2d,p) level of theory was used to calculate the NMR chemical shifts.

Table 2.4 Energies of initial silylene $[(P_2Si=)PtX]^+$ complexes (given in Hartees).

	202a'	**205a'**	**206a'**	**208a'**	**209a'**
E_0	–1817.829	–1397.447	–1589.125	–1599.317	–1597.216
E_e	–1817.794	–1397.412	–1589.086	–1599.276	–1597.175
H°	–1817.793	–1397.411	–1589.085	–1599.275	–1597.174
G°	–1817.896	–1397.513	–1589.195	–1599.391	–1597.290

Table 2.5 Energies of transition state complexes for isomerization of silylene $[(P_2Si=)PtX]^+$ to silylene $[(PSi^XP)Pt]^+$ (given in Hartees).

	202a'/202b'-TS	**205a'/205b'-TS**	**206a'/206b'-TS**	**208a'/208b'-TS**	**209a'/209b'-TS**
E_0	–1817.750	–1397.365	–1589.035	–1599.273	–1597.179
E_e	–1817.716	–1397.329	–1588.997	–1599.232	–1597.138
H°	–1817.715	–1397.329	–1588.996	–1599.232	–1597.137
G°	–1817.817	–1397.433	–1589.107	–1599.347	–1597.253

Table 2.6 Energies of final [(PSi^{X}P)Pt]+ complexes (given in Hartees).

	202b‘	**205b‘**	**206b‘**	**208b‘**	**209b‘**
E_0	–1817.858	–1397.501	–1589.173	–1599.347	–1597.232
E_e	–1817.823	–1397.465	–1589.134	–1599.306	–1597.190
H°	–1817.822	–1397.464	–1589.133	–1599.305	–1597.189
G°	–1817.925	–1397.568	–1589.245	–1599.423	–1597.308

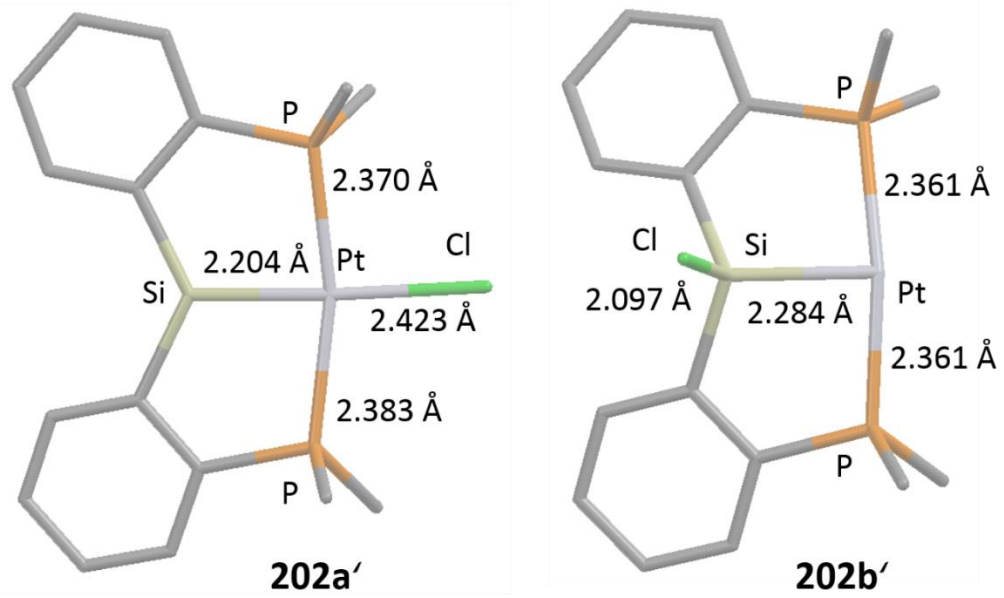

Figure 2.32 Drawings of DFT calculated structures of **202a'** (left) and **202b'** (right). Hydrogens and methyl groups of isopropyl omitted for clarity.

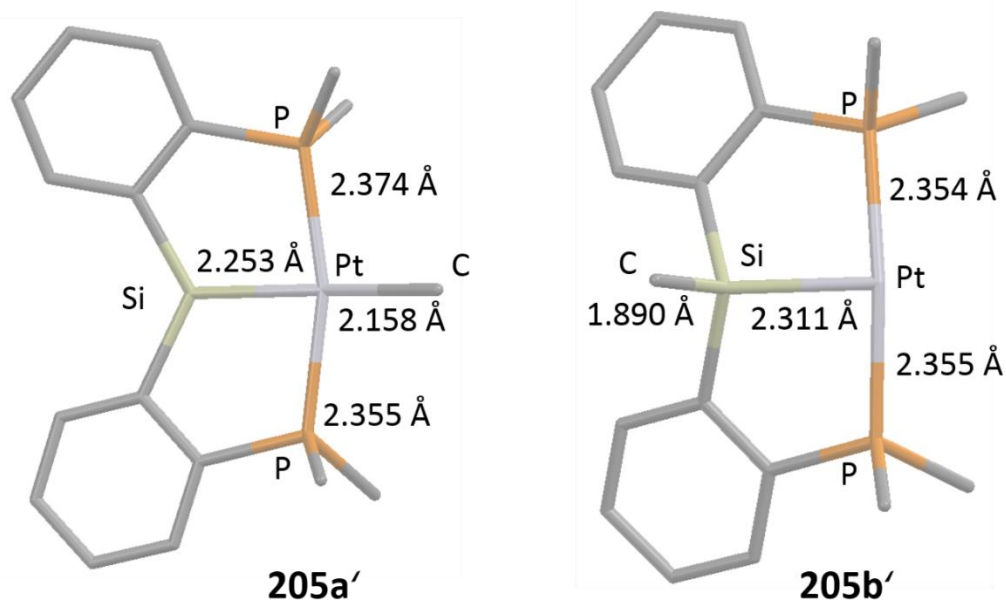

Figure 2.33 Drawings of DFT calculated structures of **205a'** (left) and **205b'** (right). Hydrogens and methyl groups of isopropyl omitted for clarity.

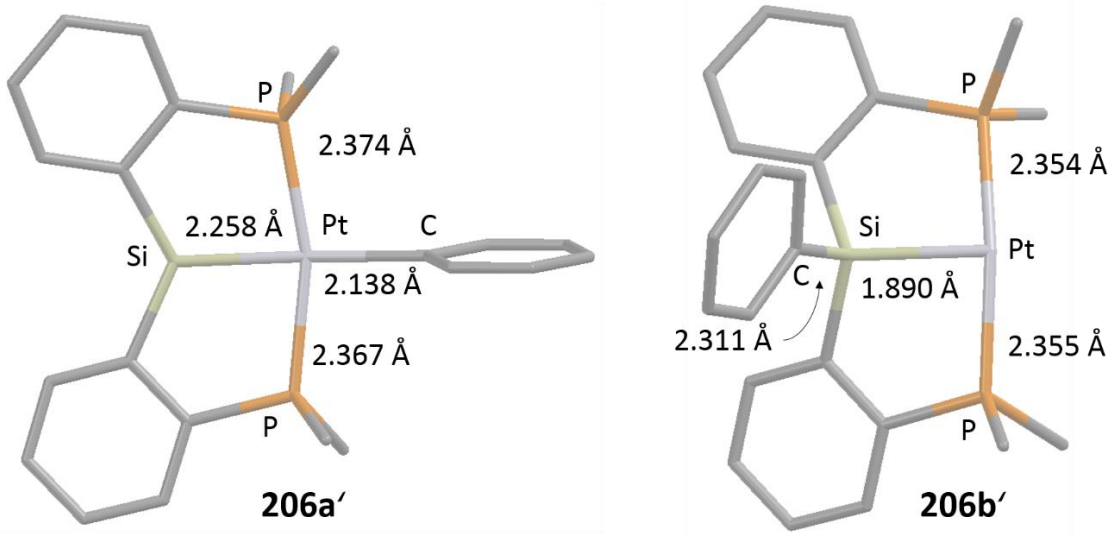

Figure 2.34 Drawings of DFT calculated structures of **206a'** (left) and **206b'** (right). Hydrogens and methyl groups of isopropyl omitted for clarity.

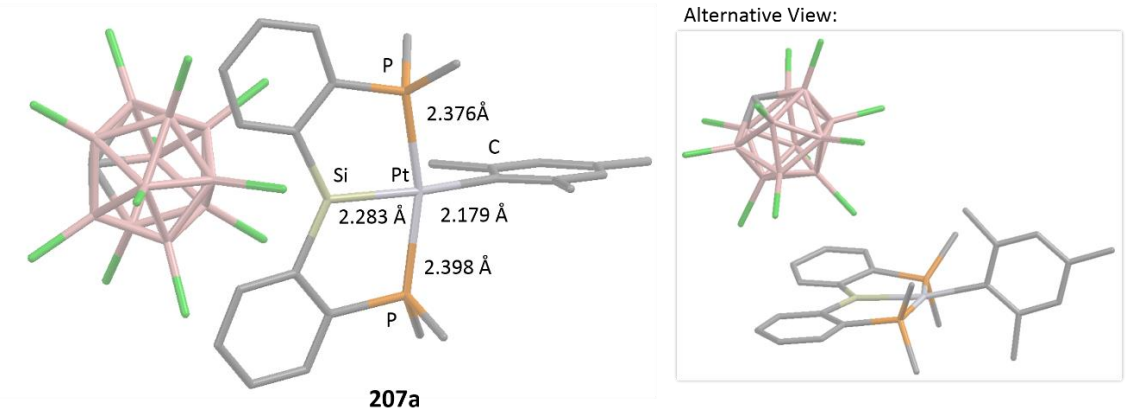

Figure 2.35 Drawings of DFT calculated structures of **207a**. Hydrogens and methyl groups of isopropyl omitted for clarity.

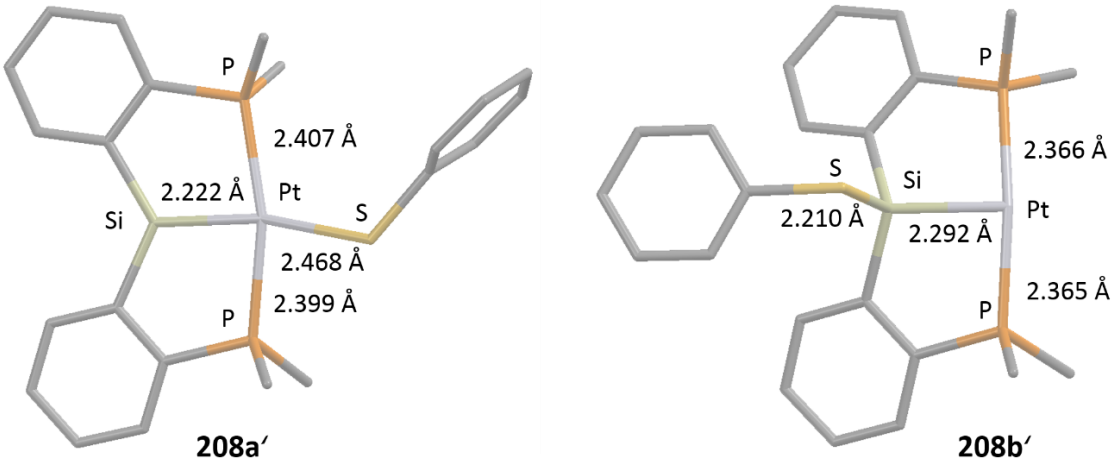

Figure 2.36 Drawings of DFT calculated structures of **208a'** (left) and **208b'** (right). Hydrogens and methyl groups of isopropyl omitted for clarity.

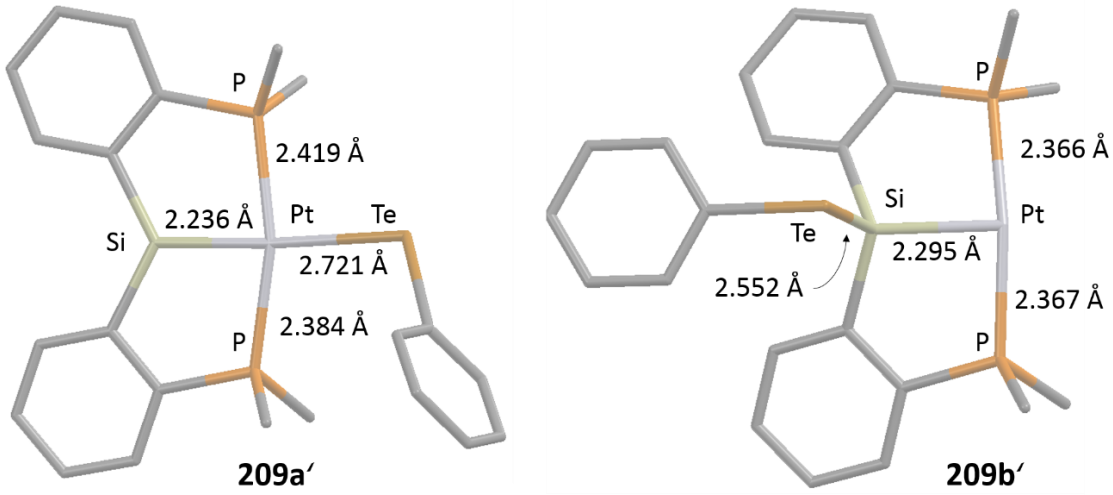

Figure 2.37 Drawings of DFT calculated structures of **209a'** (left) and **209b'** (right). Hydrogens and methyl groups of isopropyl omitted for clarity.

III. FRUSTRATED LEWIS PAIR-LIKE SPLITTING OF AROMATIC C–H BONDS AND ABSTRACTION OF HALOGEN ATOMS BY A CATIONIC [(^{F}PNP)Pt]$^{+}$ SPECIES[*]

3.1 Introduction

Platinum chemistry, particularly some of the early work by Shilov[16,17,155-158] has played a central role in the development of the modern understanding of carbon–hydrogen bond activation and the current techniques for performing such transformations selectively and efficiently. Arranging for a hydrocarbon to react with a three-coordinate d^8 fragment is a strategy that has been used in a number of successful approaches to C–Hactivation and functionalization.[18,20,159,160] Recognized as important intermediates in C–H activation, hydrocarbon σ-complexes have been the subject of many studies: direct spectroscopic observations in rare accessible cases,[28,75,87,161] indirect investigations using the tools of kinetics,[162,163] and computational work.[164]

Pincer ligands[106,165] offer a convenient framework for studies of square-planar compounds in which only one coordination site is intended to be the "reactive" site.[166] Pincer complexes are perhaps best known for their thermal stability, but equally important attributes include the prevention of undesired ligand exchange and redistribution and a high degree of control over the positioning of the ancillary donor atoms. The work we

[*] Portions of this chapter were reprinted with permission from "Frustrated Lewis pair-like splitting of aromatic C–H bonds and abstraction of halogen atoms by a cationic [(^{F}PNP)Pt]+ species" by DeMott, J. C.; Bhuvanesh, N.; Ozerov, O. V., *Chem. Sci.* **2013**, *4*, 642–649, Copyright 2013 by The Royal Society of Chemistry.

present here was inspired and influenced by two sets of findings in the literature. Peters and Harkins reported in 2002 that reacting (NNN)PtOTf with a trialkylamine base in benzene led to heterolytic C–Hactivation of the solvent (Scheme 3.1A).[167] Similar findings were reported by the Liang group with (PNP^{Ph})PtOTf.[168] The mechanism that appears to be most consistent with the results of both Liang *et al.* and Peters *et al.* involves displacement of the triflate ligand with a solvent molecule (*via* either a dissociative or associative mechanism) to form a cationic Pt–arene complex.[169,170] This intermediate could either be sufficiently acidic to be deprotonated by a relatively weak base or it could undergo C–H oxidative addition, giving rise to an even more acidic Pt^{IV} aryl/hydride species.[169-171]

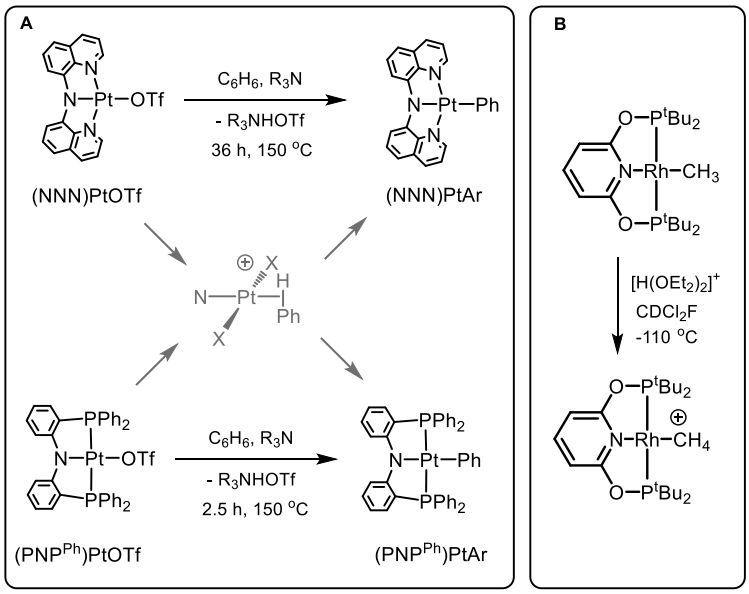

Scheme 3.1 A: C-H activation of benzene by pincer complexes of Pt by Peters *et al.*[167] and by Liang *et al.*[168] B: Synthesis of a Rh methane complex by Goldberg, Brookhart *et al.*[88]

Additionally, the seminal 2009 report by Goldberg, Brookhart *et al.* demonstrated that a neutral pyridine/bis(phosphinite) PONOP ligand can be used to allow for the observation of a unique square-planar d^8 Rh^I–methane adduct (Scheme 3.1B).[88] This finding and the above mentioned results of Peters and Liang[167,168] suggested the possibility that an anionic pincer ligand may provide access to cationic hydrocarbon complexes of Pt^{II}. η^2-C,C–arene complexes of Pt^{II} have been observed and even isolated, but primarily in systems where the ligands are considerably less sterically encumbering than a pincer ligand with bulky flanking phosphine arms.[169-171] Yamashita and Nozaki very recently reported the structure of an η^2-C,H–arene complex involving a d^8 (PBP)Rh fragment (PBP is a boryl/bis(phosphine) pincer ligand)[172] while Peters *et al.* reported a relatively long-range interaction between a cationic Pt^{II} center supported by a tripodal silyl/tris(phosphine) ligand in a C–H bond of toluene in the solid state.[137]

Our group has frequently used diarylamido/bis(phosphine) PNP pincer ligands.[106,173-178] For example, we previously reported that $[(^{Me}PNP)Ni]^+$ acts as an efficient catalyst for the coupling of acetonitrile and aldehydes.[179] Additionally, we found that a masked form of the analogous group 10 complex $[(^{Me}PNP)Pd]^+$ functions as a frustrated Lewis pair with the ability to heterolytically split alkynyl C–H bonds,[180] B–H bonds and B–B bonds (Scheme 3.2).[181]

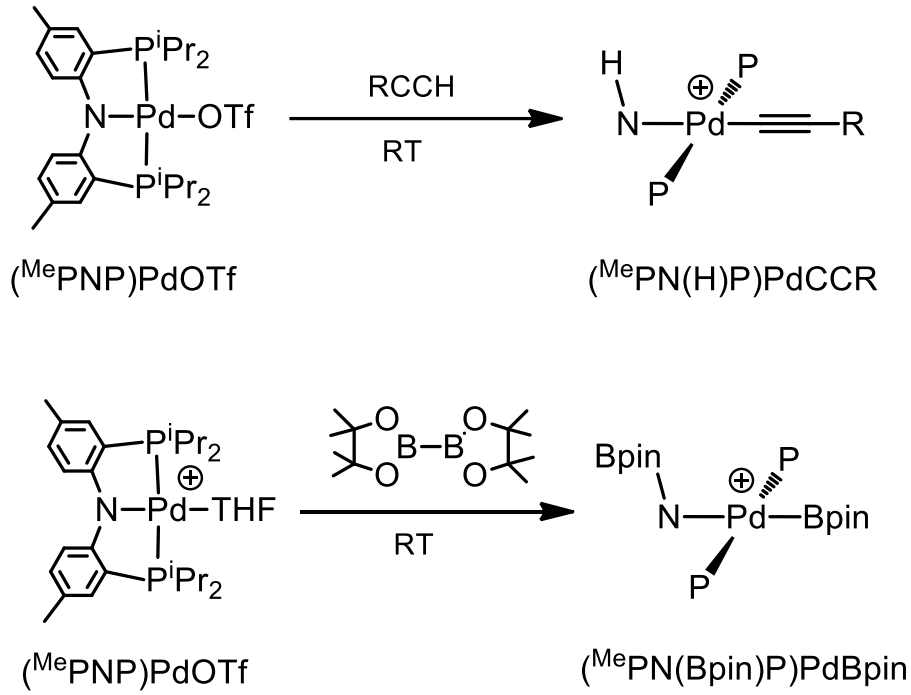

Scheme 3.2 1,2-Addition reaction of alkynyl C-H and of B-B bonds with the $[(^{Me}PNP)Pd]^+$ fragment.

We envisioned that the three-coordinate d^8 fragment $[(^{F}PNP)Pt]^+$ (^{F}PNP ligand drawn in Scheme 3.3) would be a promising design for observing hydrocarbon complexes of cationic Pt^{II} and set out to explore whether $[(^{F}PNP)Pt]^+$ could be generated with a weakly coordinating counter-anion. Aromatic hydrocarbons and halogenated hydrocarbons seemed suitable as somewhat polar and weakly coordinating solvents that could either give rise to C–H complexes themselves, or permit an added hydrocarbon substrate to bind. While we were easily able to remove an anionic ligand from a four-coordinate Pt precursor, the results we obtained were rather unexpected. Instead of hydrocarbon complexes, we observed heterolytic splitting of aromatic C–H bonds across

the Pt–N bond of the [(^{F}PNP)Pt]$^{+}$ fragment. On the other hand, certain halogenated hydrocarbons reacted with [(^{F}PNP)Pt]$^{+}$*via* the net transfer of a halogen atom – a very unusual reaction for a Pt^{II} cation. Both of these pathways derive from the non-innocence of the central amidoligand of ^{F}PNP: as a Brønsted base in the first case, and as an oxidizable ligand in the other. Nitrogenous ligands have been ubiquitous in the studies of Pd and Pt-mediated C–H activation, but a clear demonstration of the potential for these new reactivity pathways has not been previously reported.

3.2 Results and Discussion

3.2.1 C–H Activation of Arenes

Desiring to test whether the (^{F}PNP)Pt system performs similarly to the NNN- and PNP^{Ph}-supported systems,[167,168] we prepared complex (^{F}PNP)PtOTf (**301**) analogously to the reported (^{Me}PNP)PtOTf.[182] We specifically chose the ^{F}PNP ligand because of its fluorine substituents, which do not have much influence[183,184] on the reactivity at the metal but provide a very convenient and informative NMR spectroscopic probe.[185] As expected, thermolysis of **301** at 115 °C with Et_3N in C_6D_6 or *protio*-toluene produced results (Scheme 3.3) analogous to the findings of Peters *et al.*[167] and Liang *et al.* The consumption of **301** was slow; 7 days were required for completion of the reaction with toluene and in the reaction with C_6D_6, only 83% conversion was seen after 2 weeks. The corresponding Pt–aryl complexes **302a–d** were observed by NMR spectroscopy, along with <10% of

(^{F}PNP)PtH.[v] In the case of toluene, a mixture of Pt–tolyl isomers was produced. An *o* : *m* : *p* ratio of *ca.* 1 : 68 : 31 was determined by comparison with independently synthesized authentic samples (*vide infra*).

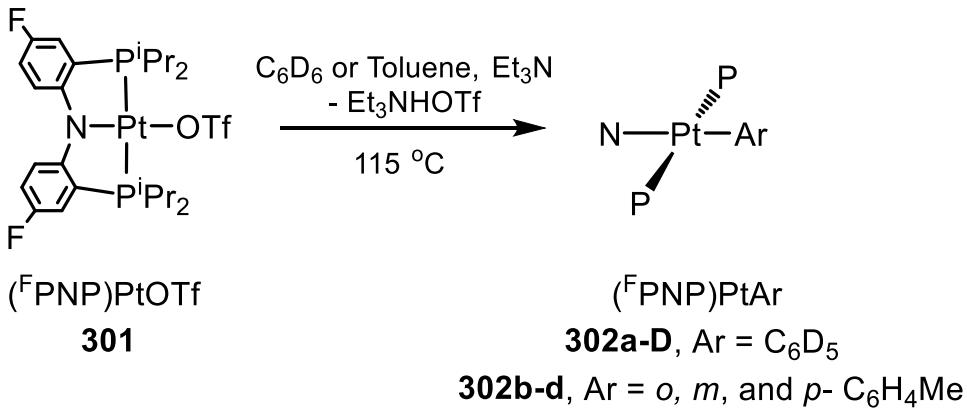

(^{F}PNP)PtOTf
301

(^{F}PNP)PtAr
302a-D, Ar = C_6D_5
302b-d, Ar = *o, m*, and *p*- C_6H_4Me

Scheme 3.3 C-H activation of arenes with **301** and base.

In order to access the [(^{F}PNP)Pt]$^{+}$ cation, we used K[B(C_6F_5)$_4$] (KBArF_{20}) to abstract the triflate from **301**. Stirring a mixture of **301** and KBArF_{20} in C_6H_6 for 4 days at ambient temperature resulted in complete consumption of **301** and full conversion to **303a**. The rate of the reaction was probably depressed by the limited solubility and the low rate of dissolution of KBArF_{20} in benzene. Heating accelerated the reaction, and at 80 °C, the analogous products **303a-D**, **303b–d** or **303e** could be synthesized from **301** and KBArF_{20} in C_6D_6, toluene or fluorobenzene after just 2–16 h.

[v] Likely formed *via* competing hydride transfer from Et$_3$N.

Compounds **303a–f** are the products resulting from formal additions of aromatic C–H bonds across the Pt–N bond in $[(^{F}PNP)Pt]^{+}$. In our previous work,[180] we pointed out that the analogous $[(^{Me}PNP)Pd]^{+}$ fragment can be viewed as a frustrated Lewis pair.[186] The lone pair on N and the empty orbital on the metal are orthogonal to each other, while the steric bulk prevents the N_{amido} from bridging, resulting in a "frustrated" arrangement. We did not observe aromatic C–H splitting with $[(^{Me}PNP)Pd]^{+}$. A single product **303a/303a-D** was observed in each of the reactions with C_6H_6 or C_6D_6. The assigned structures of **303a** and **303a-D** are consistent with the NMR spectra, including the NH proton resonance at 7.26 ppm in the ^{1}H NMR spectrum of **303a** and the overall time-averaged C_s symmetry in the ^{1}H, $^{13}C\{^{1}H\}$, $^{31}P\{^{1}H\}$ and ^{19}F NMR spectra. We have previously commented on the sensitivity of the ^{19}F NMR chemical shift exhibited by the ^{F}PNP ligand to the environment at the metal, particularly with respect to the amido–metal or amine–metal nature of the N donor.[185] In **303a**, the ^{19}F NMR resonance was detected at −111.7 ppm, which is consistent with a protonated amine form of the PNP ligand.

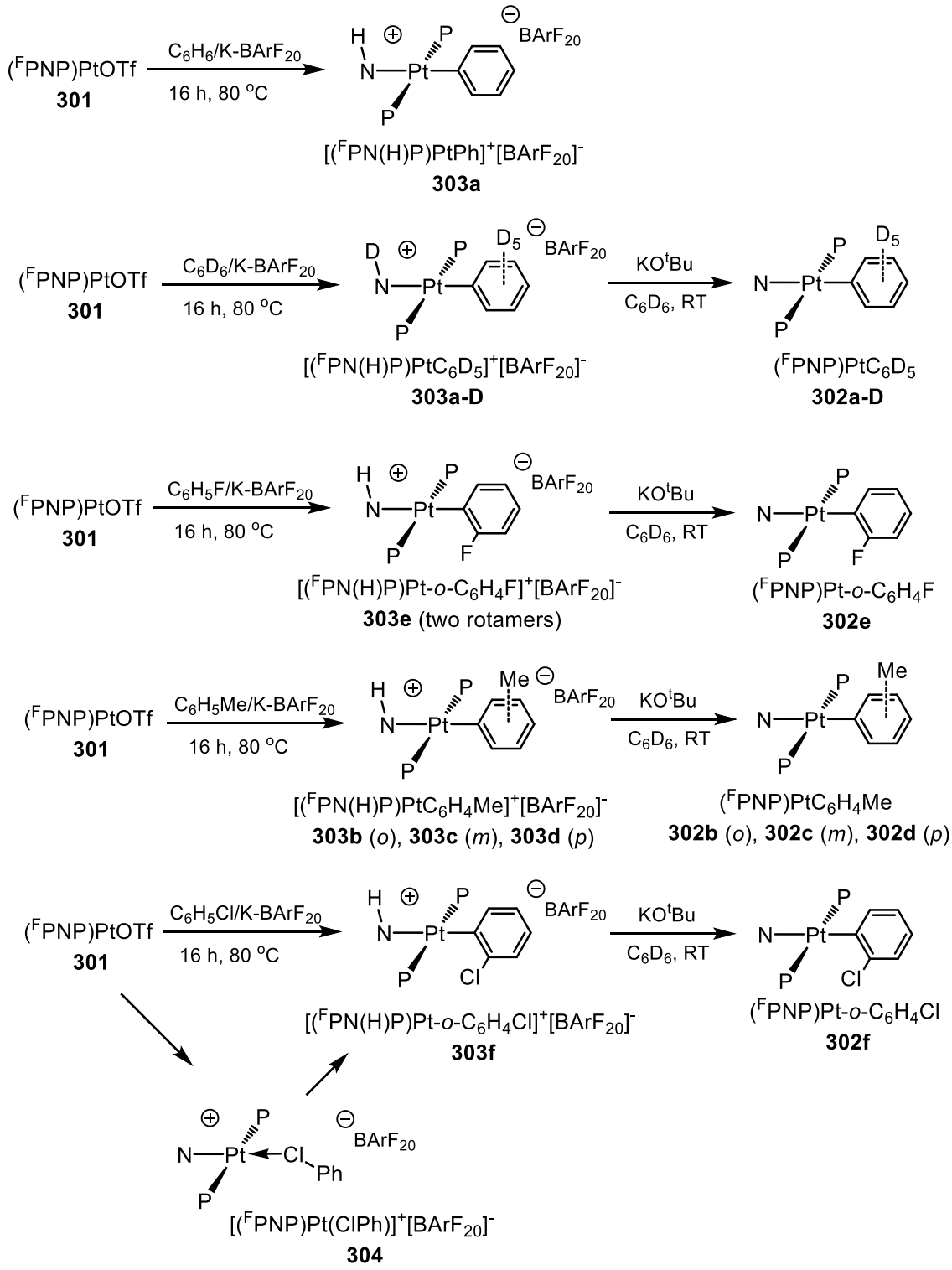

Scheme 3.4 1,2-Addition of arenes.

Similar reactions run in fluorobenzene or toluene resulted in mixtures of products. Each of these products displayed general NMR spectroscopic features that are similar to those of **303a**, including downfield NH signals, C_s symmetry at RT, and ^{19}F NMR chemical shifts around −111.3 to −111.7 ppm that can be assigned to the ^{F}PNP ligand. For fluorobenzene, only the *ortho*-fluorophenyl isomer was detected, but two spectroscopically distinct rotamers were seen (F either *syn* or *anti* with respect to NH). Deprotonation of **303e** with KO^{t}Bu led to a single neutral Pt–aryl isomer (**302e**).

For toluene, three structural isomers were formed (8% *ortho* and 92% *meta* + *para*[w]). The benzyl isomer **303g** was not detected.[187] This set of conditions yielded a higher, albeit still small, proportion of the *ortho*-isomer **303b** than the **1**/Et_3N reaction in Scheme 3.3. However, the regio-discriminating step may not be identical for these two reactions. Deprotonation (Scheme 3.4) of this product mixture resulted in a corresponding mixture of neutral *ortho*-, *meta*- and *para*-tolyl–Pt isomers. Each of these isomers **302b–d** was independently synthesized (Scheme 3.5), and protonation of **302b–d** with $[H(OEt_2)_2][B(C_6F_5)_4]$ yielded pure samples of each corresponding (^{F}PN(H)P)Pt–tolyl isomer **303b–d**. Analogous protonation and deprotonation reactions were also carried out for other Pt–aryls and for the Pt–benzyl complex **302g** (Schemes 3.4 and 3.5).

We were able to obtain an X-ray quality single crystal of **303e**. The solid-state structure supported the proposed assignment of fluorine in the *ortho*-position (Figure 3.1).

[w] The overlap of NMR resonances of **303c** and **303d** did not allow for measuring their respective contents separately.

Moreover, the F atom of the FC_6H_4 ligand was found to be disordered over the *syn*-/*anti*-positions (*vs.* NH), consistent with the observation of these rotamers in solution. An X-ray quality single crystal was also obtained from the product mixture of the reaction of **301** with $KBArF_{20}$ in toluene (Figure 3.1). Remarkably, in this case as well, we saw solid-state disorder between the two major isomers observed in solution: **303c** and **303d**. The structure was successfully modeled with a *para* (**303d**) to *meta* (**303c**) isomer ratio of 53 : 47. Both the structure of **303e** and that of **303c/d** showed a distorted square-planar environment about Pt and a tetrahedral one about N.

The reaction with C_6H_5Cl (Scheme 3.4) ultimately produced a single *ortho* isomer[182,188,189] (and a single rotamer) of **303f**. However, an intermediate was observed in the initial stages of the reaction that we tentatively assigned as **304**. Although we do not have firm structural evidence, we believe it is more likely to be the κ^1-Cl chlorobenzene complex than a π-complex (*i.e.*, an η^2-C,C–arene complex), because similar intermediates were not observed in reactions with benzene, toluene or fluorobenzene. In addition, we observed what we believe to be a similar κ^1-Br adduct in the reaction with C_6D_5Br, which will be discussed in another section. Halocarbon (CH_2Cl_2, PhBr and PhI, but not PhCl) adducts of cationic Pt^{II} fragments have been studied by Kubas *et al.*[136]

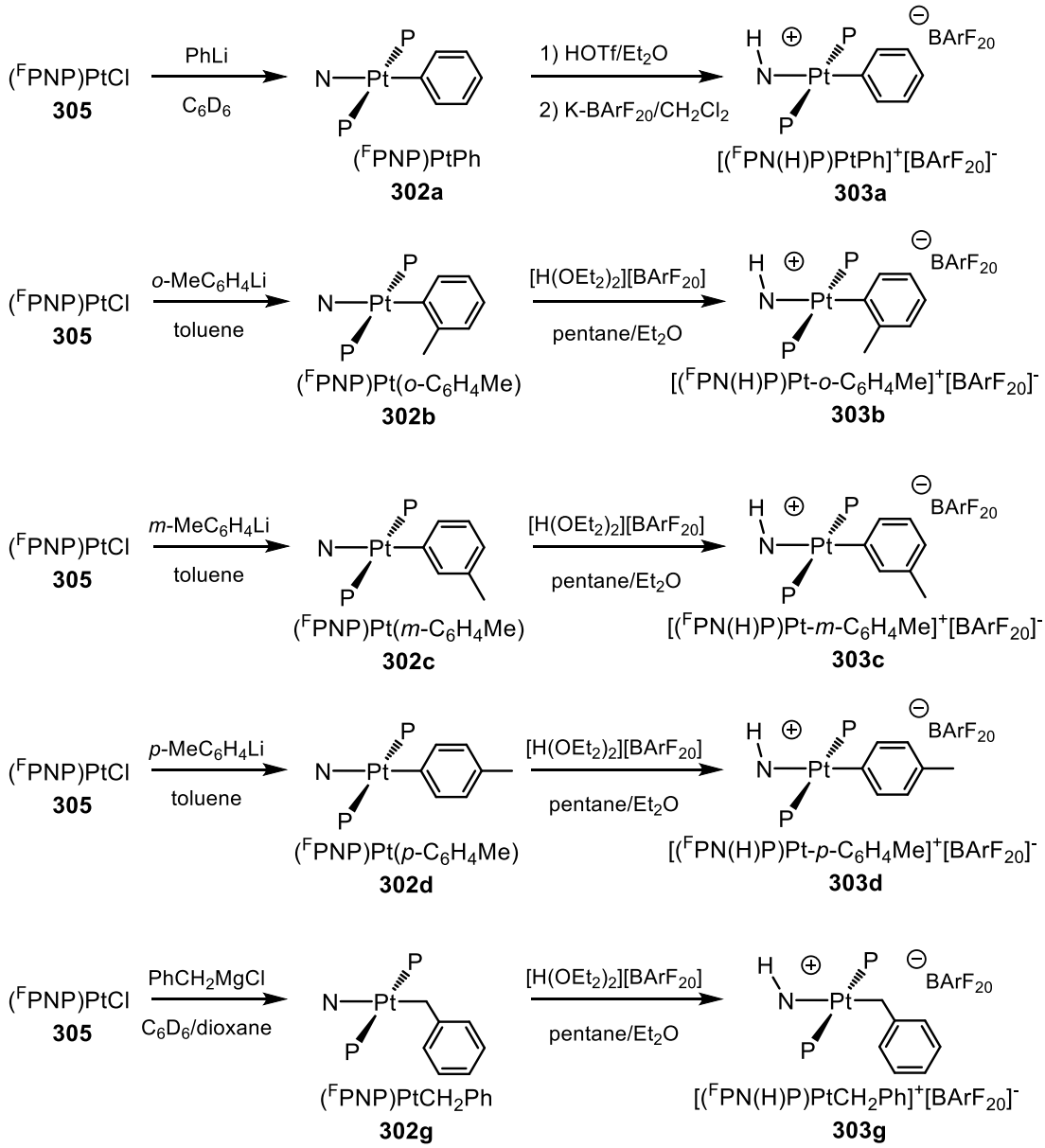

Scheme 3.5 Synthesis and protonation of (^{F}PNP)Pt-R compounds.

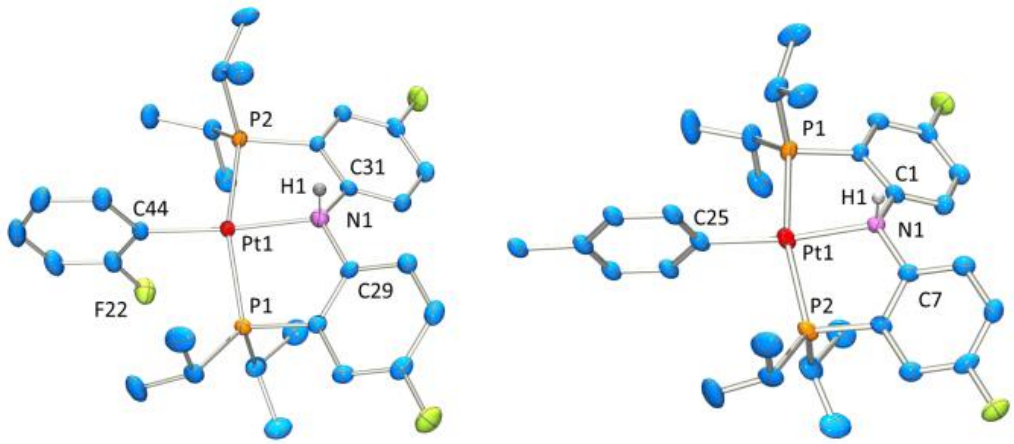

Figure 3.1 ORTEP drawings (50% probability ellipsoids) of **303e** (left) and **303c/d** (right) showing selected atom labeling. Hydrogen atoms (except for N-H) and the $BArF_{20}$ counterion are omitted for clarity. Only one of the two disordered orientations is shown for the fluorophenyl (**303e**) and tolyl (**303d** shown) groups. Selected bond distances (Å) and angles (deg) for **303e** follow: N1-Pt1, 2.159(2); P1-Pt1, 2.2828(8); P2-Pt1, 2.2780(8); Pt1-C44, 2.012(3); P1-Pt1-P2, 160.96(3); N1-Pt1-C44, 170.46(11); C44-Pt1-P1, 95.22(8); C44-Pt1-P2 99.05(8); N1-Pt1-P1, 83.34(7); N1-Pt1-P2, 84.59(7); C29-N1-Pt1, 108.82(18); C31-N1-Pt1, 116.10(18); C31-N1-C29, 119.5(2). Selected bond distances (Å) and angles (deg) for **303d** follow: N1-Pt1, 2.183(7); P1-Pt1, 2.288(2); P2-Pt1, 2.270(2); Pt1-C25, 2.072(6); P1-Pt1-P2, 161.35(8); N1-Pt1-C25, 166.8(3); C25-Pt1-P1, 93.9(3); C25-Pt1-P2 100.9(3); N1-Pt1-P1, 83.13(17); N1-Pt1-P2, 84.81(17); C1-N1-Pt1, 107.4(5); C7-N1-Pt1, 115.1(5); C1-N1-C7, 119.9(6).

3.2.2 Rotamerism

The observation of two rotamers by NMR spectroscopy suggests slow (on the NMR timescale) rotation about the Pt–C bond in **303e**. On the timescale of experimental handling, however, these two rotamers are in apparent equilibrium; the ratio changes reversibly with temperature, and recrystallization does not change the ratio of rotamers. One would expect even slower rotation about the Pt–C bond in the analogous compounds **303b** and **303f**, which have larger *ortho* substituents, but in both of these cases, only a single rotamer was observed. This was interpreted to mean that the larger substituent size

perturbs the equilibrium constant far away from unity. In compounds that have a hydrogen atom at both *ortho* positions (**303a**, **303e** and **303d**), we did not observe resolved rotamers, but the aromatic signals were broad, which is consistent with a rotation rate about the Pt–C bond that is on the order of the NMR timescale. Restricted rotation about a metal–phenyl bond is common in complexes where an aryl ligand is *cis* to two phosphine ligands of this or greater size.[190,191] However, in pincer complexes containing P^iPr_2 groups and an aryl substituent of comparable size to a phenyl ring, this is usually observed only when the aryl group is also *cis* to the central pincer atom.[192,193]

In contrast, the neutral (^{F}PNP)Pt–aryl complexes **302a–f** do not display any evidence of separately observable rotamers, showing only one sharp set of signals for each compound at ambient temperature. It is likely that the puckering of the PNP ligand upon quaternization of the N atom exacerbates the steric interactions between the isopropyl groups and the Pt–aryl bond, leading to a lower rate of rotation about Pt–C_{aryl} in the protonated complexes.

3.2.3 Probing Inter- and Intramolecular Exchange

We designed several experiments to probe whether the C–H addition across N–Pt is reversible. The first set of experiments involved thermolysis of isolated arene addition products **303a-D** and **303b–e** in a different arene (Scheme 3.6). We did not observe arene exchange for any of the combinations, indicating that the complete reversal of arene addition (including liberation of the free arene) is not kinetically accessible. However, heating **303a-D** in neat acetonitrile for 24 h at 80 °C did result in the formation of the

cationic acetonitrile adduct [(^{F}PNP)Pt(NCMe)][BArF$_{20}$] (**306**) and loss of C_6D_6 from **303a-D**. It is unclear whether the apparent elimination of C_6D_6 is simply faster in MeCN as solvent rather than arenes, or if it involves a more direct interaction of MeCN with **303a-D** that makes benzene elimination kinetically accessible.

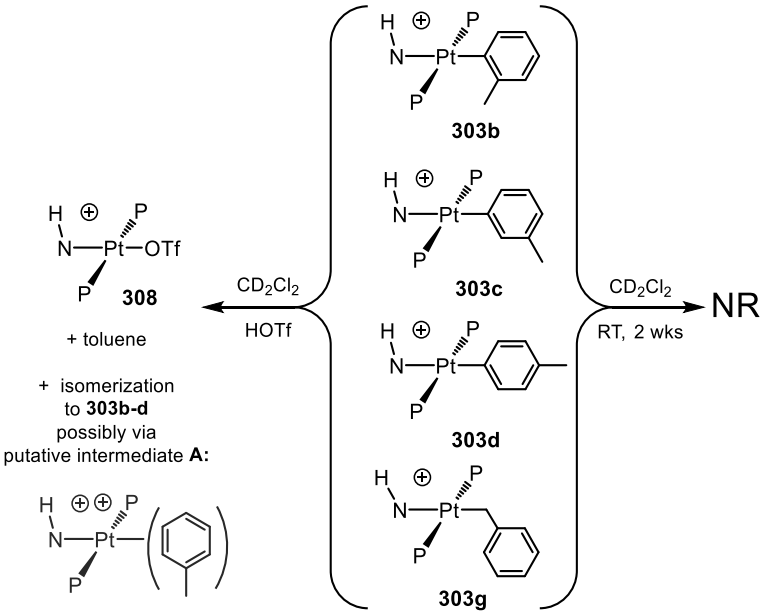

Scheme 3.6 Reactions probing intramolecular isomerization.

The second set of experiments was based on the notion that the C–H addition process and its reverse should proceed *via* the intermediacy of a [(^{F}PNP)Pt(arene)]$^{+}$ adduct (**307**). Re-forming this arene adduct from a C–H addition product such as **303a** could hypothetically reverse C–H cleavage without liberating any free arene. In the case of **303b–d**, this would lead to an intramolecular scrambling of isomers. However, solutions of pure **303b**, **303c** or **303d** did not produce any other isomers in NMR-detectable

concentrations after 2 weeks at ambient temperature (Scheme 3.6). The same was true for the benzyl isomer **303g** (not observed in the reactions of **301** with $KBArF_{20}$ in toluene). There was also no evidence of isomerization when **303c** or **303d** was exposed to (^{F}PNP)Pt(*m*-C_6H_4Me), $Me_2S–BF_3$ or $B(C_6F_5)_3$.

On the other hand, treatment of **303b–d** in CD_2Cl_2 with an HOTf–PhF solution did result in some isomerization and the formation of [(^{F}PN(H)P)PtOTf]$^+$ (**308**).[x] We propose that triflic acid can reversibly protonate **303b–d** and **303g** to give unobserved [(^{F}PN(H)P)Pt(toluene)]$^{2+}$ (**A**, Scheme 3.6), causing *ortho*/*meta*/*para* scrambling, and that the arene in **A** can be irreversibly but relatively slowly be replaced by triflate. Notably, $[H(OEt_2)_2][BArF_{20}]$ or triflic acid in ether failed to induce the isomerization. Evidently, protonated Et_2O is not a strong enough Brønsted acid. Related observations were made by Tilset *et al.*, who reported that protonation of a cationic [(diimine)Pt(Ph)(NCMe)]$^+$ complex in acetonitrile was orders of magnitude faster with HOTf than with HBF_4/Et_2O.[171] [(^{F}PN(H)P)PtOTf]$^+$ appears to be unstable in dichloromethane, producing [(^{F}PN(H)P)PtCl]$^+$ (**309**) over time.

All in all, our observations imply that the C–H addition products **303a–f** are separated from the arene adducts **307** by a barrier that is insurmountable under 100 °C. This means that (in the absence of very strong acid, which can access a different pathway through **A**) the regioselectivity of the C–H addition is achieved under kinetic control. That

[x] We first noticed that *impure* samples of **303b–d** sometimes isomerized, somewhat irreproducibly. This is likely because of the traces of excess of HOTf in reactions without the use of diethyl ether.

is interesting, considering that the *ortho*-halophenyl isomers (**303e–f**) are almost certainly thermodynamically preferred as well[194] but usually are not kinetically preferred.[188]

To probe the relative barriers to the activation of C–H bonds in various substrates, we set up a few competition experiments in which **301** was treated with $KBArF_{20}$ at 80 °C (3–24 h) in the presence of two different arenes. In all of these reactions, full conversion to the corresponding products **303a–e** and **303a-D** was observed. C_6H_6 was activated three times as fast as C_6D_6, which may indicate the importance of the C–H/C–D breaking step. However, this apparent kinetic isotope effect of approximately 3 may be a composite value,[162,163,195] and we do not have enough information for a more conclusive analysis. The *ortho*-C–H bond in fluorobenzene was decidedly more reactive than the C–H or C–D bonds of C_6H_6 or C_6D_6. Based on prior studies, we would expect the activation of the *ortho*-C–H bond in fluorobenzene to be thermodynamically more favorable,[194]but it is apparently also kinetically more facile than activation of a C–H bond in benzene. The fact that C_6H_6 was approximately three times more competitive than C_6D_6 against C_6H_5F is consistent with the 3:1 ratio for the C_6H_6–C_6D_6 competition experiment. In the C_6H_6–$C_6H_5CH_3$ competition reaction, the observed ratio of products was close to the ratio between the number of C–H bonds in C_6H_6 and the number of *meta* + *para* C–H bonds in toluene.

3.2.4 Halogen Atom Abstraction

Although complexes **303** were stable when dissolved in dichloromethane for extended periods of time at ambient temperature, dichloromethane could not be used as a

solvent for their synthesis. Treatment of **301** with $KBArF_{20}$ in dichloromethane led to the formation of a blue solution that clearly contained a paramagnetic product, which we assigned as **309a**. The addition of decamethylferrocene to this solution resulted in the formation of the diamagnetic compound **305**, which was observed in a 50% yield *vs.* an integration standard after filtration.

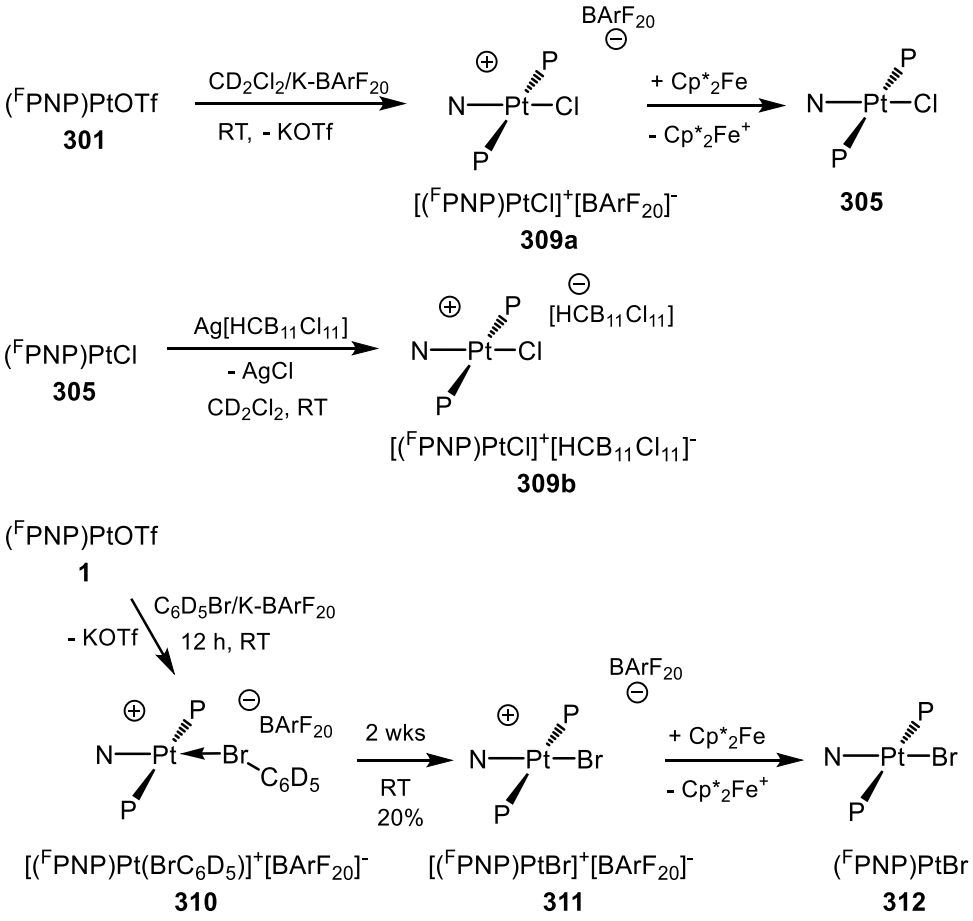

Scheme 3.7 Halogen atom abstraction and redox chemistry of $[(^{F}PNP)PtX]/[(^{F}PNP)PtX]^{+}$ complexes.

An alternative synthesis of the **309** cation was achieved *via* oxidation of a pure sample of **305** with $Ag[HCB_{11}Cl_{11}]$. This reaction allowed for the isolation of **309b** as an analytically pure solid in 44% (unoptimized) yield after work-up. An X-ray diffraction study on a single crystal of **309b** revealed its solid-state structure (Figure 3.2). In this structure, Pt maintains an approximately square-planar environment, and the $[HCB_{11}Cl_{11}]^-$ anion is well separated from the cation. Mindiola *et al.* previously studied the reversible oxidation of (^{Me}PNP)NiCl and concluded that the oxidation takes place primarily on the ligand.[196] We made similar observations in collaboration with the Nocera group concerning the oxidation of (^{Me}PNP)M(CO)$_3$ (M = Mn, Re).[197] Oxidation of **305** is expected to be a ligand-centered event as well, and so **309a/309b** should not be viewed as Pt^{III} compounds, but rather as Pt^{II} compounds with an oxidized ^{F}PNP ligand.

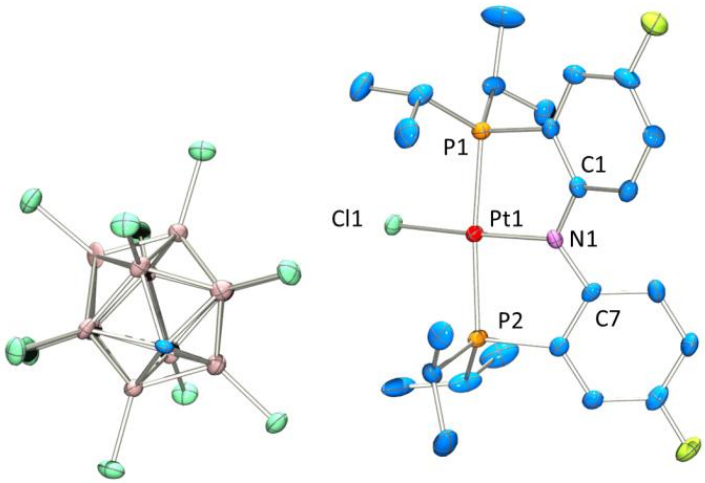

Figure 3.2 ORTEP drawing (50% probability ellipsoids) of **309b** showing selected atom labeling. Hydrogen atoms are omitted for clarity. Selected bond distances (Å) and angles (deg) follow: N1-Pt1, 1.987(6); P1-Pt1, 2.285(3); P2-Pt1, 2.304(3); Pt1-Cl1, 2.296(2); P1-Pt1-P2, 166.72(7); N1-Pt1-Cl1, 171.92(16); Cl1-Pt1-P1, 93.99(7); Cl1-Pt1-P2 97.67(7); N1-Pt1-P1, 85.20(16); N1-Pt1-P2, 84.13(16); C1-N1-Pt1, 119.9(4); C7-N1-Pt1, 118.6(4); C1-N1-C7, 121.2(6).

The reaction of **301** with $KBArF_{20}$ in C_6D_5Br led to the complete disappearance of **301** in 12 h at ambient temperature and the formation of a compound tentatively identified as **310**. Compound **310** is analogous to **304**, which is observed in the reaction with C_6H_5Cl, and showed a single ^{19}F NMR resonance at −122.9 ppm (along with three normal $BArF_{20}$ resonances), which is nearly identical to the spectrum of **304**. In the ^{1}H and $^{13}C\{^{1}H\}$ NMR spectra, **310** exhibited C_{2v}-symmetry, which is consistent with a κ^1-Br adduct. Treatment of **310** with acetonitrile resulted in the clean formation of **306** (^{19}F NMR resonance at −125.1 ppm). After two weeks in a C_6D_5Br solution, the intensity of the NMR resonances assigned to **310** were diminished (with no new ^{19}F NMR signals emerging), and broad resonances reminiscent of **311** were evident in the ^{1}H NMR spectrum. Addition of decamethylferrocene to this aged solution resulted in the appearance of NMR resonances indicative of **312** (20%). We propose that Br atom abstraction from the bound C_6D_5Br takes place over time, producing **311**. We have not yet attempted to establish the fate of the organic fragments after the abstraction of the Br atom from bromobenzene or of the Cl atom from dichloromethane.

Abstraction of a halogen atom is not a reaction associated with low-spin, closed-shell transition-metal complexes. Metalloradicals with odd numbers of electrons such as (porphyrin)Rh or (porphyrin)Ir species are known to abstract halogen atoms from halocarbons.[198,199] In contrast, Bullock's $[(PCP)Pt]^+$ or Peters'$[(SiP_3)Pt]^+$ simply coordinated dichloromethane and did not show chlorine atom abstracting reactivity.[137,200] Since Pt^{II} is reliably low-spin in its complexes, the halogen-atom abstraction observed

with [(^{F}PNP)Pt]$^{+}$ appeared likely related to the non-innocence of the ^{F}PNP ligand (Scheme 3.7). To probe this further, we initiated a theoretical study.

3.2.5 DFT Studies

The contrast between the typical low-spin reactivity for Pt in C–H activation and the apparent metalloradical-type reactivity in halogen atom abstraction led us to consider the nature of the ground state of [(^{F}PNP)Pt]$^{+}$. Although we have not observed this species directly, we thought that a comparison of the singlet and triplet energies might assist in understanding the divergent reaction pathways that can formally be defined as reactions of [(^{F}PNP)Pt]$^{+}$ with a substrate. DFT calculations performed by Prof. Dmitry G. Gusev of Wilfrid Laurier University using either the PBE0[201] or the M06-L[154] functionals with Gaussian 09,[147] predicted that the singlet state is more stable than the triplet (Figure 3.3). However, the triplet was calculated to be higher in energy by a relatively small margin (PBE0: by 12.6 kcal/mol in enthalpy and by 11.0 kcal/mol in free energy; M06-L: by 10.7 and 10.2 kcal/mol, respectively). The triplet can be best described as arising from the promotion of an electron from the lone pair of N to the empty orbital at Pt (see Figure 3.3). We do not interpret the singlet/triplet difference as evidence that the triplet [^{F}(PNP)Pt]$^{+}$ is ever present in a kinetically competent concentration in solution; indeed, we do not know whether free [^{F}(PNP)Pt]$^{+}$ in any spin state is an intermediate at all. However, this modest difference indirectly suggests that [^{F}(PNP)Pt]$^{+}$ and its singlet four-coordinate adducts may have reaction pathways accessible to them that lead to products of apparent triplet reactivity.

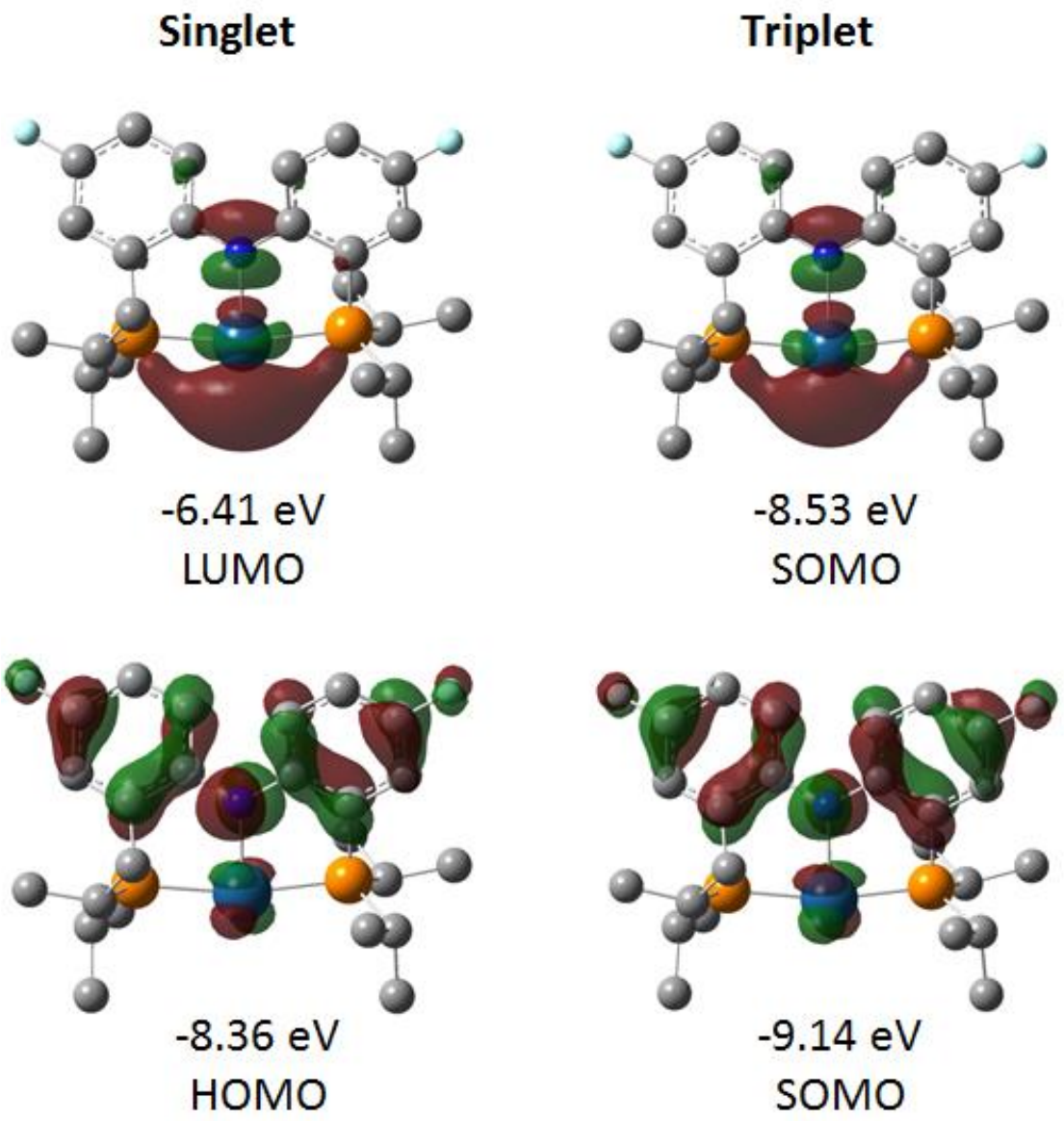

Figure 3.3 Depictions of the frontier orbitals of the singlet (left) and triplet (right) states of $[(PNP)Pt]^+$ calculated with the PBE0 functional.

3.2.6 Attempted Formation of a Dicationic Pincer-Pt-Methane σ-Complex

One strategy for circumventing the reactivity associated with the PNP ligand backbone was to reduce the availability of the lone pair on the nitrogen. We envisioned this would remove the internal base and reduce the propensity for C-H activation, as well as significantly reduce the oxidation potential thus avoiding metalloradical pathways. Additionally, protonation of cationic [(^{F}PN(H)P)PtMe][^{n}BuCB$_{11}$Cl$_{11}$] **313** would result in the dicationic complex [(^{F}PN(H)P)PtCH$_4$][^{n}BuCB$_{11}$Cl$_{11}$] **314**, where the increased electrophilic nature of the metal center might favor methane binding even more relative to the monocationic species.

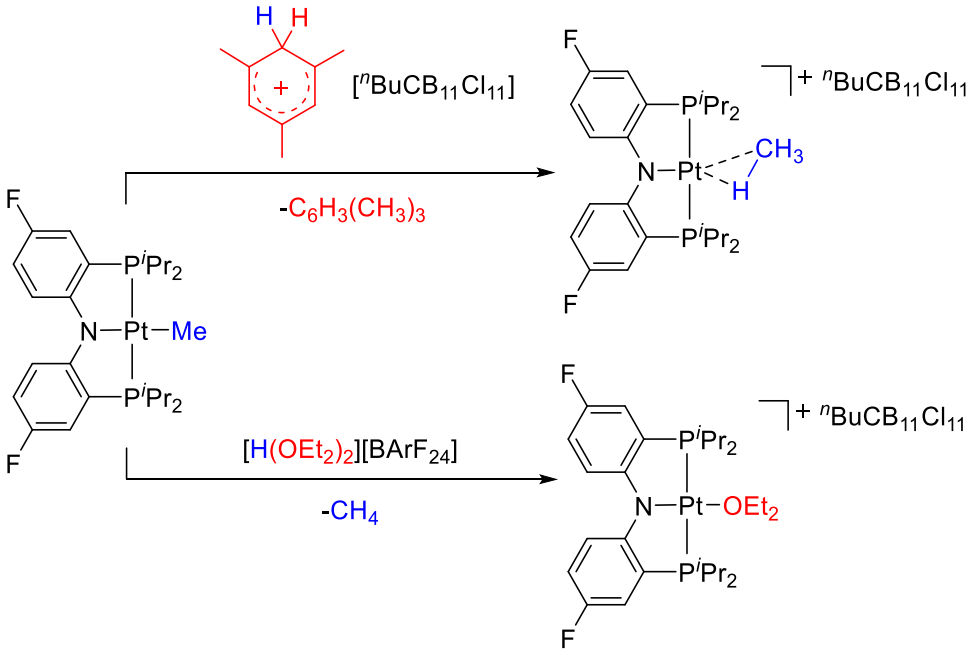

Scheme 3.8 Proposed (^{F}PNP)PtMe protonation with [H(C$_6$H$_3$(CH$_3$)$_3$)][^{n}BuCB$_{11}$Cl$_{11}$] versus [H(OEt$_2$)$_2$][BArF$_{24}$].

Starting from (^{F}PNP)PtMe **315** our strategy included the use of $[H(C_6H_3(CH_3)_3)][RCB_{11}Cl_{11}]$[202-204] (R = H, alkyl) as our proton source for the protonation of **315** to form the methane σ-complex $[(^{F}PNP)Pt(CH_4)][RCB_{11}Cl_{11}]$, **316**. The oxonium acid, $[H(OEt_2)_2][BArF_{24}]$, used by Brookhart and co-workers[88] has the potential to release two equivalents of diethyl ether upon protonation, a compound that can thermodynamically outcompete methane for the open coordination site at the metal. In contrast, the conjugate base of $[H(C_6H_3(CH_3)_3)][RCB_{11}Cl_{11}]$ is mesitylene, a bulky and weakly coordinating solvent (Scheme 3.8).

$[H(C_6H_3(CH_3)_3)][HCB_{11}Cl_{11}]$ was synthesized according to previously published procedures[202-204] by reacting $[Et_3Si{\cdot}HSiEt_3][HCB_{11}Cl_{11}]$ with HCl(g) in the presence of mesitylene. Reaction of two equivalents of $[H(C_6H_3(CH_3)_3)][HCB_{11}Cl_{11}]$ with **315** at room temperature in fluorobenzene surprisingly resulted in the formation of $[(^{F}PN(H)P)Pt\text{-}C_6H_4F][HCB_{11}Cl_{11}]$ **317**. While further studies are warranted, one explanation for the formation of the C-H activated product could be the ability of the unsaturated Pt center in $[(^{F}PN(H)P)Pt]^{2+}$ (formed after release of methane) to coordinate C_6H_5F (Scheme 3.9). Upon coordination, the hydrogens of the bound C_6H_5F would be significantly more acidic than the bulk solvent. Deprotonation of the bound C_6H_5F, would then result in the formation of **317**. It is unclear what serves as a base in the production of **317**. It is clear, however, that C_6H_5F has the ability to interact with the metal center and replace methane. This strongly suggests that the *iso*-propyl phosphines do not serve to sterically protect the unsaturated metal center and moving toward a ligand with bulkier side arms is necessary. The formation of the unsaturated intermediate $[(^{F}PN(H)P)Pt][HCB_{11}Cl_{11}]_2$ **318** is expected

to result from the protonation of Pt-methyl, as [(^{F}PN(H)P)PtMe][BArF$_{20}$] **319** is stable to methane release even at elevated temperatures.

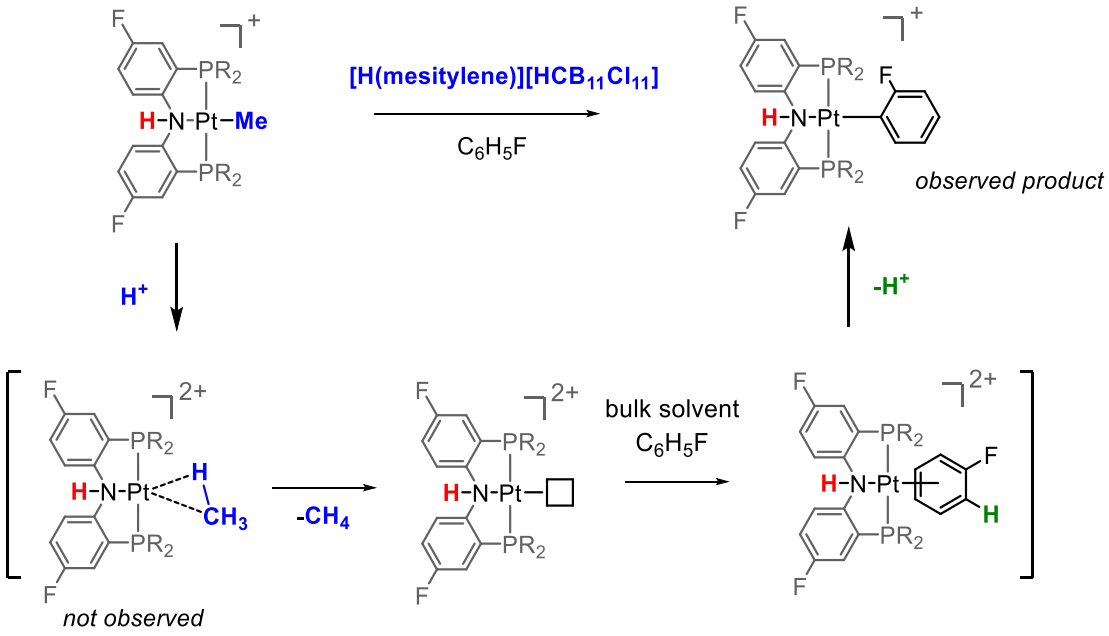

Scheme 3.9 Proposed pathway for C-H activation of C_6H_5F.

Computational work by Brookhart and co-workers[98] predicted that the dicationic fragment [(PONOP)Pt]$^{2+}$ would have a greater methane binding affinity than the previously reported **116** (Table 3.1). The PONOP ligand also offers an alternative steric profile which incorporates bulkier *tert*-butyl phosphine groups at the metal center. Applying similar reasoning as for the protonation of **315**, we again chose [H(C$_6$H$_3$(CH$_3$)$_3$)][RCB$_{11}$Cl$_{11}$] as acid for protonation of [(PONOP)PtMe][^{n}BuCB$_{11}$Cl$_{11}$] **320**.

Table 3.1 Calculated methane binding affinities for (PONOP)M species.

Complex	ΔH^o (kcal/mol)	ΔG^o (kcal/mol)*
$[Rh]^+$	–17.2	–7.8 (–11.8)
$[Pd]^{2+}$	–21.6	–12.7
$[Ir]^+$	–21.8	–11.9 (–16.1)
$[Pt]^{2+}$	–27.7	–18.1

Compound **320** was synthesized by reacting (COD)PtMeCl with PONOP **321** in the presence of Na[^{n}BuCB$_{11}$Cl$_{11}$]. The *n*-butylated carborane anion was used in order to improve solubility while maintaining robustness. This species was transferred to a J. Young NMR tube along with solid [H(C$_6$H$_3$(CH$_3$)$_3$)][^{n}BuCB$_{11}$Cl$_{11}$] and the NMR sample was cooled in liquid N_2. CD_2Cl_2 was then vacuum transferred into the NMR tube and the sample was placed in a precooled 500-MHz NMR spectrometer at –80 °C. **320** remained unreacted after 45 min at –80 °C. The NMR tube was ejected to confirm the solution had thawed and no precipitate was observed. Surprisingly, conversion of **320** was not observed until the spectrometer approached room temperature at which point a signal corresponding to [(PONOP)PtCl][^{n}BuCB$_{11}$Cl$_{11}$] **321** began to grow in. After 24 h at room temperature, **320** was completely converted into **321**. The complex [(PONOP)PtCl][HCB$_{11}$Cl$_{11}$] **322** was independently synthesized to confirm the identity of **321** (Scheme 3.10).

The reaction was repeated using C_6H_5F as solvent. No reaction of [H(C$_6$H$_3$(CH$_3$)$_3$)][^{n}BuCB$_{11}$Cl$_{11}$] with **320** was observed at room temperature. After 2 h at room temperature, the solution was placed in an oil bath at 80 °C for an additional 2 h

resulting in the formation of what is believed to be the product of C-H activation of the bulk solvent, [(PONOP)PtC$_6$H$_4$F][^{n}BuCB$_{11}$Cl$_{11}$] **323** along with the appearance of free methane (Scheme 3.10).

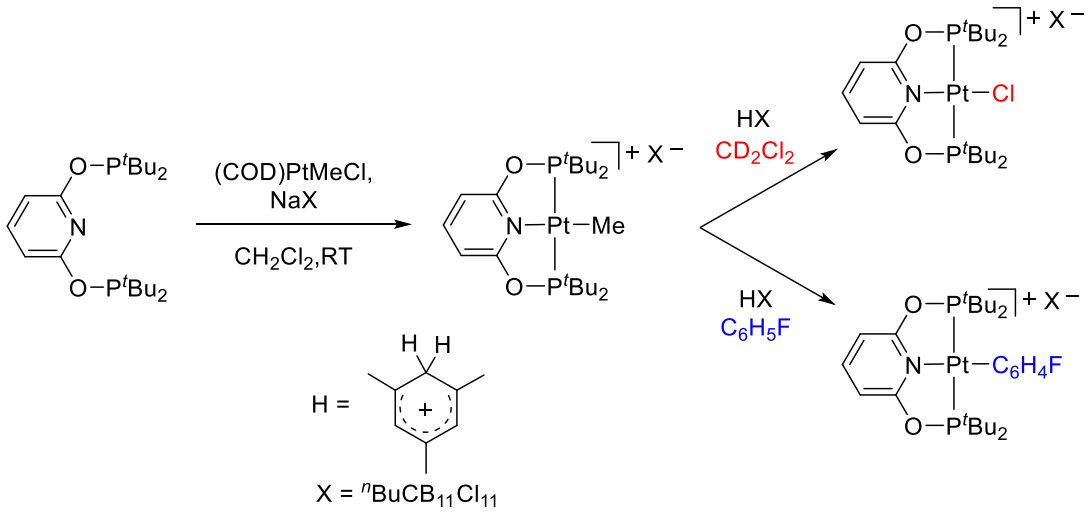

Scheme 3.10 Synthesis and protonation of (PONOP)PtMe in CD_2Cl_2 and C_6H_5F.

The lack of reactivity of **320** at –80 °C in CD_2Cl_2 and at room temperature in C_6H_5F appears to indicate that [H($C_6H_3(CH_3)_3$)][^{n}BuCB$_{11}$Cl$_{11}$] is not a strong enough acid to protonate the monocationic **320** at –80 °C to generate the dicationic methane σ-complex [(PONOP)Pt(CH_4)][^{n}BuCB$_{11}$Cl$_{11}$]$_2$, **324**. Indeed, Brookhart and co-workers required the use of the superacid conditions (HSO_3F/SbF_5 in a 1:1 ratio) in order to protonate the analogous [(PONOP)PdMe][BArF$_{24}$] species when [H(OEt_2)$_2$][BArF$_{24}$] and other acids (including superacids) were insufficient.[98]

Future studies will require the reactivity of acids stronger than $[H(C_6H_3(CH_3)_3)][^nBuCB_{11}Cl_{11}]$ for the generation of a dicationic Pt methane σ-complex. Additional complicating factors anticipated for dicationic species is their limited solubility in non-polar and weakly coordinating solvents. Overall, the preliminary studies with the neutral ^{F}PN(H)P and PONOP ligand platforms suggest that targeting a monocationic Pt methane σ-complex may be more empirically viable as long as constraints on the solubility of dicationic species and limits to the strength of superacids of weakly coordinating anions persist.

3.3 Conclusions

In summary, we have described the reactivity taking place upon removal of one of the ligands from a square-planar complex of Pt^{II}. The putative $[(^FPNP)Pt]^+$ fragment reacted with aromatic C–H bonds by net heterolytic C–H addition across the N–Pt bond when only C–H and strong C–Hal bonds were present in the substrate. When weaker C–Hal bonds were present, such as in bromobenzene or dichloromethane, the $[(^FPNP)Pt]^+$ fragment exhibited a tendency to abstract a halogen atom, a reaction quite unexpected of a Pt^{II} complex. The key to understanding the divergent reactivity of $[(^FPNP)Pt]^+$ is the non-innocence of the supporting ^{F}PNP ligand, which can function as an intramolecular component of a frustrated Lewis pair, or as a source of a single electron. This work was originally conceived with the thought of using $[(^FPNP)Pt]^+$as a scaffold for forming hydrocarbon complexes. It is now clear that a different pincer ligand is necessary to

achieve this goal, namely one with much lower Bronsted basicity and with lesser tendency to give up an electron.

3.4 Experimental

3.4.1 General Considerations

Unless otherwise noted, all manipulations and reactions were performed under argon, using standard glovebox and Schlenk line techniques. Toluene, triethylamine, pentane, C_6H_6 and C_6D_6 were dried over NaK/Ph_2CO/18-crown-6, distilled and stored over molecular sieves in an Ar-filled glovebox. Diethyl ether was dried and deoxygenated (by purging) using a solvent purification system and stored over molecular sieves in an Ar-filled glovebox. Fluorobenzene, 1,4-dioxane, acetonitrile, chlorobenzene, bromobenzene, CH_2Cl_2 and CD_2Cl_2 were dried over CaH_2, distilled or vacuum transferred and stored over molecular sieves in an Ar-filled glove box. 2-Bromotoluene, 3-bromotoluene and 4-bromotoluene were degassed and stored over molecular sieves in an Ar-filled glovebox. Triflic acid (HOTf) was vacuum transferred before use. Potassium tetrakis(pentafluorophenyl)borate ($KBArF_{20}$) was dried under vacuum overnight at ambient temperature and stored in an Ar-filled glovebox. (^{F}PNP)PtCl, (^{F}PNP)PtH and **315** were prepared according to literature procedures.[175] All other chemicals were used as received from commercial vendors. Prof. Dmitry G. Gusev of Wilfrid Laurier University conducted computational work and X-ray data solutions were determined by Dr. Nattamai Bhuvanesh with contributions from Dr. Dan Smith.

NMR spectra were recorded on a Varian iNova 300 (^{1}H NMR, 299.951 MHz; ^{13}C NMR, 75.426 MHz; ^{31}P NMR, 121.422 MHz; ^{19}F NMR, 282.211 MHz), a Varian NMRS 500 (^{1}H NMR, 499.682 MHz; ^{13}C NMR, 125.660 MHz; ^{31}P NMR, 202.265 MHz; ^{19}F NMR, 470.111 MHz) or a Varian iNova 400 (^{1}H NMR, 399.532 MHz; ^{13}C NMR, 100.473 MHz). Chemical shifts are reported in δ (ppm). For ^{1}H and ^{13}C NMR, the residual solvent peak was used to reference the spectra. ^{1}H NMR spectra in C_6D_5Br were referenced by setting the most downfield signal to 7.30 ppm. $^{13}C\{^{1}H\}$ NMR spectra in C_6D_5Br were referenced by setting the most downfield signal to 130.9 ppm. ^{19}F NMR signals (–134.3, –164.8, –168.7 ppm) and $^{13}C\{^{1}H\}$ NMR signals (149.5, 147.6, 139.6, 137.6, 135.7, 124.3 ppm) for $[BArF_{20}]^-$ were consistent between spectra and are not included below. ^{31}P NMR spectra were referenced using 85% H_3PO_4 at δ 0 ppm. ^{19}F NMR spectra were referenced using CF_3CO_2H at δ –78.5 ppm. ^{1}H-^{1}H COSY experiments were used in the assignment of ^{1}H NMR signals. Elemental analysis was performed by Complete Analysis Laboratories Inc., Parsippany, NJ, USA. FT-IR spectra were collected using a Bruker ALPHA-P FT-IR spectrometer with a diamond ATR.

3.4.1.1 Syntheses of Starting and Auxiliary Materials

(^{F}PNP)PtOTf (301). In a 50-mL Teflon screw-capped round-bottomed flask, (^{F}PNP)PtH (1.69 g, 2.67 mmol) was dissolved in 20 mL of toluene, forming a clear, yellow solution. MeOTf (332 μL, 2.94 mmol) was added via syringe, and the flask was placed in an oil bath at 110°C for 24 h. During the course of the reaction, a brown solid precipitate formed that is believed to be [(^{F}PN(Me)P)PtH][OTf]. With continued heating, this

intermediate loses methane to generate the final product. The resulting orange solution was filtered over Celite, and the volatiles were removed, yielding an oily yellow residue. The residue was redissolved in a minimal amount of toluene and layered with pentane. After recrystallization at –35°C, yellow-orange crystals were collected, washed with cold pentane and dried under vacuum, yielding a yellow solid. Isolated yield: 1.88 g, 90%. ^{1}H NMR (C_6D_6, Figure 3.4): δ 7.22 (m, 2H, Ar-*H*), 6.70 (m, 2H, Ar-*H*), 6.52 (m, 2H, Ar-*H*), 2.50 (m, 4H, C*H*Me$_2$), 1.26 (vtd, $J_{P\text{-}H}$ = 8.7 Hz, $J_{H\text{-}H}$ = 7.0 Hz, 12H, CH*Me*$_2$), 0.90 (vtd, $J_{P\text{-}H}$ = 8.1 Hz, $J_{H\text{-}H}$ = 7.2 Hz, 12H, CH*Me*$_2$). ^{13}C{^{1}H} NMR (C_6D_6): δ 160.3 (vt, $J_{P\text{-}C}$ = 9.4 Hz, C_{Ar}-N), 155.7 (d, $J_{F\text{-}C}$ = 240 Hz, C_{Ar}-F), 119.0 (m, C_{Ar}-P), 118.8 (q, $J_{F\text{-}C}$ = 318 Hz, *C*F$_3$), 118.4 (d, $J_{F\text{-}C}$ = 23 Hz, C_{Ar}-H), 118.1 (d, $J_{F\text{-}C}$ = 22 Hz, C_{Ar}-H), 116.4 (m, C_{Ar}-H), 25.2 (vt, $J_{P\text{-}C}$ = 15 Hz, *C*HMe$_2$), 18.1 (CH*Me*$_2$), 17.5 (CH*Me*$_2$). ^{19}F NMR (C_6D_6, Figure 3.5): δ –77.7, –126.9. ^{31}P{^{1}H} NMR (C_6D_6, Figure 3.6): δ 45.8 ($J_{195Pt\text{-}P}$ = 2,713 Hz).

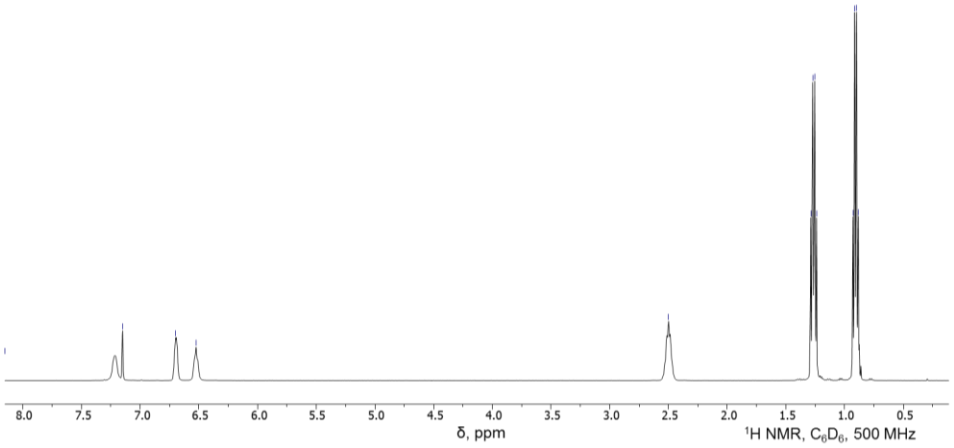

Figure 3.4 ^{1}H NMR spectrum of **301** in C_6D_6 at RT measured on a 500-MHz Varian NMRS.

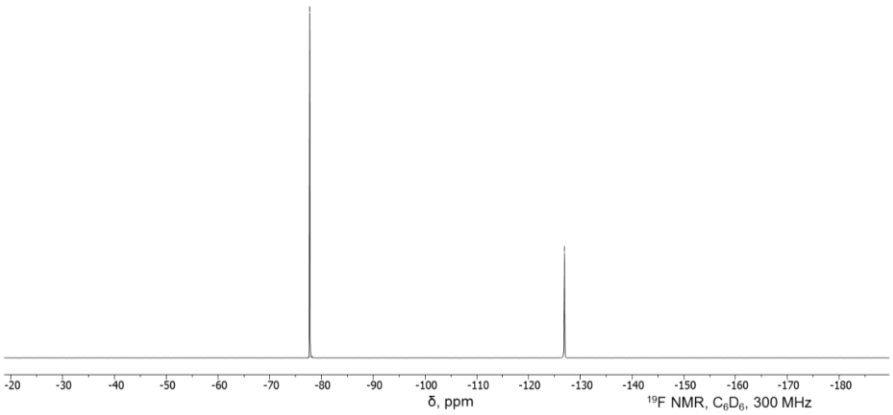

Figure 3.5 ^{19}F NMR spectrum of **301** in C_6D_6 at RT measured on a 300-MHz Varian iNova.

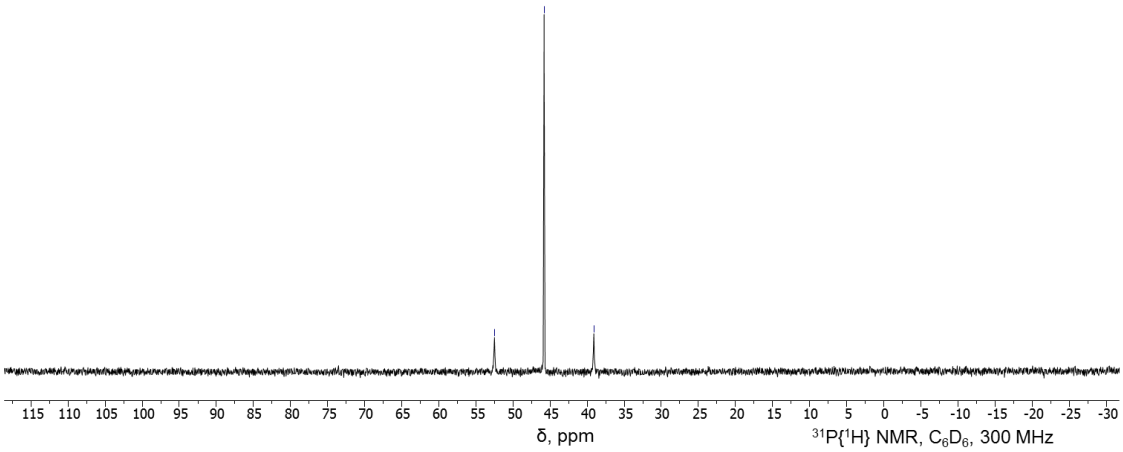

Figure 3.6 $^{31}P\{^1H\}$ NMR spectrum of **301** in C_6D_6 at RT measured on a 300-MHz Varian iNova.

(PNP)PtBr (312). In a J. Young NMR tube, **301** (17.9 mg, 0.0229 mmol) was dissolved in C_6D_6. Me_3SiBr (3.0 μL, 0.023 mmol) was added via syringe, and the solution remained clear yellow with full conversion to **312** observed by NMR. ^1H NMR (C_6D_6, Figure 3.7): δ 7.38 (m, 2H, Ar-*H*), 6.75 (m, 2H, Ar-*H*), 6.63 (vtd, $J_{P\text{-}H}$ = 8.5 Hz, $J_{H\text{-}H}$ = 3

Hz, 2H, Ar-*H*), 2.35 (m, 4H, C*H*Me$_2$), 1.31 (vtd, $J_{P\text{-}H}$ = 8 Hz, $J_{H\text{-}H}$ = 7 Hz, 12H, CH*Me*$_2$), 0.96 (app q (dvt), J = 8 Hz, 12H CH*Me*$_2$). ^{19}F NMR (C_6D_6, Figure 3.8): δ –128.5. ^{31}P{^{1}H} NMR (C_6D_6, Figure 3.9): δ 40.65 ($J_{195Pt\text{-}P}$ = 2,635 Hz).

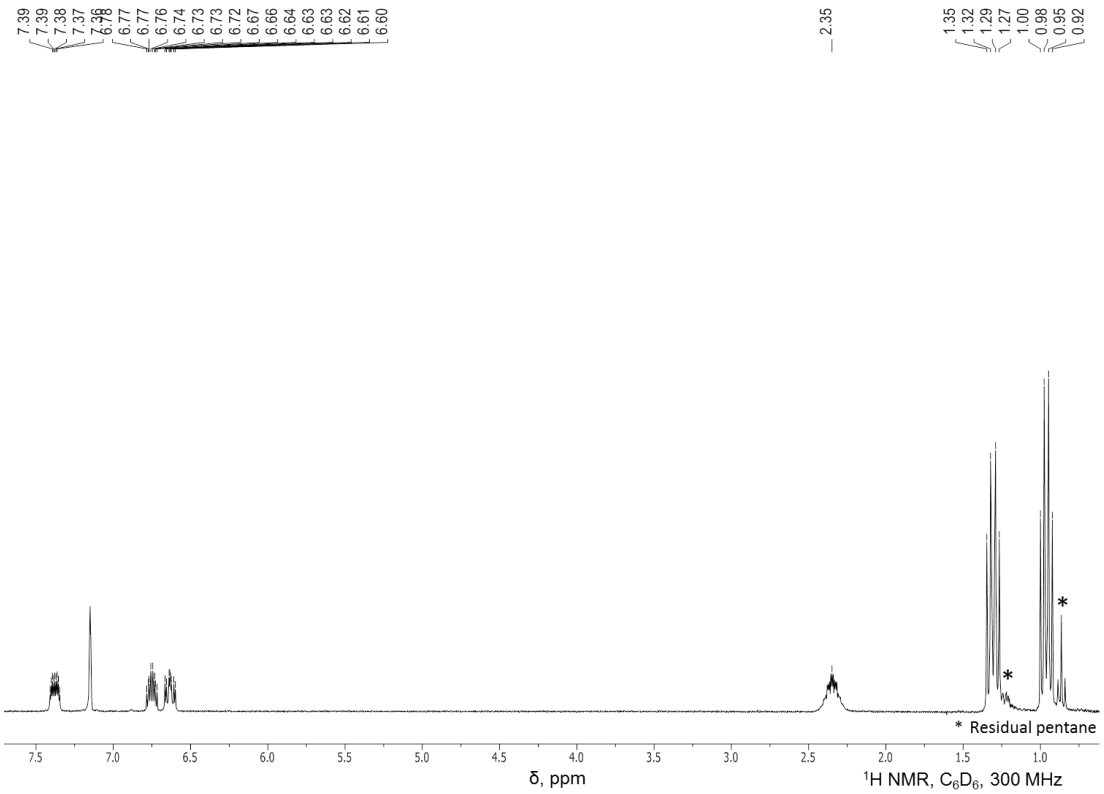

Figure 3.7 ^{1}H NMR spectrum of **312** in C_6D_6 at RT measured on a 300-MHz Varian iNova**.**

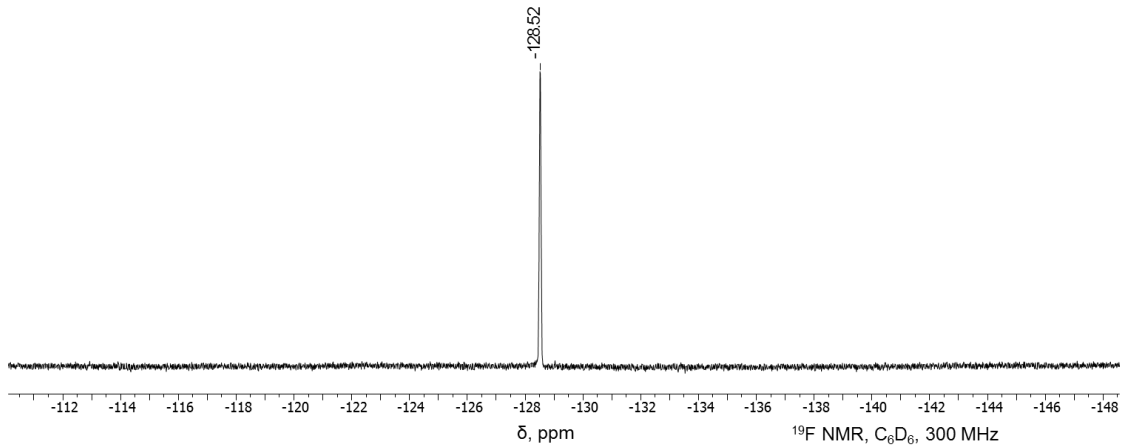

Figure 3.8 ^{19}F NMR spectrum of **312** in C_6D_6 at RT measured on a 300-MHz Varian iNova.

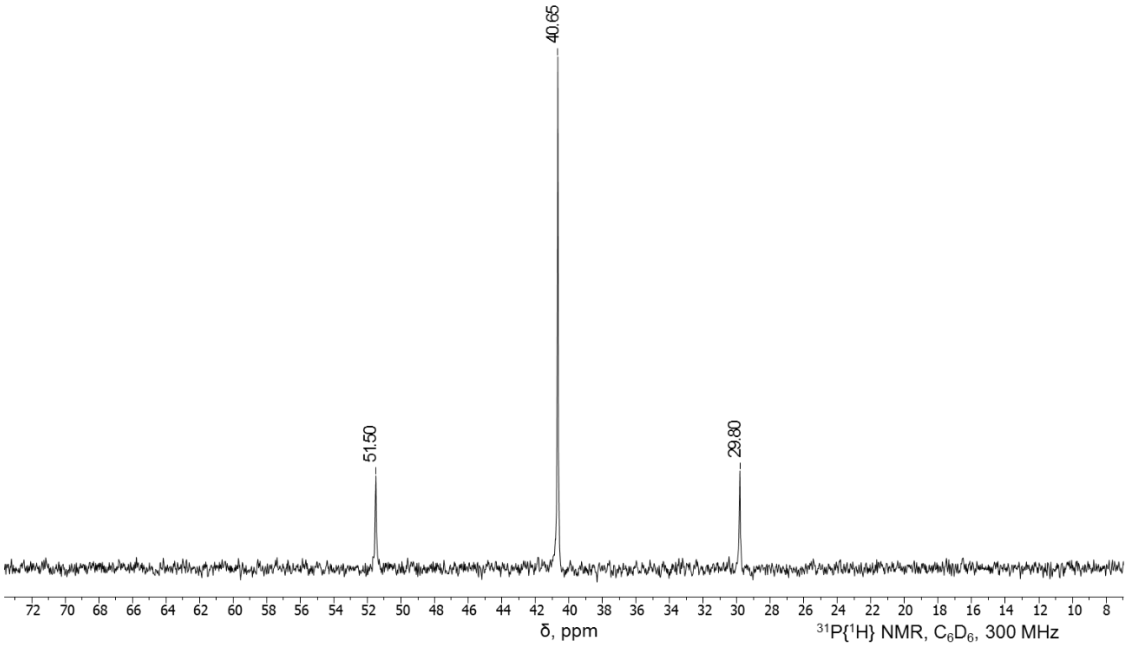

Figure 3.9 $^{31}P\{^1H\}$ NMR spectrum of **312** in C_6D_6 at RT measured on a 300-MHz Varian iNova.

Independent Synthesis of [(^{F}PN(H)P)PtOTf][BArF$_{20}$] (308). 1 (26.2 mg, 0.0335 mmol) was dissolved in about 4 mL of pentane and 1 mL of Et_2O, forming a clear yellow solution. [H(OEt$_2$)$_2$][BArF$_{20}$] (24.2 mg, 0.0292 mmol) was added, and a solid immediately

precipitated out of the solution. The volatiles were removed, and the pale blue solid was washed 3 times with pentane and then redissolved in CD_2Cl_2. This solution was filtered over Celite into a J. Young NMR tube and characterized by NMR. Please note that **308** is believed to decompose over time in CD_2Cl_2, resulting in the formation of **309**. ^{1}H NMR (CD_2Cl_2): δ 8.31 (s, $J_{195Pt-H}$ = 114Hz, 1H, N-*H),* 7.52 (m, 2H, Ar-*H*), 7.45–7.35 (m, 4H, Ar-*H*), 3.12 (m, 2H, C*H*Me$_2$), 2.98 (m, 2H, C*H*Me$_2$), 1.47 (app q (dvt), *J* = 8 Hz, 6H, CH*Me*$_2$), 1.45 (app q (dvt), *J* = 8 Hz, 6H, CH*Me*$_2$), 1.25 (app q (dvt), *J* = 9 Hz, 6H, CH*Me*$_2$), 1.24 (app q (dvt), *J* = 9 Hz, 6H, CH*Me*$_2$). ^{19}F NMR (CD_2Cl_2): δ –77.3, –107.5. ^{31}P{^{1}H} NMR (CD_2Cl_2): δ 47.1 ($J_{195Pt-P}$ = 2,474 Hz).

Independent Synthesis of [(^{F}PN(H)P)PtCl][BArF$_{20}$] (309). (^{F}PNP)PtCl (32.7 mg, 0.0491 mmol) was dissolved in CD_2Cl_2 in a J. Young NMR tube, forming a clear yellow solution. [H(OEt$_2$)$_2$][BArF$_{20}$] (41.2 mg, 0.0498) was added, and upon shaking, the solution became a clear, very pale blue. After a few minutes, a small amount of white precipitate was also observed. ^{1}H NMR (CD_2Cl_2, Figure 3.10): δ 8.01 (s, $J_{195Pt-H}$ = 86 Hz, 1H, N-*H*), 7.44 (m, 2H, Ar-*H*), 7.40 (m, 2H, Ar-*H*), 7.36 (m, 2H, Ar-*H*), 3.05 (m, 2H, C*H*Me$_2$), 2.88 (m, 2H, C*H*Me$_2$), 1.50 (vtd, J_{P-H} = 9 Hz, J_{H-H} = 7 Hz, 6H, CH*Me*$_2$), 1.42 (vtd, J_{P-H} = 9 Hz, J_{H-H} = 7 Hz, 6H, CH*Me*$_2$), 1.33 (vtd, J_{P-H} = 9 Hz, J_{H-H} = 7 Hz, 6H, CH*Me*$_2$), 1.28 (vtd, J_{P-H} = 9 Hz, J_{H-H} = 7 Hz, 6H, CH*Me*$_2$). ^{19}F NMR (CD_2Cl_2, Figure 3.11): δ –109.4. ^{31}P{^{1}H} NMR (CD_2Cl_2, Figure 3.12): δ 41.7 ($J_{195Pt-P}$ = 2,445 Hz).

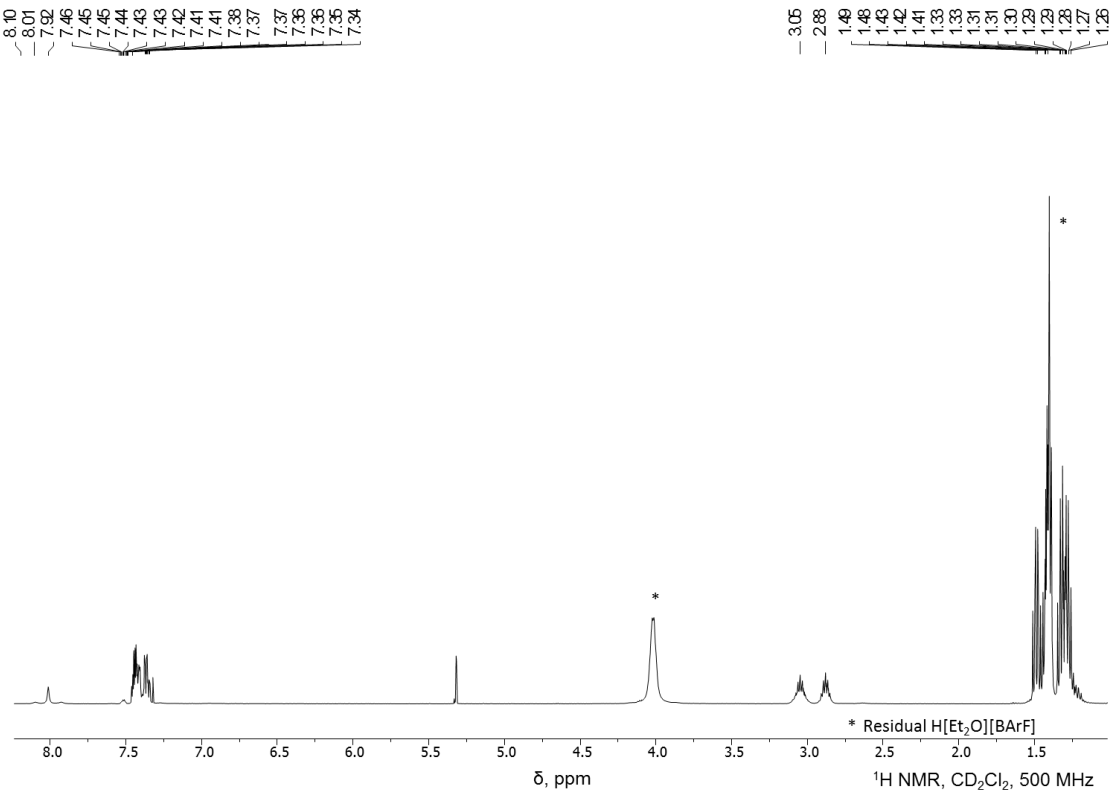

Figure 3.10 ^{1}H NMR spectrum of **309** in CD_2Cl_2 at RT measured on a 500-MHz Varian NMRS.

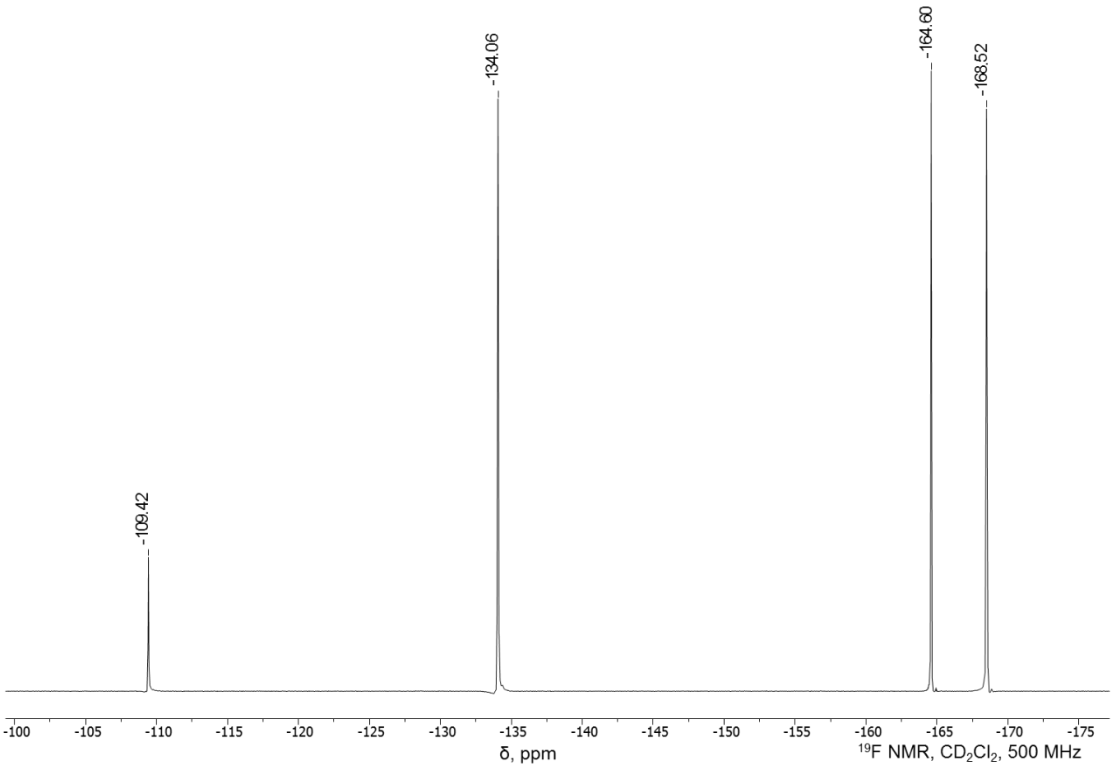

Figure 3.11 ^{19}F NMR spectrum of **309** in CD_2Cl_2 at RT measured on a 500-MHz Varian NMRS.

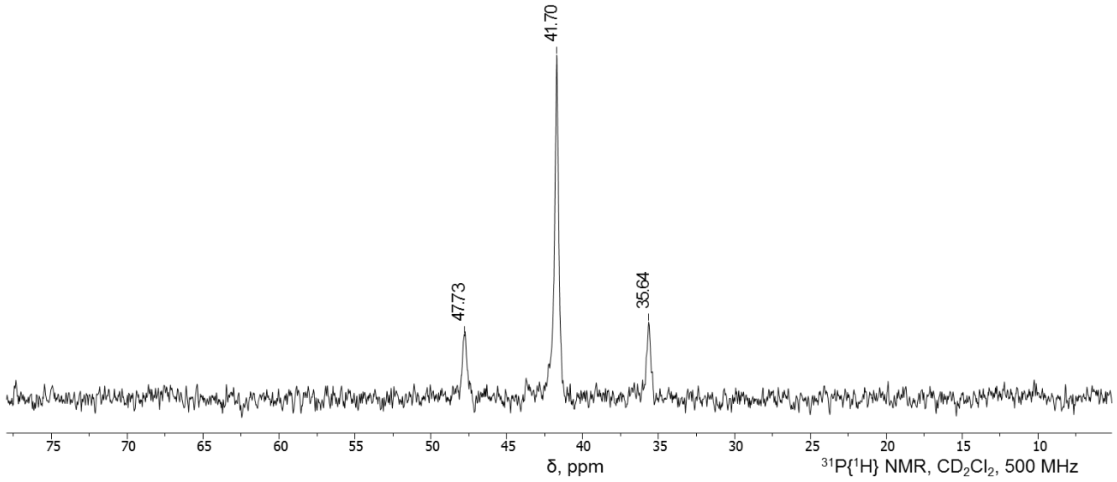

Figure 3.12 $^{31}P\{^1H\}$ NMR spectrum of **309** in CD_2Cl_2 at RT measured on a 500-MHz Varian NMRS.

[(^{F}PNP)Pt-NCMe][BArF$_{20}$] (306). 301 (14.6 mg, 0.0187 mmol) and KBArF$_{20}$ (13.4 mg, 0.0187 mmol) were added to a J. Young NMR tube. MeCN was added, forming an orange solution containing some undissolved KBArF$_{20}$. The NMR tube was placed on an NMR tube rotator overnight, after which the ^{19}F NMR spectrum showed full conversion to the product. The contents were transferred to a 10-mL Schlenk flask, and the volatiles were removed. The resulting oily solid was washed with isooctane and dried, yielding a yellow solid that was somewhat soluble in C_6D_6. ^{1}H NMR (C_6D_6, Figure 3.13): δ 7.06–7.02 (m, 2H, Ar-*H*), 6.58–6.53 (m, 4H, Ar-*H*), 1.96 (m, 4H, C*H*Me$_2$), 1.41 (s, 3H, NC*Me*), 0.92 (vtd, $J_{P\text{-}H}$ = 9 Hz, $J_{H\text{-}H}$ = 7 Hz, 12H, CH*Me*$_2$), 0.76 (vtd, $J_{P\text{-}H}$ = 9 Hz, $J_{H\text{-}H}$ = 7 Hz, 12H, CH*Me*$_2$). ^{13}C{^{1}H} NMR (C_6D_6): δ 159.8 (vt, $J_{P\text{-}C}$ = 10 Hz, C_{Ar}-N), 156.1 (dvt, $J_{F\text{-}C}$ = 242 Hz, $J_{P\text{-}C}$ = 5 Hz, C_{Ar}-F), 137.7 (t, $J_{P\text{-}C}$ = 14 Hz), 119.7 (d, $J_{F\text{-}C}$ = 23 Hz, C_{Ar}-H), 118.0 (d, $J_{F\text{-}C}$ = 23 Hz, C_{Ar}-H), 116.8 (m), 116.6 (app q, J = 6.4 Hz, C_{Ar}-H), 25.3 (vt, $J_{P\text{-}C}$ = 16 Hz, *C*HMe$_2$), 17.6 (CH*Me*$_2$), 17.2 (CH*Me*$_2$), 1.29 (NC*Me*). ^{19}F NMR (C_6D_6, Figure 3.14): δ –125.1. ^{31}P{^{1}H} NMR (C_6D_6, Figure 3.15): δ 48.9 ($J_{195Pt\text{-}P}$ = 2,474 Hz).

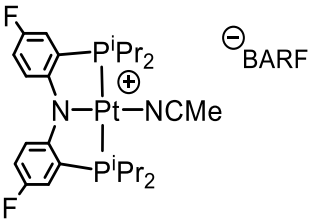

[(^{F}PNP)Pt-NCMe][BArF$_{20}$]
306

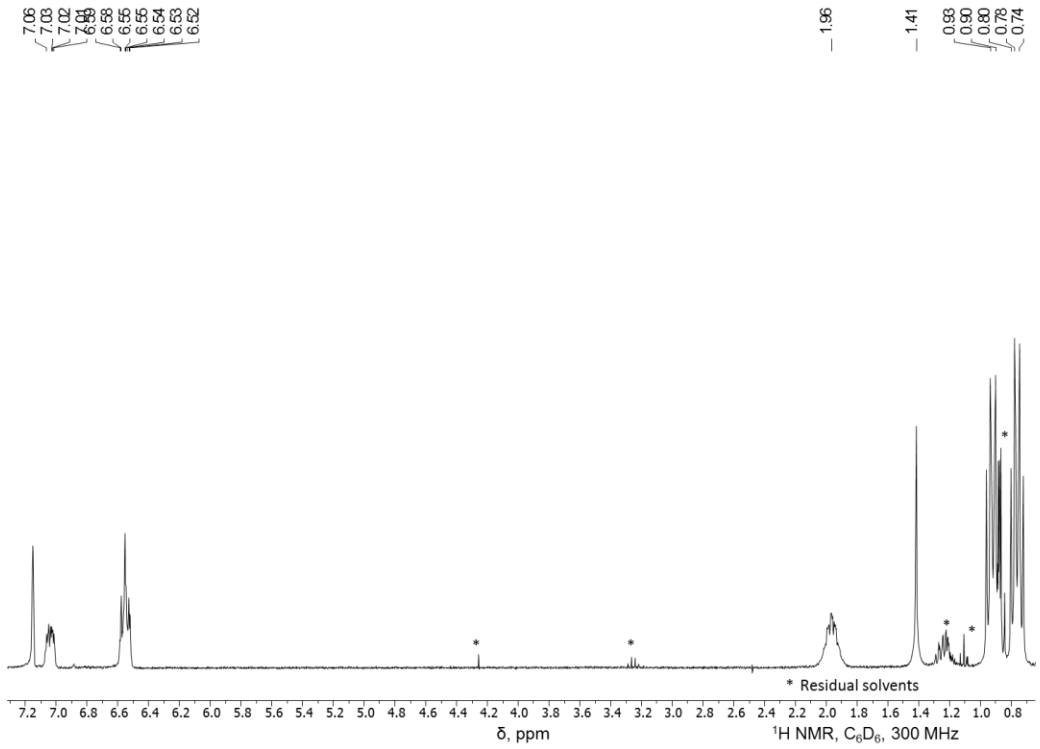

Figure 3.13 ^{1}H NMR spectrum of **306** in C_6D_6 at RT measured on a 300-MHz Varian iNova.

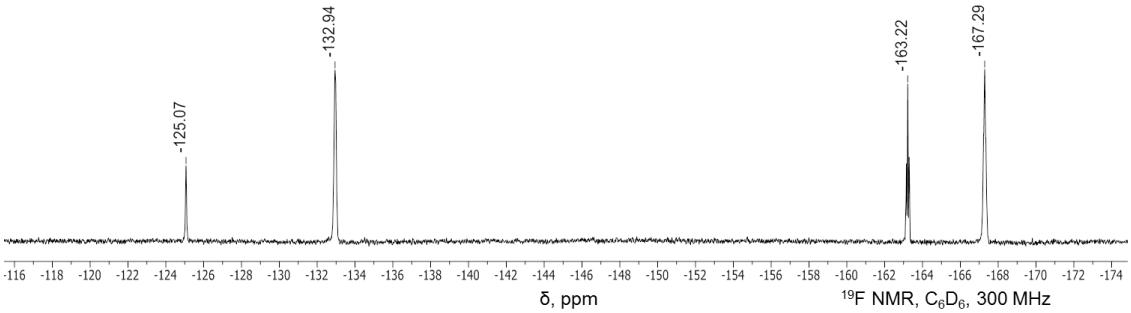

Figure 3.14 ^{19}F NMR spectrum of **306** in C_6D_6 at RT measured on a 300-MHz Varian iNova.

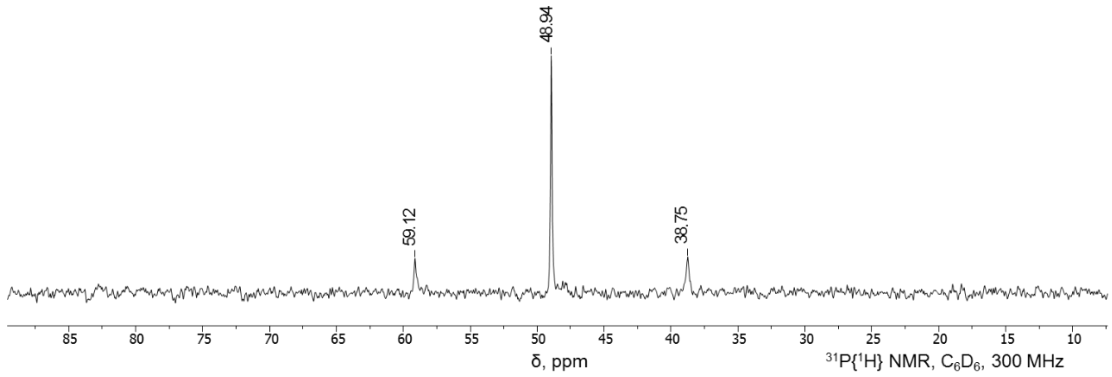

Figure 3.15 $^{31}P\{^{1}H\}$ NMR spectrum of **306** in C_6D_6 at RT measured on a 300-MHz Varian iNova.

***o*-Tolyllithium.** 2-bromotoluene (173 mg, 1.01 mmol) was transferred to a small vial. About 5 mL of pentane was added, and the solution was chilled to –35°C in a glovebox freezer. ^{n}BuLi (310 μL, 2.5 M solution in hexanes, 0.775 mmol) was added via syringe. The solution was allowed to stir at RT overnight, resulting in the formation of a white precipitate. The solvent was decanted off of the solid, and the solid was washed with 3 × 3 mL of pentane and then dried under vacuum. The solid was stored at –35°C. For NMR characterization, an aliquot of the solid was transferred to an NMR tube and mixed with a ~4:1 C_6D_6:Et_2O solution. Isolated yield: 62 mg, 81%. ^{1}H NMR (C_6D_6/Et_2O): δ 8.19 (m, 1H, Ar-*H*), 7.32–7.23 (m, 3H, Ar-*H*), 2.74 (s, 3H, CH_3).

***m*-Tolyllithium.** 3-bromotoluene (154 mg, 0.901 mmol) was transferred to a small vial. About 5 mL of pentane was added, and the solution was chilled to –35°C in a glovebox freezer. ^{n}BuLi (280 μL, 2.5 M solution in hexanes, 0.700 mmol) was added via syringe. The solution was allowed to stir at RT overnight, resulting in the formation of a

white precipitate. The solvent was decanted off of the solid, and the solid was washed with 3 × 3 mL of pentane and then dried under vacuum. The solid was stored at –35°C. For NMR characterization, an aliquot of the solid was transferred to an NMR tube and mixed with a ~4:1 C_6D_6:Et_2O solution. Isolated yield: 59.7 mg, 87%. ^{1}H NMR (C_6D_6/Et_2O): δ 8.04 (br s, 1H, Ar-*H*), 8.00 (d, *J* = 6.6 Hz, 1H, Ar-*H*), 7.18 (overlapping with C_6D_6 signal, 1H, Ar-*H*), 6.97 (d of multiplets, *J* = 7.5 Hz, 1H, Ar-*H*), 2.30 (s, 3H, C*H*$_3$).

***p*-Tolyllithium.** 4-bromotoluene (208 mg, 1.22 mmol) was transferred to a small vial. About 5 mL of pentane was added, and the solution was chilled to –35°C in a glovebox freezer. ^{n}BuLi (370 μL, 2.5 M solution in hexanes, 0.925 mmol) was added via syringe. The solution was allowed to stir at RT overnight, resulting in the formation of a white precipitate. The solvent was decanted off of the solid, and the solid was washed with 3 × 3 mL of pentane and then dried under vacuum. The solid was stored at –35°C. For NMR characterization, an aliquot of the solid was transferred to an NMR tube and mixed with a ~4:1 C_6D_6:Et_2O solution. Isolated yield: 77 mg, 85%. ^{1}H NMR (C_6D_6/Et_2O): δ 8.04 (d, *J* = 7 Hz, 2H, Ar-*H*), 7.08 (d, *J* = 7 Hz, 2H, Ar-*H*), 2.24 (s, 3H, C*H*$_3$).

[H(OEt$_2$)$_2$][BArF$_{20}$]. This procedure was modified from the one reported in the literature.[205] $KBArF_{20}$ (412 mg, 0.574 mmol) was dissolved in approximately 10 mL of dry Et_2O under Ar. A 100-mL Schlenk flask was filled with HCl gas, and the $KBArF_{20}$ solution was transferred into this flask via syringe. The flask was opened to an Ar atmosphere and allowed to stand in an ice bath. After 30 min, the clear colorless supernatant was cannula transferred through a filter away from the precipitated KCl. Washes were also cannula transferred into the final vessel containing the product solution.

The volatiles were removed, and the flask was transferred into a glovebox. The resulting white solid was collected, dried under vacuum and stored at –35°C. Isolated yield: 378 mg, 79.5%. ^{1}H NMR (CD_2Cl_2): δ 16.4 (br s, 1H, Et_2O-*H*), 4.06 (br s, 8H, C*H*$_2$), 1.42 (t, *J* = 6.5 Hz, 12H, C*H*$_3$).

3.4.1.2 Syntheses of Neutral (PNP)Pt-R Complexes from (PNP)PtCl.

(^{F}PNP)PtC$_6$H$_5$ (302a). (^{F}PNP)PtCl (40.7 mg, 0.0610 mmol) was dissolved in C_6D_6 in a J. Young NMR tube. PhLi (41 μL, 1.8 M solution in Et_2O, 0.077 mmol) was added via syringe. After 10 min, the ^{19}F NMR spectrum showed full conversion to the product. The solution was filtered over a pad of Celite and silica gel and washed through with toluene. The volatiles were then removed, and the resulting yellow solid was redissolved in C_6D_6 for characterization. Isolated yield: 35 mg, 82%. ^{1}H NMR (C_6D_6, Figure 3.16): δ 7.64 (dd, *J* = 7.6 Hz, 1.9 Hz, $J_{195Pt-H}$ = 54 Hz, 2H, *o*-Ph-*H*), 7.55 (m, 2H, Ar-*H*), 7.14 (m, 2H, *m*-Ph-*H*), 6.98 (td, *J* = 7.6 Hz, 1.9 Hz, 1H, *p*-Ph-*H*), 6.75 (m, 4H, Ar-*H*), 2.08 (m, 4H, C*H*Me$_2$), 0.90–0.83 (m, 24H, CH*Me*$_2$). ^{13}C{^{1}H} NMR (C_6D_6): δ 160.7 (vt, J_{P-C} = 9 Hz, C_{Ar}-N), 154.5 (dvt, J_{F-C} = 236 Hz, J_{P-C} = 5 Hz, C_{Ar}-F), 139.5 (t, J_{P-C} = 2.3 Hz, $J_{195Pt-C}$ = 28 Hz), 136.9 (t, J_{P-C} = 9 Hz), 127.9 (overlapping with C_6D_6 signal), 122.1 (t, J_{P-C} = 1.3 Hz), 121.4 (vtd, J_{P-C} = 21 Hz, J_{F-C} = 4.5 Hz, C_{Ar}-P), 118.6 (d, J_{F-C} = 21 Hz, C_{Ar}-H), 118.2 (d, J_{F-C} = 22 Hz, C_{Ar}-H), 115.2 (app q, *J* = 6 Hz, C_{Ar}-H), 24.1 (vt, J_{P-C} = 15 Hz, *C*HMe$_2$), 17.7 (CH*Me*$_2$), 17.0 (CH*Me*$_2$). ^{19}F NMR (C_6D_6, Figure 3.17): δ –130.5. ^{31}P{^{1}H} NMR (C_6D_6, Figure 3.18): δ 40.1 ($J_{195Pt-P}$ = 2,848 Hz).

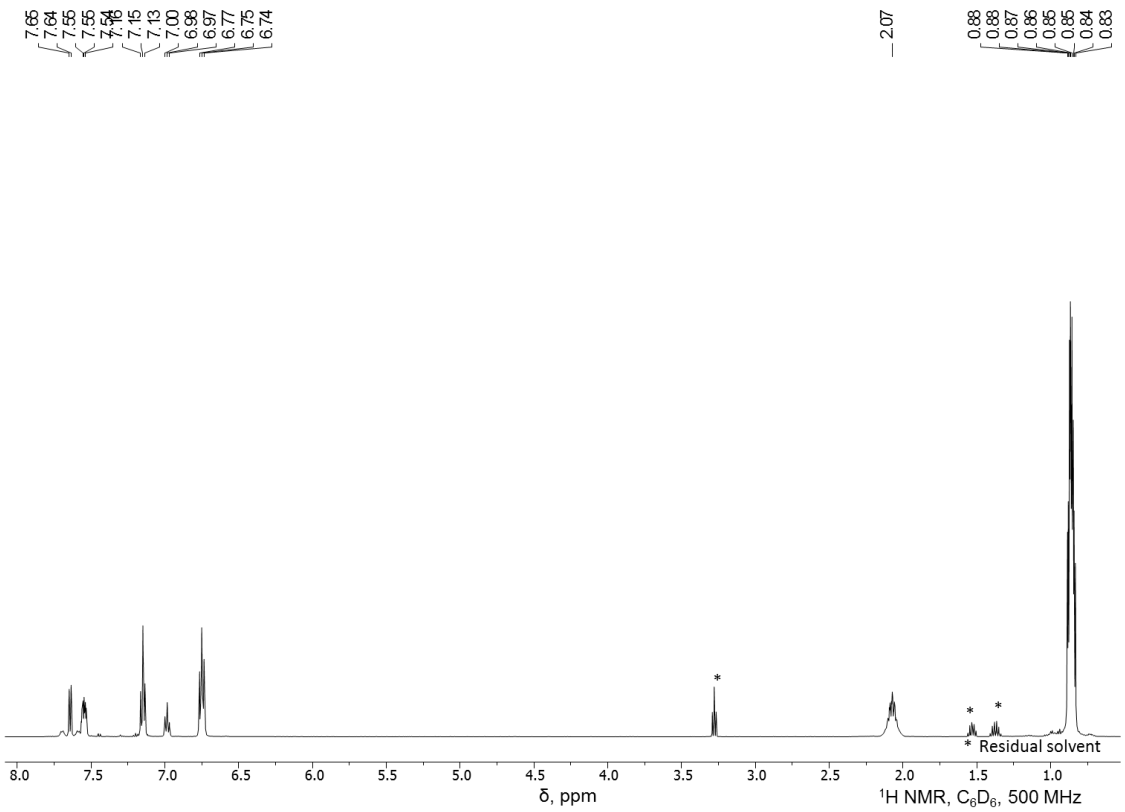

Figure 3.16 ^{1}H NMR spectrum of **302a** in C_6D_6 at RT measured on a 500-MHz Varian NMRS.

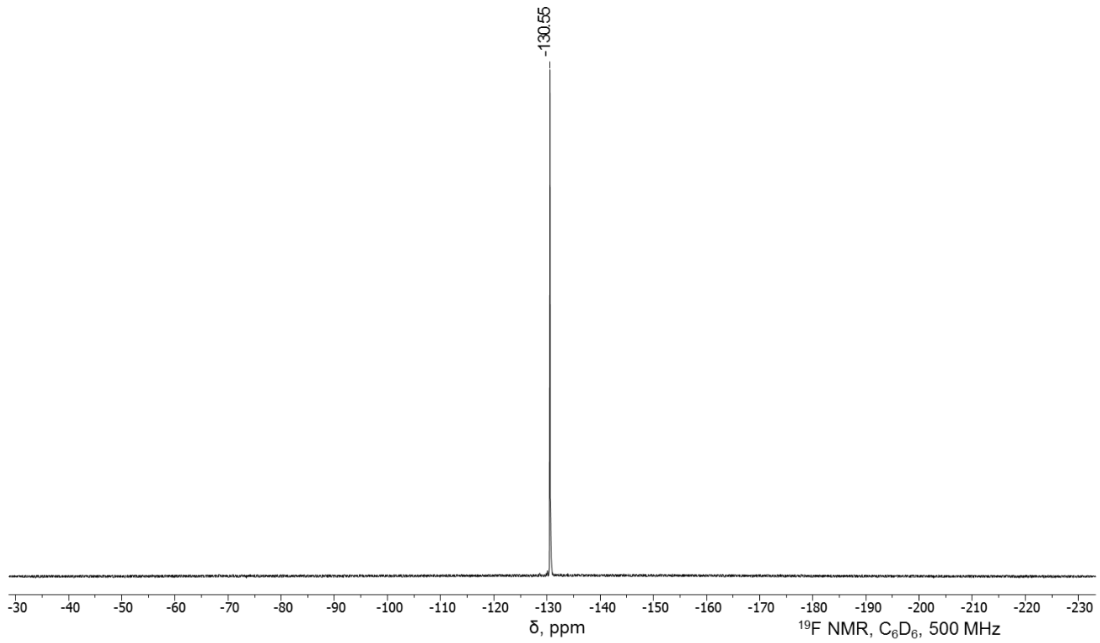

Figure 3.17 ^{19}F NMR spectrum of **302a** in C_6D_6 at RT measured on a 500-MHz Varian NMRS.

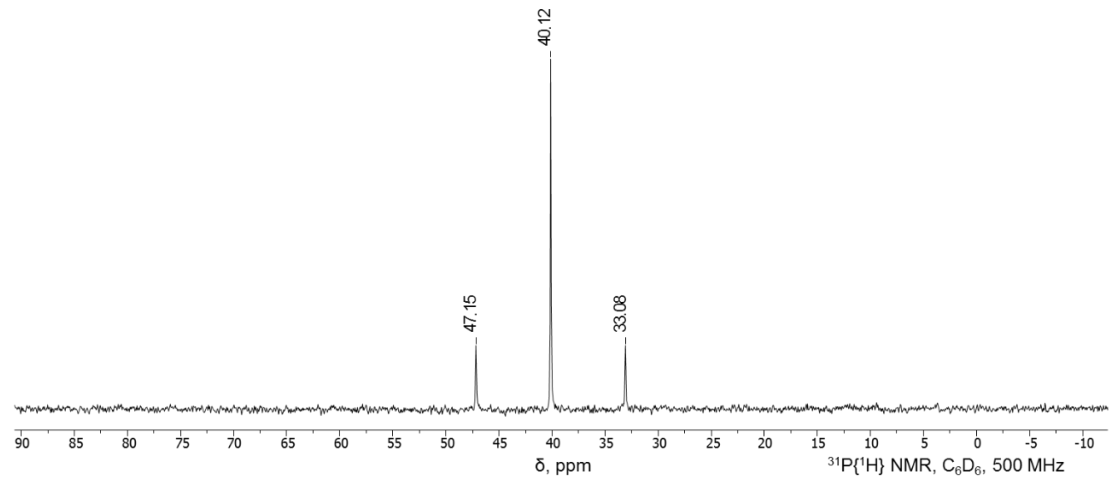

Figure 3.18 $^{31}P\{^1H\}$ NMR spectrum of **302a** in C_6D_6 at RT measured on a 500-MHz Varian NMRS.

(^{F}PNP)Pt-*o*-C_6H_4Me (302b). (^{F}PNP)PtCl (52.2 mg, 0.0783 mmol) and *o*-tolyllithium (9.8 mg, 0.10 mmol) were combined in a 10-mL Schlenk flask and stirred overnight in about 4 mL of toluene. The solution was then filtered over a pad of Celite and silica gel, the volatiles were removed and the resulting oily yellow solid was redissolved in pentane. The solution was filtered a second time over Celite and silica gel and eluted with pentane. The resulting pale blue solid was recrystallized from pentane at –35 °C, washed with cold pentane and dried under vacuum. Isolated yield: 32 mg, 57%. ^{1}H NMR (C_6D_6, Figure 3.19): δ 7.65 (m, $J_{195Pt-H}$ = 52.9 Hz, 1H, ortho C-*H* of C_6H_4Me), 7.48 (dquint, J = 9.2 Hz, 2.3 Hz, 2H, Ar-*H*), 7.13 (m, 1H, *meta* C-*H* of C_6H_4Me), 7.03 (m, 2H, *meta* and *para* C-*H* of C_6H_4Me), 6.73 (m, 4H, Ar-*H*), 2.68 (s, 3H, C_6H_4*Me*), 2.06 (m, 4H, C*H*Me_2), 0.83 (m, 24H, CH*Me*$_2$). ^{13}C{^{1}H} NMR (C_6D_6): δ 160.2 (vt, J_{P-C} = 9 Hz, C_{Ar}-N), 154.5 (dvt, J_{F-C} = 236 Hz, J_{P-C} = 5 Hz, C_{Ar}-F), 143.4 (t, J_{P-C} = 2.3 Hz), 138.8 (t, J_{P-C} = 2.4 Hz), 136.5, 125.0 ($J_{195Pt-C}$ = 55 Hz), 122.5, 121.5 (vt, J_{P-C} = 22 Hz, C_{Ar}-P), 118.4 (d, J_{F-C} = 22 Hz, C_{Ar}-H), 118.3 (d, J_{F-C} = 22 Hz, C_{Ar}-H), 115.2 (app q, J = 6 Hz, C_{Ar}-H), 28.0 (C_6H_4*C*H_3), 24.9 (vt, J_{P-C} = 15 Hz, *C*HMe_2), 23.4 (vt, J_{P-C} = 15 Hz, *C*HMe_2), 17.37 (CH*Me*$_2$), 17.35 (CH*Me*$_2$), 17.0 (CH*Me*$_2$), 16.5 (CH*Me*$_2$). ^{19}F NMR (C_6D_6): δ –130.5. ^{31}P{^{1}H} NMR (C_6D_6): δ 40.3 ($J_{195Pt-P}$ = 2,901 Hz).

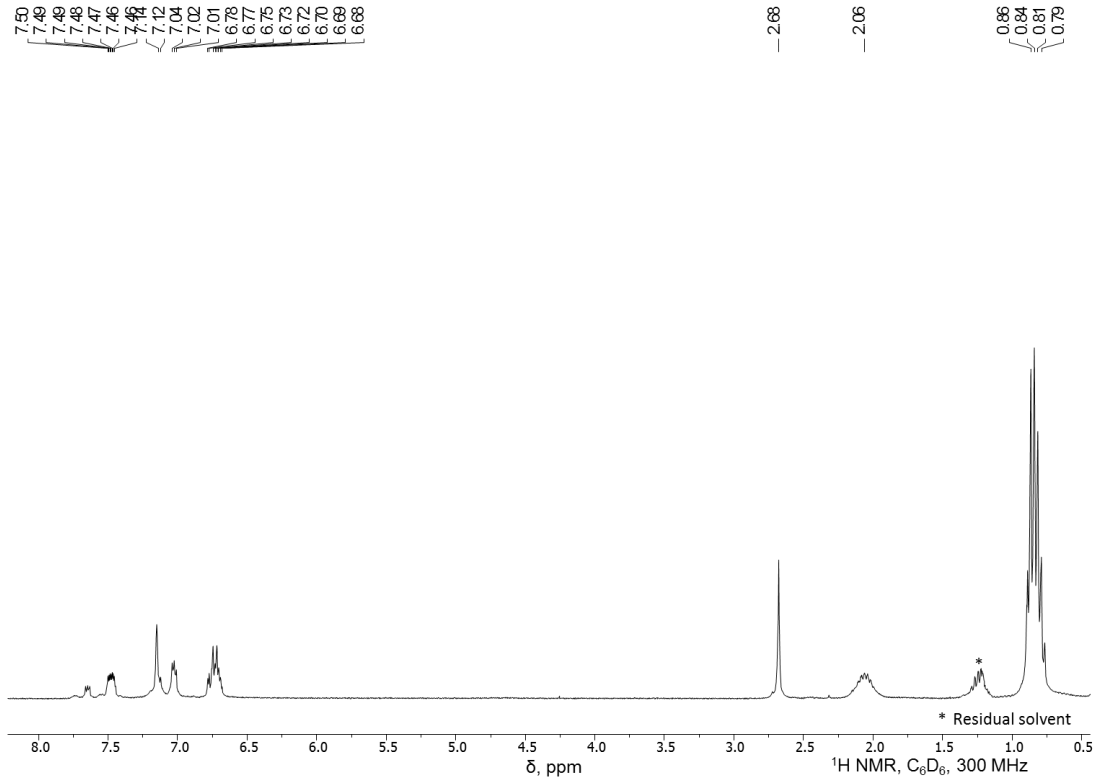

Figure 3.19 ^{1}H NMR spectrum of **302b** in C_6D_6 at RT measured on a 300-MHz Varian iNova.

(^{F}PNP)Pt-*m*-C$_6$H$_4$Me (302c). (^{F}PNP)PtCl (50.2 mg, 0.075 mmol) and *m*-tolyllithium (9.0 mg, 0.10 mmol) were combined in a 10-mL Schlenk flask and stirred overnight in about 4 mL of toluene. The solution was then filtered over a pad of Celite and silica gel, the volatiles were removed and the resulting oily yellow solid was redissolved in pentane. The solution was filtered a second time over Celite and silica gel and eluted with pentane. The resulting pale blue solid was recrystallized from pentane at –35 °C, washed with cold pentane and dried under vacuum. Isolated yield: 36 mg, 66%. ^{1}H NMR (C_6D_6, Figure 3.20): δ 7.57 (br s, $J_{195Pt-H}$ = 54.6 Hz, 1H, C-*H ortho* to Pt and Me), 7.56 (m, 2H, Ar-*H*), 7.48 (d, J = 7.4 Hz, $J_{195Pt-H}$ = 53.6 Hz, 1H, C-*H ortho* to Pt, *para* to Me),

7.10 (t, J = 7.4 Hz, 1H, *meta* C-*H* of C_6H_4Me), 6.82 (d, J = 7.4 Hz, 1H, *para* C-*H* of C_6H_4Me), 6.76 (m, 4H, Ar-*H*), 2.31 (s, 3H, C_6H_4*Me*), 2.11 (m, 4H, C*H*Me_2), 0.89 (m, 24H, CH*Me*$_2$). $^{13}C\{^1H\}$ NMR (C_6D_6): δ 160.7 (vt, $J_{P\text{-}C}$ = 10 Hz, C_{Ar}-N), 154.5 (dvt, $J_{F\text{-}C}$ = 231 Hz, $J_{P\text{-}C}$ = 5 Hz, C_{Ar}-F), 140.3 (t, $J_{P\text{-}C}$ = 2.5 Hz), 136.7 (t, $J_{P\text{-}C}$ = 9 Hz), 136.6 (t, $J_{P\text{-}C}$ = 2.4 Hz), 136.4, 123.0, 121.5 (vtd, $J_{P\text{-}C}$ = 22 Hz, $J_{F\text{-}C}$ = 4 Hz, C_{Ar}-P), 118.7 (d, $J_{F\text{-}C}$ = 22 Hz, C_{Ar}-H), 118.3 (d, $J_{F\text{-}C}$ = 22 Hz, C_{Ar}-H), 115.2 (app q, J = 6 Hz, C_{Ar}-H), 24.2 (vt, $J_{P\text{-}C}$ = 16 Hz, *C*HMe_2), 22.7 (C_6H_4*C*H_3), 17.8 (CH*Me*$_2$), 17.0 (CH*Me*$_2$). ^{19}F NMR (C_6D_6): δ –130.3. $^{31}P\{^1H\}$ NMR (C_6D_6): δ 40.0 ($J_{195Pt\text{-}P}$ = 2,855 Hz).

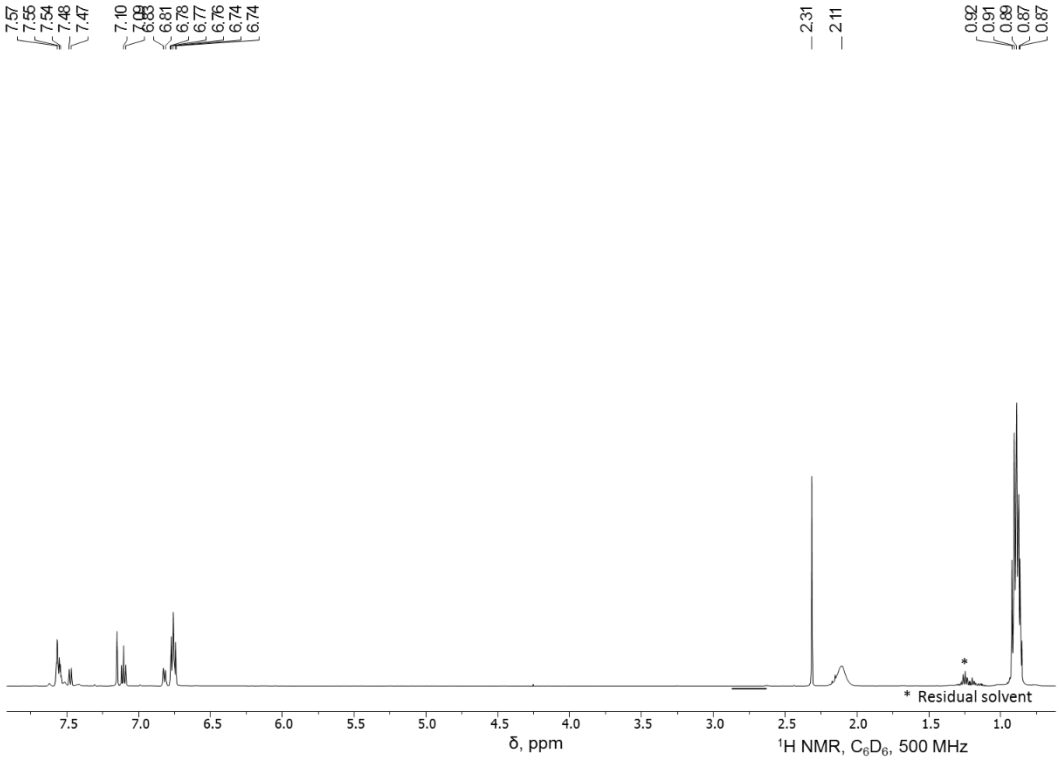

Figure 3.20 ^1H NMR spectrum of **302c** in C_6D_6 at RT measured on a 500-MHz Varian NMRS.

(^{F}PNP)Pt-*p*-C_6H_4Me (302d). (^{F}PNP)PtCl (118 mg, 0.177 mmol) and *p*-tolyllithium (19.5 mg, 0.199 mmol) were combined in a 25 mL Schlenk flask and stirred overnight in about 7 mL of toluene. The solution was then filtered over a pad of Celite and silica gel, the volatiles were removed and the resulting oily yellow solid was redissolved in pentane. The solution was filtered a second time over Celite and silica gel and eluted with pentane. The resulting pale blue solid was recrystallized from pentane at –35 °C, washed with cold pentane and dried under vacuum. Isolated yield: 94 mg, 72%. ^{1}H NMR (C_6D_6, Figure 3.21): δ 7.56 (m, $J_{195Pt-H}$ = 51.9 Hz, 4H, *ortho* C-*H* of C_6H_4Me and Ar-*H*), 7.04 (d, J = 7.6 Hz, 2H, *meta* C-*H* of C_6H_4Me), 6.76 (m, 4H, Ar-*H*), 2.27 (s, 3H, C_6H_4*Me*), 2.10 (m, 4H, C*H*Me_2), 0.88 (m, 24H, CH*Me*$_2$). ^{13}C{^{1}H} NMR (C_6D_6): δ 160.8 (vt, J_{P-C} = 8.8 Hz, C_{Ar}-N), 154.5 (dvt, J_{F-C} = 237 Hz, J_{P-C} = 5 Hz, C_{Ar}-F), 139.2 (t, J_{P-C} = 9.3 Hz, $J_{195Pt-C}$ = 30 Hz), 132.0 (t, J_{P-C} = 9 Hz), 130.5 (t, J_{P-C} = 1.5 Hz), 129.0 ($J_{195Pt-C}$ = 60 Hz, C_{Ar}-Pt), 121.6 (vtd, J_{P-C} = 22.4 Hz, J_{F-C} = 4 Hz, C_{Ar}-P), 118.7 (d, J_{F-C} = 21 Hz, C_{Ar}-H), 118.3 (d, J_{F-C} = 23 Hz, C_{Ar}-H), 115.2 (app q, J = 6 Hz, C_{Ar}-H), 24.2 (vt, J_{P-C} = 15.4 Hz, *C*HMe_2), 21.2 (C_6H_4*C*H_3), 17.8 (CH*Me*$_2$), 17.0 (CH*Me*$_2$). ^{19}F NMR (C_6D_6): δ –130.6. ^{31}P{^{1}H} NMR (C_6D_6): δ 40.0 ($J_{195Pt-P}$ = 2,853 Hz).

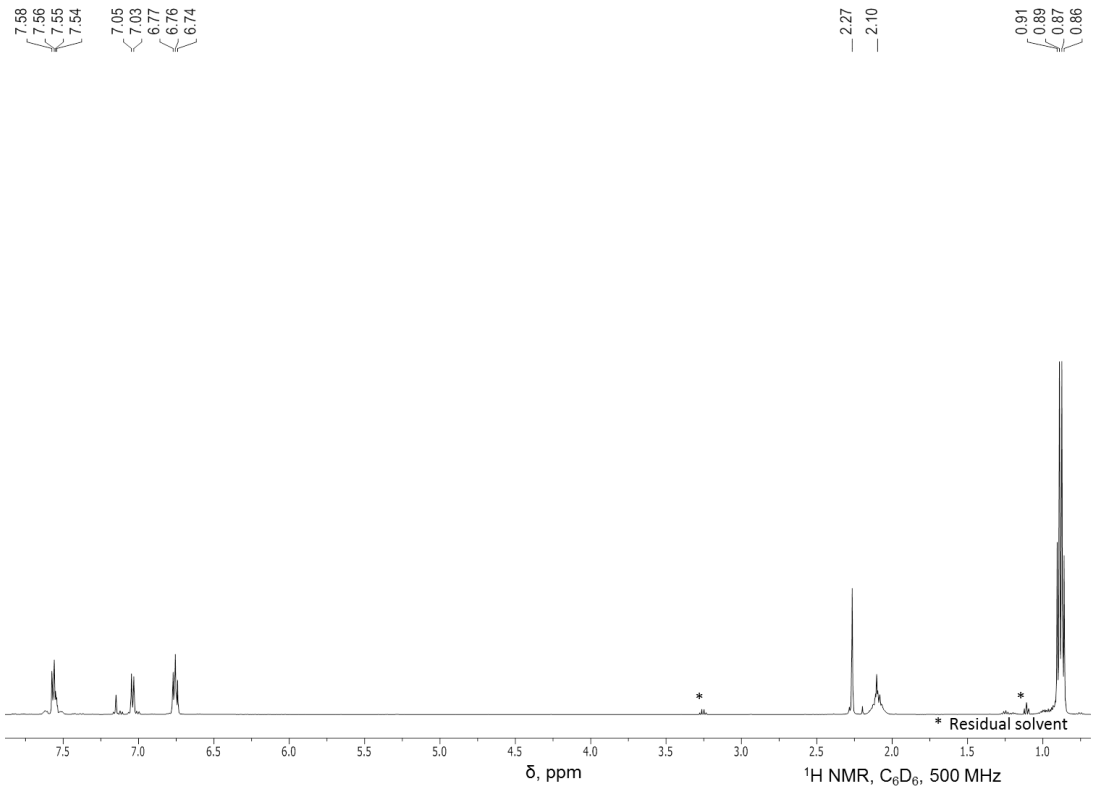

Figure 3.21 ^{1}H NMR spectrum of **302d** in C_6D_6 at RT measured on a 500-MHz Varian NMRS.

(^{F}PNP)PtCH$_2$C$_6$H$_5$ (302g). (^{F}PNP)PtCl (40.8 mg, 0.0612 mmol) was dissolved in C_6D_6 in a J. Young NMR tube, producing a clear yellow solution. About 0.5 mL of dioxane was added, followed by BnMgCl (73 μL, 1.0 M solution in Et_2O, 0.073 mmol). A white precipitate was immediately generated. The NMR tube was covered with Al foil and placed on an NMR tube rotator for 16 h, after which the ^{19}F NMR spectrum showed full conversion to the product. The solution was filtered through a pad of Celite and silica gel, yielding a clear yellow solution. The volatiles were removed, and the product was recrystallized from pentane at –35°C. The resulting yellow solid was collected and dried under vacuum. Isolated yield: 18.6 mg, 42.1%. ^{1}H NMR (C_6D_6, Figure 3.22): δ 7.52 (t, *J*

= 9 Hz, 2H, Ar-*H*), 7.49 (d, *J* = 7.5 Hz, 2H, Ar-*H*), 7.17 (t, *J* = 7.6 Hz, 2H, Ar-*H*), 6.97 (t, *J* = 7.5 Hz, 1H, $CH_2C_6H_5$), 6.81 (m, 2H, $CH_2C_6H_5$), 6.73 (m, 2H, $CH_2C_6H_5$), 3.32 (t, $J_{P\text{-}H}$ = 6 Hz, $J_{195Pt\text{-}H}$ = 95 Hz, 2H, $CH_2C_6H_5$), 1.94 (m, 4H, $CHMe_2$), 1.02 (app q (dvt), *J* = 8 Hz, 12H, $CHMe_2$), 0.90 (app q (dvt), *J* = 7.7 Hz, 12H, $CHMe_2$). $^{13}C\{^1H\}$ NMR (C_6D_6): δ 160.3 (vt, $J_{P\text{-}C}$ = 10 Hz, C_{Ar}-N), 154.5 (dvt, $J_{F\text{-}C}$ = 236 Hz, $J_{P\text{-}C}$ = 5 Hz, C_{Ar}-F), 152.5 (t, $J_{P\text{-}C}$ = 2 Hz, $J_{195Pt\text{-}C}$ = 39 Hz), 130.6 ($J_{195Pt\text{-}C}$ = 46 Hz), 127.6, 123.6, 121.9 (vtd, $J_{P\text{-}C}$ = 23 Hz, $J_{F\text{-}C}$ = 5 Hz, C_{Ar}-P), 118.2 (d, $J_{F\text{-}C}$ = 11 Hz, C_{Ar}-H), 117.9 (d, $J_{F\text{-}C}$ = 22 Hz, C_{Ar}-H), 115.3 (app q, *J* = 6 Hz, C_{Ar}-H), 24.9 (vt, $J_{P\text{-}C}$ = 15 Hz, $CHMe_2$), 18.3 ($CHMe_2$), 17.6 ($CHMe_2$), –3.4 (t, $J_{P\text{-}C}$ = 6 Hz, $J_{195Pt\text{-}C}$ = 602 Hz, $CH_2C_6H_5$). ^{19}F NMR (C_6D_6, Figure 3.23): δ –130.6. $^{31}P\{^1H\}$ NMR (C_6D_6, Figure 3.24): δ 38.7 ($J_{195Pt\text{-}P}$ = 2,910 Hz).

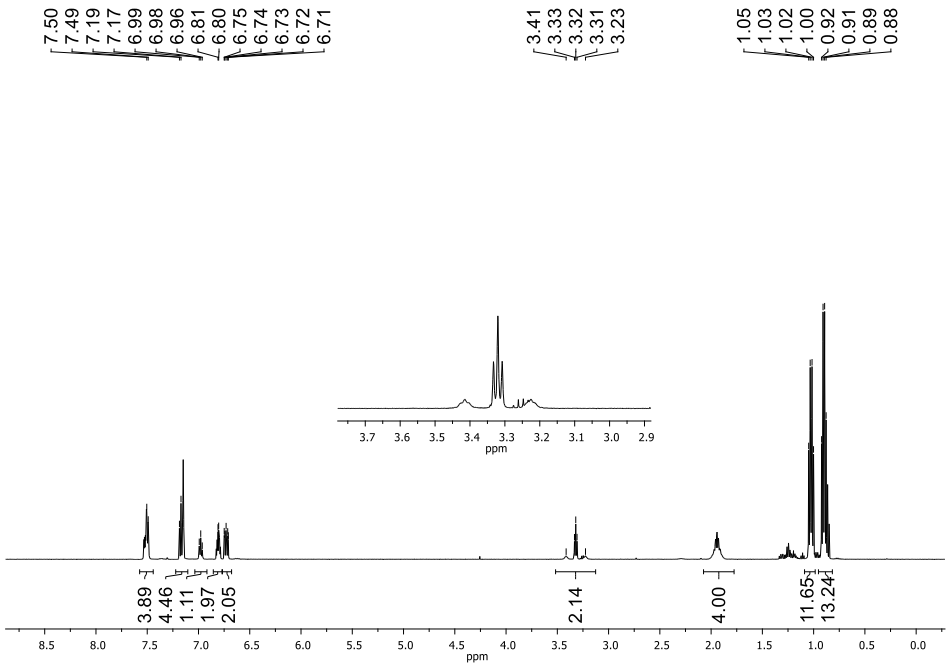

Figure 3.22 ^1H NMR spectrum of **302g** in C_6D_6 at RT measured on a 500-MHz Varian NMRS.

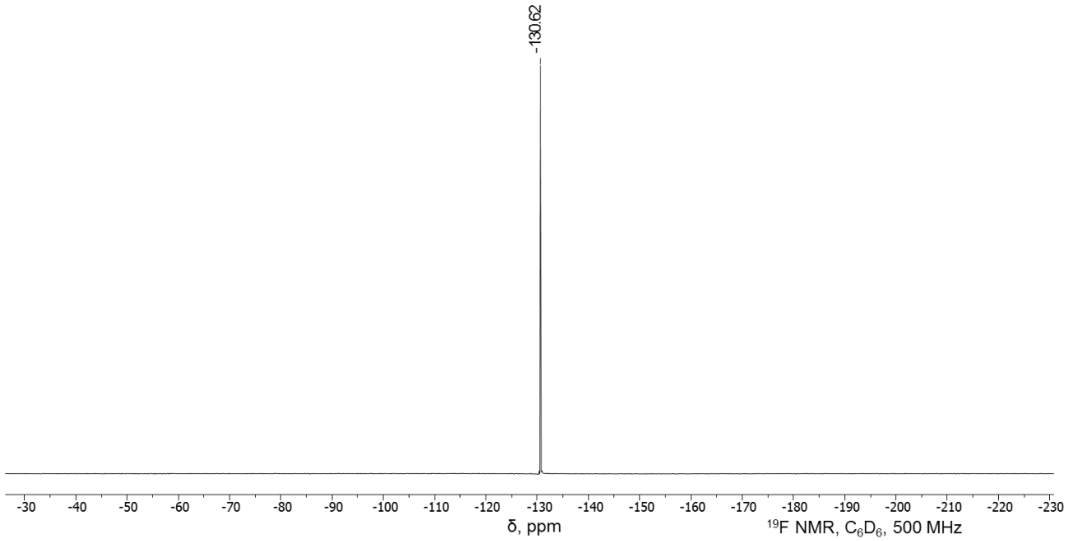

Figure 3.23 ^{19}F NMR spectrum of **302g** in C_6D_6 at RT measured on a 500-MHz Varian NMRS.

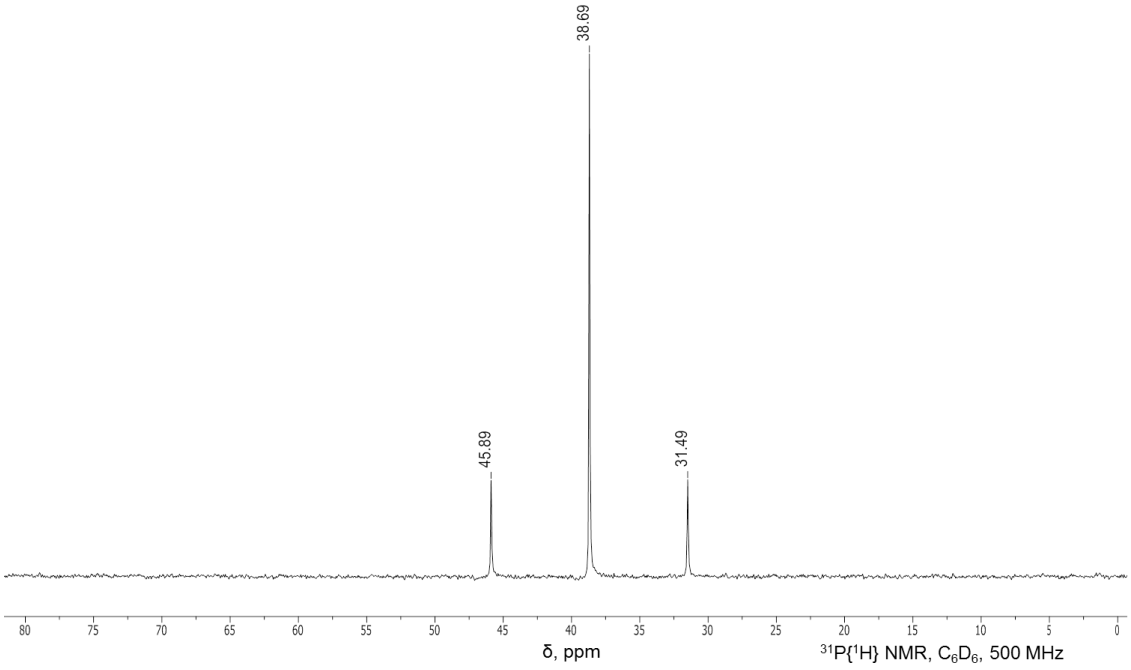

Figure 3.24 $^{31}P\{^1H\}$ NMR spectrum of **302g** in C_6D_6 at RT measured on a 500-MHz Varian NMRS.

3.4.1.3 C-H Activation of Arenes with 301/NEt_3

301 Plus NEt_3 in C_6D_6. 301 (22.0 mg, 0.0280 mmol) was transferred to a J. Young NMR tube and dissolved in toluene, forming a clear, yellow solution. NEt_3 (5.0 μL, 0.036 mmol) was added via syringe, and the NMR tube was placed in an oil bath at 115°C. The reaction was monitored by ^{19}F NMR. After 2 weeks, about 17% of the original **301** remained, with approximately 79% conversion of the total starting material to (^{F}PNP)PtC_6D_5 (**302a-D**) and 4% conversion to (^{F}PNP)PtH.

301 Plus NEt_3 in Toluene. 301 (23.0 mg, 0.0294 mmol) was transferred to a J. Young NMR tube and dissolved in toluene, forming a clear, yellow solution. NEt_3 (5.0 μL, 0.036 mmol) was added via syringe, and the NMR tube was placed in an oil bath at 115°C. The reaction was monitored by ^{19}F NMR. After 7 days, the complete disappearance of **301** was noted, with about 90% conversion to (^{F}PNP)PtC_6H_4Me (**302b-d**) and 10% conversion to (^{F}PNP)PtH. The volatiles were removed, and the residual solid was redissolved in C_6D_6, filtered over Celite and silica gel and characterized by NMR. The ^{1}H NMR spectrum showed an **302b:302c:302d** tolyl isomeric ratio of approximately 1%:68%:31%.

3.4.1.4 Reactions of 301 with $KBArF_{20}$ in Arene Solvents

[(^{F}PN(H)P)PtC_6H_5][$BArF_{20}$] (303a). 301 (18.1 mg, 0.0232 mmol) and $KBArF_{20}$ (17.1 mg, 0.0238 mmol) were added to a 5 mL round-bottomed Teflon screw-capped flask. C_6H_6 (2 mL) was added, forming an orange solution containing some undissolved $KBArF_{20}$. The solution was left to stir at RT. After 24 h, the solution had become a

brownish green, and after 4 days, the solution had become a pale green. The complete disappearance of starting material was confirmed by ^{19}F NMR. The volatiles were removed, yielding a pale blue-green solid. The solid was washed with pentane, dried, extracted with CD_2Cl_2 and filtered through a pad of Celite into a J. Young NMR tube for characterization. ^{1}H NMR (CD_2Cl_2, Figure 3.25): δ 7.52 and 7.51 (overlapping br signals, 2H, Ar-*H*), 7.38 (td, J = 8.4 Hz, 3 Hz, 2H, *o*-Ph-*H*, ^{195}Pt coupling buried), 7.36 (t, J = 7.5 Hz, 2H, Ar-*H*), 7.35 (d, J = 7.5 Hz, 2H, Ar-*H*), 7.26 (br s, $J_{195Pt-H}$ = 37 Hz, 1H, N-*H*), 7.05 (t, J = 7.8 Hz, 2H, *m*-Ph-*H*), 6.94 (t, J = 7.2 Hz, 1H, *p*-Ph-*H*), 2.81 (m, 2H, C*H*Me$_2$), 2.68 (m, 2H, C*H*Me$_2$), 1.20 (m, 12H, CH*Me*$_2$), 1.07 (vtd, J_{P-H} = 9 Hz, J_{H-H} = 7.5 Hz, 6H, CH*Me*$_2$), 0.88 (vtd, J_{P-H} = 9 Hz, J_{H-H} = 7.3 Hz, 6H, CH*Me*$_2$). ^{19}F NMR (CD_2Cl_2): δ –111.7. ^{31}P{^{1}H} NMR (CD_2Cl_2): δ 41.3 ($J_{195Pt-P}$ = 2,819 Hz). IR (solid): 3240 cm^{-1} (N-H).

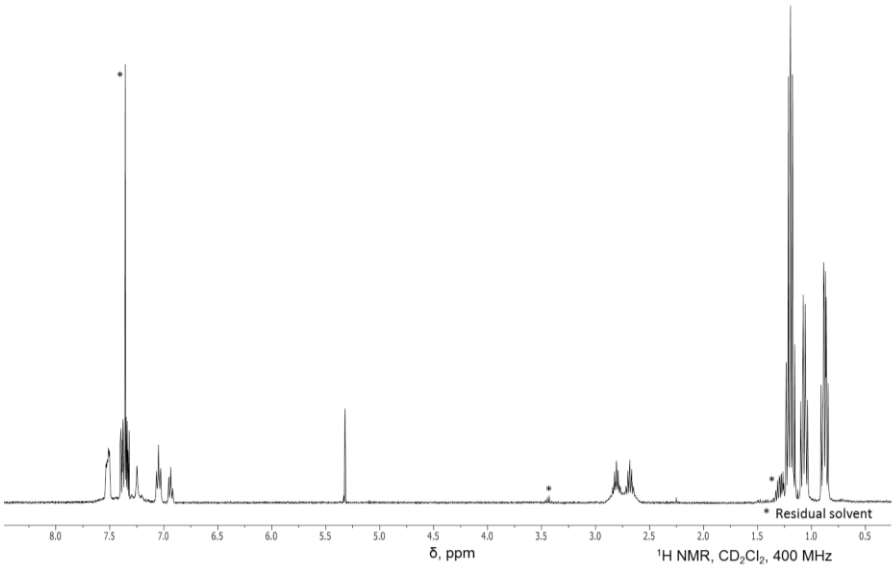

Figure 3.25 ^{1}H NMR spectrum of **303a** in CD_2Cl_2 at RT measured on a 400-MHz Varian iNova.

[(^{F}PN(D)P)PtC$_6$D$_5$][BArF$_{20}$] (303a-D). 301 (100 mg, 0.128 mmol) and KBArF$_{20}$ (93.0 mg, 0.130 mmol) were added to a round-bottomed Teflon screw-capped flask. About 3 mL of C_6D_6 was added, forming an orange solution containing some undissolved KBArF$_{20}$. The flask was then placed in an oil bath at 80 °C. After 2 h, the solution had a cloudy orange appearance, and after 16 h, the reaction became a cloudy green. Conversion to the product was confirmed by NMR. The solution was filtered over a pad of Celite and rinsed through with CH_2Cl_2. The volatiles were removed under vacuum, yielding a pale green solid that was recrystallized from a CH_2Cl_2 solution layered with pentane at –35 °C. The crystals were collected, washed with pentane and dried under vacuum, yielding a pale blue solid. Conversion to the final product was also achieved by performing this reaction at RT for 4 days. Isolated yield: 111 mg, 61%. ^{1}H NMR (CD_2Cl_2, Figure 3.26): δ 7.52 and 7.51 (overlapping br signals, 2H, Ar-*H*), 7.36 (t, *J* = 7.5 Hz, 2H, Ar-*H*), 7.35 (d, *J* = 7.5 Hz, 2H, Ar-*H*), 2.81 (m, 2H, C*H*Me$_2$), 2.68 (m, 2H, C*H*Me$_2$), 1.23 (m, 12H, CH*Me*$_2$), 1.07 (app q (dvt), *J* = 8 Hz, 6H, CH*Me*$_2$), 0.88 (app q (dvt), *J* = 8 Hz, 6H, CH*Me*$_2$). ^{13}C{^{1}H} NMR (CD_2Cl_2, Figure 3.27): δ 162.4 (dvt, $J_{F\text{-}C}$ = 256 Hz, $J_{P\text{-}C}$ = 4 Hz, C_{Ar}-F), 144.6 (vtd, $J_{P\text{-}C}$ = 7 Hz, $J_{F\text{-}C}$ = 3 Hz, C_{Ar}-N), 136.2 (overlapping with BArF$_{20}$ signal), 132.3 (vtd, $J_{P\text{-}C}$ = 18 Hz, $J_{F\text{-}C}$ = 6 Hz, C_{Ar}-P), 128.4 (br s), 126.1, 124.5 (t, $J_{P\text{-}C}$ = 8 Hz), 121.5 (d, $J_{F\text{-}C}$ = 23 Hz, C_{Ar}-H), 120.0 (d, $J_{F\text{-}C}$ = 23 Hz, C_{Ar}-H), 26.5 (vt, $J_{P\text{-}C}$ = 14 Hz, *C*HMe$_2$), 23.6 (vt, $J_{P\text{-}C}$ = 15 Hz, *C*HMe$_2$), 18.0 (CH*Me*$_2$), 17.8 (CH*Me*$_2$), 17.6 (CH*Me*$_2$), 16.9 (CH*Me*$_2$). ^{19}F NMR (CD_2Cl_2, Figure 3.28): δ –111.7. ^{31}P{^{1}H} NMR (CD_2Cl_2, Figure 3.29): δ 41.2 ($J_{195Pt\text{-}P}$ = 2,820 Hz). Elemental analysis, found (calculated) for $C_{54}H_{34}D_6BF_{22}NP_2Pt$: C, 46.25 (46.50); H, 2.09 (2.34). IR (solid): 2405 cm^{-1} (N-D).

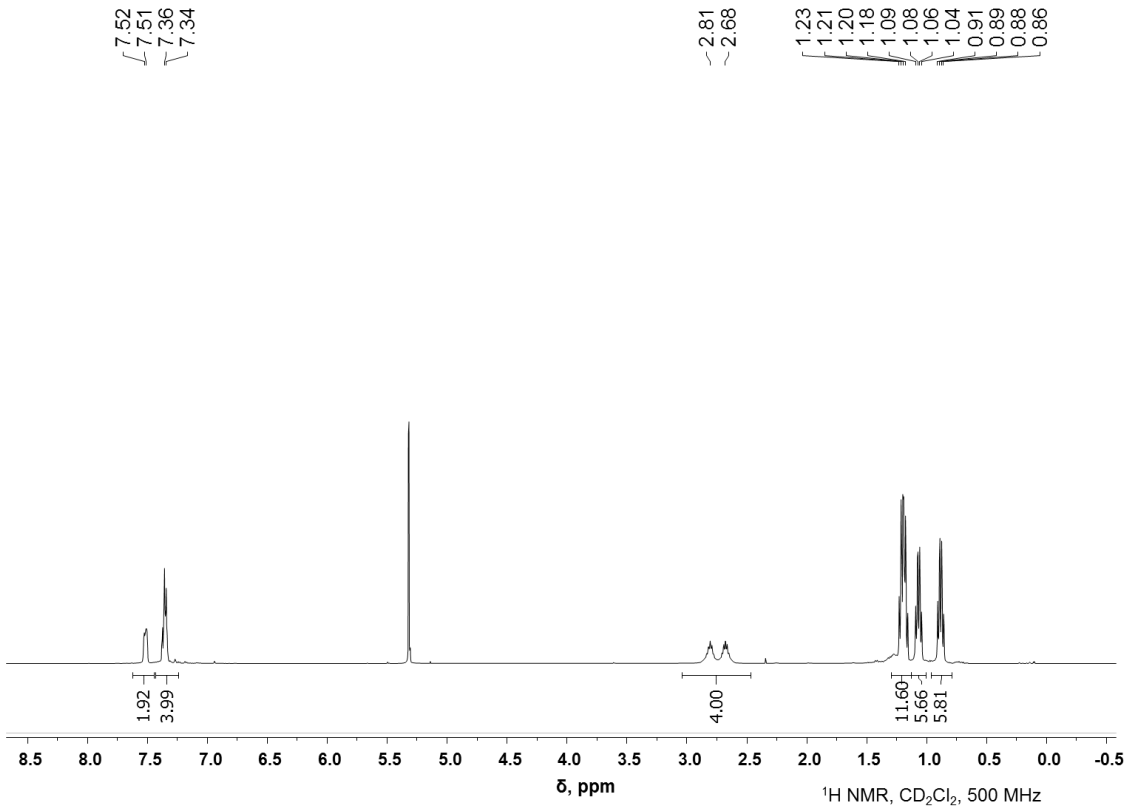

Figure 3.26 ^{1}H NMR spectrum of **303a-D** in CD_2Cl_2 at RT measured on a 500-MHz Varian NMRS.

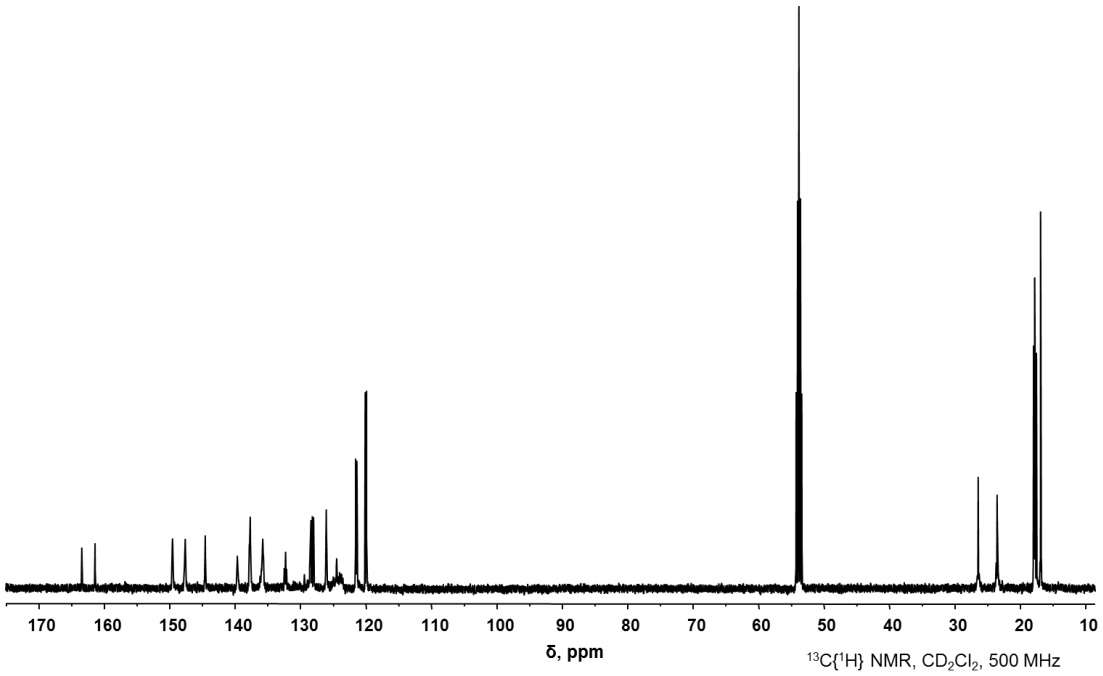

Figure 3.27 $^{13}C\{^{1}H\}$ NMR spectrum of **303a-D** in CD_2Cl_2 at RT measured on a 500-MHz Varian NMRS.

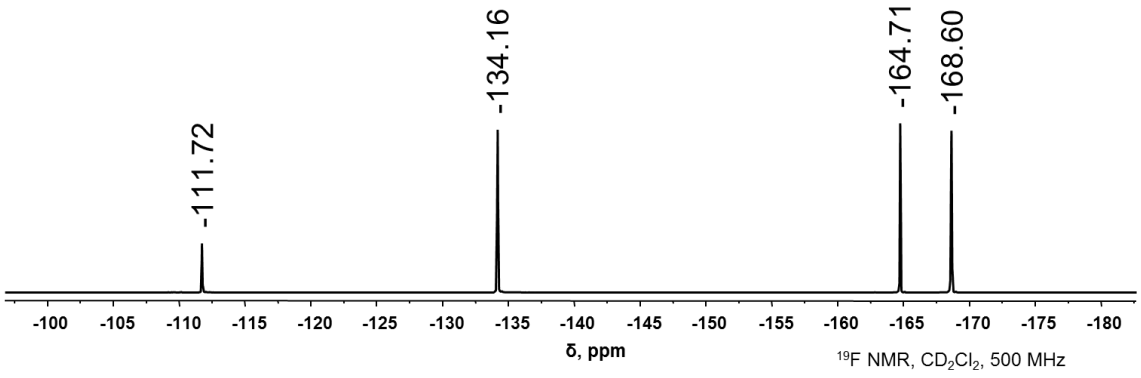

Figure 3.28 ^{19}F NMR spectrum of **303a-D** in CD_2Cl_2 at RT measured on a 500-MHz Varian NMRS.

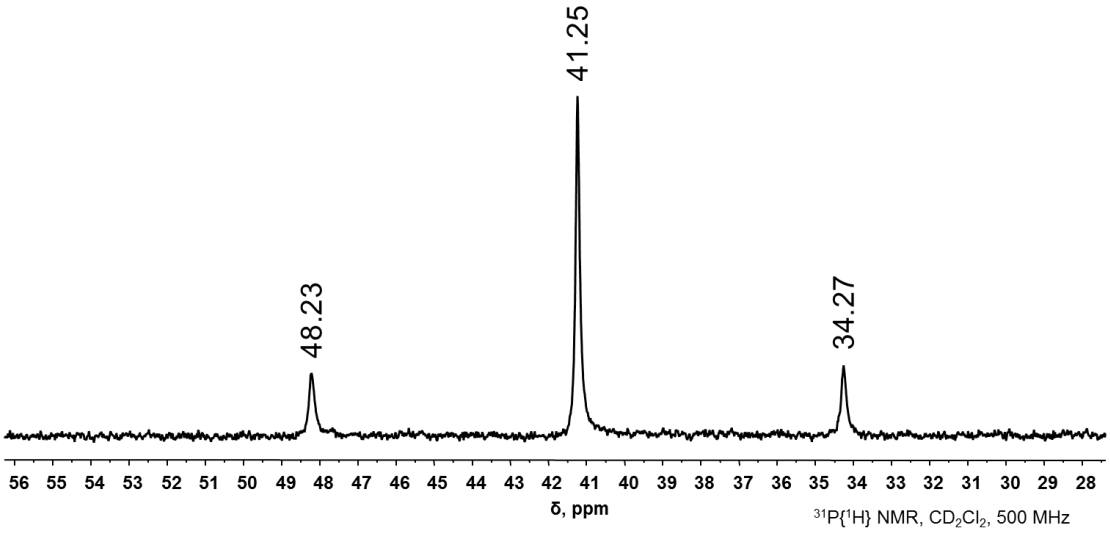

Figure 3.29 $^{31}P\{^{1}H\}$ NMR spectrum of **303a-D** in CD_2Cl_2 at RT measured on a 500-MHz Varian NMRS.

[(^{F}PN(H)P)PtC$_6$H$_4$Me][BArF$_{20}$] (303b-d). 301 (107 mg, 0.137 mmol) and $KBArF_{20}$ (98 mg, 0.14 mmol) were added to a 10-mL round-bottomed Teflon screw-capped flask. Approximately 5 mL of C_6H_5Me was added, forming a yellow solution containing some undissolved $KBArF_{20}$. The flask was then placed in an oil bath at 80 °C. After 2 h, the solution had become cloudy brown, and after 16 h, the solution had become cloudy blue. The solution was then filtered over a pad of Celite and washed through with CH_2Cl_2. The volatiles were removed under vacuum, yielding an oily blue residue. A minimal amount of CH_2Cl_2 was used to redissolve the solids, and the solution was layered with pentane. After recrystallization at –35 °C, the resulting pale blue solid was washed with pentane and dried under vacuum. Isolated yield: 165 mg, 84%. The ratio of **303b**:(**303c** plus **303d**) in the product mixture was approximately 8%:92% (**303c** and **303d** signals overlap). Characterization was achieved by comparing the ^{1}H NMR and $^{13}C\{^{1}H\}$

NMR spectra (Figure 3.30 and Figure 3.31) of the product mixture to those of the independently synthesized isomers (see below). ^{19}F NMR (CD_2Cl_2, Figure 3.32): δ –111.7. $^{31}P\{^1H\}$ NMR (CD_2Cl_2, Figure 3.33): δ 41.1 (br, $J_{195Pt-P}$ = 2,840 Hz). Elemental analysis, found (calculated) for $C_{55}H_{41}BF_{22}NP_2Pt$: C, 47.07 (47.13); H, 3.02 (2.95). IR (solid): 3240 cm^{-1} (N-H).

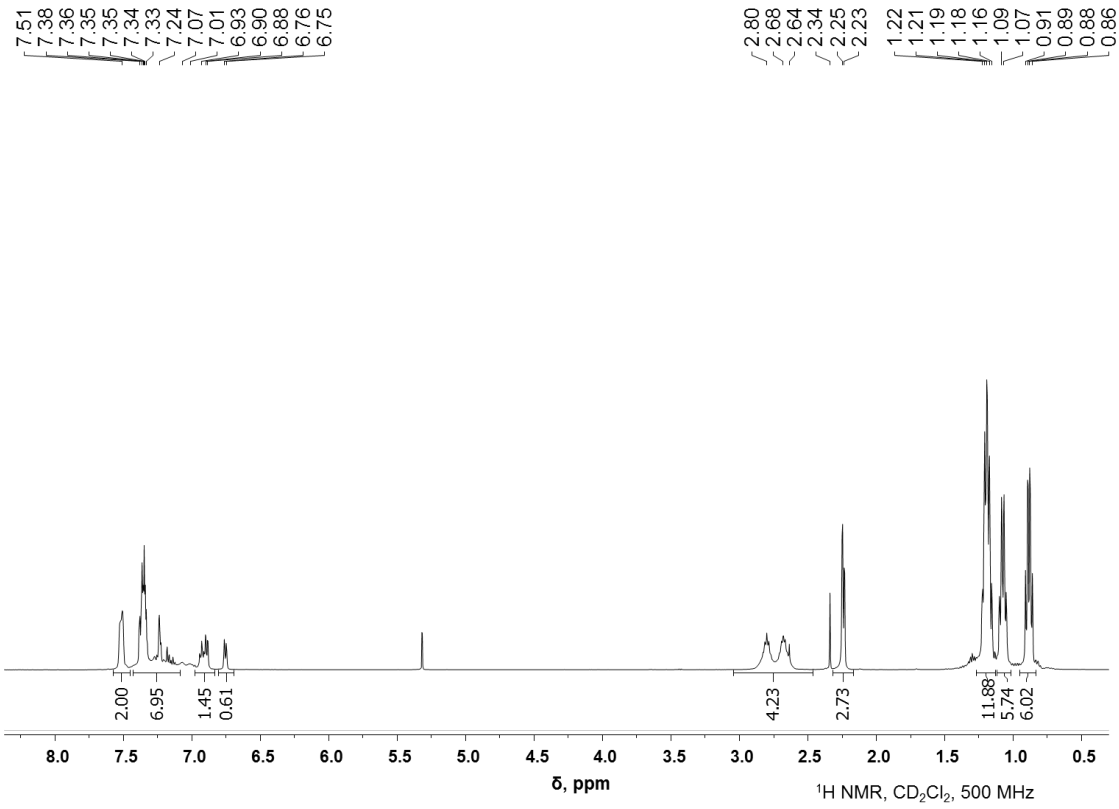

Figure 3.30 ^1H NMR spectrum of the **303b-d** product mixture in CD_2Cl_2 at RT measured on a 500-MHz Varian NMRS.

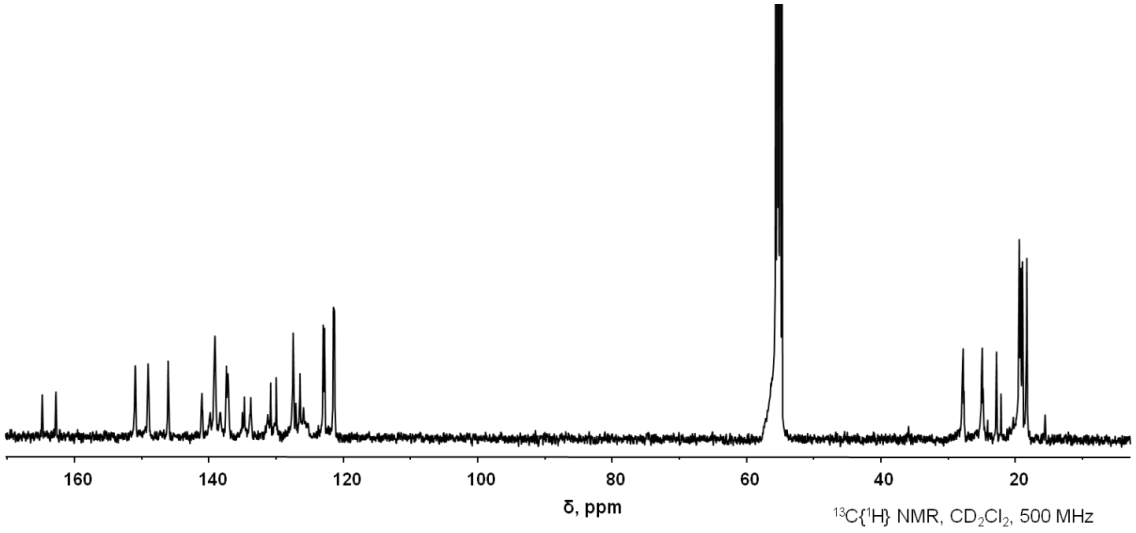

Figure 3.31 $^{13}C\{^{1}H\}$ NMR spectrum of the **303b-d** product mixture in CD_2Cl_2 at RT measured on a 500-MHz Varian NMRS.

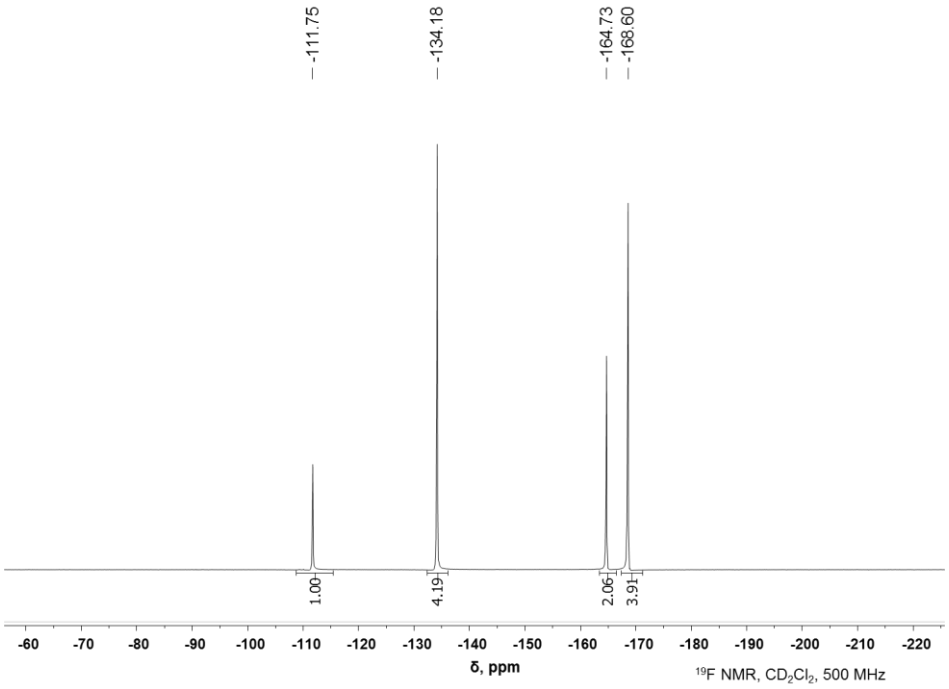

Figure 3.32 ^{19}F NMR spectrum of the **303b-d** product mixture in CD_2Cl_2 at RT measured on a 500-MHz Varian NMRS.

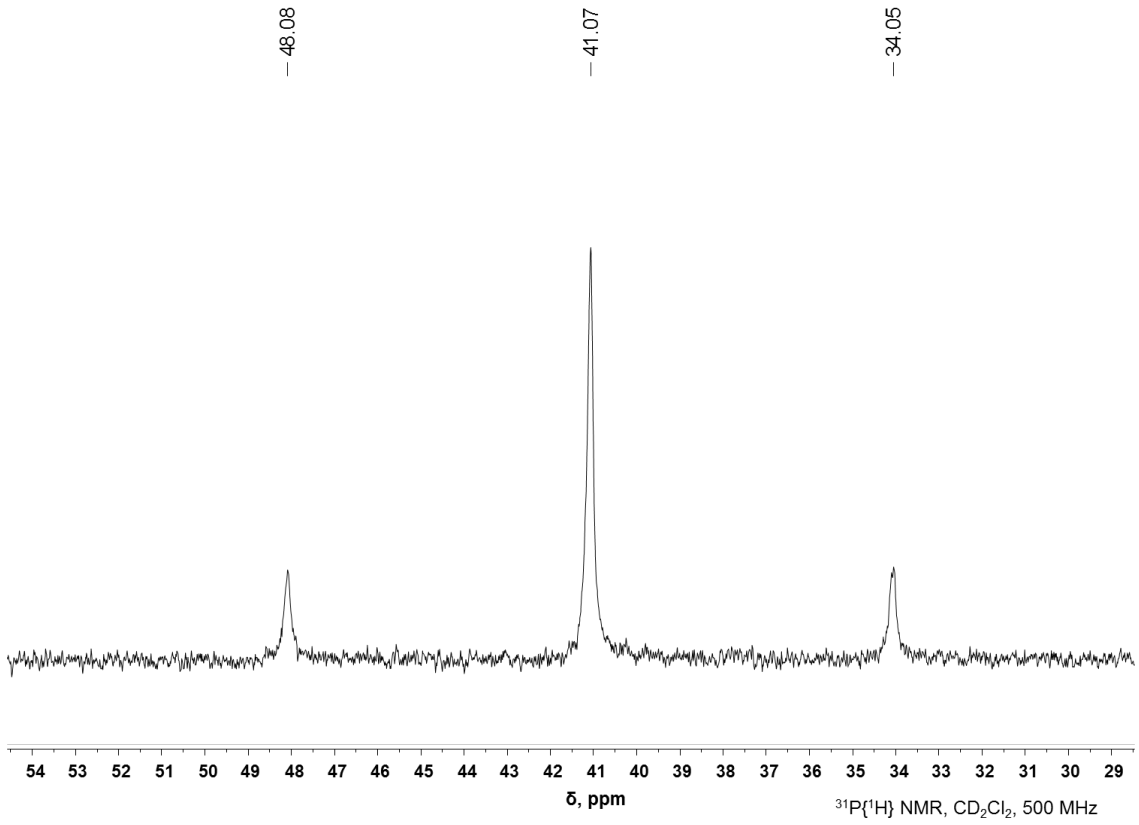

Figure 3.33 $^{31}P\{^{1}H\}$ NMR spectrum of the **303b-d** product mixture in CD_2Cl_2 at RT measured on a 500-MHz Varian NMRS.

[(^{F}PN(H)P)PtC$_6$H$_4$F][BArF$_{20}$] (303e). 301 (99 mg, 0.13 mmol) and $KBArF_{20}$ (91 mg, 0.13 mmol) were added to a round-bottomed Teflon screw-capped flask. C_6H_5F was added, forming a yellow solution containing some undissolved $KBArF_{20}$. The flask was then placed in an oil bath at 80 °C. After 2 h, the solution had a pale green appearance. The solution was filtered over a pad of Celite and eluted with CH_2Cl_2 and C_6H_5F. The volatiles were removed under vacuum, yielding an oily blue residue along with a white solid. A minimal amount of CH_2Cl_2 was used to redissolve the solids, and the solution was layered with pentane. The resulting blue crystals were collected and washed with cold

pentane. After drying under vacuum, a pale blue solid was collected. Isolated yield: 120 mg, 71%. ^{1}H NMR (CD_2Cl_2, Figure 3.34): δ 7.52 (m, Ar-*H* overlapping with N-*H* signal and *o*-*H* of minor rotamer), 7.47 (br s, $J_{195Pt-H}$ = 40 Hz, N-*H*, major rotamer), 7.37 (m, Ar-*H*), 7.26 (ddd, *J* = 7.4 Hz, 4.5 Hz, 1.1 Hz, $J_{195Pt-H}$ = 74 Hz, *o*-aryl-*H*, major rotamer), 7.06 (app q, *J* = 7.3 Hz, *m*-aryl-*H*, major rotamer), 7.02 (app q, *J* = 7.0 Hz, *m*-aryl-*H*, minor rotamer), 6.94 (t, *J* = 7.4 Hz, *m*-aryl-*H*, major rotamer), 6.92 (t, *J* = 7.4 Hz, *m*-aryl-*H*, minor rotamer), 6.87 (td, *J* = 8.2 Hz, 1.3 Hz, *p*-aryl-*H*, major rotamer), 6.86 (td, *J* = 8.2 Hz, 1.3 Hz, *p*-aryl-*H*, minor rotamer), 2.83 (m, 2H, C*H*Me$_2$), 2.71 (m, 2H, C*H*Me$_2$), 1.18 (m, CH*Me*$_2$), 1.17 (vtd, J_{P-H} = 9 Hz, J_{H-H} = 7 Hz, CH*Me*$_2$), 1.10 (vtd, J_{P-H} = 9 Hz, J_{H-H} = 7 Hz, 12H, CH*Me*$_2$), 0.89 (vtd, J_{P-H} = 9 Hz, J_{H-H} = 7 Hz, CH*Me*$_2$), 0.84 (vtd, J_{P-H} = 9 Hz, J_{H-H} = 7 Hz, CH*Me*$_2$). ^{13}C{^{1}H} NMR (CD_2Cl_2, Figure 3.35): δ 162.3 (dvt, J_{F-C} = 254 Hz, J_{P-C} = 5 Hz, C_{Ar}-F), 144.7 (vtd, J_{P-C} = 8 Hz, J_{F-C} = 2.5 Hz, C_{Ar}-N, major rotamer), 144.4 (vt, J_{P-C} = 8 Hz, C_{Ar}-N, minor rotamer), 137.4, 131.8 (vtd, J_{P-C} = 18 Hz, J_{F-C} = 6 Hz, C_{Ar}-P), 126.3 (d, J_{F-C} = 8 Hz), 126.1 (d, J_{F-C} = 8 Hz), 125.9 (m), 125.2, 124.9, 121.6 (d, J_{F-C} = 24 Hz, C_{Ar}-H), 121.2, 120.2 (d, J_{F-C} = 23 Hz, C_{Ar}-H), 115.4 (d, J_{F-C} = 27 Hz, C_{Ar}-H), 114.7 (d, J_{F-C} = 27 Hz, C_{Ar}-H), 26.7 (vt, J_{P-C} = 15 Hz, *C*HMe$_2$), 26.0 (vt, J_{P-C} = 14 Hz, *C*HMe$_2$), 24.9 (vt, J_{P-C} = 14 Hz, *C*HMe$_2$), 23.3 (vt, J_{P-C} = 15 Hz, *C*HMe$_2$), 18.1 (CH*Me*$_2$, major rotamer), 17.9 (CH*Me*$_2$, minor rotamer), 17.7 (CH*Me*$_2$, major rotamer), 17.7 (CH*Me*$_2$, minor rotamer), 17.5 (CH*Me*$_2$, minor rotamer), 17.3 (CH*Me*$_2$, major rotamer), 17.1 (CH*Me*$_2$, minor rotamer), 16.8 (CH*Me*$_2$, major rotamer). ^{19}F NMR (CD_2Cl_2, Figure 3.36 and Table 3.2): δ –92.7 ($J_{195Pt-F}$ = 390 Hz, major rotamer), –94.7 ($J_{195Pt-F}$ = 317 Hz, minor rotamer), –111.3 (major rotamer), –111.4 (minor rotamer). ^{31}P{^{1}H} NMR (CD_2Cl_2, Figure

3.37): δ 43.4 ($J_{195Pt-P}$ = 2,716 Hz, minor rotamer), 43.0 ($J_{195Pt-P}$ = 2,700 Hz, major rotamer). Elemental analysis, found (calculated) for $C_{54}H_{39}BF_{23}NP_2Pt$: C, 46.04 (46.11); H, 2.71 (2.79). IR (solid): 3233 cm^{-1} (N-H).

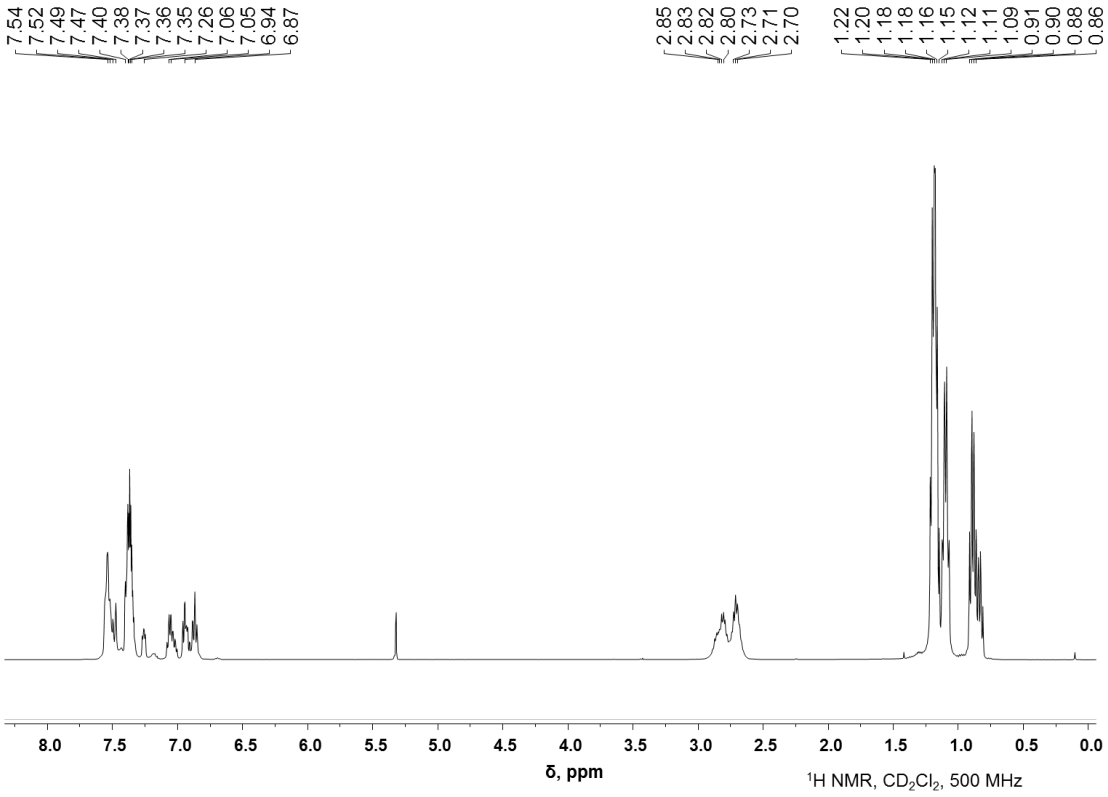

Figure 3.34 ^{1}H NMR spectrum of **303e** in CD_2Cl_2 at RT measured on a 500-MHz Varian NMRS.

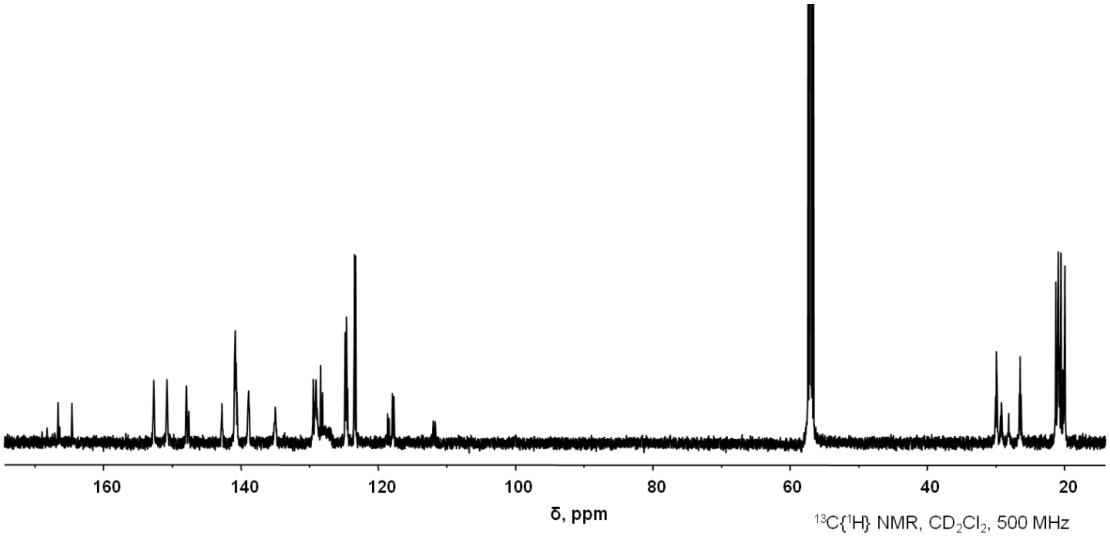

Figure 3.35 $^{13}C\{^{1}H\}$ NMR spectrum of **303e** in CD_2Cl_2 at RT measured on a 500-MHz Varian NMRS.

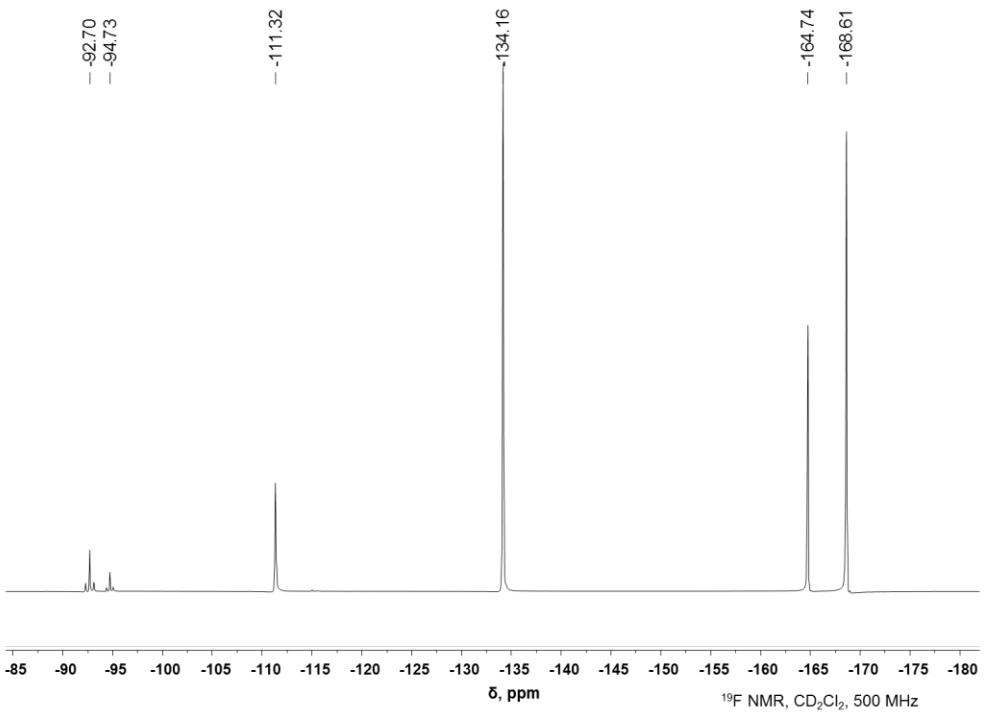

Figure 3.36 ^{19}F NMR spectrum of **303e** in CD_2Cl_2 at RT measured on a 500-MHz Varian NMRS.

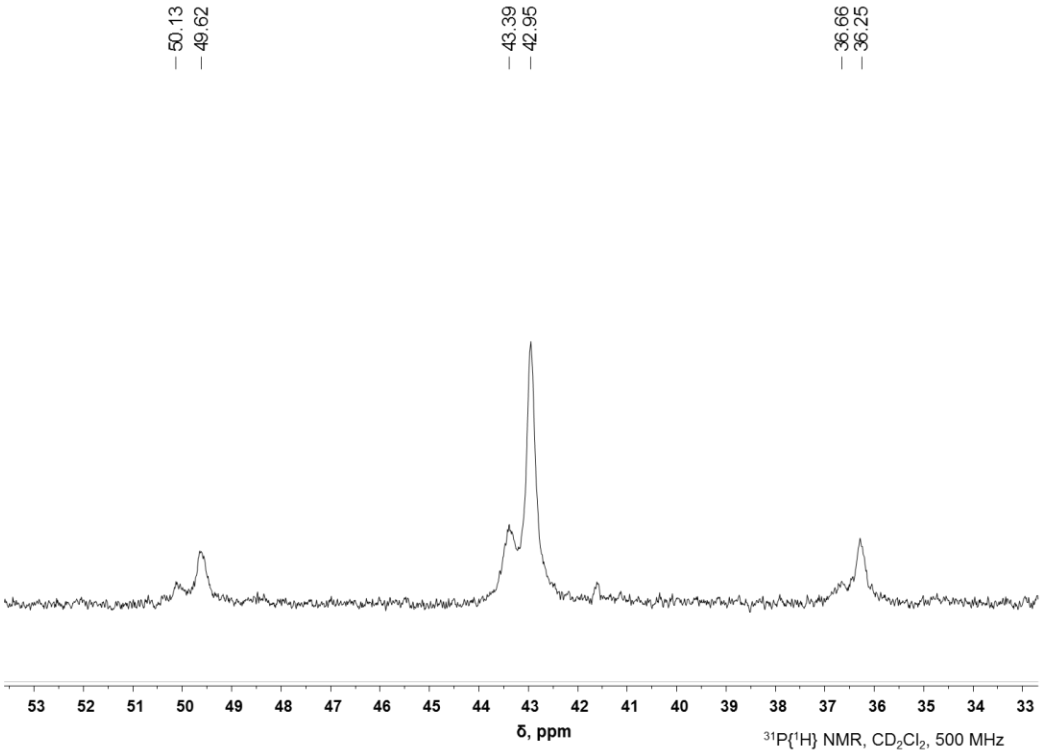

Figure 3.37 $^{31}P\{^{1}H\}$ NMR spectrum of **303e** in CD_2Cl_2 at RT measured on a 500-MHz Varian NMRS.

Table 3.2 ^{19}F NMR VT study monitoring the *ortho* fluorine resonances of rotamer A and rotamer B for **303e** in C_6D_5Br from –20°C to 120°C.

T, (°C)	Integration A	Integration B
-20	1	0.49
RT	1	0.51
40	1	0.52
60	1	0.54
80	1	0.56
100	1	0.58
120	1	0.59

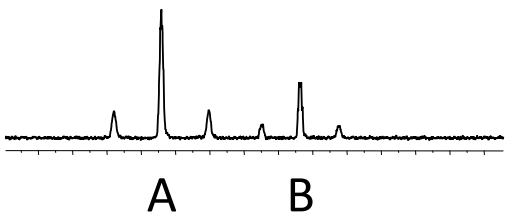

[(^{F}PN(H)P)PtC$_6$H$_4$Cl][BArF$_{20}$] (303f). **301** (21.8 mg, 0.0279 mmol) and KBArF$_{20}$ (19 mg, 0.026 mmol) were added to a 10-mL round-bottomed Teflon screw-capped flask. About 5 mL of C$_6$H$_5$Cl was added, forming a yellow solution. An aliquot was taken after 15 min, and 2 new signals were observed by ^{19}F NMR. The signal at –110.8 ppm corresponded to a C-H activation product, and the signal at –122.8 ppm is believed to be indicative of a Pt-chlorobenzene adduct (**304**). After 1 h at RT, the signal at –122.8 ppm was the major peak. After 48 h at RT, this signal was no longer visible by ^{19}F NMR, and full conversion to the C-H activation product was observed. The formation of (^{F}PNP)PtCl was not observed upon addition of decamethyl ferrocene (6 mg, 0.02 mmol). Conversion to the C-H activation product could also be achieved by heating the sample overnight at 80 °C. **[(^{F}PNP)Pt-ClC$_6$H$_5$][BArF$_{20}$] (304).** ^{19}F NMR (C$_6$H$_5$Cl): δ –122.8. ^{31}P{^{1}H} NMR (C$_6$H$_5$Cl): δ 48.6 ($J_{195Pt-P}$ = 2,515 Hz).

[(^{F}PN(H)P)PtC$_6$H$_4$Cl][BArF$_{20}$] (303f). ^{1}H NMR (CD_2Cl_2, Figure 3.38): δ 7.51 (m, 2H, Ar-*H*), 7.45 (br s, 1H, N-*H*, ^{195}Pt coupling buried), 7.36 (m, 4H, Ar-*H*), 7.23 (dd, *J* = 6.7 Hz, 2.5 Hz, 1H, *ortho* C-*H* of C$_6$H$_4$Cl, ^{195}Pt coupling buried), 7.19 (dd, *J* = 6.8 Hz, 2.5 Hz, 1H, *meta* C-*H* of C$_6$H$_4$Cl), 7.01 (m, 2H, *meta* and *para* C-*H* of C$_6$H$_4$Cl), 2.80 (m, 4H, C*H*Me$_2$), 1.19 (app q (dvt), *J* = 8 Hz, 12H, CH*Me*$_2$), 1.10 (app q (dvt), *J* = 8.5 Hz, 6H, CH*Me*$_2$), 0.87 (vtd, J_{P-H} = 9.5 Hz, J_{H-H} = 7.7 Hz, 6H, CH*Me*$_2$). ^{13}C{^{1}H} NMR (CD_2Cl_2, Figure 3.39): δ 162.4 (d, J_{F-C} = 233 Hz, *C*$_{Ar}$-F), 144.7, 140.3 (t, J_{P-C} = 3 Hz), 138.3 ($J_{195Pt-C}$ = 38 Hz), 131.5 (m), 128.9 ($J_{195Pt-C}$ = 33 Hz), 127.2 ($J_{195Pt-C}$ = 69 Hz), 126.1, 123.9 (t, J_{P-C} = 9 Hz), 122.5, 121.5 (d, J_{F-C} = 24 Hz, *C*$_{Ar}$-H), 120.2 (d, J_{F-C} = 23 Hz, *C*$_{Ar}$-H), 26.9 (vt, J_{P-C} = 14.3 Hz, *C*HMe$_2$), 23.1 (vt, J_{P-C} = 15 Hz, *C*HMe$_2$), 18.0 (CH*Me*$_2$), 17.4 (CH*Me*$_2$),

17.2 (CH*Me*$_2$), 16.6 (CH*Me*$_2$). ^{19}F NMR (CD_2Cl_2, Figure 3.40): δ –111.3. ^{31}P{^{1}H} NMR (CD_2Cl_2, Figure 3.41): δ 41.5 ($J_{195Pt-P}$ = 2,775 Hz). IR (solid): 3235 cm^{-1} (N-H).

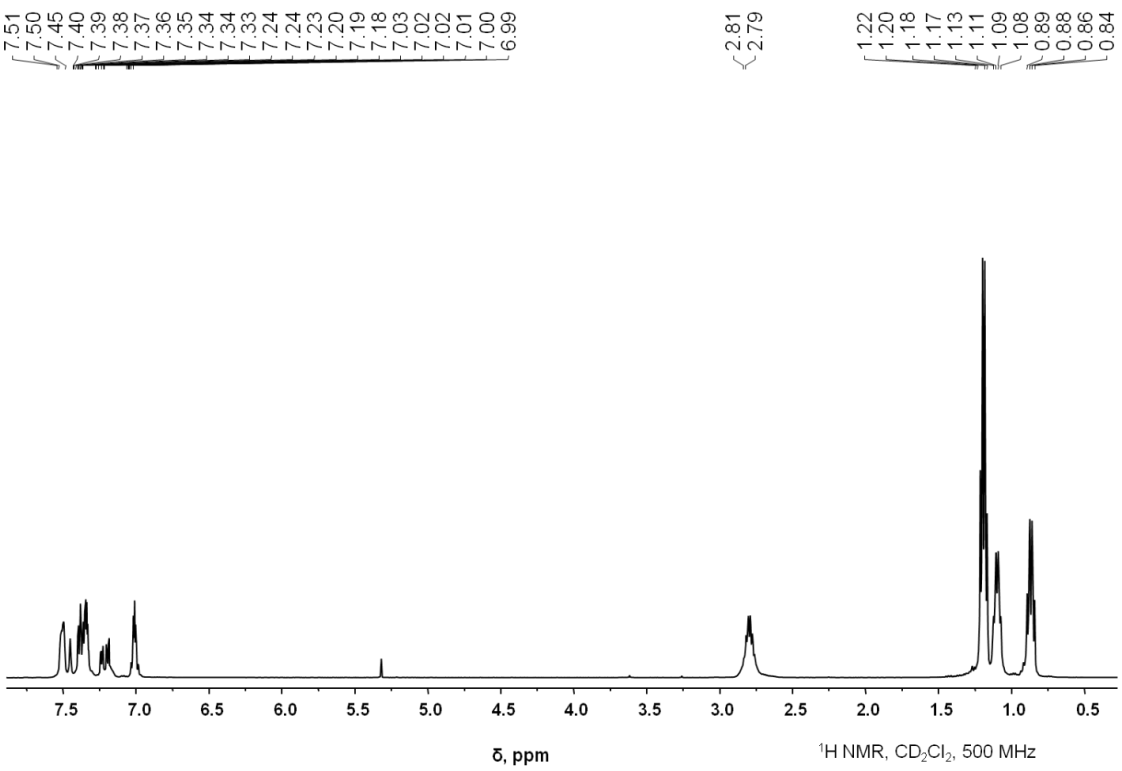

Figure 3.38 ^{1}H NMR spectrum of **303f** in CD_2Cl_2 at RT measured on a 500-MHz Varian NMRS.

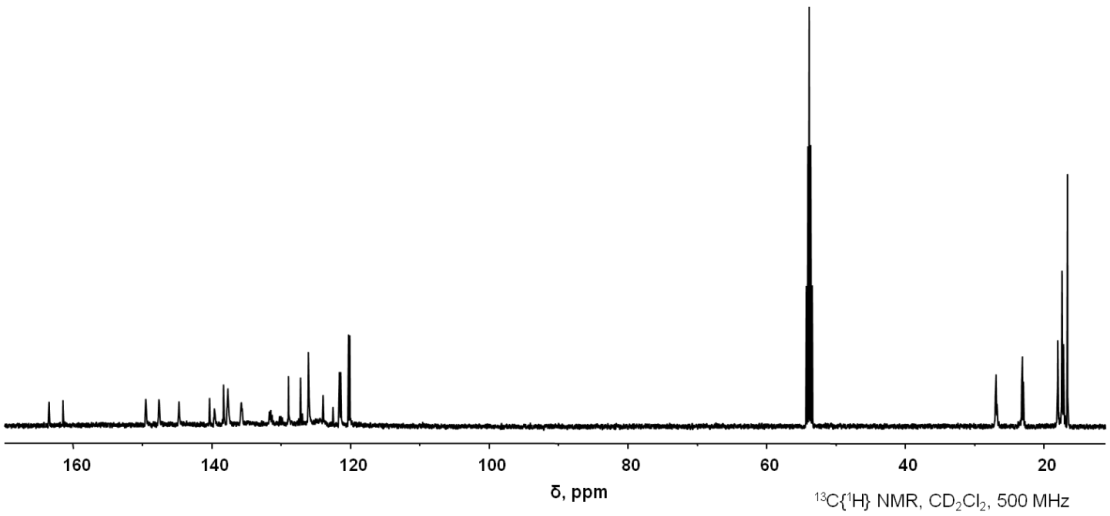

Figure 3.39 $^{13}C\{^{1}H\}$ NMR spectrum of **303f** in CD_2Cl_2 at RT measured on a 500-MHz Varian NMRS.

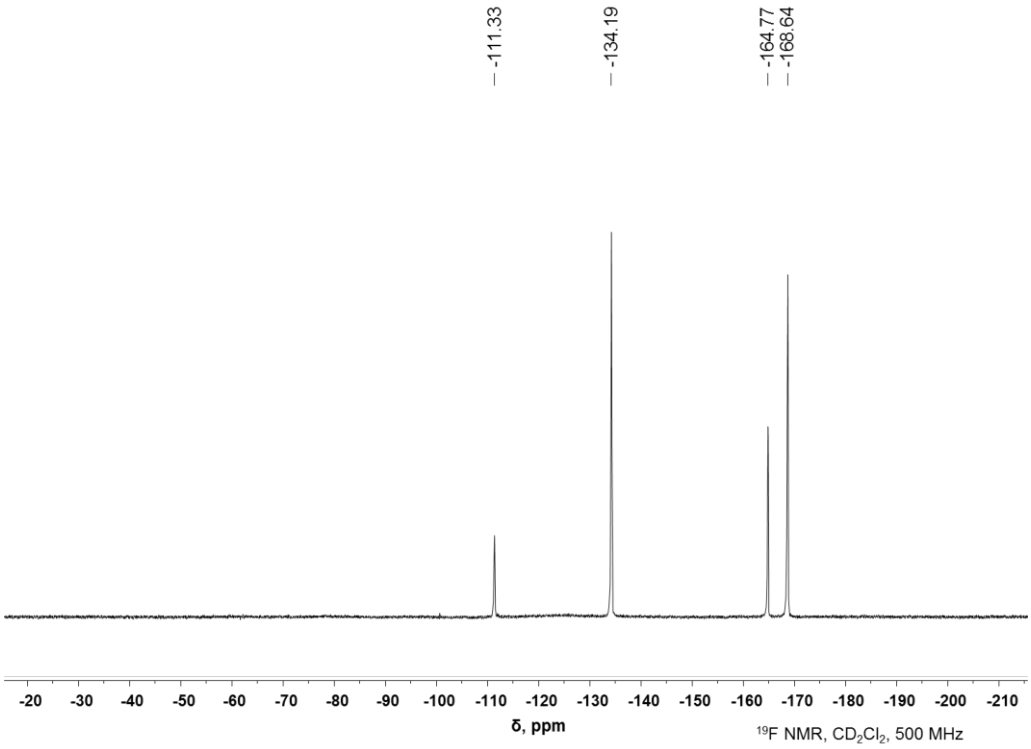

Figure 3.40 ^{19}F NMR spectrum of **303f** in CD_2Cl_2 at RT measured on a 500-MHz Varian NMRS.

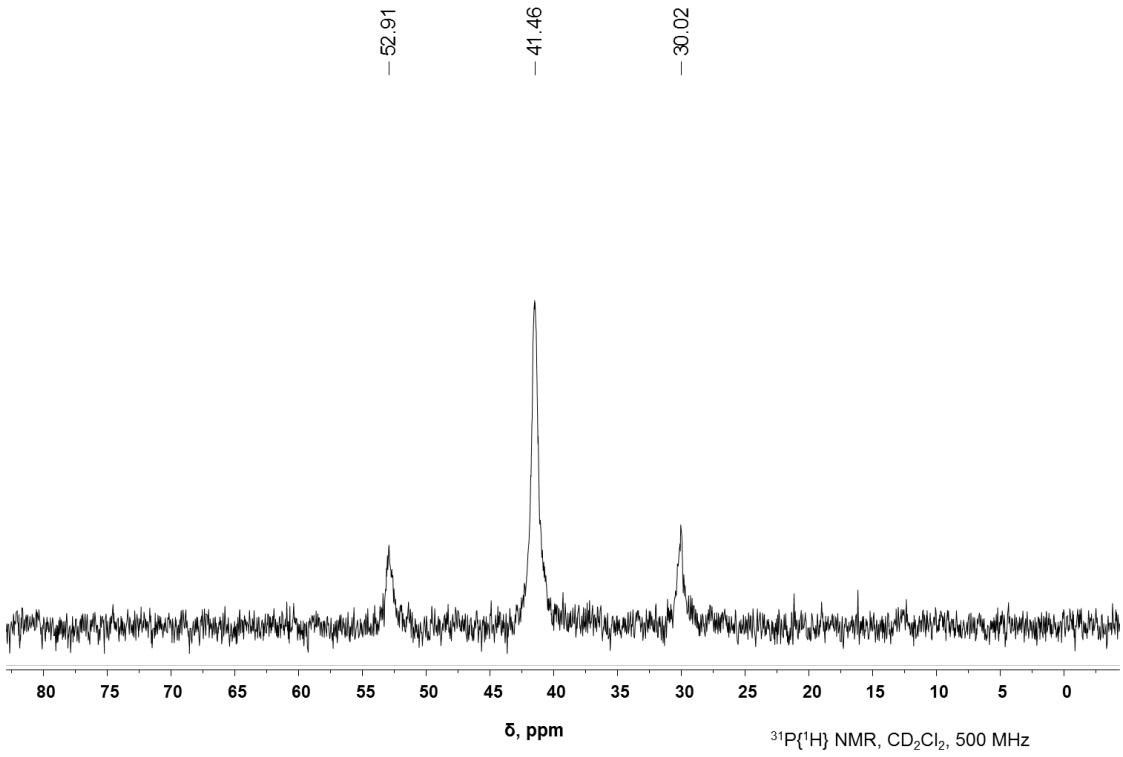

Figure 3.41 $^{31}P\{^{1}H\}$ NMR spectrum of **303f** in CD_2Cl_2 at RT measured on a 500-MHz Varian NMRS.

Activation of Bromobenzene and Observation of [(^{F}PNP)Pt-BrC_6D_5][$BArF_{20}$] (310). 301 (21.4 mg, 0.0274 mmol) and $KBArF_{20}$ (19 mg, 0.026 mmol) were transferred to a J. Young NMR tube. C_6D_5Br was added, forming a yellow-orange solution. A capillary containing 1-fluorooctane in C_6D_6 was used to track the conversion of (^{F}PNP)PtOTf to the products. After 2 h, a new signal was observed in the ^{19}F NMR spectrum at –122.9 ppm, corresponding to what is believed to be [(^{F}PNP)Pt-BrC_6D_5][$BArF_{20}$] (**310**). After a total of 12 h, **301** was no longer observed by NMR. Continued monitoring of the reaction mixture showed no C-H activation products, even

after 2 weeks at RT. The addition of MeCN led to the formation of **306**. A decrease in the $BArF_{20}$ signals relative to the ^{19}F NMR signals of the ligand was noted after 2 weeks. Reduction of the reaction mixture with decamethyl ferrocene led to the formation of (^{F}PNP)PtBr (**312**) (20% conversion). **[(^{F}PNP)Pt-BrC_6D_5][$BArF_{20}$] (310).** ^1H NMR (C_6D_5Br, Figure 3.42): δ 7.24 (br s, 2H, Ar-*H*), , 6.75 (t, J = 8 Hz, 2H, Ar-*H*), 6.67 (m, 2H, Ar-*H*), 2.05 (m, 4H, C*H*Me_2), 0.99 (vtd, J_{P-H} = 9 Hz, J_{H-H} = 8 Hz, 12H, CH*Me*$_2$), 0.89 (app q (dvt), J = 7 Hz, 12H, CH*Me*$_2$). $^{13}C\{^1H\}$ NMR (C_6D_5Br): δ 158.3 (vt, J_{P-C} = 10 Hz, C_{Ar}-N), 156.0 (d, J_{F-C} = 244 Hz, C_{Ar}-F), 119.6 (d, J_{F-C} = 22.5 Hz, C_{Ar}-H), 117.2 (d, J_{F-C} = 21.5 Hz, C_{Ar}-H), 116.4 (m, C_{Ar}-P), 116.3 (m, C_{Ar}-H), 25.3 (vt, J_{P-C} = 29 Hz, *C*HMe_2), 17.5 (CH*Me*$_2$), 16.9 (CH*Me*$_2$). ^{19}F NMR (C_6D_5Br, Figure 3.43): δ –122.9. $^{31}P\{^1H\}$ NMR (C_6D_5Br, Figure 3.44): δ 46.9 ($J_{195Pt-P}$ = 2,490 Hz). **(^{F}PNP)PtBr (312).** ^{19}F NMR (C_6D_5Br): –128.5. $^{31}P\{^1H\}$ NMR (C_6D_5Br): δ 40.8 ($J_{195Pt-P}$ = 2,623 Hz).

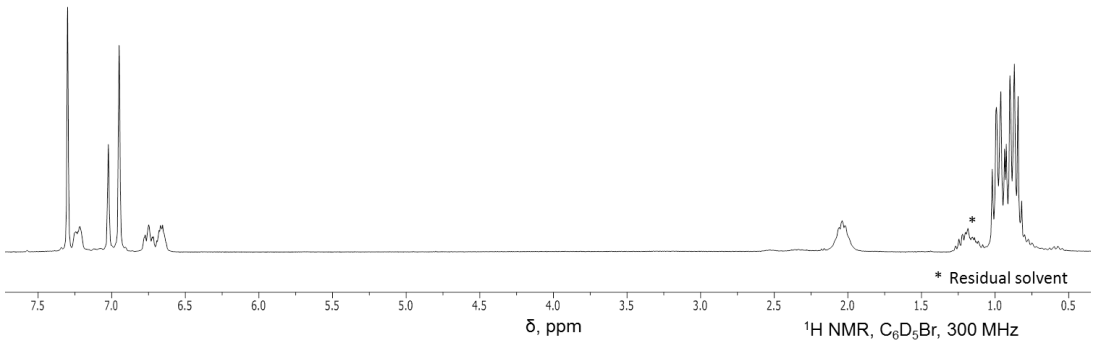

Figure 3.42 ^1H NMR spectrum of **310** in C_6D_5Br at RT measured on a 300-MHz Varian iNova.

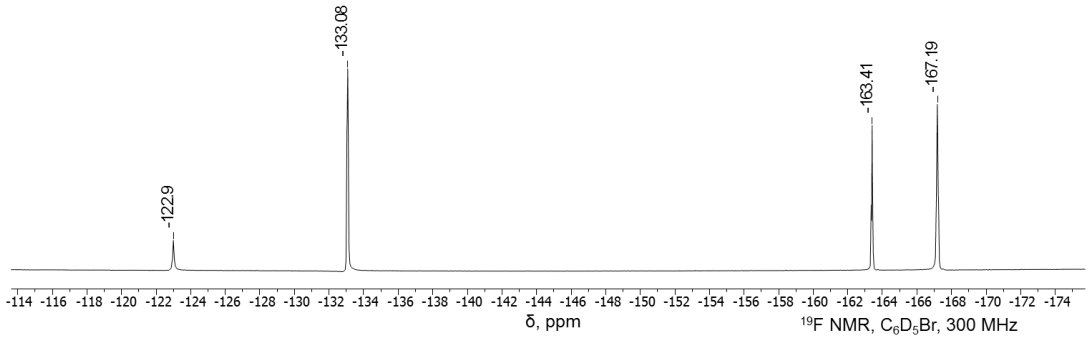

Figure 3.43 ^{19}F NMR spectrum of **310** in C_6D_5Br at RT measured on a 300-MHz Varian iNova.

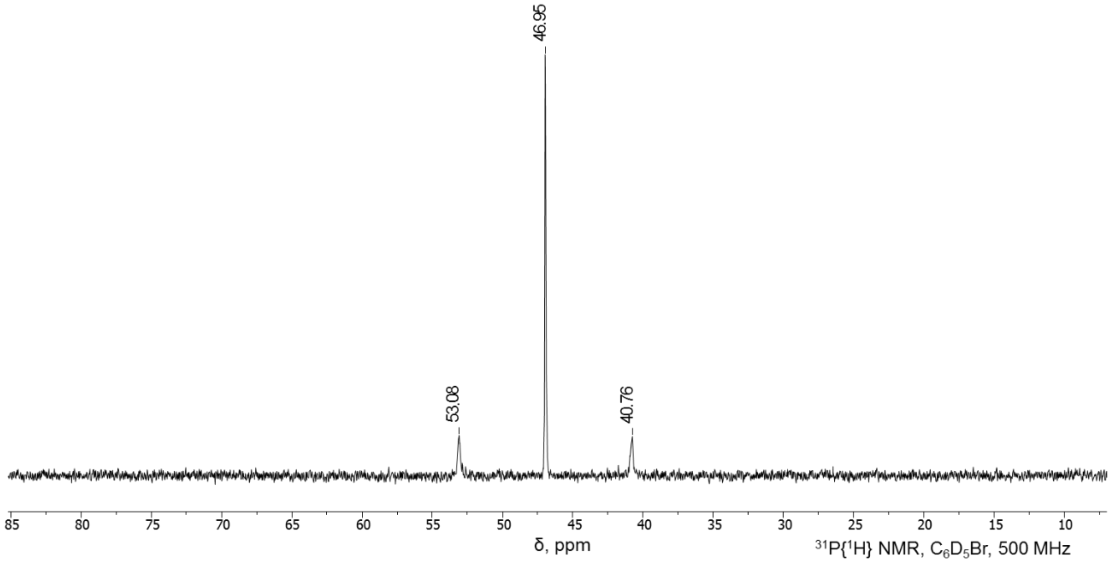

Figure 3.44 ^{31}P{^{1}H} NMR spectrum of **310** in C_6D_5Br at RT measured on a 500-MHz Varian NMRS.

3.4.1.5 Syntheses of $[(^{F}PN(H)P)Pt\text{-}R]^{+}$ by Protonation of $(^{F}PNP)Pt\text{-}R$

$[(^{F}PN(H)P)Pt\text{-}C_6H_5][BArF_{20}]$ (303a). 302a (21 mg, 0.030 mmol) was dissolved in about 3 mL of pentane in a small vial, forming a clear yellow solution. HOTf (15.4 µL, 1.88 M solution in Et_2O, 0.0290 mmol) was added, and a white precipitate immediately crashed out of the solution. The solvent was decanted off, and the solid was washed with 3 × 3 mL of pentane, dried under vacuum and then dissolved in 3 mL of CH_2Cl_2. $KBArF_{20}$ (21 mg, 0.029 mmol) was added, and the solution was stirred overnight at RT. The solution was filtered over Celite, the volatiles were removed and the residual oily blue solid was redissolved in CD_2Cl_2 for characterization. The NMR spectra matched those of the compound synthesized via the C-H activation experiment described above.

Protonation of $(^{F}PNP)PtC_6H_4Me$ Isomers. The protonated tolyl isomers were independently synthesized to help confirm the characterization of the products from the toluene C-H activation reactions. The neutral $(^{F}PNP)PtC_6H_4Me$ species were reacted with a substoichiometric amount of $[H(OEt_2)_2][BArF_{20}]$ (0.9 eq). The mixtures were dissolved in approximately 5 mL of a 3:1 mixture of pentane and diethyl ether and stirred for 30 min. The resulting solids were loaded onto a bed of Celite, rinsed with pentane and diethyl ether and then washed through with CH_2Cl_2. The volatiles were removed and the isolated solids were redissolved in CD_2Cl_2 for characterization.

$[(^{F}PN(H)P)Pt\text{-}o\text{-}C_6H_4Me][BArF_{20}]$ (303b). Isolated yield: 36 mg, 59%. ^{1}H NMR (CD_2Cl_2, Figure 3.45): δ 7.49 (m, 2H, Ar-*H*), 7.37 (m, 2H, Ar-*H*), 7.32 (m, 2H, Ar-*H*), 7.27 (br s, $J_{195Pt\text{-}H}$ = 32.6 Hz, 1H, N-*H*), 7.21 (d, *J* = 7.4 Hz, $J_{195Pt\text{-}H}$ = 66.8 Hz, 1H, *o*-tolyl-*H*), 6.99 (d, *J* = 7.4 Hz, 1H, *m*-tolyl-*H*), 6.92 (t, *J* = 7.2 Hz, 1H, tolyl-*H*), 6.87 (td, *J* = 7.4

Hz, 1.3 Hz, 1H, tolyl-*H*), 2.82 (m, 2H, C*H*Me$_2$), 2.68 (m, 2H, C*H*Me$_2$), 2.63 (s, 3H, C$_6$H$_4$*Me*), 1.20 (app q (dvt), *J* = 8 Hz, 6H, CH*Me*$_2$), 1.14 (app q (dvt), *J* = 8 Hz, 6H, CH*Me*$_2$), 1.05 (app q (dvt), *J* = 8 Hz, 6H, CH*Me*$_2$), 0.83 (app q (dvt), *J* = 8 Hz, 6H, CH*Me*$_2$). ^{13}C{^{1}H} NMR (CD_2Cl_2): δ 162.3 (d, $J_{F\text{-}C}$ = 257 Hz, C_{Ar}-F), 144.5, 141.2 (t, $J_{P\text{-}C}$ = 2.3 Hz), 136.1 (t, $J_{P\text{-}C}$ = 2.4 Hz, $J_{195Pt\text{-}C}$ = 42 Hz), 131.7 (m), 129.5 ($J_{195Pt\text{-}C}$ = 40 Hz), 126.2 (br s), 126.1 ($J_{195Pt\text{-}C}$ = 66 Hz), 124.5, 124.4, 121.5 (d, $J_{F\text{-}C}$ = 23 Hz, C_{Ar}-H), 120.1 (d, $J_{F\text{-}C}$ = 23 Hz, C_{Ar}-H), 27.4 (C$_6$H$_4$*C*H$_3$), 26.7 (vt, $J_{P\text{-}C}$ = 14.3 Hz, *C*HMe$_2$), 23.1 (vt, $J_{P\text{-}C}$ = 15.2 Hz, *C*HMe$_2$), 18.0 (CH*Me*$_2$), 17.6 (CH*Me*$_2$), 17.2 (CH*Me*$_2$), 16.5 (CH*Me*$_2$). ^{19}F NMR (CD_2Cl_2): δ –111.6. ^{31}P{^{1}H} NMR (CD_2Cl_2): δ 40.3 ($J_{195Pt\text{-}P}$ = 2,848 Hz).

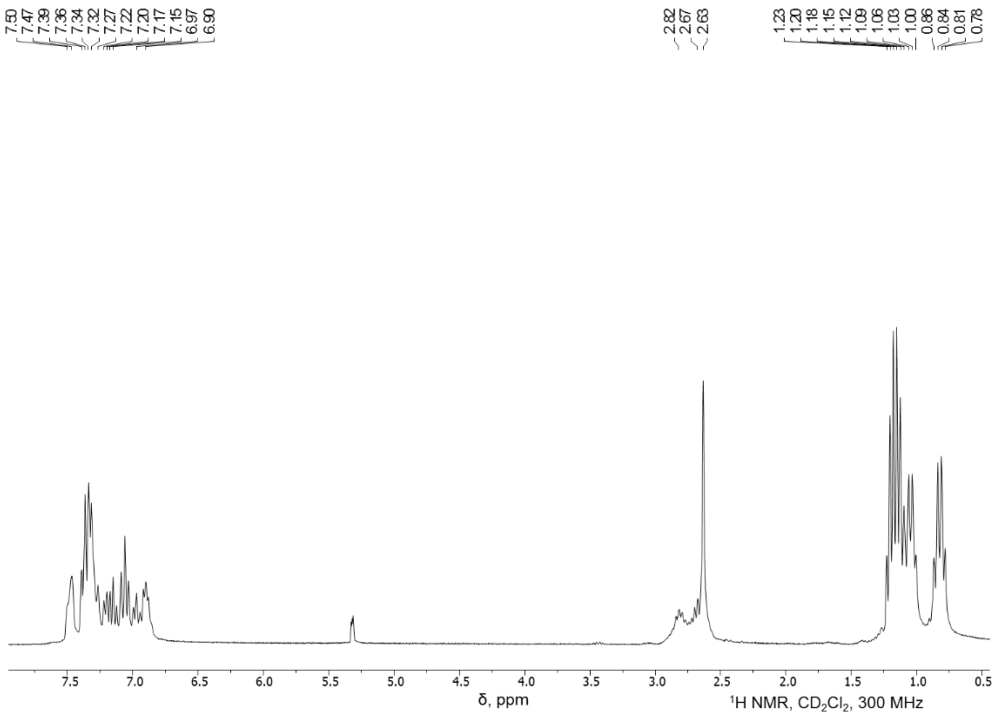

Figure 3.45 ^{1}H NMR spectrum of **303b** in CD_2Cl_2 at RT measured on a 300-MHz Varian iNova.

[(^{F}PN(H)P)Pt-*m*-C_6H_4Me][$BArF_{20}$] (303c). Isolated yield: 51 mg, 73%. ^{1}H NMR (CD_2Cl_2, Figure 3.46): δ 7.52 (m, 2H, Ar-*H*), 7.36 (m, 5H, Ar-*H* and *o*-C*H* of tolyl), 7.24 (br s, $J_{195Pt-H}$ = 34.9 Hz, 1H, N-*H*), 7.05 (br m, 1H, *o*-C*H*), 6.93 (t, *J* = 7.5 Hz, 1H, *m*-C*H*), 6.76 (d, *J* = 7.5 Hz, 1H, *p*-C*H*), 2.80 (m, 2H, C*H*Me_2), 2.68 (m, 2H, C*H*Me_2), 2.25 (s, 3H, C_6H_4*Me*), 1.20 (m, 12H, CH*Me*$_2$), 1.08 (vtd, J_{P-H} = 9 Hz, J_{H-H} = 7 Hz, CH*Me*$_2$), 0.89 (vtd, J_{P-H} = 9 Hz, J_{H-H} = 7 Hz, CH*Me*$_2$). ^{13}C{^{1}H} NMR (CD_2Cl_2): δ 162.3 (dvt, J_{F-C} = 256 Hz, J_{P-C} = 4 Hz, C_{Ar}-F), 144.6 (vtd, J_{P-C} = 7 Hz, J_{F-C} = 3 Hz, C_{Ar}-N), 138.6, 136.9, 133.3, 132.3 (vtd, J_{P-C} = 17 Hz, J_{F-C} = 6 Hz, C_{Ar}-P), 128.7, 126.0, 125.0, 124.5, 121.5 (d, J_{F-C} = 23 Hz, C_{Ar}-H), 120.0 (d, J_{F-C} = 23 Hz, C_{Ar}-H), 26.4 (vt, J_{P-C} = 13 Hz, *C*HMe_2), 23.5 (vt, J_{P-C} = 15 Hz, *C*HMe_2), 21.5 (C_6H_4*C*H_3), 18.0 (CH*Me*$_2$), 17.9 (CH*Me*$_2$), 17.6 (CH*Me*$_2$), 17.0 (CH*Me*$_2$). ^{19}F NMR (CD_2Cl_2): δ –111.8. ^{31}P{^{1}H} NMR (CD_2Cl_2): δ 41.0 ($J_{195Pt-P}$ = 2,838 Hz).

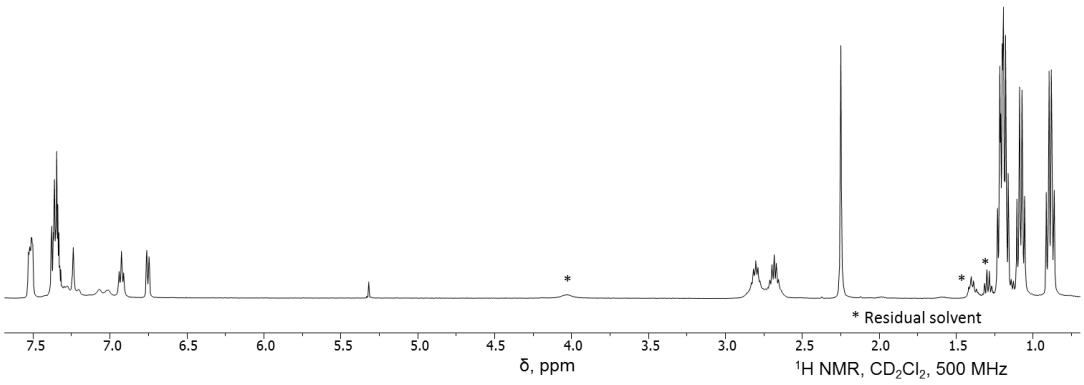

Figure 3.46 ^{1}H NMR spectrum of **303c** in CD_2Cl_2 at RT measured on a 500-MHz Varian NMRS.

[(^{F}PN(H)P)Pt-*p*-C_6H_4Me][$BArF_{20}$] (303d). Isolated yield: 49 mg, 80%. ^{1}H NMR (CD_2Cl_2, Figure 3.47 and Figure 3.48): δ 7.51 (m, 2H, Ar-*H*), 7.44–7.0 (very broad signal, 2H, *o*-C*H*), 7.36 (m, 4H, Ar-*H*), 7.22 (br s, $J_{195Pt-H}$ = 37.6 Hz, 1H, N-*H*), 6.89 (d, *J* = 7.7 Hz, 2H, *m*-C*H*), 2.80 (m, 2H, C*H*Me_2), 2.67 (m, 2H, C*H*Me_2), 2.23 (s, 3H, C_6H_4*Me*), 1.19 (m, 12H, CH*Me*$_2$), 1.07 (vtd, J_{P-H} = 9 Hz, J_{H-H} = 8 Hz, CH*Me*$_2$), 0.88 (dvt, J_{H-H} = 9 Hz, J_{P-H} = 8 Hz, CH*Me*$_2$). ^{13}C{^{1}H} NMR (CD_2Cl_2): δ 162.3 (dvt, J_{F-C} = 256 Hz, J_{P-C} = 5 Hz, C_{Ar}-F), 144.6 (vtd, J_{P-C} = 8 Hz, J_{F-C} = 3 Hz, C_{Ar}-N), 135.9 (t, J_{P-C} = 2.4 Hz, overlapping with $BArF_{20}$ signal, $J_{195Pt-C}$ = 42 Hz), 133.6, 132.4 (vtd, J_{P-C} = 17 Hz, J_{F-C} = 6 Hz, C_{Ar}-P), 129.9, 126.1, 121.5 (d, J_{F-C} = 23 Hz, C_{Ar}-H), 120.0 (d, J_{F-C} = 23 Hz, C_{Ar}-H), 26.4 (vt, J_{P-C} = 14.7 Hz, *C*HMe_2), 23.6 (vt, J_{P-C} = 15.2 Hz, *C*HMe_2), 20.8 ($C_6H_4CH_3$), 18.1 (CH*Me*$_2$), 17.9 (CH*Me*$_2$), 17.6 (CH*Me*$_2$), 17.0 (CH*Me*$_2$). ^{19}F NMR (CD_2Cl_2): δ –111.4. ^{31}P{^{1}H} NMR (CD_2Cl_2): δ 41.1 ($J_{195Pt-P}$ = 2,830 Hz).

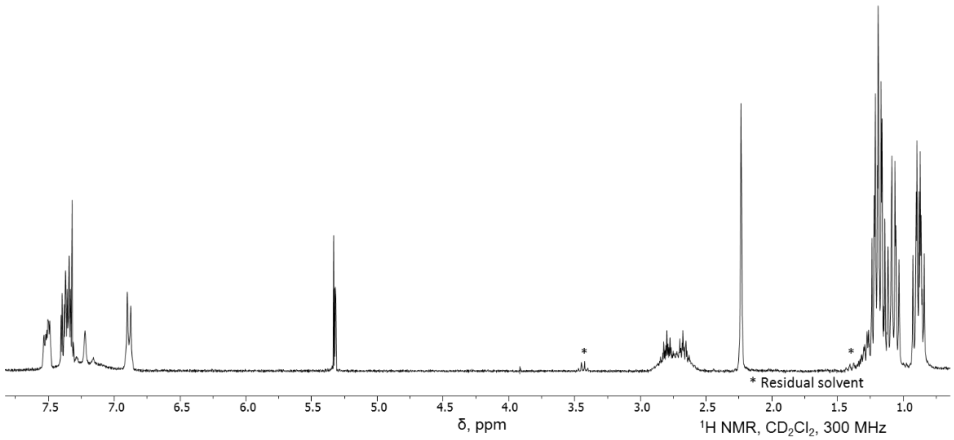

Figure 3.47 ^{1}H NMR spectrum of **303d** in CD_2Cl_2 at RT measured on a 300-MHz Varian iNova.

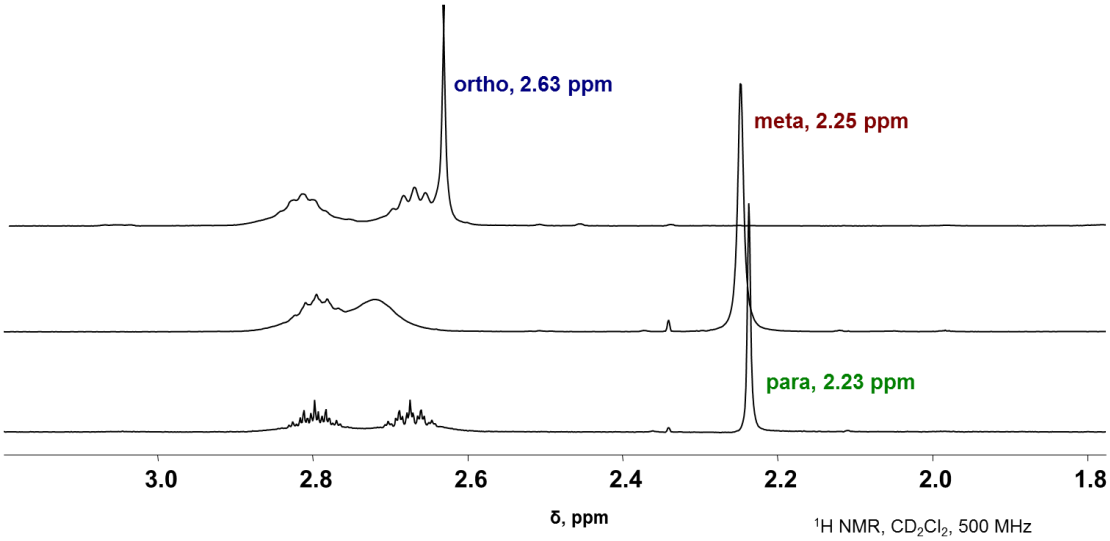

Figure 3.48 ^{1}H NMR spectra of the tolyl methyl resonances for **303b**, **303c**, and **303d** in CD_2Cl_2 at RT measured on a 500-MHz Varian NMRS.

[(^{F}PN(H)P)PtCH$_2$C$_6$H$_5$][BArF$_{20}$] (303g). In a 25 mL Schlenk flask covered with Al foil, **302g** (18.6 mg, 0.0257 mmol) was dissolved in approximately 5 mL of a 1:1 Et_2O/pentane solution. [H(OEt$_2$)$_2$][BArF$_{20}$] (19.4 mg, 0.0234 mmol, 0.9 eq) was added, and the formation of a white precipitate was noted after 30 min. The solution was stirred overnight, and the formation of additional precipitate was observed after 12 h. The volatiles were removed, and the resulting solid was resuspended in pentane, loaded on a bed of Celite, rinsed with pentane and then washed through with CH_2Cl_2. The volatiles were removed, and the solid was redissolved in CD_2Cl_2 for characterization. ^{1}H NMR (CD_2Cl_2, Figure 3.49): δ 7.42–7.38 (m, 2H, Ar-*H*), 7.38–7.32 (m, 6H, Ar-*H* overlapping with o-C*H* of benzyl), 7.23 (t, *J* = 7.5 Hz, 2H, *m*-C*H* of benzyl), 7.12 (t, *J* = 8 Hz, 1H, *p*-C*H* of benzyl), 7.09 (br s, $J_{195Pt-H}$ = 35 Hz, 1H, N-*H*), 3.46 (t, *J* = 6.3 Hz, $J_{195Pt-H}$ = 95 Hz, 2H, C*H*$_2$C$_6$H$_5$), 2.85 (m, 2H, C*H*Me$_2$), 2.41 (m, 2H, C*H*Me$_2$), 1.32 (app q (dvt), *J* = 8 Hz,

6H, CH*Me*$_2$), 1.28 (app q (dvt), J = 7.5 Hz, 6H, CH*Me*$_2$), 1.15 (app q (dvt), J = 8 Hz, 6H, CH*Me*$_2$), 1.10 (vtd, $J_{P\text{-}H}$ = 9 Hz, $J_{H\text{-}H}$ = 7 Hz, 6H, CH*Me*$_2$). ^{19}F NMR (CD_2Cl_2, Figure 3.50): δ –111.5. $^{31}P\{^1H\}$ NMR (CD_2Cl_2, Figure 3.51): δ 41.1 ($J_{195Pt\text{-}P}$ = 2,954 Hz).

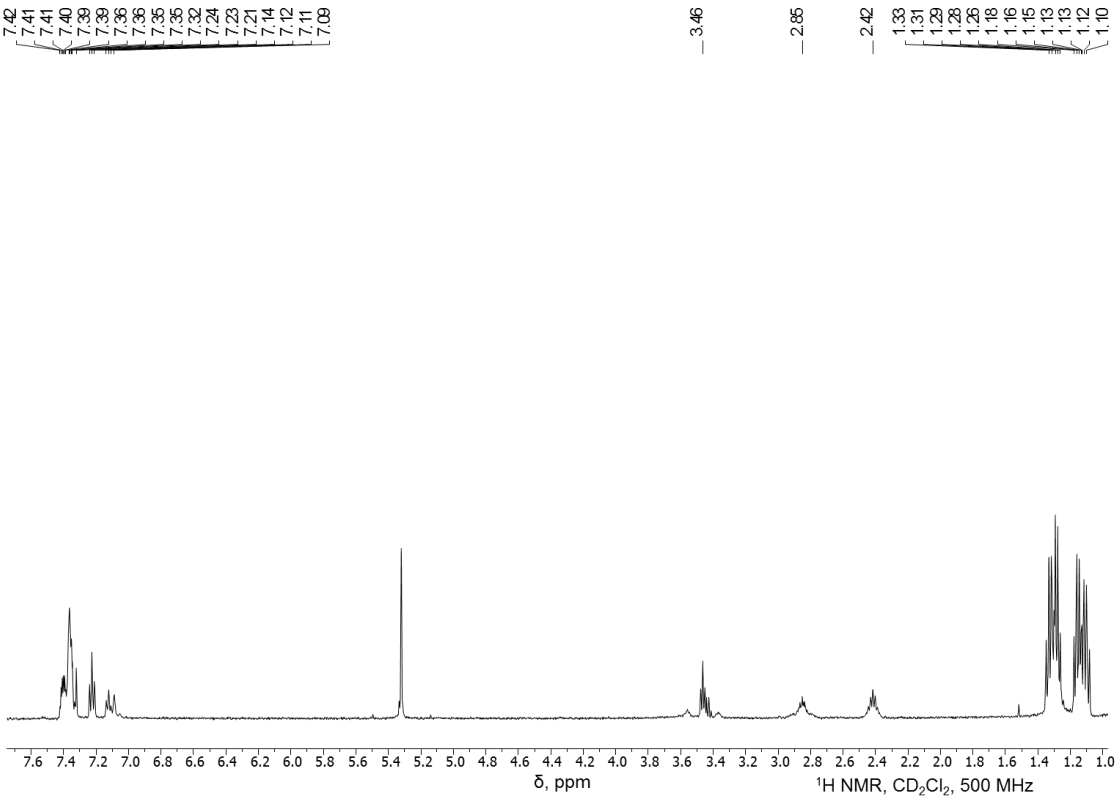

Figure 3.49 ^{1}H NMR spectrum of **303g** in CD_2Cl_2 at RT measured on a 500-MHz Varian NMRS.

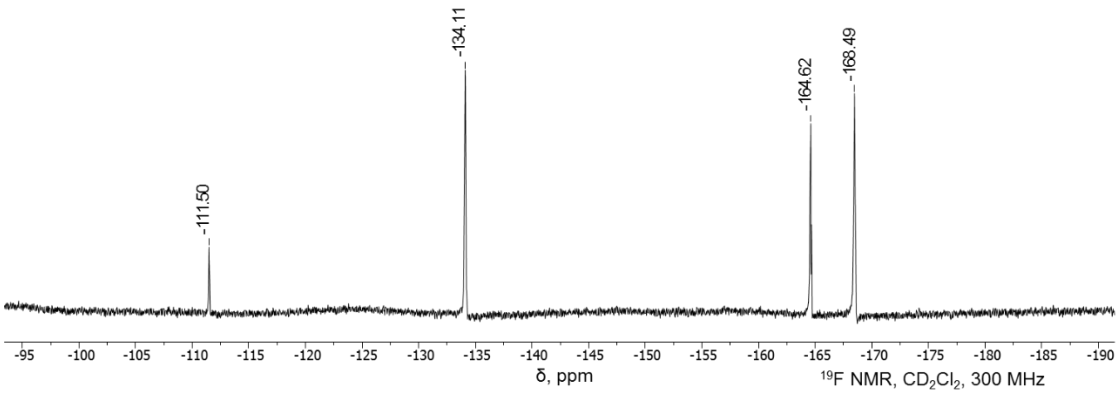

Figure 3.50 ^{19}F NMR spectrum of **303g** in CD_2Cl_2 at RT measured on a 300-MHz Varian iNova.

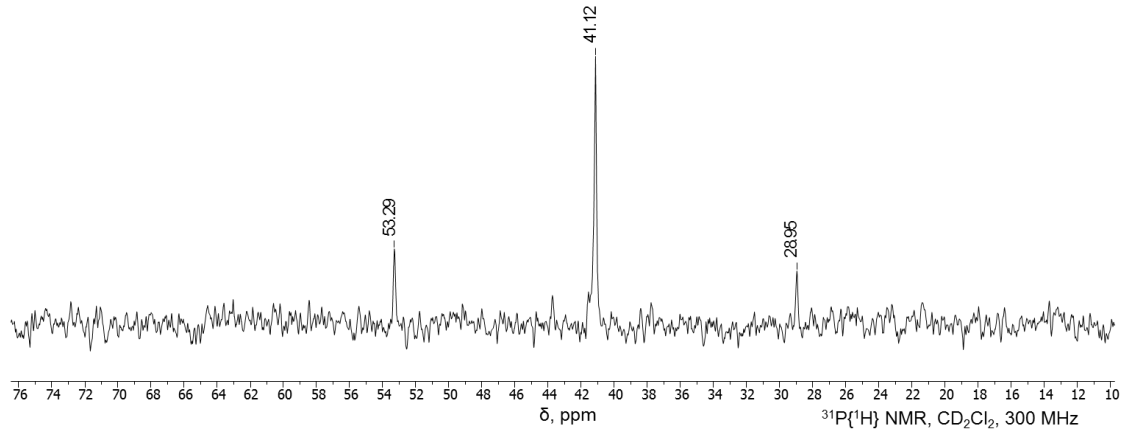

Figure 3.51 $^{31}P\{^1H\}$ NMR spectrum of **303g** in CD_2Cl_2 at RT measured on a 300-MHz Varian iNova.

3.4.1.6 Syntheses of (^{F}PNP)Pt-R by Deprotonation of [(^{F}PN(H)P)Pt-R]$^{+}$

(^{F}PNP)PtC$_6$D$_5$ (302a-D). 303a-D (29 mg, 0.023 mmol) was transferred to a J. Young NMR tube and dissolved in C_6D_6. KO^{t}Bu (3 mg, 0.03 mmol) was added, and the NMR tube was shaken, yielding a yellow solution with a colorless precipitate. Full conversion to **302a-D** was confirmed by ^{19}F NMR, using fluorobenzene as an internal standard. The solution was filtered into a 10-mL Schlenk flask, the volatiles were removed and the resulting yellow solid was redissolved in C_6D_6 for characterization. ^{1}H NMR (C_6D_6): δ 7.55 (m, 2H, Ar-*H*), 6.75 (m, 4H, Ar-*H*), 2.08 (m, 4H, C*H*Me$_2$), 0.90–0.83 (m, 24H, CH*Me*$_2$). ^{19}F NMR (C_6D_6): δ –130.6. ^{31}P{^{1}H} NMR (C_6D_6): δ 40.1 ($J_{195Pt-P}$ = 2,848 Hz).

Deprotonation of 303b-d with KO^{t}Bu. [(^{F}PN(H)P)PtC$_6$H$_4$Me][BArF$_{20}$] (65 mg, 0.047 mmol) was transferred to a J. Young NMR tube and dissolved in C_6D_6. KO^{t}Bu (6 mg, 0.05 mmol) was added, and the NMR tube was shaken, yielding a yellow solution with a colorless precipitate. The ^{19}F NMR spectrum showed full conversion to **302b-d**, and the ^{1}H NMR spectrum showed a **302b**:(**302c** plus **302d**) ratio of 8%:92% (**302c** and **302d** signals overlap).

(^{F}PNP)PtC$_6$H$_4$F (302e). 303e (19.8 mg, 0.0141 mmol) was transferred to a J. Young NMR tube and dissolved in C_6D_6. KO^{t}Bu (2 mg, 0.02 mmol) was added, and the NMR tube was shaken, yielding a yellow solution with a colorless precipitate. The ^{19}F NMR spectrum showed full conversion to **302e**. ^{1}H NMR (C_6D_6, Figure 3.52): δ 7.61 (m, $J_{195Pt-H}$ = 65 Hz, 1H, *ortho* C-*H* of C$_6$H$_4$F), 7.52 (m, 2H, Ar-*H*), 6.95–6.91 (m, 3H, *meta* and *para* C-*H* of C$_6$H$_4$F), 6.77–6.71 (m, 4H, Ar-*H*), 2.17 (m, 2H, C*H*Me$_2$), 2.04 (m, 2H,

C*H*Me$_2$), 0.96–0.79 (m, 24H, CH*Me*$_2$). ^{13}C{^{1}H} NMR (CD_2Cl_2): δ 166.8 (d, $J_{F\text{-}C}$ = 227 Hz, C_{Ar}-F), 160.6 (br s, C_{Ar}-N), 154.2 (d, $J_{F\text{-}C}$ = 237 Hz, C_{Ar}-F), 140.5 (dvt, $J_{F\text{-}C}$ = 18 Hz, $J_{P\text{-}C}$ = 2 Hz, C_{Ar}-H), 124.0 ($J_{Pt\text{-}C}$ = 58 Hz, C_{Ar}-Pt), 123.5 (dvt, $J_{F\text{-}C}$ = 7.5 Hz, $J_{P\text{-}C}$ = 1.4 Hz, C_{Ar}-H), 121.3 (vt, $J_{P\text{-}C}$ = 18 Hz, C_{Ar}-P), 120.7 (m), 118.5 (d, $J_{F\text{-}C}$ = 21.5 Hz, C_{Ar}-H), 117.9 (d, $J_{F\text{-}C}$ = 22.5 Hz, C_{Ar}-H), 115.0 (br s, C_{Ar}-H), 113.5 (d, $J_{F\text{-}C}$ = 29 Hz, C_{Ar}-H), 25.3 (vt, $J_{P\text{-}C}$ = 15 Hz, *C*HMe$_2$), 23.8 (vt, $J_{P\text{-}C}$ = 15 Hz, *C*HMe$_2$), 17.6 (br, CH*Me*$_2$), 17.3 (CH*Me*$_2$), 17.0 (CH*Me*$_2$). ^{19}F NMR (C_6D_6, Figure 3.53): δ –92.3 ($J_{195Pt\text{-}F}$ = 338 Hz), –131.3. ^{31}P{^{1}H} NMR (C_6D_6, Figure 3.54): δ 42.1 ($J_{195Pt\text{-}P}$ = 2,770 Hz).

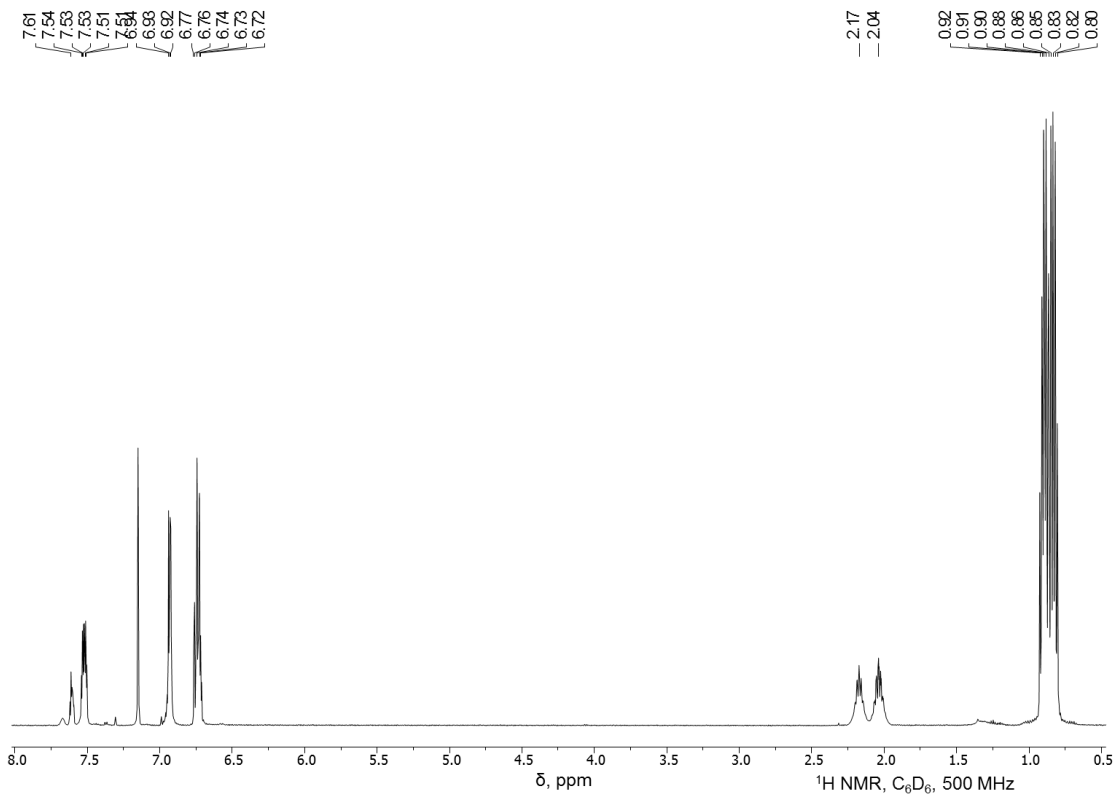

Figure 3.52 ^{1}H NMR spectrum of **302e** in C_6D_6 at RT measured on a 500-MHz Varian NMRS.

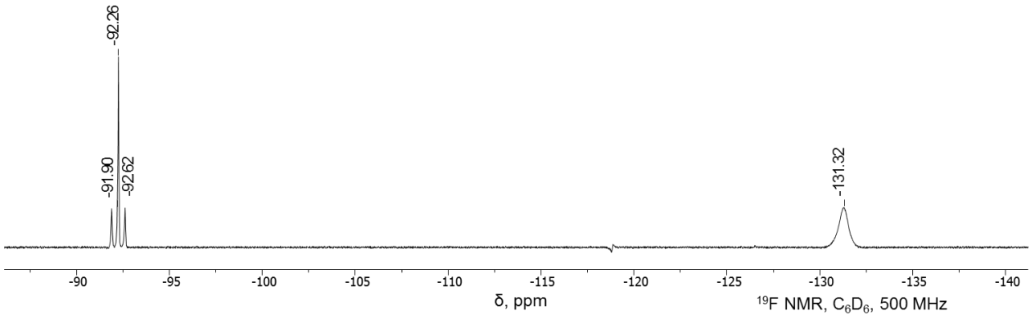

Figure 3.53 ^{19}F NMR spectrum of **302e** in C_6D_6 at RT measured on a 500-MHz Varian NMRS.

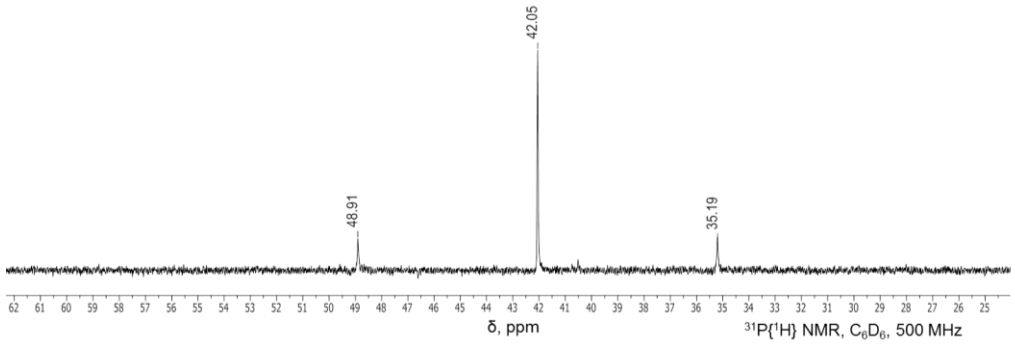

Figure 3.54 $^{31}P\{^1H\}$NMR spectrum of **302e** in C_6D_6 at RT measured on a 500-MHz Varian NMRS.

(^{F}PNP)PtC_6H_4Cl (302f). 303f (24.2 mg, 0.0170 mmol) was transferred to a J. Young NMR tube and dissolved in C_6D_6. KO^{t}Bu (2 mg, 0.02 mmol) was added, and the NMR tube was shaken, yielding a yellow solution and a colorless precipitate. The solution was filtered over Celite and silica gel, and the resulting clear yellow solution was used for characterization. ^1H NMR (C_6D_6, Figure 3.55): δ 7.59 (dd, J = 7.5 Hz, 1.9 Hz, $J_{195Pt-H}$ = 60.6 Hz, 1H, *ortho* C-*H* of C_6H_4Cl), 7.47 (br s, 2H, Ar-*H*), 7.31 (d, J = 7.6 Hz, 1H, *meta*

C-*H* of C_6H_4Cl), 6.90 (td, *J* = 7.6 Hz, 1.8 Hz, 1H, *meta* C-*H* of C_6H_4Cl), 6.79 (td, *J* = 7.6 Hz, 1.9 Hz, 1H, *para* C-*H* of C_6H_4Cl), 6.72 (m, 4H, Ar-*H*), 2.29 (m, 2H, C*H*Me_2), 2.04 (m, 2H, C*H*Me_2), 0.98–0.77 (m, 24H, CH*Me*$_2$). $^{13}C\{^1H\}$ NMR (CD_2Cl_2): δ 160.3 (vt, $J_{P\text{-}C}$ = 10 Hz, C_{Ar}-N), 154.2 (d, $J_{F\text{-}C}$ = 233 Hz, C_{Ar}-F), 143.5 (t, $J_{P\text{-}C}$ = 3 Hz), 141.1 (t, $J_{P\text{-}C}$ = 2 Hz), 137.3 (t, $J_{P\text{-}C}$ = 9 Hz), 127.9, 125.6 ($J_{195Pt\text{-}C}$ = 56 Hz, C_{Ar}-Pt), 123.5, 121.4 (m, C_{Ar}-P), 118.4 (d, $J_{F\text{-}C}$ = 21 Hz, C_{Ar}-H), 117.9 (d, $J_{F\text{-}C}$ = 22 Hz, C_{Ar}-H), 115.1 (app q, *J* = 6 Hz, C_{Ar}-H), 25.5 (vt, $J_{P\text{-}C}$ = 15.6 Hz, *C*HMe_2), 23.6 (vt, $J_{P\text{-}C}$ = 15.3 Hz, *C*HMe_2), 17.5 (CH*Me*$_2$), 17.4 (CH*Me*$_2$), 17.2 (CH*Me*$_2$), 16.8 (CH*Me*$_2$). ^{19}F NMR (C_6D_6, Figure 3.56): δ –130.2. $^{31}P\{^1H\}$ NMR (C_6D_6, Figure 3.57): δ 41.6 ($J_{195Pt\text{-}P}$ = 2,809 Hz).

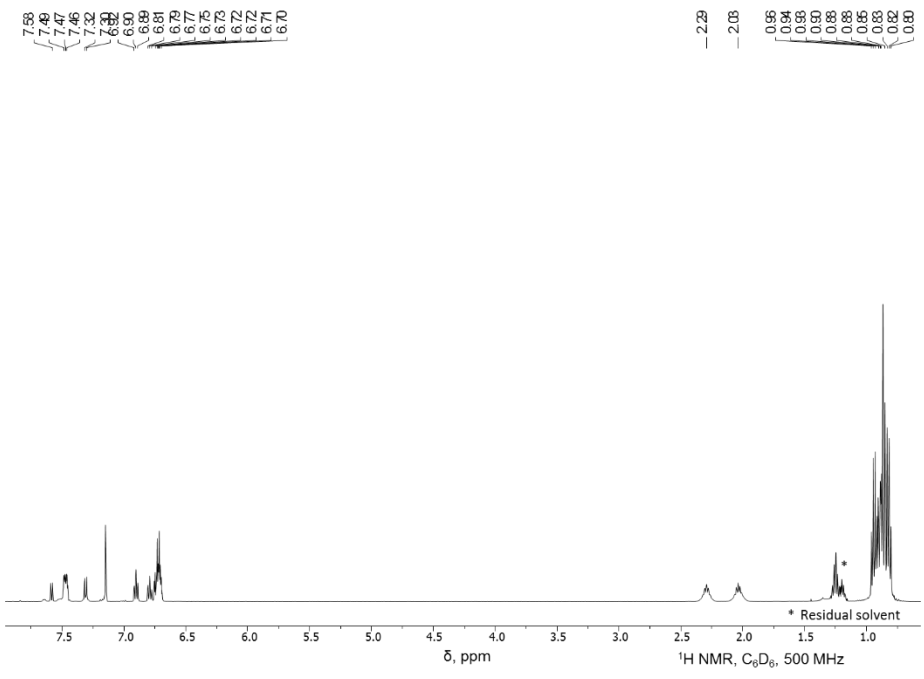

Figure 3.55 ^1H NMR spectrum of **302f** in C_6D_6 at RT measured on a 500-MHz Varian NMRS.

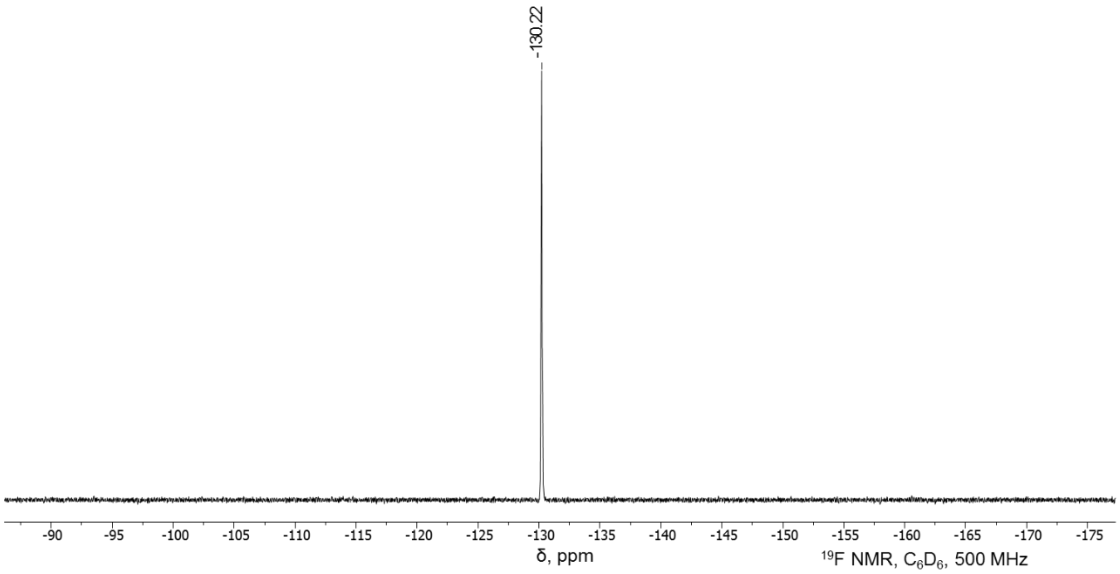

Figure 3.56 ^{19}F NMR spectrum of **302f** in C_6D_6 at RT measured on a 500-MHz Varian NMRS.

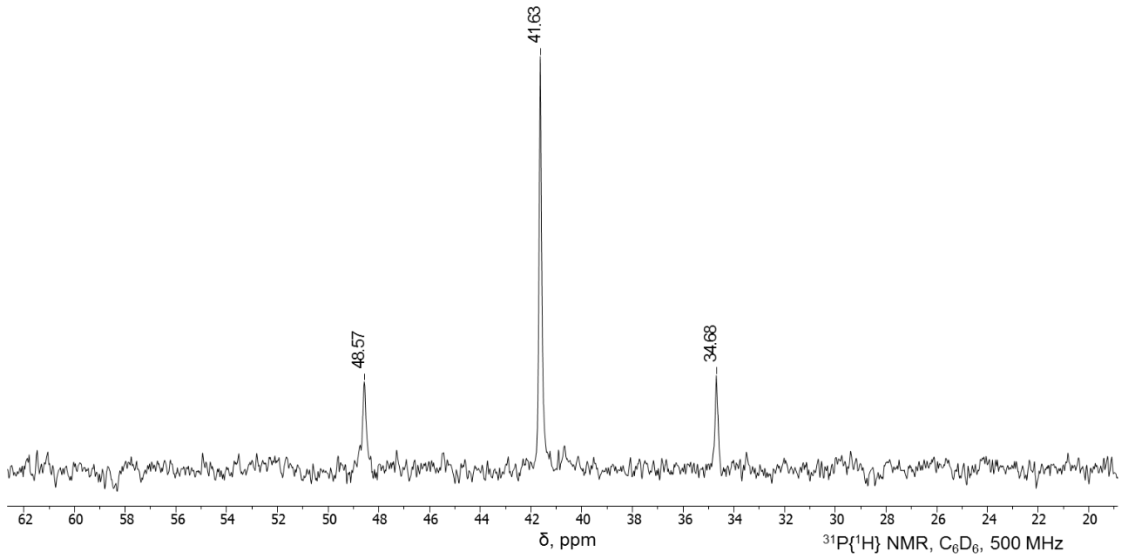

Figure 3.57 ^{31}P{^{1}H}NMR spectrum of **302f** in C_6D_6 at RT measured on a 500-MHz Varian NMRS.

3.4.1.7 Activation of Dichloromethane

[(^{F}PNP)PtCl][BArF$_{20}$] (309a). 301 (20.8 mg, 0.0266 mmol) and KBArF$_{20}$ (21 mg, 0.029 mmol) were transferred to a J. Young NMR tube. CD_2Cl_2 was added, and the solution immediately went from a bright yellow color to a darker brown/green, followed by a more gradual change to a blue solution. NMR spectra provided evidence for a paramagnetic species. Upon the addition of decamethyl ferrocene (10 mg, 0.031 mmol), the solution changed from dark blue to orange/brown. After filtering the solution over Celite, (^{F}PNP)PtCl (50% conversion) was observed by ^{19}F NMR.

[(^{F}PNP)PtCl][HCB$_{11}$Cl$_{11}$] (309b). The paramagnetic [(^{F}PNP)PtCl]$^{+}$ species was independently generated by reacting (^{F}PNP)PtCl (54.3 mg, 0.0814 mmol) with Ag[$HCB_{11}Cl_{11}$] (51.3 mg, 0.0815 mmol) in CD_2Cl_2. The solution was stirred for 5 min in a 10-mL Schlenk flask covered with Al foil and then filtered over Celite through a glass microfiber into a J. Young NMR tube. No product signals were observed by $^{31}P\{^{1}H\}$ or ^{19}F NMR. Broad signals were observed in the ^{1}H NMR spectrum (Figure 3.58) along with the C-H signal of the carborane anion. Crystals were obtained from a CH_2Cl_2 solution that was layered with pentane and cooled to –35 °C. One of the crystals was used for X-ray diffraction studies. The remaining crystals were washed with cold pentane and dried under vacuum. Isolated yield of the remaining fraction: 42 mg, 44%. Elemental analysis, found (calculated) for $C_{25}H_{35}B_{11}Cl_{11}F_2NP_2Pt$: C, 25.18 (25.26); H, 2.98 (2.97).

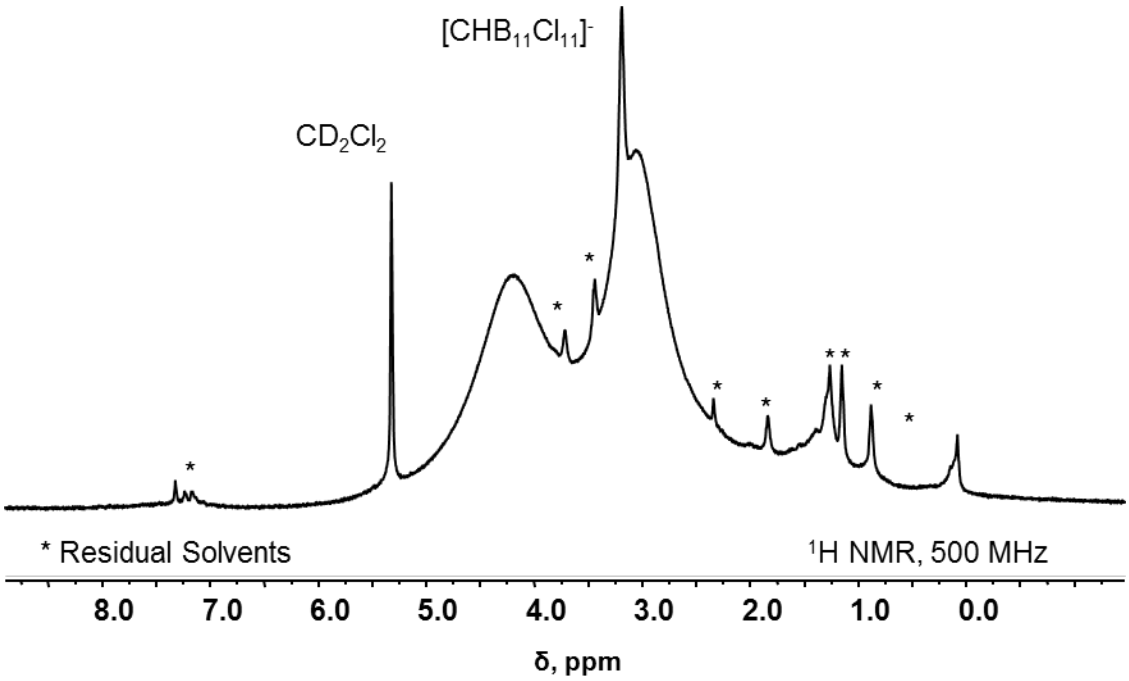

Figure 3.58 ^{1}H NMR spectrum of **309b** in CD_2Cl_2 at RT measured on a 500-MHz Varian NMRS.

3.4.1.8 Crossover and Competition Studies

Crossover Studies. A solid sample of **303b-d** yielded no crossover products when dissolved or suspended in C_6D_6 (minimally soluble) or fluorobenzene in a J. Young NMR tube. The solutions were monitored at RT for up to 48 h, and no changes were observed by ^{19}F, ^{31}P or ^{1}H NMR. Additionally, no changes were observed after heating at 80 °C for up to 48 h. Similar observations were made for **303e** in C_6D_6 (minimally soluble) or toluene (minimally soluble) and **303a-D** in toluene (minimally soluble) or fluorobenzene.

Thermolysis of 303a-D in the Presence of MeCN. 303a-D (26.8 mg, 0.0192 mmol) was transferred to a J. Young NMR tube and dissolved in CD_2Cl_2, forming a pale

blue solution. Fluorobenzene (5.0 µL) was added as an internal standard, followed by 300 µL of MeCN. The solution was monitored at RT for 5 days, and no changes were observed by NMR. The volatiles were removed, and the resulting solid was dissolved in neat MeCN. After heating at 80 °C for 24 h, the solution had become clear green, and the formation of **306** (approximately 26%) was observed by ^{19}F and ^{31}P NMR.

Table 3.3 Arene solvent molar ratios, observed C-H activation product ratios and adjusted molar-weighted ratios for competition studies.

Solvent Mixture	Molar Ratio	Observed Ratio of Products		Molar-Weighted Product Ratio
C_6D_6:PhF	1.06	**303e**:**303a-D**	16:1	17:1
C_6H_6:PhF	1.05	**303e**:**303a**	5.3:1	5.5:1
C_6H_6:C_6D_6	0.994	**303a**:**303a-D**	3.2:1	3.2:1
C_6H_6:toluene	1.19	**303a**:**303b-d**	2.3:1	2.0:1

C_6D_6 vs PhF. 301 (20.3 mg, 0.0260 mmol) was combined with $KBArF_{20}$ (20.2 mg, 0.0281 mmol) in a J. Young NMR tube, and a 1:1 (by volume) C_6D_6:C_6H_5F solution (prepared by combining 1.00 mL of C_6D_6 and 1.00 mL of C_6H_5F) was added, forming a cloudy orange solution. After combining the reagents at RT, the ^{19}F NMR spectrum showed only starting material. After heating the NMR tube for 30 min at 80 °C, **303e** was observed to be the major product by ^{19}F NMR. After 24 h at 80 °C, a pale blue solution containing a white precipitate had formed. The ^{19}F and ^{1}H NMR spectra showed a **303e**:**303a-D** ratio of approximately 16:1 (see Table 3.3).

C_6H_6 vs PhF. A 1:1 (by volume) solution of C_6H_6:C_6H_5F was prepared by combining 1.00 mL of C_6H_6 and 1.00 mL of C_6H_5F in a small vial. **301** (25.0 mg, 0.0320

mmol) and $KBArF_{20}$ (23.3 mg, 0.0325 mmol) were transferred as solids into a Teflon-stoppered round-bottomed flask. The C_6H_6:C_6H_5F solution was added, and the reaction flask was placed in an oil bath at 80 °C. After 3 h, the solution had become a pale blue with a grey precipitate. The volatiles were removed, and the products were extracted with CD_2Cl_2 and passed through a layer of Celite into a J. Young NMR tube. The ^{19}F NMR and ^1H NMR spectra showed a **303e**:**303a** ratio of approximately 5:1.

C_6H_6 vs C_6D_6. A 1:1 (by volume) solution of C_6H_6:C_6D_6 was prepared by combining 1.00 mL of C_6H_6 and 1.00 mL of C_6D_6 in a small vial. **301** (22.4 mg, 0.0287 mmol) and $KBArF_{20}$ (21.2 mg, 0.0295 mmol) were transferred as solids into a Teflon-stoppered round-bottomed flask. The C_6H_6:C_6D_6 solution was added, and the reaction flask was placed in an oil bath at 80 °C. After 3 h, the solution had become a pale blue with a grey precipitate. The volatiles were removed, and the products were extracted with CD_2Cl_2 and passed through a layer of Celite into a J. Young NMR tube. The ^1H NMR spectrum showed a **303a**:**303a-D** ratio of approximately 3:1.

C_6H_6 vs C_6H_5Me. A 1:1 (by volume) solution of C_6H_6:C_6H_5Me was prepared by combining 1.00 mL of C_6H_6 and 1.00 mL of C_6H_5Me in a small vial. **301** (21.7 mg, 0.0278 mmol) and $KBArF_{20}$ (20.9 mg, 0.0279 mmol) were transferred as solids into a Teflon-stoppered round-bottomed flask. The C_6H_6:C_6H_5Me solution was added, and the reaction flask was placed in an oil bath at 80 °C. After 3 h, the solution had become a pale blue with a grey precipitate. The volatiles were removed, and the products were extracted with CD_2Cl_2 and passed through a layer of Celite into a J. Young NMR tube. The ^1H NMR spectrum showed a **303a**:**303b-d** ratio of approximately 2.3:1.

3.4.1.9 Probing the Interconversion of Isomers of Tolyl Isomers 303b-d

Monitoring the Isomerization of 303b in CD_2Cl_2. 303b (36 mg, 0.026 mmol) was dissolved in CD_2Cl_2 in a J. Young NMR tube, forming a pale blue solution. The solution was monitored at RT by ^{1}H, ^{19}F and ^{31}P NMR spectroscopy for up to 2 weeks. No changes were observed. Addition of neat HOTf (9.0 μL, 0.10 mmol, 4 eq) resulted in the formation of **308** as the major product and a **303b**:**303c**:**303d**:free toluene ratio of approximately 9%:35%:16%:40%.

Monitoring the Isomerization of 303c in CD_2Cl_2. 303c (51 mg, 0.036 mmol) was dissolved in CD_2Cl_2 in a J. Young NMR tube, forming a pale blue solution. The solution was monitored at RT by ^{1}H, ^{19}F and ^{31}P NMR spectroscopy for up to 2 weeks, but no changes were observed. A 0.11 M solution of HOTf was prepared in fluorobenzene. 20 min after the addition of the HOTf solution (33 μL, 0.0036 mmol, 0.1 eq), some **303d** was observed along with the appearance of free toluene (Figure 3.59). After 16 h at RT, the **303b**:**303c**:**303d**:free toluene ratio was 3%:70%:26%:1%. An additional portion of the HOTf solution (163 μL, 0.0179 mmol, 0.5 eq) was added, and after another 16 h at RT, the **303b**:**303c**:**303d**:free toluene ratio was 11%:56%:18%:15%. Finally, 19.0 μL of neat HOTf (0.233 mmol total, 6.46 eq) was added to the NMR tube, and the **303b**:**303c**:**303d**:free toluene ratio became 6%:25%:10%:59%. The major product was identified as **8**.

Monitoring the Isomerization of 303d in CD_2Cl_2. 303d (49 mg, 0.035 mmol) was dissolved in CD_2Cl_2 in a J. Young NMR tube, forming a pale blue solution. The solution was monitored at RT by ^{1}H, ^{19}F and ^{31}P NMR spectroscopy for up to 2 weeks,

but no changes were observed. A 0.11 M solution of HOTf was prepared in fluorobenzene. 20 min after the addition of the HOTf solution (90.0 μL, 0.0099 mmol, 0.28 eq), some formation of **303c** was observed along with the appearance of free toluene. After 16 h, the **303b**:**303c**:**303d**:free toluene ratio was approximately 2%:9%:80%:9%. An additional portion of the HOTf solution (286 μL, 0.0315 mmol, 0.9 eq) was added, and after another 16 h at RT, the **303b**:**303c**:**303d**:free toluene ratio was approximately 3%:24%:59%:14%. Finally, 18.0 μL of neat HOTf (0.235 mmol total, 6.7 eq) was added to the NMR tube, and the **303b**:**303c**:**303d**:free toluene ratio became approximately 3%:22%:35%:39%. The major product was identified as **308**.

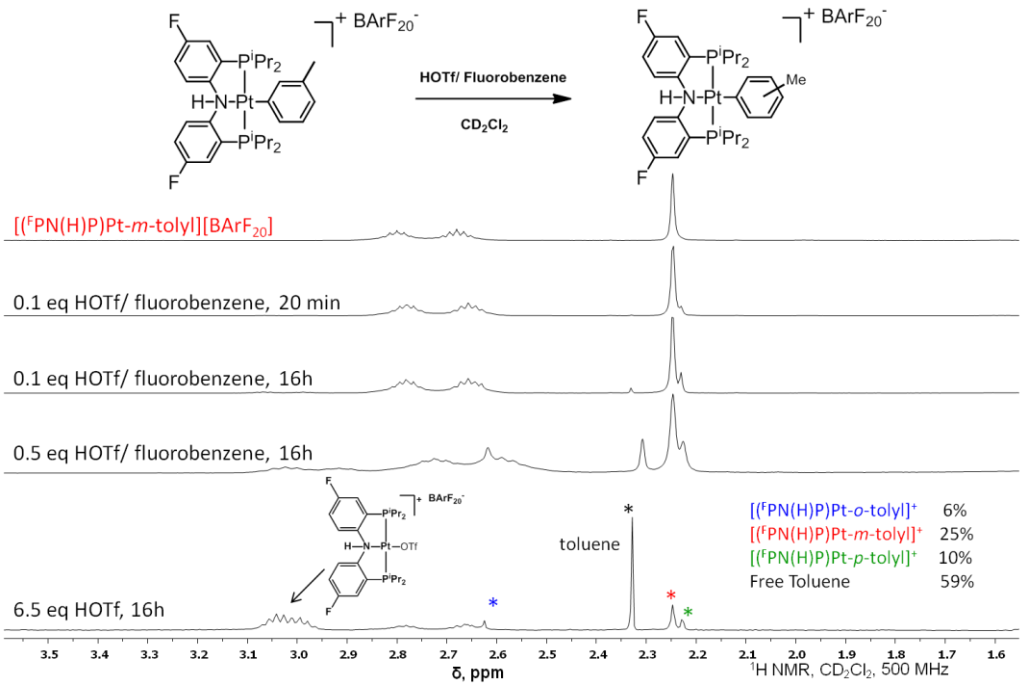

Figure 3.59 ^{1}H NMR spectra showing the isomerization of **303c** upon addition of HOTf in CD_2Cl_2 at RT measured on a 500-MHz Varian NMRS.

Monitoring the Isomerization of 303g in CD_2Cl_2. 303g (19.8 mg, 0.0141 mmol) was dissolved in CD_2Cl_2 in a J. Young NMR tube, forming a pale blue solution. The solution was monitored at RT by ^{1}H, ^{19}F and ^{31}P NMR spectroscopy for up to 2 weeks, but no changes were observed. Then, 5.0 μL of neat HOTf (0.057 mmol, 4 eq) was added to the NMR tube. After 16 h at RT, the starting material had been completely consumed, and the **303b**:**303c**:**303d**:free toluene ratio was approximately 2%:39%:9%:50%. The major product was identified as **308**.

Attempted Isomerization of 303c in the Presence of 302c. 303c (12.8 mg, 9.13 μmol) was dissolved in CD_2Cl_2 in a J. Young NMR tube, forming a pale blue solution. A 5.33 mM solution of **302c** was prepared in CD_2Cl_2, and 84 μL of this solution (0.45 μmol) was added to the NMR tube. No changes were observed after 12 h at RT. Up to one equivalent of **302c** (6.6 mg, 9.1 μmol) was added, but no changes were observed after 24 h.

Attempted Isomerization of 303c in the Presence of BF_3. 303c (9.0 mg, 6.4 μmol) was dissolved in CD_2Cl_2 in a J. Young NMR tube, forming a pale blue solution. A 47.5 mM solution of $BF_3{\cdot}SMe_2$ was prepared in CD_2Cl_2, and 7.0 μL of this solution (0.33 μmol) was added to the NMR tube. No changes were observed after 12 h at RT. Up to one equivalent of $BF_3{\cdot}SMe_2$ (135 μL, 6.41 μmol) was added, but no changes were observed after 24 h.

Attempted Isomerization of 303c in the Presence of $[H(OEt_2)_2][BArF_{20}]$. 303c (9.0 mg, 6.4 μmol) was dissolved in CD_2Cl_2 in a J. Young NMR tube, forming a pale blue solution. A 0.0128 M solution of $[H(OEt_2)_2][BArF_{20}]$ was prepared in Et_2O, and 25 μL of

this solution (0.33 μmol) was added to the NMR tube. No changes were observed after 12 h at RT. Up to one equivalent of $[H(OEt_2)_2][BArF_{20}]$ (0.50 mL, 6.4 μmol) was added, but no changes were observed after 24 h.

Attempted Isomerization of 303c in the Presence of $B(C_6F_5)_3$. 303d (25.8 mg, 0.0184 mmol) was added to a CD_2Cl_2 solution of $B(C_6F_5)_3$ (4.88 μmol, 0.265 eq) in a J. Young NMR tube. The solution was monitored for 3 days, but no changes were observed by NMR.

Attempted Isomerization of 303c in the Presence of $[H(OEt_2)_2][OTf]$. 303c (32.1 mg, 0.0228 mmol) was dissolved in CD_2Cl_2 in a J. Young NMR tube, forming a pale blue solution. A 1.88 M solution of HOTf was prepared in Et_2O, and 12.0 μL of this solution (0.0226 mmol) was added to the NMR tube. After 16 h, no changes were observed by ^1H, ^{19}F, and ^{31}P NMR. A total of 3.4 equivalents of $[H(OEt_2)_2][OTf]$ (0.0775 mmol) was added with no isomerization observed after 5 days at RT.

3.4.2 DFT Studies

All calculations were carried out in Gaussian 09[147] using the PBE1PBE (also known as PBE0)[201] and M06-L[154] functionals, tight optimizations, and the ultrafine integration grid (a pruned (99,590) grid). The basis sets[y] included Def2-QZVPP (with the corresponding ECP) for Pt,[206] 6-311+G(2df) for the N, F, and P atoms, and 6-31+G(d,p) for all other atoms. The default PCM method (solvent = tetrahydrofurane) was used for all

[y] These basis sets are available from the EMSL Basis Set Library (bse.pnl.gov).

calculations of this work with the UFF radii scaled by 1.1 (explicit hydrogens). The optimized geometries were verified to have no negative harmonic frequencies by frequency calculations which also provided the enthalpies and free energies reported here. The free energies were calculated under P = 302 atm in THF.[207,208] Results are summarized in Tables 3.4 and 3.5 and models are shown in Figures 3.60 and 3.61.

Table 3.4 Calculated bond distance data (in Å) and angles (deg) using PBE1PBE functional for $[(^{F}PNP)Pt]^{+}$.

	$[(^{F}PNP)Pt]^{+}$ Singlet PBE1PBE	$[(^{F}PNP)Pt]^{+}$ Triplet PBE1PBE
Pt-P	2.327	2.298
Pt-N	1.964	2.090
N-C_{Ar}	1.393	1.381
P-Pt-P	166.59	167.02
P-Pt-N	83.29	83.51
C_{Ar}-N-C_{Ar}	122.94	124.15
C_{Ar}-N-Pt	118.53	117.93

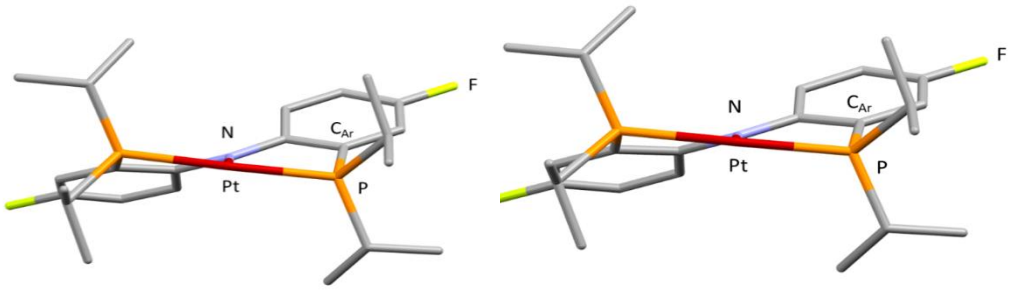

[(^{F}PNP)Pt]$^{+}$ Singlet PBE1PBE [(^{F}PNP)Pt]$^{+}$ Triplet PBE1PBE

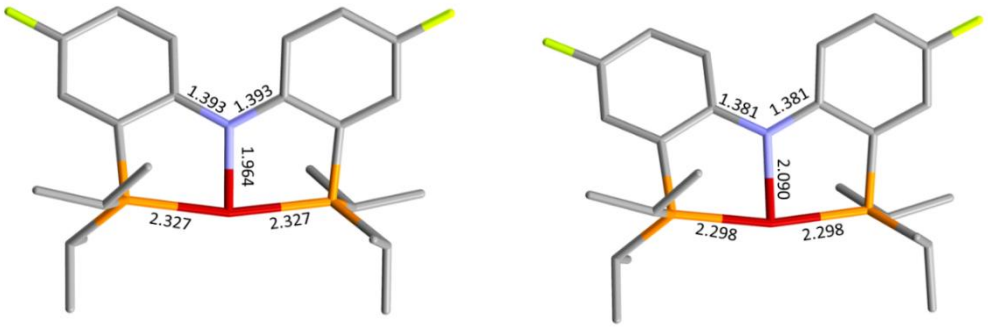

[(^{F}PNP)Pt]$^{+}$ Singlet PBE1PBE [(^{F}PNP)Pt]$^{+}$ Triplet PBE1PBE

Figure 3.60 PBE1PBE optimized geometries for singlet and triplet states of [(^{F}PNP)Pt]$^{+}$.

Table 3.5 Calculated bond distance data (in Å) and angles (deg) using M06-L functional for [(^{F}PNP)Pt]$^{+}$.

	[(^{F}PNP)Pt]$^{+}$ Singlet M06-L	[(^{F}PNP)Pt]$^{+}$ Triplet M06-L
Pt-P	2.342	2.314
Pt-N	1.994	2.142
N-C_{Ar}	1.391	1.377
P-Pt-P	164.11	163.51
P-Pt-N	82.05	81.75
C_{Ar}-N-C_{Ar}	123.69	125.02
C_{Ar}-N-Pt	118.16	117.49

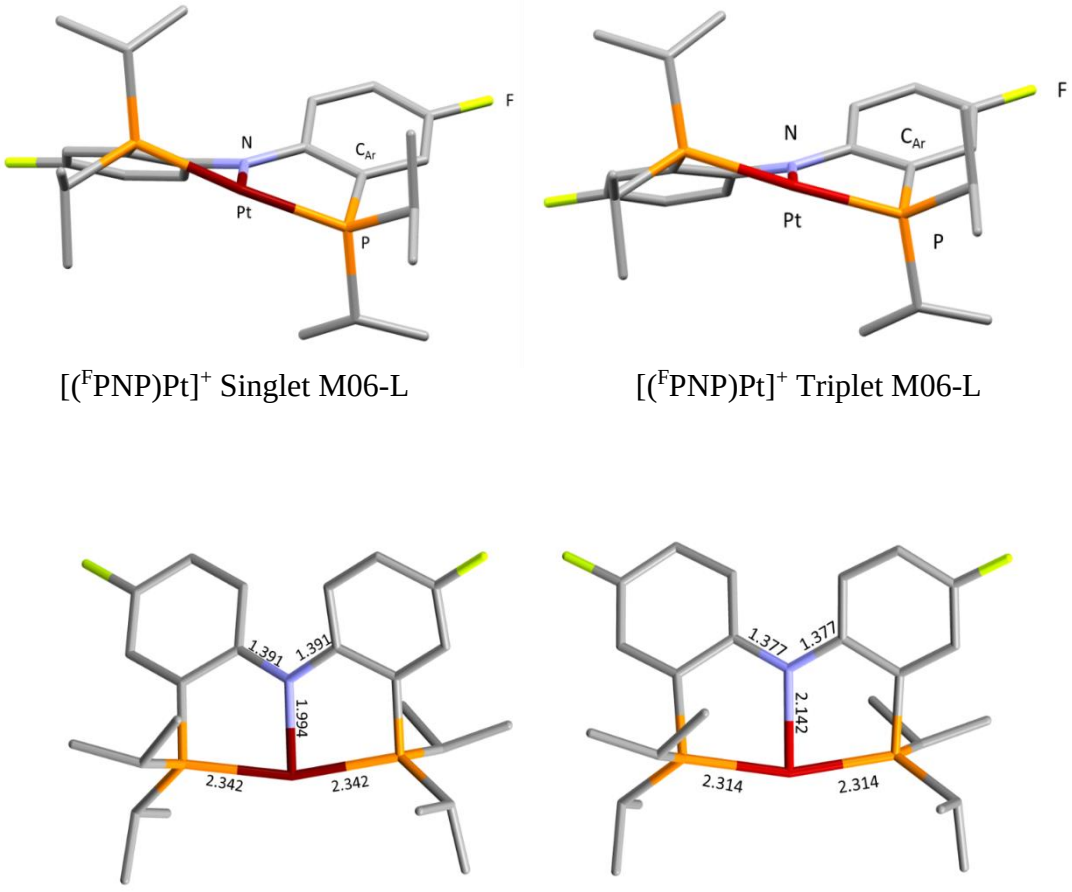

[(^{F}PNP)Pt]$^{+}$ Singlet M06-L [(^{F}PNP)Pt]$^{+}$ Triplet M06-L

[(^{F}PNP)Pt]$^{+}$ Singlet M06-L [(^{F}PNP)Pt]$^{+}$ Triplet M06-L

Figure 3.61 M06-L optimized geometries for singlet and triplet states of [(^{F}PNP)Pt]$^{+}$.

3.4.3 Details of X-Ray Diffractometry Studies

3.4.3.1 X-Ray Data Collection, Solution, and Refinement for 303e.

A pale blue, multi-faceted block of suitable size (0.20 × 0.11 × 0.06 mm) was selected from a representative sample of crystals of the same habit using an optical microscope and mounted onto a nylon loop. Low temperature (110 K) X-ray data were

obtained on a Bruker APEXII CCD based diffractometer (Mo sealed X-ray tube, K_α = 0.71073 Å). All diffractometer manipulations, including data collection, integration and scaling were carried out using the Bruker APEXII software.[206] An absorption correction was applied using SADABS.[207] The space group was determined on the basis of systematic absences and intensity statistics and the structure was solved by direct methods and refined by full-matrix least squares on F^2. The structure was solved in the monoclinic $P2_1/c$ space group using XS[208] (incorporated in SHELXTL). No missed symmetry was reported by PLATON.[143] All non-hydrogen atoms were refined with anisotropic thermal parameters. Hydrogen atoms were placed in idealized positions and refined using riding model. Deuterium atoms of the solvent molecules were not placed due to solvent disorder. The structure was refined (weighted least squares refinement on F^2) and the final least-squares refinement converged to R_1 = 0.0285 ($I > 2\sigma(I)$, 10152 data) and wR_2 = 0.0670 (F^2, 11953 data, 757 parameters, 1 restraints). The fluorine atom on the metallated fluorobenzene residue was found to reside with partial occupancy on C(43) and C(45) and was refined as such.

3.4.3.2 X-Ray Data Collection, Solution, and Refinement for 303c/d.

A Leica MZ 75 microscope was used to identify a suitable pale blue blocks with very well defined faces with dimensions (max, intermediate, and min) 0.15 mm × 0.13 mm × 0.10 mm from a representative sample of crystals of the same habit. The crystal mounted on a nylon loop was then placed in a cold nitrogen stream (Oxford) maintained at 110 K.

A BRUKER APEX 2 X-ray (three-circle) diffractometer was employed for crystal screening, unit cell determination, and data collection. The goniometer was controlled using the APEX2 software suite, v2008-6.0.[9] The sample was optically centered with the aid of a video camera such that no translations were observed as the crystal was rotated through all positions. The detector was set at 6.0 cm from the crystal sample (APEX2, 512x512 pixel). The X-ray radiation employed was generated from a Mo sealed X-ray tube (K_α= 0.70173Å with a potential of 40 kV and a current of 40 mA) fitted with a graphite monochromator in the parallel mode (175 mm collimator with 0.5 mm pinholes).

Sixty data frames were taken at widths of 0.5°. These reflections were used in the auto-indexing procedure to determine the unit cell. A suitable cell was found and refined by nonlinear least squares and Bravais lattice procedures. The unit cell was verified by examination of the h k l overlays on several frames of data. No super-cell or erroneous reflections were observed. After careful examination of the unit cell, a standard data collection procedure was initiated using omega scans.

Integrated intensity information for each reflection was obtained by reduction of the data frames with the program APEX2.[9] The integration method employed a three dimensional profiling algorithm and all data were corrected for Lorentz and polarization factors, as well as for crystal decay effects and were finally merged and scaled to produce a suitable data set. The absorption correction program SADABS[10] was employed to correct the data for absorption effects (as well as systematic errors).

Systematic reflection conditions and statistical tests of the data suggested the space group $P2_1/n$. A solution was obtained readily using SHELXTL (XS).[11] The tolyl group

attached to the Pt was disordered with *para* and *meta* isomers, which was modeled successfully, with a ratio of 53:47 respectively. The hydrogen atoms were placed in idealized positions geometrically and were set riding on the respective parent atoms. All non-hydrogen atoms were refined with anisotropic thermal parameters. The structure was refined (weighted least squares refinement on F^2) to convergence (Figure 3.62).[209]

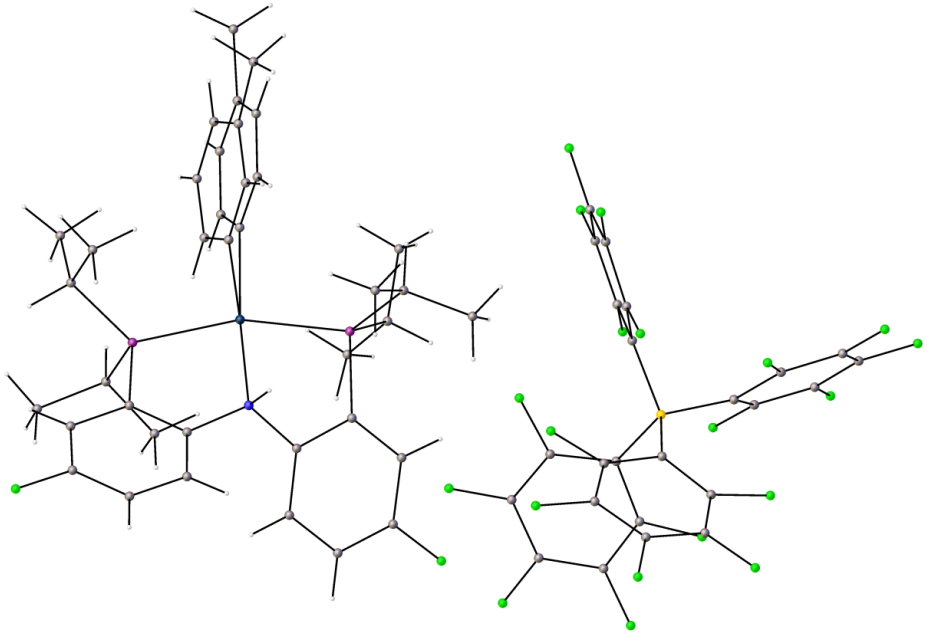

Figure 3.62 Olex2 structure plot of **303c-d** showing tolyl group attached to Pt as disordered with *para* and *meta* isomers modeled successfully in a ratio of 53:47, respectively.

3.4.3.3 X-Ray Data Collection, Solution, and Refinement for 309b.

A Leica MZ 75 microscope was used to identify a suitable blue blocks with very well defined faces with dimensions (max, intermediate, and min) 0.60 mm × 0.08 mm ×

0.04 mm from a representative sample of crystals of the same habit. The crystal mounted on a nylon loop was then placed in a cold nitrogen stream (Oxford) maintained at 110 K.

A BRUKER APEX 2 X-ray (three-circle) diffractometer was employed for crystal screening, unit cell determination, and data collection. The goniometer was controlled using the APEX2 software suite, v2008-6.0.[9] The sample was optically centered with the aid of a video camera such that no translations were observed as the crystal was rotated through all positions. The detector was set at 6.0 cm from the crystal sample (APEX2, 512x512 pixel). The X-ray radiation employed was generated from a Mo sealed X-ray tube (K_α = 0.70173Å with a potential of 40 kV and a current of 40 mA) fitted with a graphite monochromator in the parallel mode (175 mm collimator with 0.5 mm pinholes).

Sixty data frames were taken at widths of 0.5°. These reflections were used in the auto-indexing procedure to determine the unit cell using CELL_NOW.* Two components were identified and refined by nonlinear least squares and Bravais lattice procedures. The orientation matrices were verified by examination of the h k l overlays on several frames of data. No super-cell or erroneous reflections were observed.

After careful examination of the unit cell, a standard data collection procedure was initiated using omega scans. Integrated intensity information for each reflection was obtained by reduction of the data frames with the program APEX2.[9] The integration method employed a three dimensional profiling algorithm and all data were corrected for Lorentz and polarization factors, as well as for crystal decay effects and were finally merged and scaled to produce a suitable data set. The absorption correction program TWINABS[10] was employed to correct the data for absorption effects (as well as systematic

errors) and also to separate the twin components. Only the major component was used for structure solution as well as least squares refinement.

Systematic reflection conditions and statistical tests of the data suggested the space group $P2_1/c$. A solution was obtained readily using SHELXTL (XS).[11] Hydrogen atoms were placed in idealized positions and were set riding on the respective parent atoms. All non-hydrogen atoms were refined with anisotropic thermal parameters. The structure was refined (weighted least squares refinement on F^2) to convergence.[11,13]

3.4.4 Protonation Experiments for (PNP)PtMe and [(PONOP)PtMe]$^+$

3.4.4.1 Synthesis of Carborane Acids

$[H(C_6H_3(CH_3)_3)][HCB_{11}Cl_{11}]$.[202-204] **[**$Et_3Si{\cdot}HSiEt_3][HCB_{11}Cl_{11}]$ (156 mg, 0.207 mmol) was transferred to a 25 mL screw-capped Schlenk flask. 3 mL of mesitylene was added and the solution became slightly pale yellow with most of the silylium undissolved. The solution was degassed and the flask was placed in liquid N_2. Approximately 1 atm of $HCl_{(g)}$ was condensed into the flask. The solution was allowed to warm to RT behind a blast shield and stirred for 8 h. The solution changed color to clear bright yellow over the course of the reaction. Volatiles were removed yielding a pale yellow solid. To assess the purity of the product and the amount of residual mesitylene present, low temperature NMR studies were conducted on an aliquot of the product dissolved in CD_2Cl_2. Yield of **$[H(C_6H_3(CH_3)_3)][HCB_{11}Cl_{11}]{\cdot}0.5(C_6H_3(CH_3)_3)$** 124 mg, 85%. The same procedure was followed for **$[H(C_6H_3(CH_3)_3)][BuCB_{11}Cl_{11}]$**. NMR data: **$[H(C_6H_3(CH_3)_3)][HCB_{11}Cl_{11}]$**: ^{1}H NMR ($CD_2Cl_2$, 400 MHz, 193 K, Figure 3.63): δ 7.51 (s, 1H, Ar-C*H*), 4.40 (s, 2H, Ar-

CH_2), 3.26 (s, 1H, *H*-C$B_{11}Cl_{11}$), 2.85 (s, 3H, Ar-*p*-CH_3), 2.68 (s, Ar-*o*-CH_3, 6H). **[H(C$_6$H$_3$(CH$_3$)$_3$)][BuCB$_{11}$Cl$_{11}$]**: ^{1}H NMR (CD_2Cl_2, 400 MHz, 193 K, Figure 3.64): δ 7.53 (s, 1H, Ar-C*H*), 4.47 (s, 2H, Ar-CH_2), 2.86 (s, 3H, Ar-*p*-CH_3), 2.71 (s, Ar-*o*-CH_3, 6H), 2.17 (m, 2H, -CH_2-), 1.70 (m, 2H, -CH_2-), 1.16 (m, 2H, -CH_2-), 0.84 (t, J_{H-H} = 15 Hz, 3H, -CH_3).

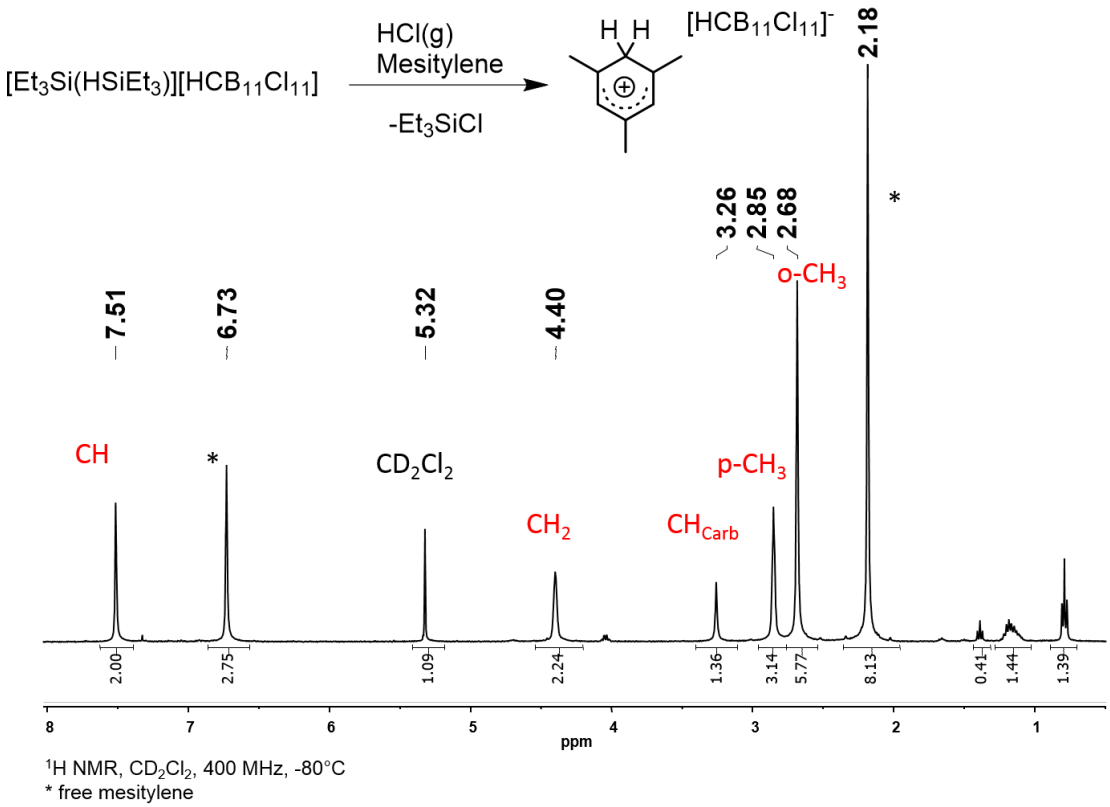

Figure 3.63 ^{1}H NMR spectrum of **[H(C$_6$H$_3$(CH$_3$)$_3$)][HCB$_{11}$Cl$_{11}$]** in CD_2Cl_2 at 193 K measured on a 400-MHz Varian NMRS.

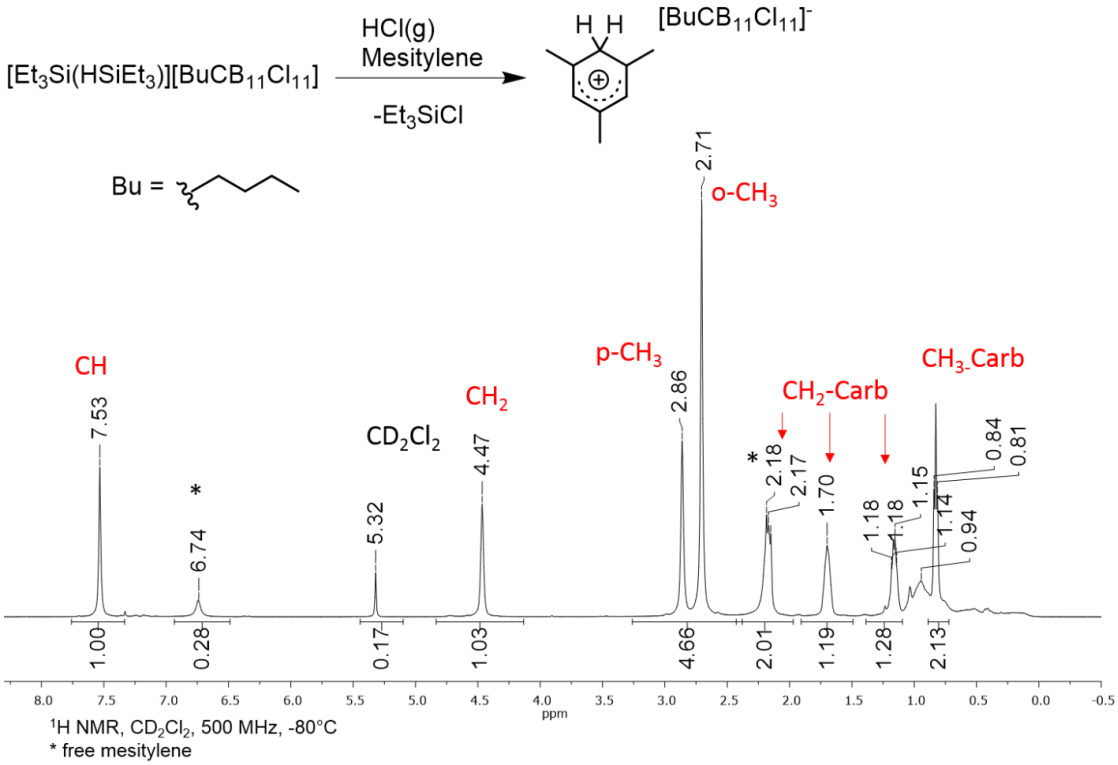

Figure 3.64 ^{1}H NMR spectrum of **[H(C$_6$H$_3$(CH$_3$)$_3$)][BuCB$_{11}$Cl$_{11}$]** in CD_2Cl_2 at 193 K measured on a 500-MHz Varian NMRS.

3.4.4.2 Protonation Experiments

Protonation of (^{F}PNP)PtMe (315). In a base-free glovebox, **315** (16 mg, 0.025 mmol) was combined with [H(C$_6$H$_3$(CH$_3$)$_3$)][HCB$_{11}$Cl$_{11}$]·0.5(C$_6$H$_3$(CH$_3$)$_3$) (36 mg, 0.051 mmol) as solids in a J. Young tube. Fluorobenzene was added and the NMR tube was inverted several times. The ^{31}P{^{1}H} NMR spectrum in C_6H_5F showed a mixture of two products, with 70% of the mixture corresponding to a signal at 39.8 ppm ($J_{Pt\text{-}P}$ = 2,770 Hz) and approximately 30% corresponding to a signal at 41.5 ppm ($J_{Pt\text{-}P}$ =2,760 Hz, poor resolution). The ^{19}F NMR spectrum (Figure 3.65) in C_6H_5F contains two signals for what

is believed to be rotamers of [(^{F}PN(H)P)Pt-C_6H_4F][$HCB_{11}Cl_{11}$] **317** at 91.7 ppm (J_{Pt-F} = 390 Hz) and 93.8 ppm (J_{Pt-F} = 315 Hz).

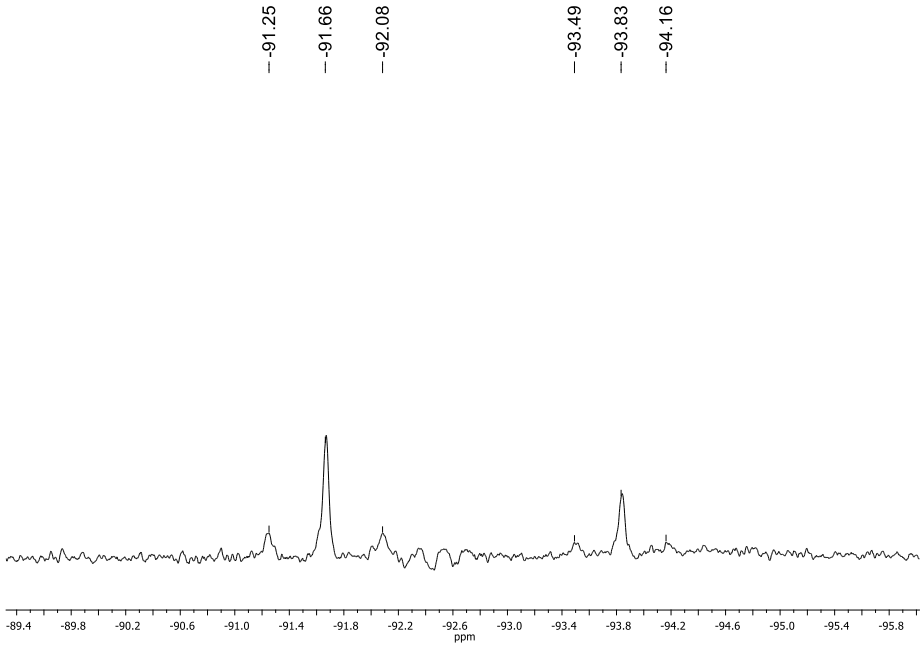

Figure 3.65 ^{19}F NMR spectrum of protonation reaction of **315** with 2 equiv. **[H($C_6H_3(CH_3)_3$)][$HCB_{11}Cl_{11}$]·0.5($C_6H_3(CH_3)_3$)** in C_6H_5F measured on a 500-MHz Varian NMRS at RT.

[(PONOP)PtMe][^{n}BuCB$_{11}$Cl$_{11}$] (320). PONOP (201 mg, 0.503 mmol), (COD)PtMeCl (168 mg, 0.475 mmol), and Na[^{n}BuCB$_{11}$Cl$_{11}$] (280 mg, 0.466 mmol) were mixed in CH_2Cl_2 at RT for 1 h. The solution was filtered over a pad of Celite. The volatiles were removed and solid was mixed with THF and sonicated for an hour. After decanting the supernatant, *iso*-octane was added, and the mixture was sonicated for an additional hour. The solid was collected, washed with pentane, and dried under vacuum. Yield: 81%.

^{1}H NMR (CD_2Cl_2, Figure 3.66): δ 8.08 (t, J_{H-H} = 10 Hz, J_{PH} = 1 Hz, 1H, Ar-*H*), 7.05 (d, J_{HH} = 10 Hz, 2H, Ar-*H*), 1.43 (vt, J_{P-H} = 8 Hz, 36H, -C(C*H*$_3$)$_3$), 2.25 (m, 2H, -C*H*$_2$-), 1.84 (m, 2H, -C*H*$_2$-), 1.24 (m, 2H, -C*H*$_2$-), 1.18 (t, J_{Pt-H} = 80 Hz, J_{P-H} = 5 Hz, 3H, Pt-C*H*$_3$), 0.89 (t, J_{H-H} = 7.5 Hz, 3H, -C*H*$_3$). ^{13}C{^{1}H} NMR (125.670 MHz, CD_2Cl_2): δ 163.4 (t, J_{P-C} = 7 hz, C_{Ar}-OP), 147.4 (C_{Ar}), 105.5 (t, J_{P-C} = 2 Hz, C_{Ar}), 42.26 (vt, J_{P-C} = 9 Hz, P-*C*(CH$_3$)$_3$), 27.2 (2 overlapping vt, J_{P-C} = 2 Hz, P-C(*C*H$_3$)$_3$). ^{31}P{^{1}H} NMR (CD_2Cl_2, Figure 3.66): δ 181.1 (J_{Pt-P} = 2868 Hz).

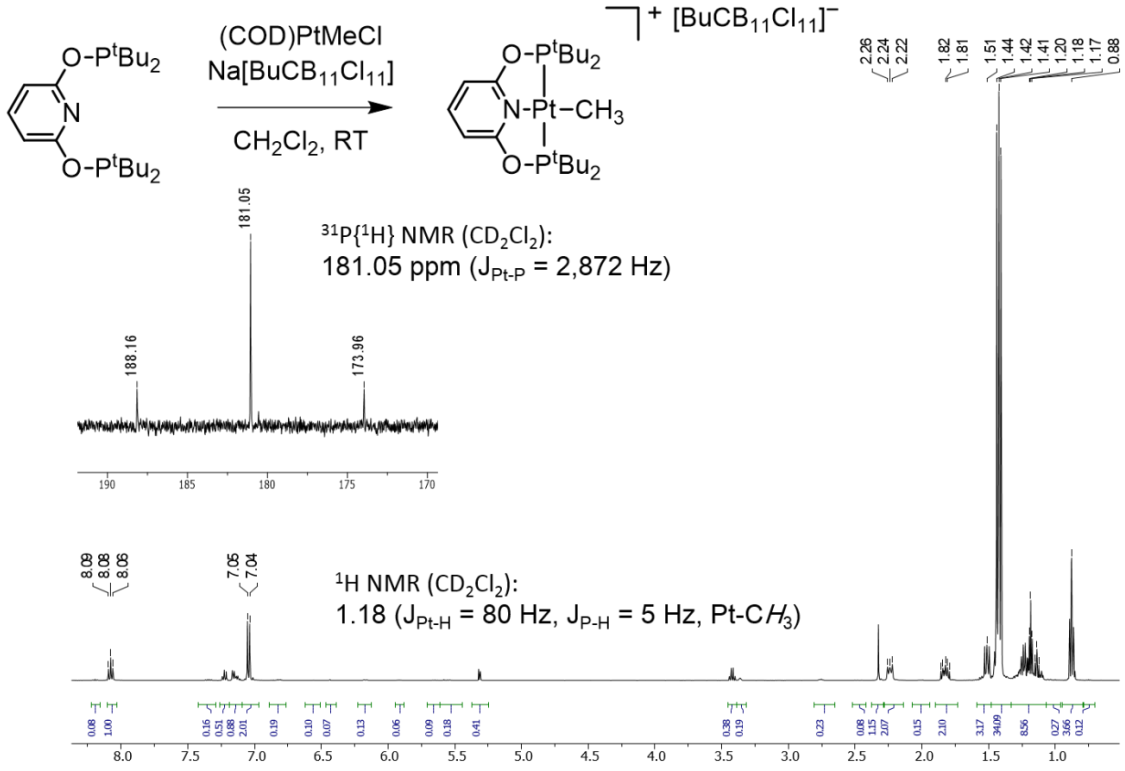

Figure 3.66 ^{1}H NMR spectrum and inset of ^{31}P{^{1}H} NMR spectrum for **320** measured on a 500-MHz Varian NMRS at RT.

Protonation of [(PONOP)PtMe][^{n}BuCB$_{11}$Cl$_{11}$] in CD_2Cl_2. In a base-free glovebox, **320** (32 mg, 0.027 mmol) and [H($C_6H_3(CH_3)_3$)][^{n}BuCB$_{11}$Cl$_{11}$]·($C_6H_3(CH_3)_3$) (22 mg, 0.027 mmol) were transferred to a J. Young NMR tube as solids then placed in liquid N_2. CD_2Cl_2 was vacuum transferred into the NMR tube and the sample was placed in a pre-cooled 500 MHz NMR spectrometer at –80 °C. **320** remained unreacted after 45 min at –80 °C (Figure 3.67). The spectrometer temperature was increased to –60 °C and the starting material remained unreacted. The sample was ejected to confirm the solution was homogeneous, and no precipitate was observed. At this point, the spectrometer was slowly warmed to RT and some conversion of the **320** to **321** was observed. After 24 h at RT, **320** was completely converted into **321** (Figure 3.68).

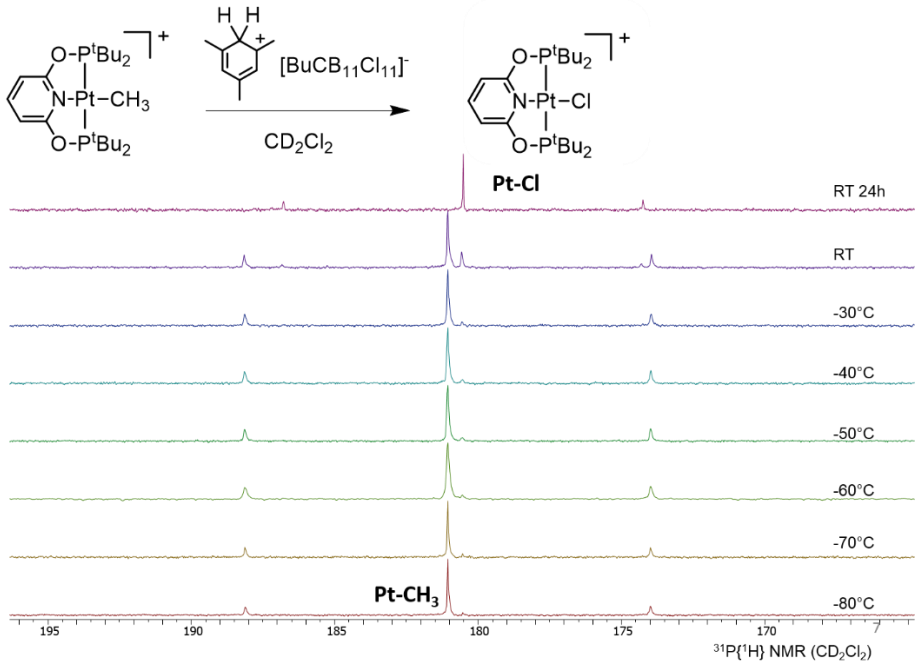

Figure 3.67 Stack spectra for protonation of **320** in CD_2Cl_2 from –80 °C to RT measured on a 500-MHz Varian NMRS.

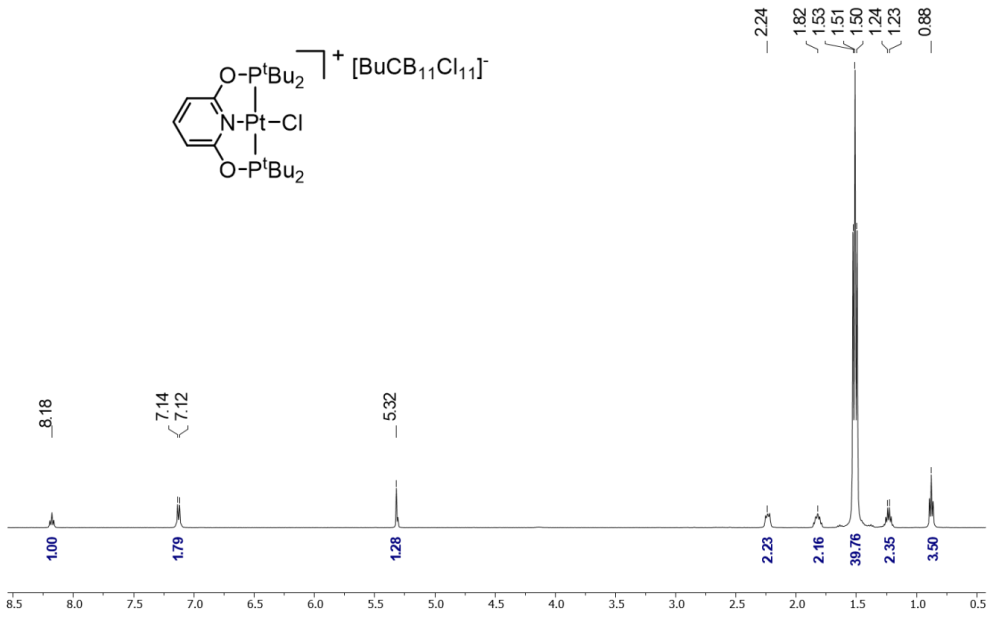

Figure 3.68 ^{1}H NMR spectrum for **321** product isolated from protonation of **320** measured on a 500-MHz Varian NMRS at RT.

[(PONOP)PtCl][HCB$_{11}$Cl$_{11}$] (322). [(PONOP)PtCl]Cl·NCMe[209] (29 mg, 0.041 mmol) was dissolved in CD_2Cl_2 in a J. Young NMR tube and Na[HCB$_{11}$Cl$_{11}$] (22 mg, 0.04 mmol) was added. After 30 min at RT, the contents of the NMR tube were filtered over a pad of Celite and the volatiles were removed. The white solid was dissolved in CD_2Cl_2 and ^{1}H NMR spectroscopy showed the formation of [(PONOP)PtCl][HCB$_{11}$Cl$_{11}$]·NCMe. Sonication in THF for 1 h followed by sonication in *iso*-octane for 1 h allowed for the isolation of **322** with less than 5% MeCN. ^{1}H NMR (CD_2Cl_2, Figure 3.69): δ 8.19 (tt, J_{H-H} = 10 Hz, J_{PH} = 1 Hz, 1H, Ar-*H*), 7.13 (d, J_{HH} = 10 Hz, 2H, Ar-*H*), 3.21 (br s, 1H, *H*-CB$_{11}$Cl$_{11}$), 1.52 (vt, J_{P-H} = 10 Hz, 36H, -C(C*H*$_3$)$_3$). ^{31}P{^{1}H} NMR (CD_2Cl_2): δ 180.4 (J_{Pt-P} = 2534 Hz).

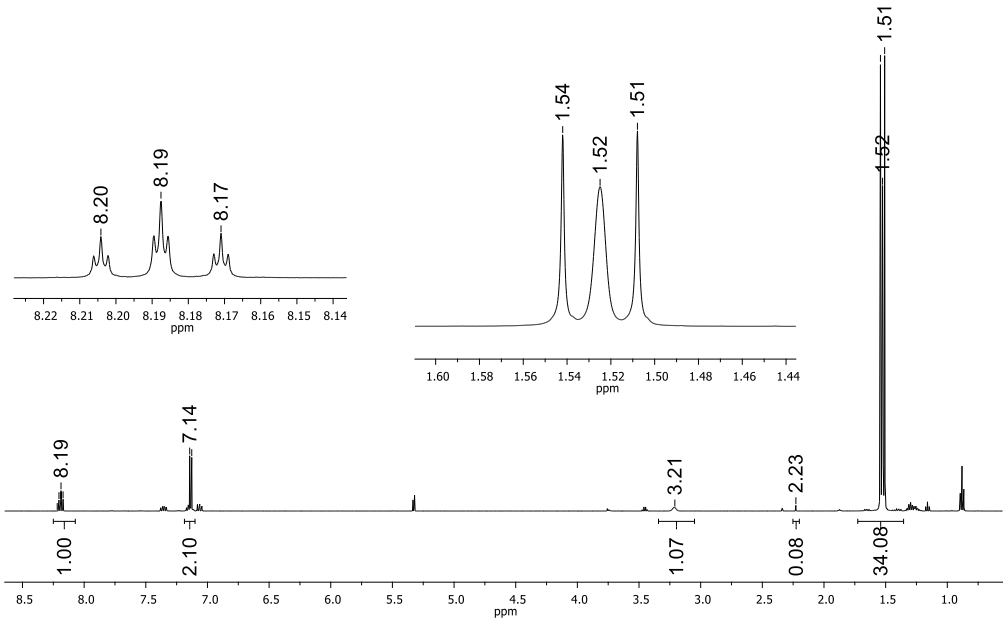

Figure 3.69 ^{1}H NMR spectrum for [PONOP-Pt-Cl][$HCB_{11}Cl_{11}$] **322** measured on a 500-MHz Varian NMRS at RT.

Protonation of 320 in C_6H_5F to Give 323. 320 (22 mg, 0.019 mmol) and [$H(C_6H_3(CH_3)_3)$][$^{n}BuCB_{11}Cl_{11}$]·0.3($C_6H_3(CH_3)_3$) (15 mg, 0.020 mmol) were combined as solids in a J. Young NMR tube in base-free box. Fluorobenzene was added making a yellow homogeneous solution. No immediate changes were observed at RT. After 2 h at 80 °C, at least two new compounds were observed by $^{31}P\{^{1}H\}$ NMR spectroscopy, with the starting material accounting for approximately 55% of the reaction mixture. A new triplet was observed by ^{19}F NMR spectroscopy at –87.7 ppm (J_{Pt-F} = 296 Hz, Figure 3.71) and free methane was apparent from the ^{1}H NMR spectrum in C_6H_5F. An additional 6 days at RT yielded a product mixture consistenting of approximately 22% starting

material, 56% of what is believed to be **323**, and 22% of unidentified products (Figure 3.70).

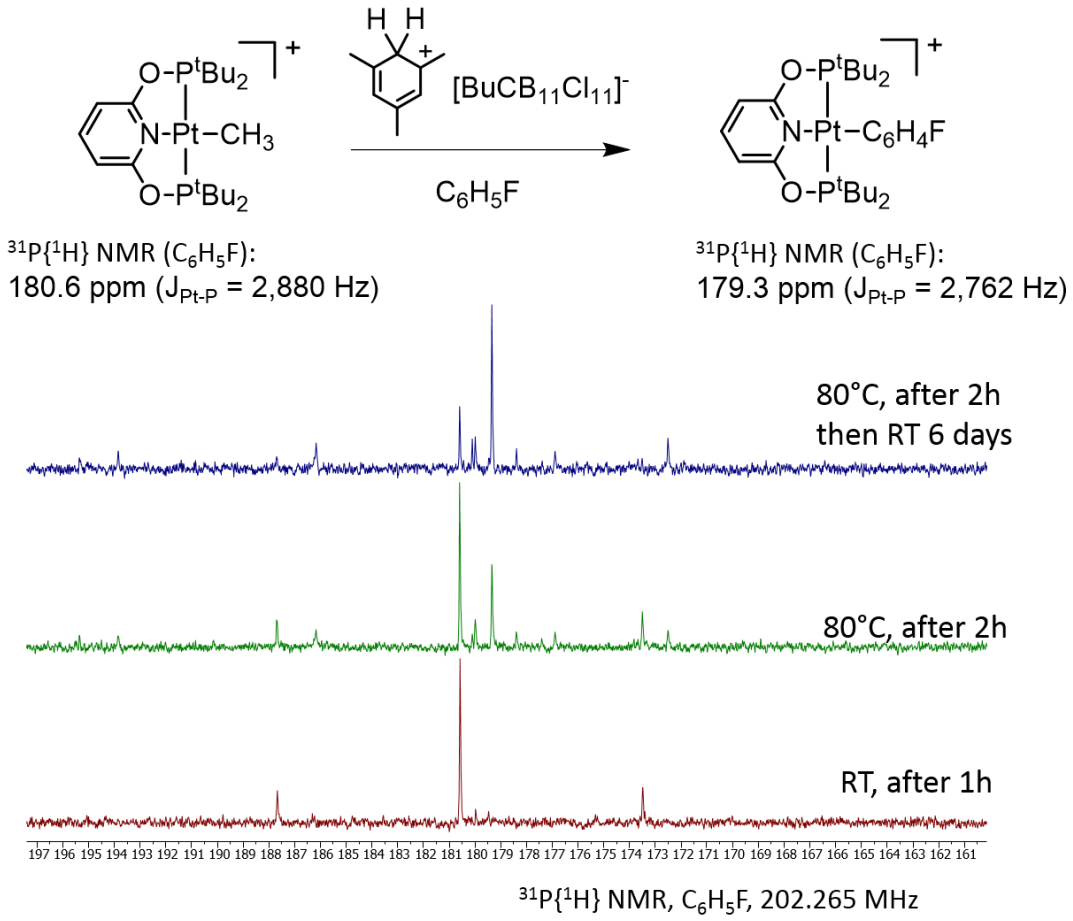

Figure 3.70 $^{31}P\{^{1}H\}$ NMR stack spectra for protonation of **320** to give **323** measured on a 500-MHz Varian NMRS.

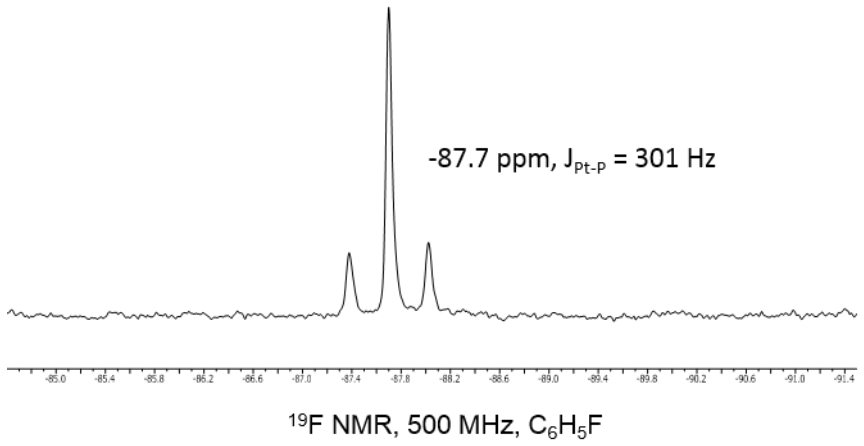

Figure 3.71 ^{19}F NMR spectrum for product of the protonation of **320**, measured on a 500-MHz Varian NMRS.

IV. CYCLOMETALLATION OF THE NNN PINCER LIGAND IN COMPLEXES OF PLATINUM[*]

4.1 Introduction

Pincer complexes have gained in popularity in part because they offer a robust and well-defined framework for study of elementary reactions at transition metal centers.[106,165] Our group, among many others, has been particularly attracted to pincer ligands based on the diarylamido central unit with *ortho*-positioned side donors (Chart 4.1).[125,173-176,210-216] They provide a semi-rigid framework for binding transition metals while the amido donor may display redox[114,196,197,217] or acid/base[114,180,218] non-innocence. Carbazole can be regarded as a special diarylamine with greatly reduced basicity of the amido donor and increased rigidity of the ligand backbone.[191,219-222] We recently explored[223] Pd complexes of the bis(imino)carbazolyl (NNN) pincer ligand pioneered by Gibson *et al*.[224-226] Here we report the synthesis of NNN complexes of Pt, and observations of unexpectedly facile cyclometallation.

[*] Portions of this chapter have been submitted to Inorganic Chemistry Frontiers and are reprinted with permission from "Cyclometallation of the NNN Pincer Ligand in Complexes of Platinum" by DeMott, J. C.; Dekarske, J. R.; McCulloch, B. J.; Ozerov, O. V., *Inorg. Chem. Front.* Submitted manuscript, **2015**.

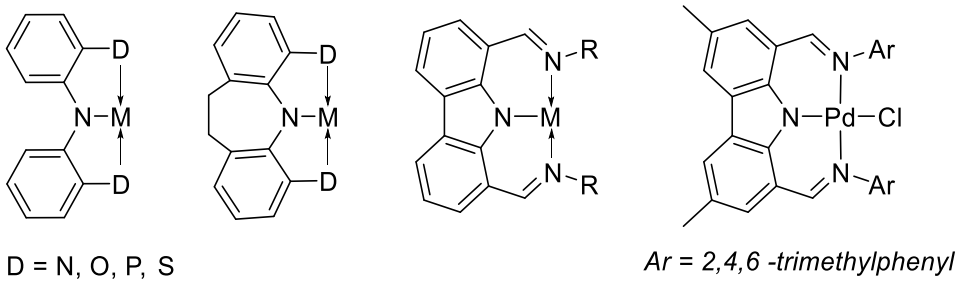

Chart 4.1 Examples of diarylamido based pincer complexes.

4.2 Results and Discussion

Thermolysis of (NNN)Me with $(MeCN)_2PtCl_2$ in mesitylene for 24 h at reflux led to the formation of (NNN)PtCl (**401**) that was isolated in 41% yield (Scheme 4.1). Although it required considerably more forcing conditions, this preparation mimicked the synthesis of (NNN)PdCl,[118] and also the related syntheses of PNP pincer complexes of group 10 metals by N-Me cleavage.[175]

To assess the oxidation potential of the (NNN)PtCl relative to (NNN)PdCl, cyclic voltammery was performed on a 0.2 mM solution of (NNN)PtCl in CH_2Cl_2 with $[Bu_4N][PF_6]$ as the supporting electrolyte. The quasi-reversible oxidation of (NNN)PtCl was observed at $E_{1/2}$ = 0.65 V (vs Fc/Fc^+). This is very similar to the $E_{1/2}$ = 0.72 V (vs Fc/Fc^+) found for (NNN)PdCl[223] and provides support for a ligand based oxidation.

The synthesis of (NNN)PtMe (**402**) was accomplished by treatment of **401** with MeMgCl in toluene followed by heating the mixture at 80 °C for 20 h, with a 74% isolated yield. **401** and **402** displayed the expected C_{2v} symmetry in their ^1H and ^{13}C NMR spectra. The Pt-bound Me group in **402** gave rise to singlet resonances in the ^1H NMR (δ 0.32

ppm) and $^{13}C\{^{1}H\}$ NMR (–10.5 ppm) spectra with the expected satellite peaks from coupling to ^{195}Pt ($^{2}J_{Pt\text{-}H}$ = 70 Hz, $^{1}J_{Pt\text{-}C}$ = 772 Hz).

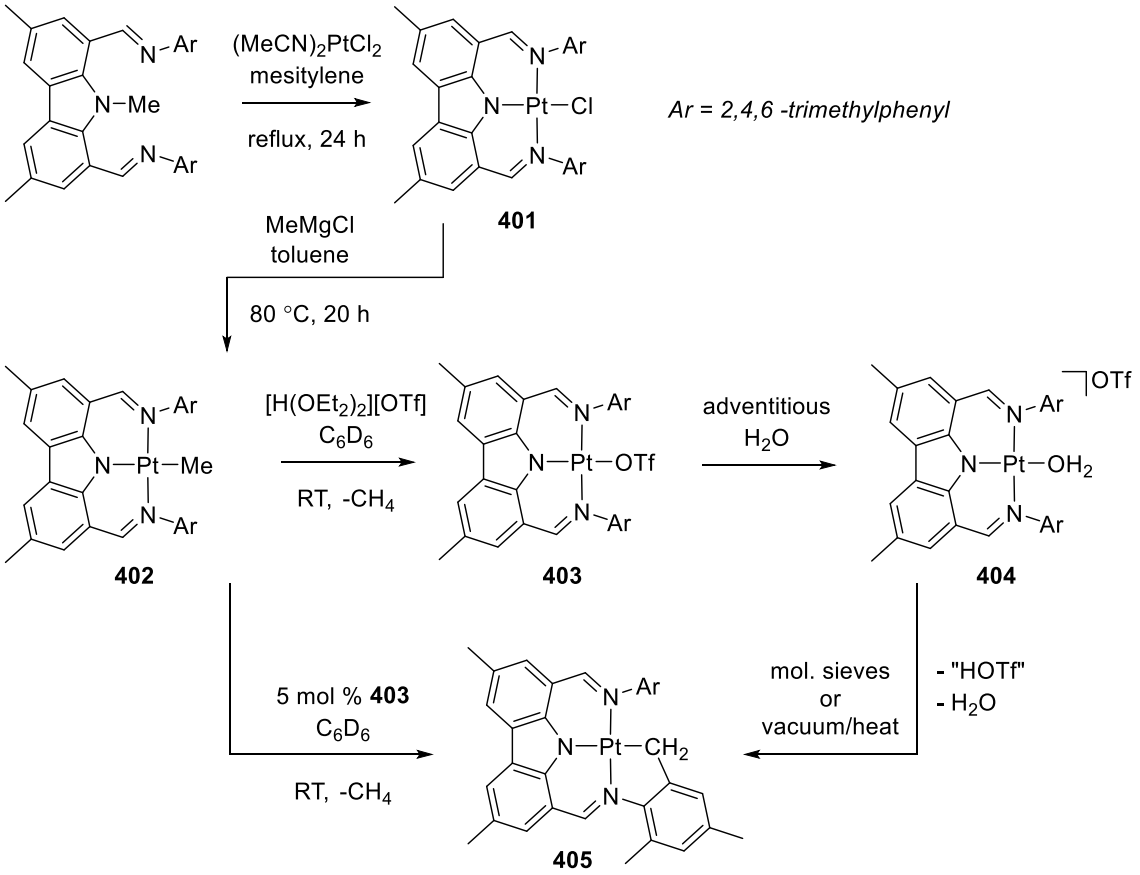

Scheme 4.1 Syntheses and reactivity of (NNN)Pt complexes.

A suspension of **402** in benzene rapidly reacted with one equiv of triflic acid (in an ether solution) to lose methane and produce (NNN)PtOTf, **403**. When the reaction was performed under thoroughly dry conditions, 89% yield of pure **403** was isolated. It was noticed that in some reactions an impurity was present that was identified as the water

adduct [(NNN)Pt-OH_2][OTf] **404**. We previously noted an analogous water adduct formation in the synthesis of the Pd analog (NNN)PdOTf.[223] However, unlike in the Pd case, molecular sieves or application of vacuum were not effective at removing water from **404** and (re)generating **403**. A small sample of the pure water adduct **404** was isolated following passing crude **403** through silica gel. The ^{1}H NMR signal corresponding to the coordinated water molecule was observed at 4.86 ppm in C_6D_6. We were able to obtain two single crystals of **404** with different co-crystallized molecules: one contained a molecule of benzene in the asymmetric unit, while the other contained half of a disordered molecule of fluorobenzene as well as a molecule of triflic acid (Figure 4.1 and Figure 4.2). Triflic acid appears to be hydrogen bonded to the triflate anion of **404**. The presence of HOTf was confirmed by its observation in the NMR spectrum of the dissolved crystals from the same batch. The geometries of the central **404** cations in both structures are very similar. The corresponding Pt-N and Pt-O distances are statistically indistinguishable while the angles about Pt define a nearly perfect square planar environment with only 0–2° differences between the two structures. Similar to the structure of (NNN)PdCl, the NNN ligand is nearly perfectly planar and π-stacking of the carbazole units is evident in the solid-state structures of **404**.

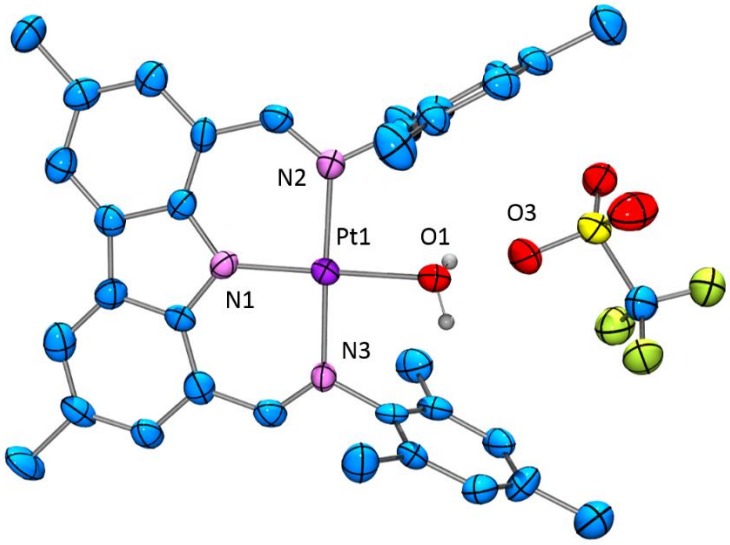

Figure 4.1 ORTEP drawing (50% probability ellipsoids) of **404**·C_6D_6. Omitted for clarity: H atoms and C_6D_6. Selected distance (Å) and angles (deg) follow: Pt1-O1, 2.078(6); Pt1-N1, 1.933(6); Pt1-N2, 2.018(6); Pt1-N3, 2.023(6); N2-Pt1-N3, 177.1(2); N1-Pt1-O1, 175.7(2); N1-Pt1-N2, 91.0(3); N1-Pt1-N3, 90.5(3); N2-Pt1-O1, 87.9(2); N3-Pt1-O1, 90.8(2).

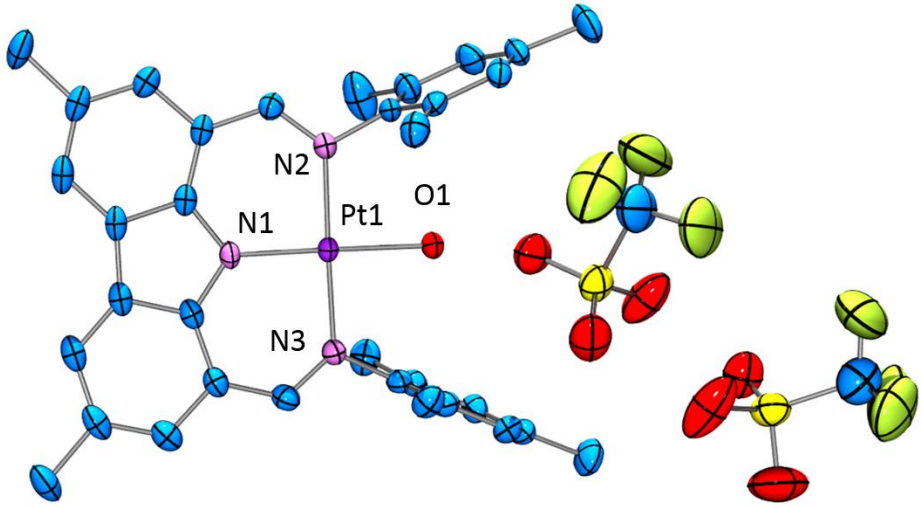

Figure 4.2 ORTEP drawing (50% probability ellipsoids) of **404**·HOTf·½C_6H_5F. Omitted for clarity: H atoms and C_6H_5F. Selected distance (Å) and angles (deg) follow: Pt1-O1, 2.088(2); Pt1-N1, 1.938(3); Pt1-N2, 2.021(3); Pt1-N3, 2.012(3); N2-Pt1-N3, 178.35(11); N1-Pt1-O1, 178.63(11); N1-Pt1-N2, 90.84(12); N1-Pt1-N3, 90.82(12); N2-Pt1-O1, 90.16(10); N3-Pt1-O1, 88.18(11).

Treatment of **403**/**404** mixtures with molecular sieves or heating under vacuum led to the appearance of a new Pt product in the mixture, which was identified as cyclometallated (κ^4-*NNN*-2,4-$Me_2C_6H_2CH_2$)Pt (**405**). **405** arises from cyclometallation of one of the mesityl substituents with formal loss of triflic acid from **403**. We were able to prepare pure **405** by treatment of **403** with Et_3N in benzene at ambient temperature. The ^1H and ^{13}C NMR spectra of **405** are consistent with partial loss of symmetry associated with cyclometallation. The equivalent protons of the Pt-bound CH_2 group resonate at δ 2.35 ppm in C_6D_6. The ^{195}Pt NMR chemical shifts[227] of **402** (–2483 ppm) and **405** (–2589 ppm) are quite similar, and distinct from those of **401** (–1849 ppm) and **403** (–1493 ppm). Interestingly, we found that **403** serves as the catalyst for cyclometallation of **402**. The latter is indefinitely stable in C_6D_6 solutions at ambient temperature, but addition of 5% **403** led to the appearance of 15% of **405** and free methane within 5 min (and 80% conversion to **405** after 18 h). Since **403** loses HOTf under vacuum and to a weak base such as water, it seems plausible that **402** can serve as the base to promote cyclometallation of **403** to **405** by accepting the formal equivalent of HOTf, evolving methane and regenerating **403**.

The solid-state structure of **405** was determined by X-ray diffraction methods (Figure 4.3. The coordination environment about Pt is approximately square-planar and is defined by the tetradentate cyclometallated NNN ligand. With the exception of the intact mesityl group, this molecule possesses a remarkably flat extended conjugated system about the Pt center. Not surprisingly, molecules of **405** in the solid state display extensive π-stacking (Figure 4.3).

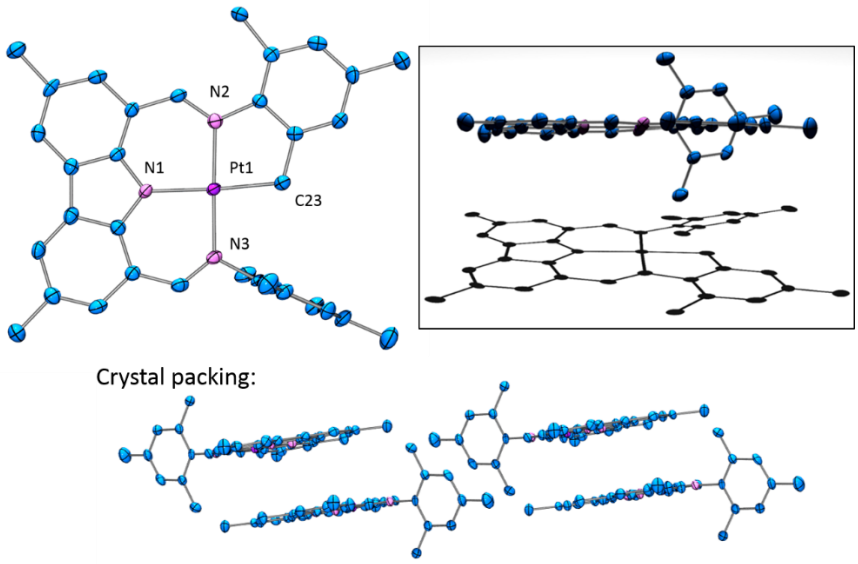

Figure 4.3 ORTEP drawing (50% probability ellipsoids) of **405**. Omitted for clarity: H atoms. Selected distance (Å) and angles (deg) follow: Pt1-C23, 2.027(5); Pt1-N1, 2.007(4); Pt-N2, 2.011(4); Pt-N3, 2.012(4); N2-Pt1-N3, 178.37(15); N1-Pt1-C23, 176.43(16); N1-Pt1-N2, 92.89(16); N1-Pt1-N3, 88.70(16); N2-Pt1-C23, 83.59(18); N3-Pt1-C23, 94.82(18).

Mesityl is a common substituent on a nitrogen atom in polydentate ligands. Cyclometallation of an N-mesityl moiety is well documented in the chemistry of early transition,[228-231] lanthanide,[232] and main group[233-235] metals. However, it is quite rare for late metals[236-238] and the existing examples have not been formed by electrophilic cyclometallation observed in **403**. On the other hand, cyclometallation of the NNN ligand in this work can be related to the literature examples of intermolecular C-H activation by Pt^{II}-OTf complexes of amido-based pincer ligands (Scheme 4.2). In those examples from Peters,[167] Liang,[168] and our own work,[218] activation of aromatic solvents proceeded

sluggishly at elevated temperatures in contrast to the rapid ambient-temperature C-H activation of **403**.

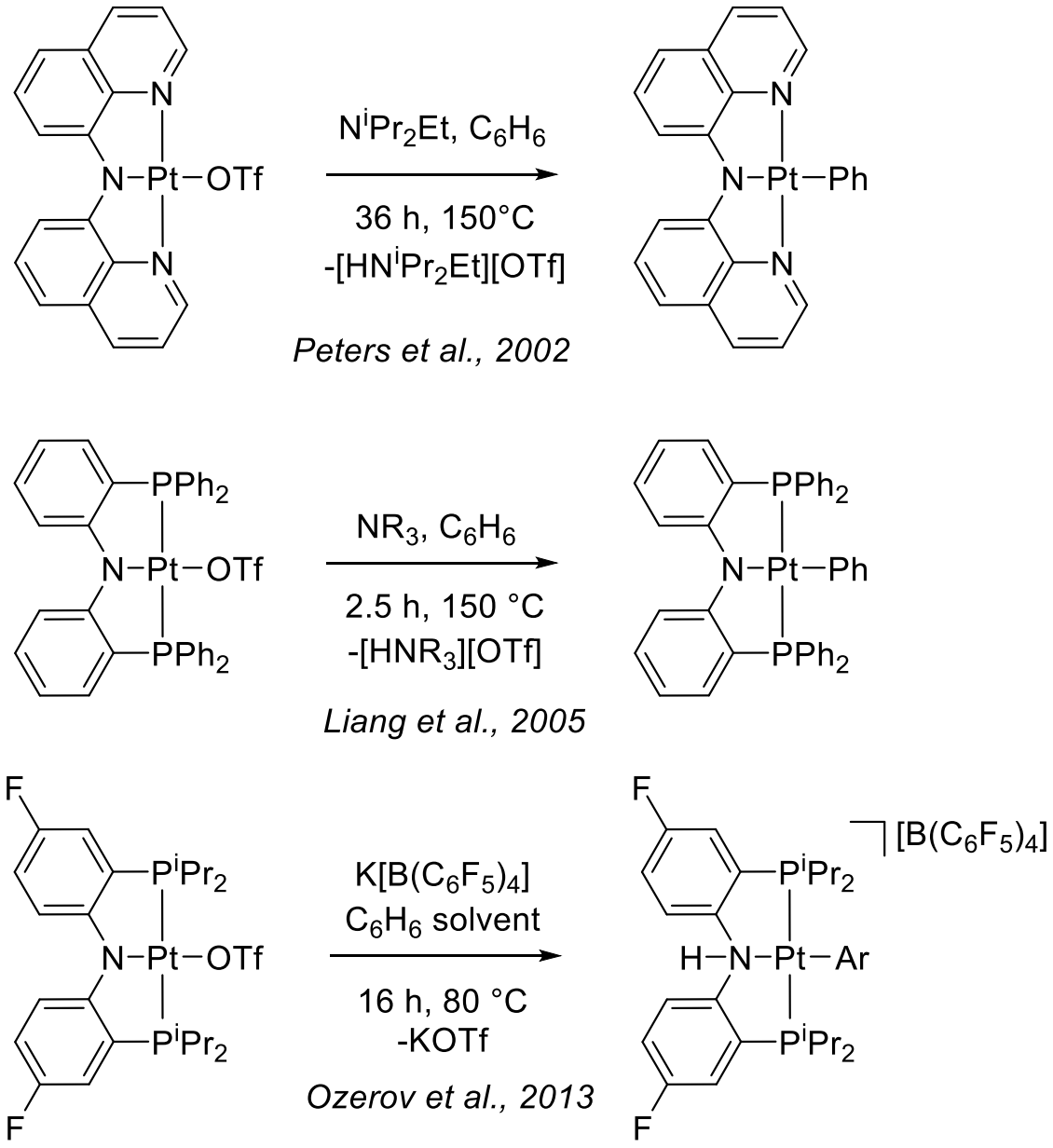

Scheme 4.2 C–H activation of benzene by (XNX)Pt-OTf pincer complexes.

While the intramolecular nature of the reaction in **403** cannot be underestimated, it is worth pointing out that the examples in Scheme 4.2 were judged to proceed by a dissociative mechanism. This loss of triflate may be more facile in the NNN system as evidenced by the ready displacement of it by water (for both Pt and Pd), which is not observed for the corresponding PNP complexes. The steric bulk projected by the mesityl groups of the NNN ligand towards the non-pincer coordination site at the square planar metal center may be favouring coordination of smaller ligands (e.g., water). We hypothesize that evolution of the NNN ligand aimed at preventing cyclometallation while preserving strong steric pressure on the reactive site may lead to exciting intermolecular reactivity, and this will be a subject of future studies.

4.3 Synthesis of (NNN)Pt(IV) Complexes

An alternative route to **403** would involve the reaction of **402** with an alkyl-triflate, forming **403** upon C-C reductive elimination. Surprisingly the reaction of **402** with MeOTf in C_6D_6 at room temperature resulted in the formation of the Pt(IV) cyclometallated species **406** (Scheme 4.3). Monitoring the reaction by ^{1}H NMR spectroscopy demonstrated the formation of free methane instead of the expected formation of ethane. While we were unable to obtain a crystal structure for **406**, ^{1}H NMR spectroscopy revealed a C_1 symmetric species possessing a Pt bound methyl group (1.09, $J_{Pt\text{-}H}$ = 81 Hz) in addition to two diasterotopic Pt-CH_2 hydrogens (3.77, $J_{H\text{-}H}$ = 15 Hz, $J_{Pt\text{-}H}$ = 90 Hz and 2.54, $J_{H\text{-}H}$ = 15 Hz) resulting from the cyclometallation of a mesityl group. The ^{19}F NMR chemical shift for the triflate group was consistent with an outer sphere anion, suggesting

the species has a five-coordinate Pt center. The ^{195}Pt NMR chemical shift (–1277 ppm) is significantly downfield relative to the Pt(II) cyclometallated species (–2589 ppm) and within the expected region for Pt(IV) species.[227] Similar results were observed for the reaction of EtOTf with **402** yielding the Pt(IV) cyclometallated ethyl species **407** (Scheme 4.3).

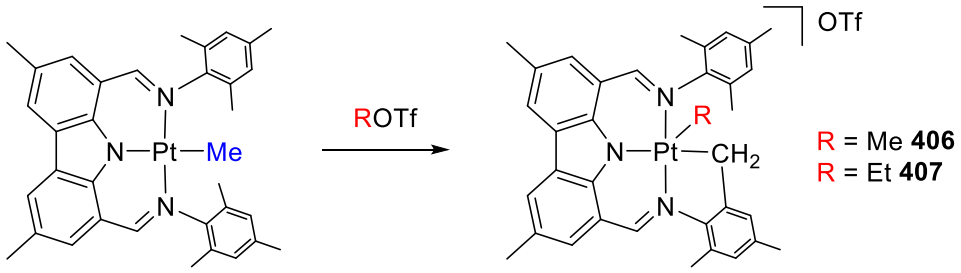

Scheme 4.3 Synthesis of **406** and **407**.

Retention of the ethyl group in the formation of **407** prompted us to question whether or not these species were the result of Pt(IV) C-H activation. While Pt(II) C-H activation is well known, Pt(IV) C-H activation is rare.[239-243] Generally speaking, two pathways to the Pt(IV) cyclometallated products can be envisioned (Scheme 4.4). In the first pathway, the unsaturated Pt(II) metal center is responsible for C-H activation and in the second pathway, the C-H activation occurs at the open coordination site of the Pt(IV) metal center. Again, retention of the ethyl group initially appeared to be strong support for the Pt(IV) pathway.

Seeking to examine whether or not the reaction of **402** with HOTf could be the result of Pt(IV) C-H activation, a deuterium labelling study was conducted. Reaction of **402** with DOTf in C_6D_6 led to the observation of 1:4 mixture of CH_3D:CH_4 (Scheme 4.4). This suggests that the predominant "H" source was the mesityl sidearm and not DOTf, consistent with a Pt(IV) C-H activation pathway. ^{2}H NMR spectroscopy demonstrated that deuterium was only incorporated into the *ortho* methyl group of the mesityl sidearm. This observation is also consistent with Pt(IV) C-H activation although quantification of the deuterium incorporation needs to be studied further.

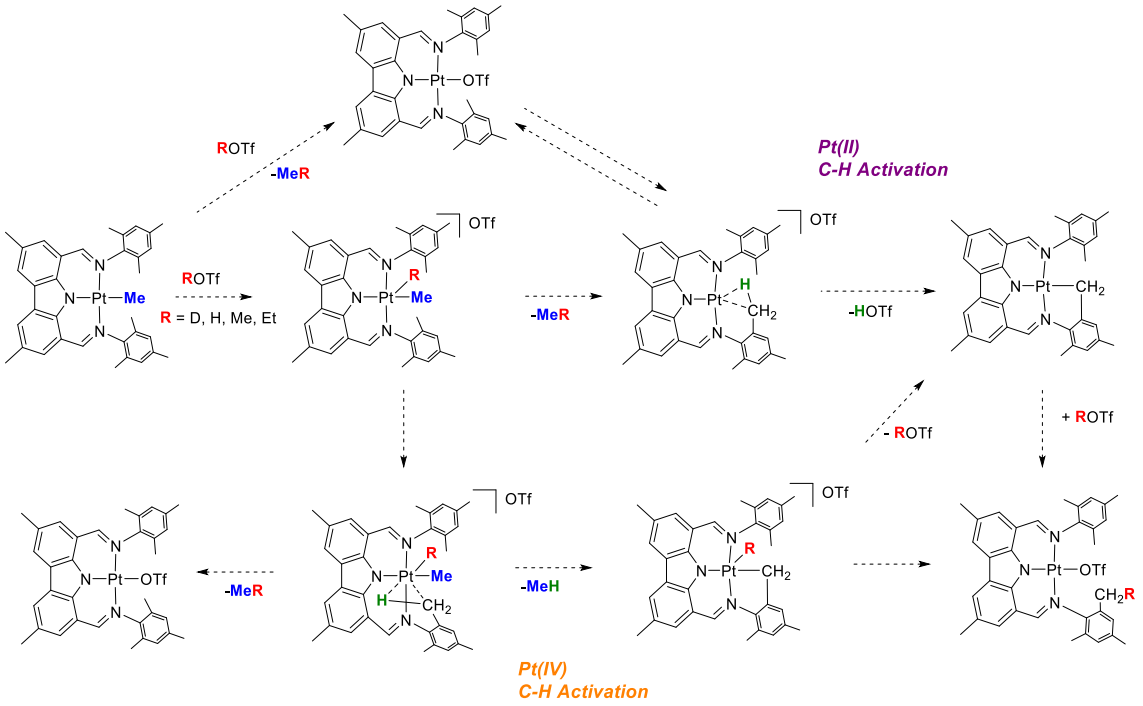

Scheme 4.4 Proposed mechanistic pathways for Pt(II) versus Pt(IV) C-H activation.

Caution needs to be taken in interpreting the results of **402** protonation in terms of the ratio of CH_3D/CH_4 formation. Very high KIEs (~20) have been reported for the addition of H+/D+ to Pt-alkyl.[244] The significant kinetic preference for HOTf versus DOTf reactivity could result in the inflation of the amount of CH_4 produced due to the presence of minor HOTf impurities that will kinetically out-compete the more abundant DOTf. Minor HOTf impurities could also be an alternative explanation for the formation of methane in the reaction of **402** with MeOTf or EtOTf. To assess if HOTf impurities played a role in the synthesis of **406** or **407**, their syntheses were performed with and without a base present.

The reaction of **402** with HOTf is very fast (15 min) relative to the reaction with MeOTf (2 h) and EtOTf (16 h). If minor amounts of HOTf played a significant role in the reaction of MeOTf or EtOTf, we would expect to observe differences in the rate of product formation with base versus without base. Monitoring the reaction of MeOTf with or without 2,6-di-*tert*-butylpyridine, the rates of product formation were not significantly different. However, while methane was observed with only a trace amount of ethane for the reaction without base, methane and ethane were observed in comparable amounts for the reaction with base. Within the first 20 minutes the only species observed in the ^1H NMR spectrum for both reactions were starting material and what is believed to be $[(NNN)PtMe_2][OTf]$ (**408**).

Additionally, if there was a significant about of HOTf impurity we would have expected to see **403** during the course of the reaction. In both cases, **403** is a component of the final reaction mixture (3:1 ratio for no base:base) but it is unclear if it is the result

of alkane RE to form **403**, or if **402** could serve as a base to remove the mesityl proton from a Pt(IV) species to give methane and **403**. No significant rate differences were observed in the analogous reactions with EtOTf, and further study is needed to elucidate whether or not a Pt(IV) C-H activation pathway is at play.

4.4 Conclusions

In summary, a series of Pt complexes supported by a bis(imino)carbazolyl pincer ligand possessing mesityl sidearms has been synthesized. Comparison to the previously reported (NNN)PdCl,[223] demonstrates very similar metrics, redox potentials, and facile displacement of triflate by water at the metal center. This behavior is in contrast to that observed for analogous (PNP)MOTf complexes and is believed to result from the alternative steric profile and extended steric bulk of the mesityl groups. Surprisingly, weak bases including **402** in the presence of a catalytic amount of **403** were observed to consume an equivalent of HOTf to form the cyclometallated mesityl complex **405** through facile intramolecular C-H activation at room temperature.

4.5 Experimental

4.5.1 General Considerations and Physical Methods

Unless otherwise noted, all manipulations and reactions were performed under argon, using standard glovebox and Schlenk line techniques. Toluene, triethylamine, pentane, and C_6D_6 were dried over NaK/Ph_2CO/18-crown-6, distilled and stored over molecular sieves in an Ar-filled glovebox. Diethyl ether was dried and deoxygenated (by

purging) using a solvent purification system and stored over molecular sieves in an Ar-filled glovebox. Fluorobenzene and CH_2Cl_2 were dried over CaH_2, distilled, and stored over molecular sieves in an Ar-filled glovebox. Portions of the experimental work were carried out in collaboration with John Dekarske. X-ray data solutions and refinement were conducted by Billy McCulloch.

NMR spectra were recorded on a Varian iNova 300 spectrometer (^{1}H NMR, 299.956 MHz, ^{13}C NMR, 75.433 MHz, ^{19}F NMR, 282.214 MHz, ^{31}P NMR, 121.426 MHz), a Varian iNova 400 spectrometer (^{1}H NMR, 399.497 MHz, ^{31}P NMR, 161.737 MHz, ^{13}C NMR, 100.465 MHz, ^{195}Pt NMR, 85.474 MHz) and a Varian iNova 500 spectrometer (^{1}H NMR, 499.678 MHz, ^{13}C NMR, 125.670 MHz, ^{19}F NMR, 470.125 MHz, ^{31}P NMR, 202.276 MHz) in noted solvents. Chemical shifts are given in δ (ppm). ^{19}F NMR spectra were referenced externally using CF_3COOH at δ –78.5 ppm. ^{31}P NMR spectra were referenced externally with 85% phosphoric acid at δ 0. ^{195}Pt NMR spectra were referenced externally with K_2PtCl_4 aqueous solution at δ –1620. ^{1}H NMR and ^{13}C NMR spectra were referenced using the solvent signals. Elemental analyses were performed by CALI, Inc. (Parsippany, NJ).

4.5.2. Synthesis and Characterization of Pt Complexes

4.5.2.1 Synthesis of Pt Complexes

(NNN)PtCl (401). (NNN)Me[223] (3.12 g, 6.25 mmol) was dissolved in approximately 150 mL mesitylene. $(MeCN)_2PtCl_2$[245] (2.17 g, 6.23 mmol) was added to the 250-mL Schlenk flask. Reaction was put under reflux in an oil bath at 180 °C for 24

h. Reaction changed color from yellow to brown-orange after approximately an hour sitting in the oil bath. Volatiles were removed by vacuum. The resulting oily brown residue was filtered through Celite and silica gel using toluene. Volatiles were removed under vacuum which yielded an orange powder. Solid was filtered off and washed with cold pentane (3 × 10 mL). Yield: 1.8 g, 41%. ^{1}H NMR (300 MHz, C_6D_6, Figure 4.4): δ 8.16 (s, 2H, Ar-*H*), 8.15 (s, 2H, N=C*H*), 7.10 (s, 2H, Ar-*H*), 6.84 (s, 4H, Ar-*H*), 2.45 (s, 6H, Ar-C*H*$_3$), 2.32 (s, 12H, Ar-C*H*$_3$), 2.18 (s, 6H, Ar-C*H*$_3$). ^{13}C{^{1}H} NMR (75.4 MHz, $CDCl_3$, Figure 4.5): δ 157.8 (C=N), 151.8 (CAr), 136.2 (CAr), 135.7 (CAr), 131.3 (CAr), 130.9 (CAr), 128.4 (CAr), 128.0 (CAr), 125.6 (CAr), 117.1 (CAr), 21.5 (Ar-CH_3), 21.0 (Ar-CH_3), 18.5 (Ar-CH_3). ^{195}Pt NMR (85.7 MHz, $CDCl_3$, Figure 4.6): δ –1849. Elem. An. Found (Calculated) for $C_{34}H_{34}N_3PtCl$: C, 57.07 (57.10); H, 4.73 (4.79)%.

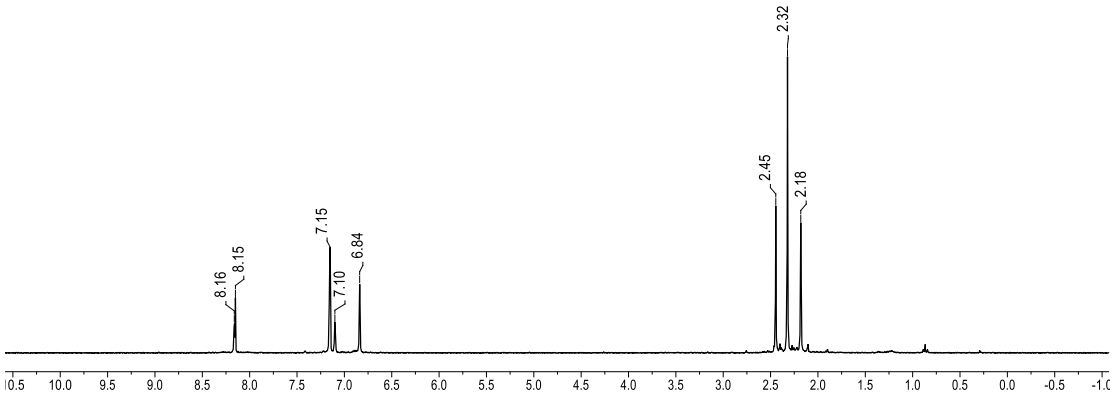

Figure 4.4 ^{1}H NMR spectrum of **401** in C_6D_6 at 23 °C measured on a 300-MHz Varian iNova.

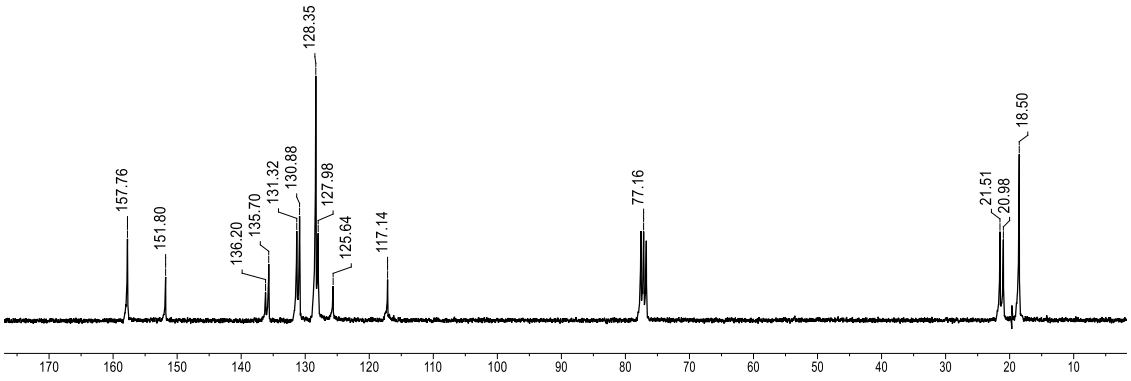

Figure 4.5 $^{13}C\{^{1}H\}$ NMR spectrum of **401** in $CDCl_3$ at 23 °C measured on a 300-MHz Varian iNova.

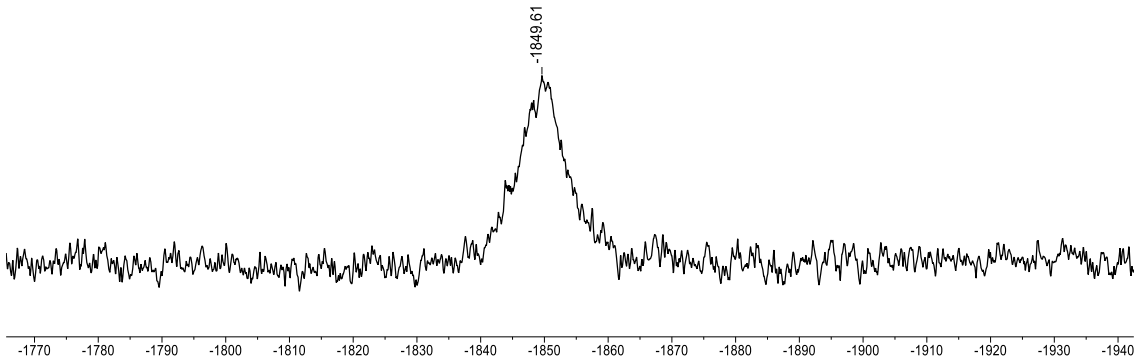

Figure 4.6 $^{195}Pt\{^{1}H\}$ NMR spectrum of **401** in $CDCl_3$ at 23 °C measured on a 400-MHz Varian iNova.

(NNN)PtMe (402). **401** (0.196 g, 0.274 mmol) was dissolved in approximately 30 mL toluene. MeMgCl (0.90 mL, 2.7 mmol) was added to flask via syringe. Flask was heated in oil bath at 80 °C for 20 h. The product was filtered through Celite and silica gel using toluene. Volatiles were removed under vacuum yielding a red powder. The solid

was collected without further purification. Yield: 141 mg, 73.6%. ^{1}H NMR (300 MHz, C_6D_6, Figure 4.7): δ 8.50 (s, 2H, N=C*H*), 8.33 (s, 2H, Ar-*H*), 7.26 (s, 2H, Ar-*H*), 6.83 (s, 4H, Ar-*H*), 2.53 (s, 6H, Ar-CH_3), 2.24 (s, 12H, Ar-CH_3), 2.19 (s, 6H, Ar-CH_3), 0.32 (s, 3H, J_{Pt-H}= 69.6 Hz, Pt-CH_3). ^{1}H NMR (300 MHz, CD_2Cl_2, Figure 4.8): δ 8.79 (s, 2H, J_{Pt-H} = 98 Hz, N=C*H*), 8.56 (s, 2H, Ar-*H*), 7.73 (s, 2H, Ar-*H*), 6.93 (s, 4H, Ar-*H*), 2.72 (s, 6H, Ar-CH_3), 2.32 (s, 6H, Ar-CH_3), 2.13 (s, 12H, Ar-CH_3), –0.39 (s, 3H, J_{Pt-H}= 70.5 Hz, Pt-CH_3). ^{13}C{^{1}H} NMR (100.5 MHz, $CDCl_3$, Figure 4.9): 158.0 (C=N), 151.2 (CAr), 138.77 (CAr), 135.5 (CAr), 131.0 (CAr), 130.8 (CAr), 128.4 (CAr), 127.4 (CAr), 127.0 (CAr), 117.6 (CAr), 21.7 (Ar-CH3), 20.9 (Ar-CH3), 18.1 (Ar-CH_3), −10.5 (s, J_{Pt-C} = 772 Hz, Pt-Me). ^{195}Pt NMR (85.7 MHz, CD_2Cl_2, Figure 4.10): δ –2483. Elem. An. Found (Calculated) for $C_{35}H_{37}N_3Pt$: C, 60.53 (60.51); H, 5.46 (5.37)%.

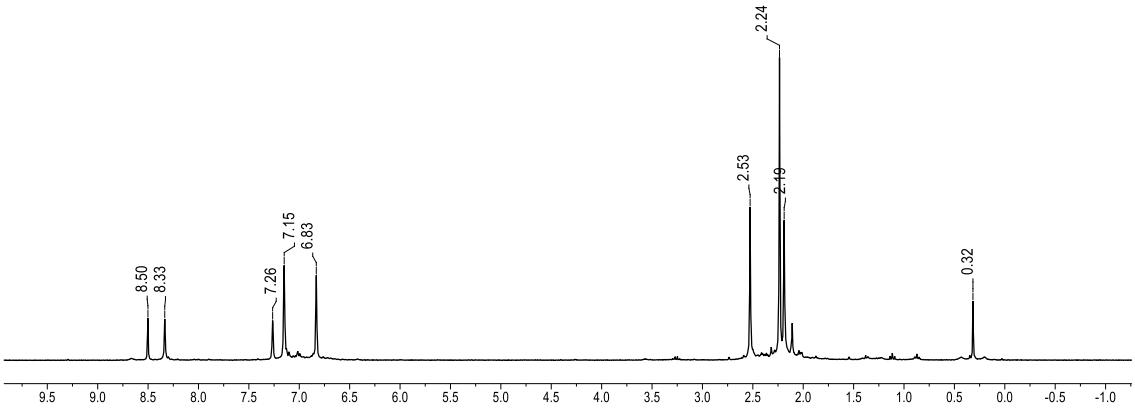

Figure 4.7 ^{1}H NMR spectrum of **402** in C_6D_6 at 23 °C measured on a 300-MHz Varian iNova.

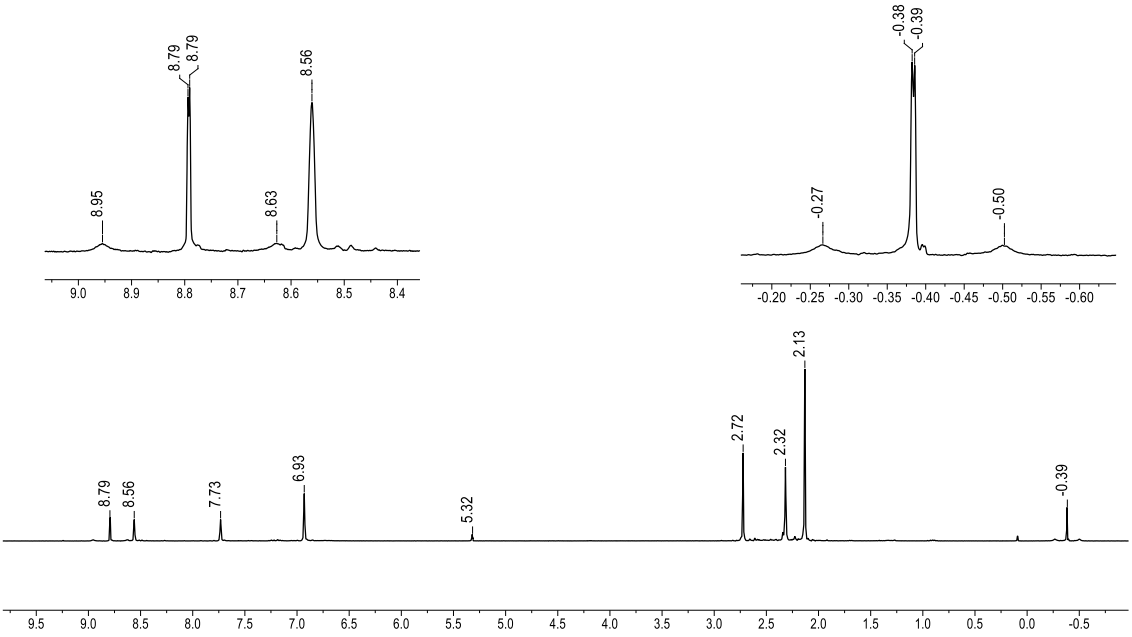

Figure 4.8 ^{1}H NMR spectrum of **402** in CD_2Cl_2 at 23 °C measured on a 300-MHz Varian iNova with insets showing ^{195}Pt coupling for N=C*H* and Pt-CH_3.

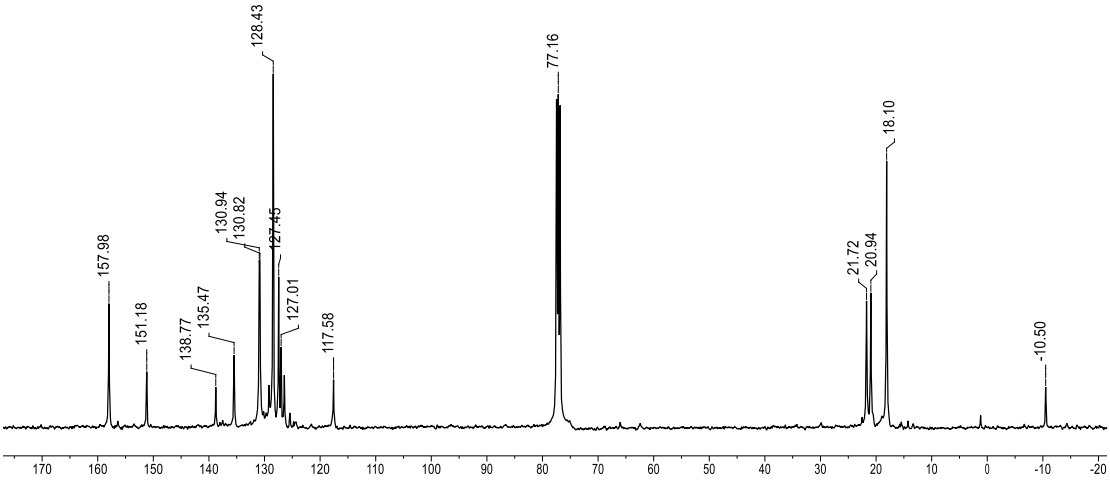

Figure 4.9 ^{13}C{^{1}H} NMR spectrum of **402** in $CDCl_3$ at 23 °C measured on a 300-MHz Varian iNova.

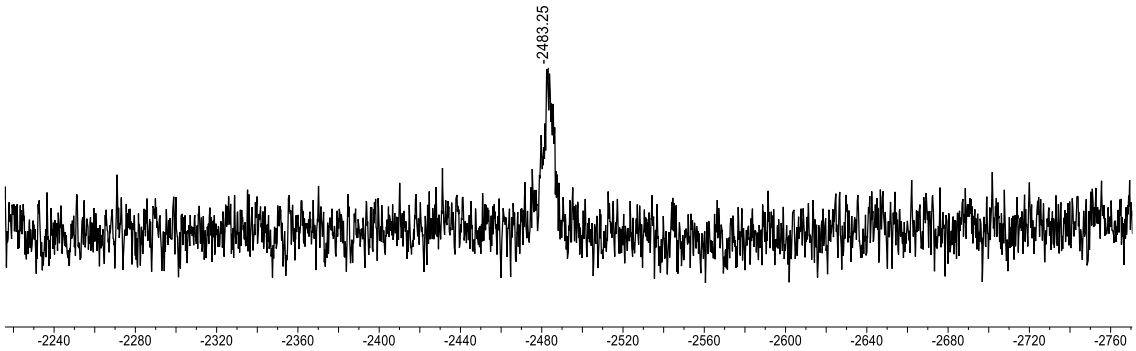

Figure 4.10 $^{195}Pt\{^{1}H\}$ NMR spectrum of **402** in $CDCl_3$ at 23 °C measured on a 400-MHz Varian iNova.

(NNN)PtOTf (403). 402 (64 mg, 0.092 mmol) was dissolved in C_6D_6 in a J. Young NMR tube forming a red solution with some solid remaining undissolved due to low solubility. HOTf (34 μL of 2.7 M solution in Et_2O, 0.092 mmol) was added via syringe and solution immediately became yellow-orange. In situ ^{1}H NMR analysis at 15 min showed the presence of free methane. Volatiles were removed yielding an orange solid. Solid was washed with cold pentane (3 × 1 mL) and dried under vacuum. Yield: 68 mg, 89%. ^{1}H NMR (300 MHz, C_6D_6, Figures 4.11 and 4.13): δ 8.04 (s, 2H, Ar-*H*), 7.83 (s, 2H, N=C*H*), 7.00 (s, 2H, Ar-*H*), 6.92 (s, 4H, Ar-*H*), 2.50 (s, 12H, Ar-CH_3), 2.41 (s, 6H, Ar-CH_3), 2.22 (s, 6H, Ar-CH_3). $^{13}C\{^{1}H\}$ NMR (75.4 MHz, C_6D_6, Figure 4.14): 160.7, 149.4, 136.7, 135.9, 132.4, 131.8, 129.4, 125.5, 117.0, 21.1, 21.0, 19.5, -*C*F_3 signal not resolved. ^{19}F NMR (282.2 MHz, C_6D_6, Figures 4.12 and 4.15): δ −77.78. ^{195}Pt NMR (85.7 MHz, C_6D_6, Figure 4.16): δ –1493. Elem. An. Found (Calculated) for $C_{35}H_{34}F_3N_3O_3SPt$: C, 50.57 (50.72); H, 4.18 (4.14)%.

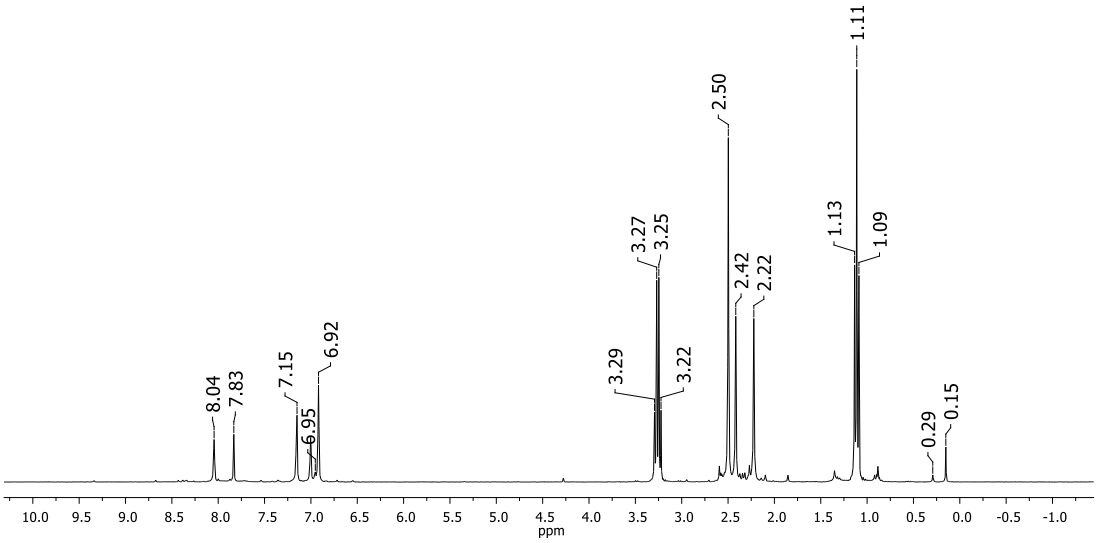

Figure 4.11 In situ ^{1}H NMR spectrum of **403** in C_6D_6 at 23 °C measured on a 500-MHz Varian iNova.

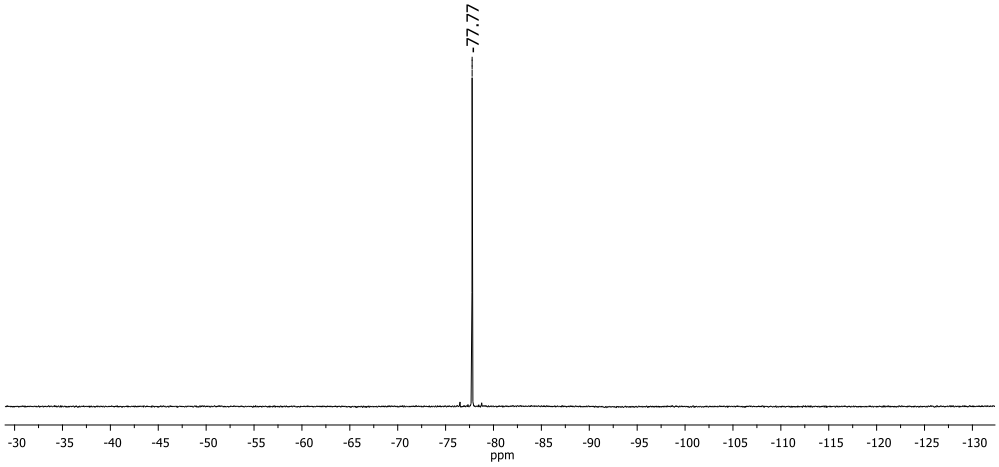

Figure 4.12 In situ ^{19}F NMR spectrum of **403** in C_6D_6 at 23 °C measured on a 300-MHz Varian iNova.

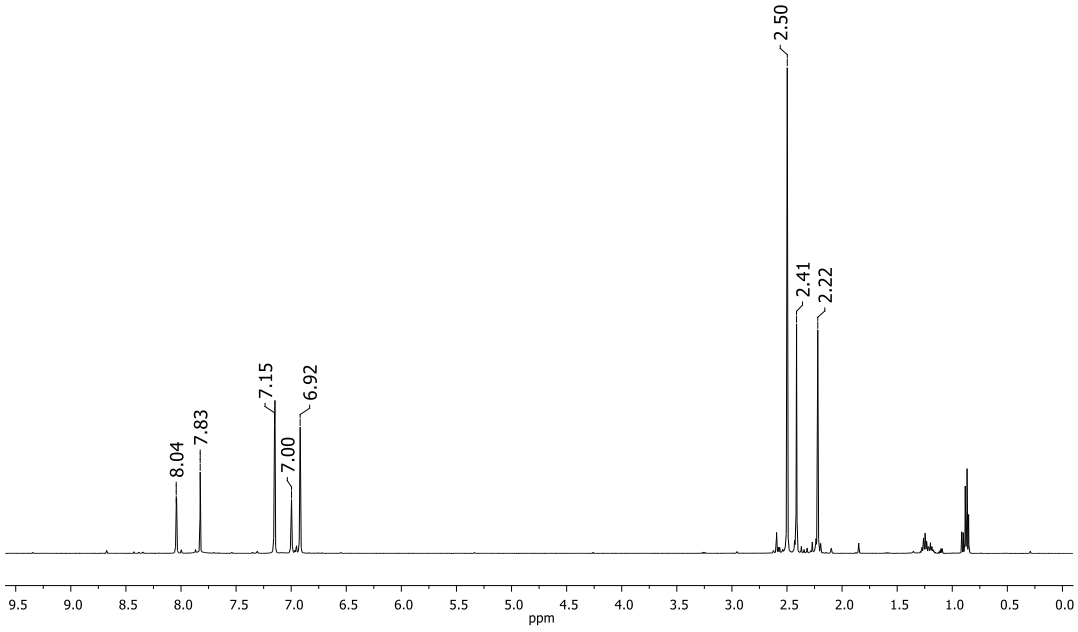

Figure 4.13 ^{1}H NMR spectrum of **403** in C_6D_6 at 23 °C measured on a 500-MHz Varian iNova.

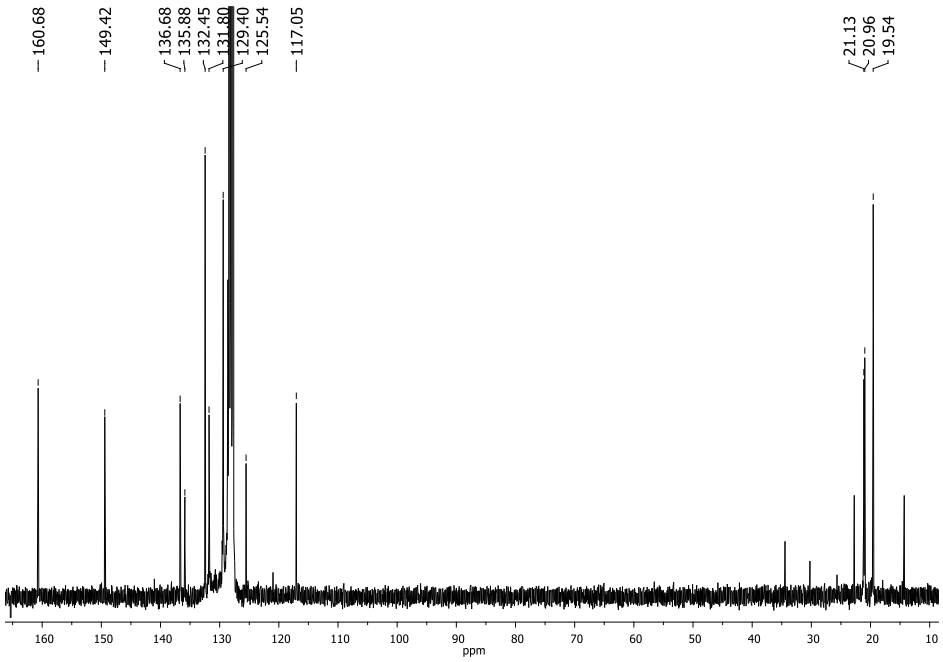

Figure 4.14 $^{13}C\{^{1}H\}$ NMR spectrum of **403** in $CDCl_3$ at 23 °C measured on a 300-MHz Varian iNova.

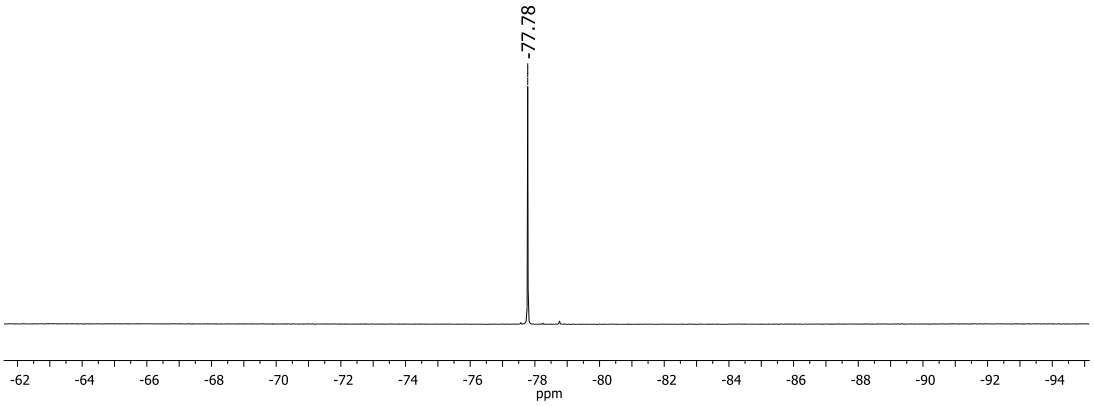

Figure 4.15 In situ ^{19}F NMR spectrum of **403** in C_6D_6 at 23 °C measured on a 300-MHz Varian iNova.

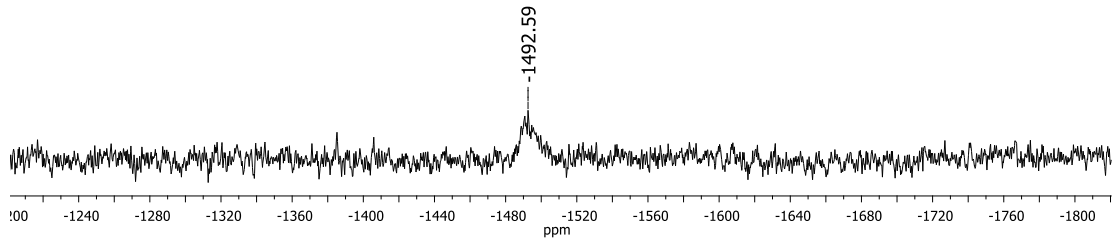

Figure 4.16 $^{195}Pt\{^1H\}$ NMR spectrum of **403** in $CDCl_3$ at 23 °C measured on a 400-MHz Varian iNova.

[(NNN)PtOH$_2$]OTf (404). 402 (0.14 g, 0.20 mmol) was dissolved in toluene in a 25 mL Schlenk flask. HOTf (0.10 mL, 0.20 mmol) was added via syringe. After 20 h at room temperature, volatiles were removed under vacuum yielding an orange solid. The solid was redissolved in fluorobenzene and filtered over Celite and silica gel using fluorobenzene. Orange crystals of **405** were obtained from a solution of fluorobenzene

layered with pentane. The supernatant was decanted from the crystals and the volatiles were removed generating a yellow-orange powder found to be **404**. ^{1}H NMR (300 MHz, C_6D_6, Figure 4.17): δ 8.07 (s, 2H, Ar-*H*), 7.73 (s, 2H, N=C*H*), 7.12 (s, 2H, Ar-*H*), 7.07 (s, 4H, Ar-*H*), 4.86 (br, 2H, Pt-OH_2), 2.45 (s, 6H, Ar-CH_3), 2.35 (s, 6H, Ar-CH_3), 2.20 (s, 12H, Ar-CH_3). ^{13}C{^{1}H} NMR (75.4 MHz, C_6D_6, Figure 4.18): 158.6 (C=N), 145.9 (C_{Ar}), 138.8 (C_{Ar}), 135.8 (C_{Ar}), 132.0 (C_{Ar}), 130.8 (C_{Ar}), 129.4 (C_{Ar}), 128.8 (C_{Ar}), 125.9 (C_{Ar}), 117.1 (C_{Ar}), 21.12 (Ar-CH_3), 21.0 (Ar-CH_3), 18.0 (Ar-CH_3), *C*F_3 signal not resolved. ^{19}F NMR (282.2 MHz, C_6D_6, Figure 4.19): δ –78.70. Elem. An. Found (Calculated) for $C_{35}H_{36}F_3N_3O_4SPt$: C, 49.43 (49.64); H, 4.44 (4.29)%.

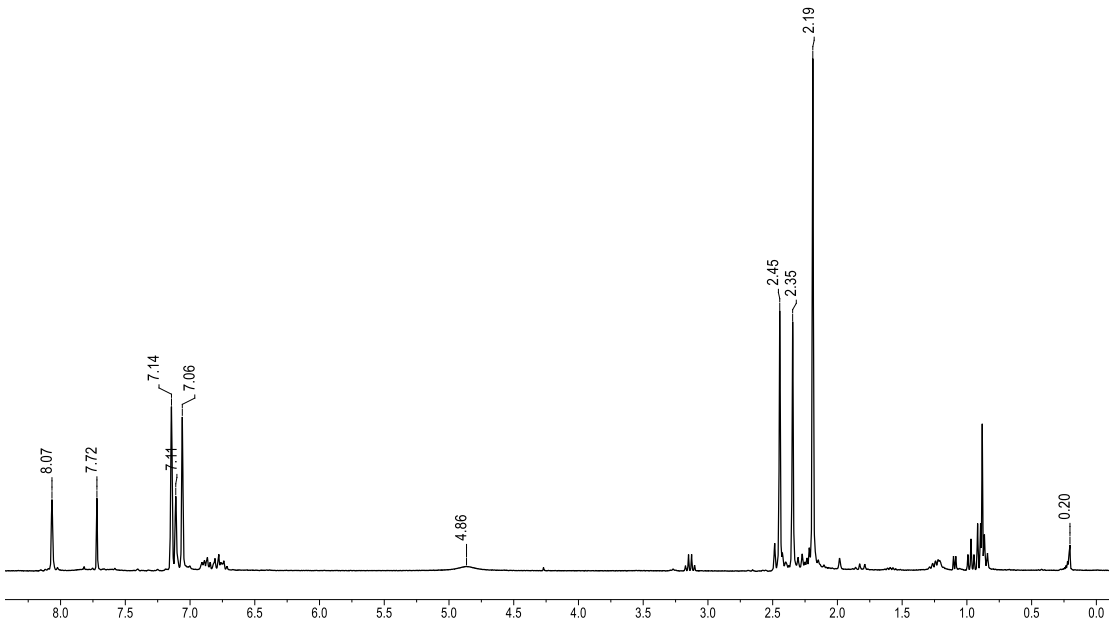

Figure 4.17 ^{1}H NMR spectrum of **404** in C_6D_6 at 23 °C measured on a 300-MHz Varian iNova.

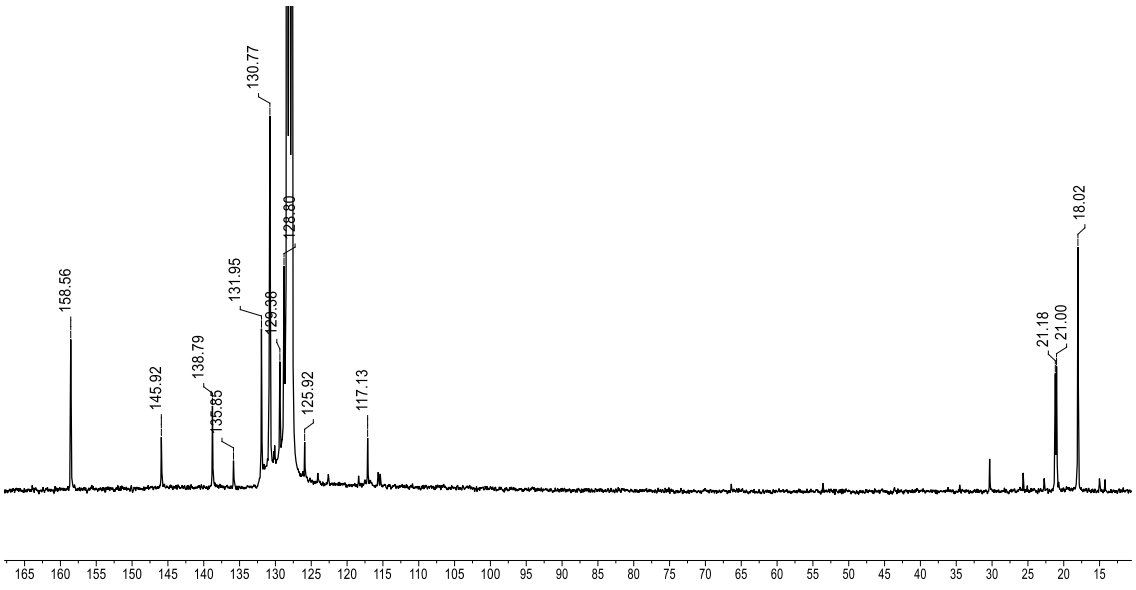

Figure 4.18 $^{13}C\{^{1}H\}$ NMR spectrum of **404** in C_6D_6 at 23 °C measured on a 300-MHz Varian iNova.

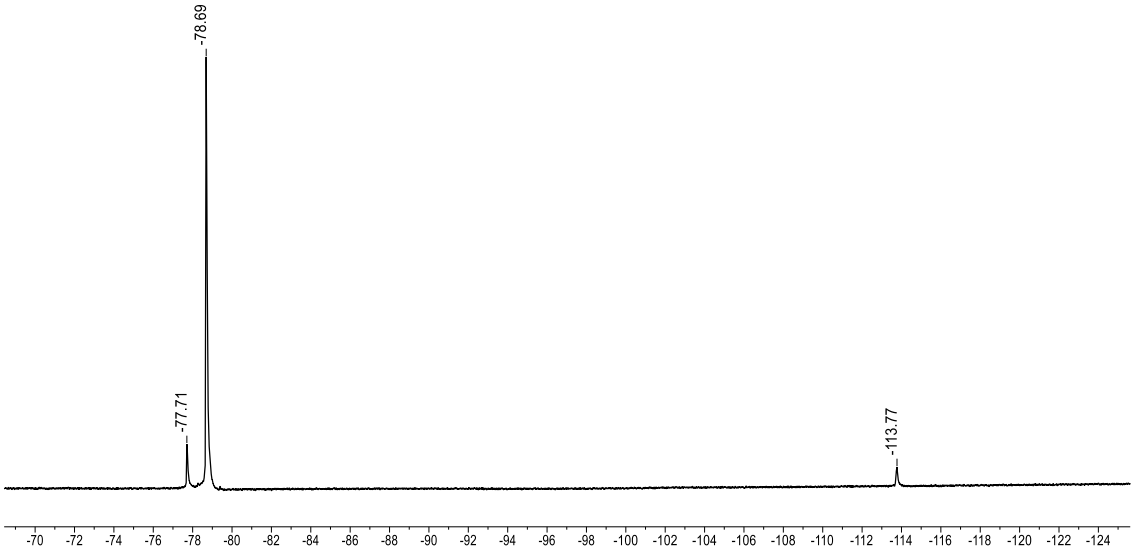

Figure 4.19 $^{19}F\{^{1}H\}$ NMR spectrum of **404** in C_6D_6 at 23 °C measured on a 300-MHz Varian iNova.

Cyclometallated (NNN)Pt (405). 403 (22 mg, 0.027 mol) was transferred to a J. Young NMR tube. C_6D_6 (0.6 mL) was added, giving an orange solution but not all of the solid was dissolved. Upon addition of NEt_3 (4 μL, 0.03 mmol), the solution immediately became red. After mixing for 30 min on an NMR tube spinner, ^{1}H NMR analysis showed complete conversion to cyclometallated product. The solution was filtered over a pad of silica gel and Celite. Volatiles were removed, yielding an orange-red solid. Solid was washed with cold pentane (3 × 1 mL) and dried under vacuum. Yield: 11 mg, 59%. ^{1}H NMR (500 MHz, C_6D_6, Figure 4.20): δ 9.29 (s, 1H, J_{Pt-H} = 93 Hz, N=C*H*), 8.43 (s, 1H, J_{Pt-H} = 90 Hz, N=C*H*), 8.37 (s, 1H, Ar-*H*), 8.31 (s, 1H, Ar-*H*), 7.50 (s, 1H, Ar-*H*), 7.34 (s, 1H, Ar-*H*), 7.00 (s, 1H, Ar-*H*), 6.96 (s, 2H, Ar-*H*), 6.52 (s, 1H, Ar-*H*), 2.95 (s, 2H, J_{Pt-H} = 66 Hz, Pt-C*H*$_2$-Ar), 2.56 (s, 3H, Ar-C*H*$_3$), 2.53 (s, 3H, Ar-C*H*$_3$), 2.35 (s, 3H, Ar-C*H*$_3$), 2.32 (s, 3H, Ar-C*H*$_3$), 2.28 (s, 6H, Ar-C*H*$_3$), 2.09 (d, 3H, Ar-C*H*$_3$). ^{1}H NMR (300 MHz, CD_2Cl_2, Figure 4.21): δ 9.68 (s, 1H, J_{Pt-H} = 90 Hz, N=C*H*), 8.77 (s, 1H, J_{Pt-H} = 90 Hz, N=C*H*), 8.58 (s, 1H, Ar-*H*), 8.53 (s, 1H, Ar-*H*), 7.90 (s, 1H, Ar-*H*), 7.78 (s, 1H, Ar-*H*), 7.06 (s, 2H, Ar-*H*), 6.93 (s, 1H, Ar-*H*), 6.76 (s, 1H, Ar-*H*), 2.85 (s, 3H, Ar-C*H*$_3$), 2.76 (s, 3H, Ar-C*H*$_3$), 2.74 (s, 3H, Ar-C*H*$_3$), 2.46 (s, 3H, Ar-C*H*$_3$), 2.35 (s, 2H, coupling to Pt obscured, Pt-C*H*$_2$-Ar), 2.27 (s, 3H, Ar-C*H*$_3$), 2.19 (d, 6H, Ar-C*H*$_3$). ^{13}C{^{1}H} NMR (75.4 MHz, CD_2Cl_2, Figure 4.22): δ 157.3, 155.1, 152.4, 151.4, 151.2, 138.2, 138.0, 136.2, 135.9, 131.9, 131.0, 130.9, 130.4, 129.6, 128.6, 128.0, 127.8, 127.7, 127.7, 126.7, 126.3, 118.8, 118.1, 24.5, 21.7, 21.0, 20.4, 17.9, 16.4. ^{195}Pt NMR (85.7 MHz, C_6D_6, Figure 4.23): δ –2589. Elem. An. Found (Calculated) for $C_{34}H_{33}N_3Pt$: C, 60.28 (60.17); H, 4.87 (4.90)%.

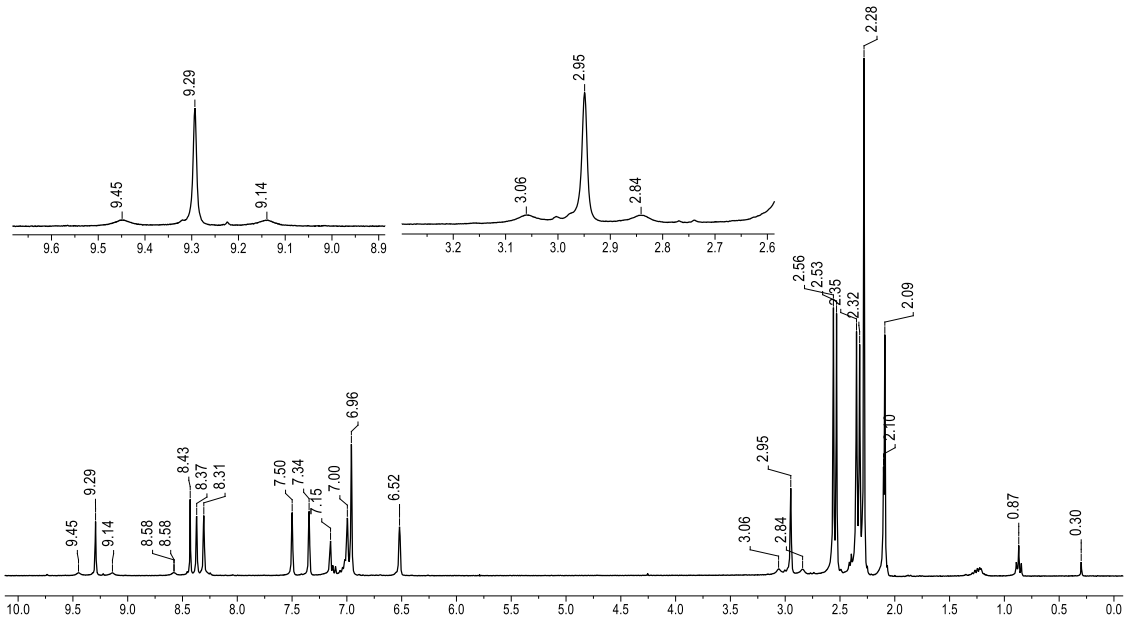

Figure 4.20 ^{1}H NMR spectrum of **405** in C_6D_6 at 23 °C measured on a 500-MHz Varian iNova with insets showing coupling to ^{195}Pt.

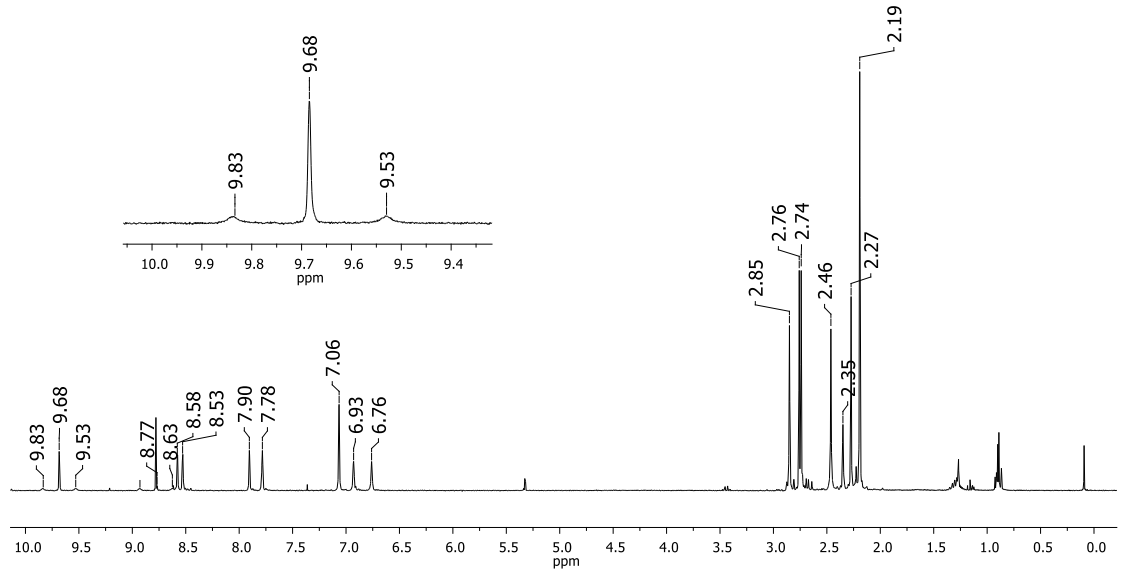

Figure 4.21 ^{1}H NMR spectrum of **405** in CD_2Cl_2 at 23 °C measured on a 300-MHz Varian iNova with inset showing coupling to ^{195}Pt.

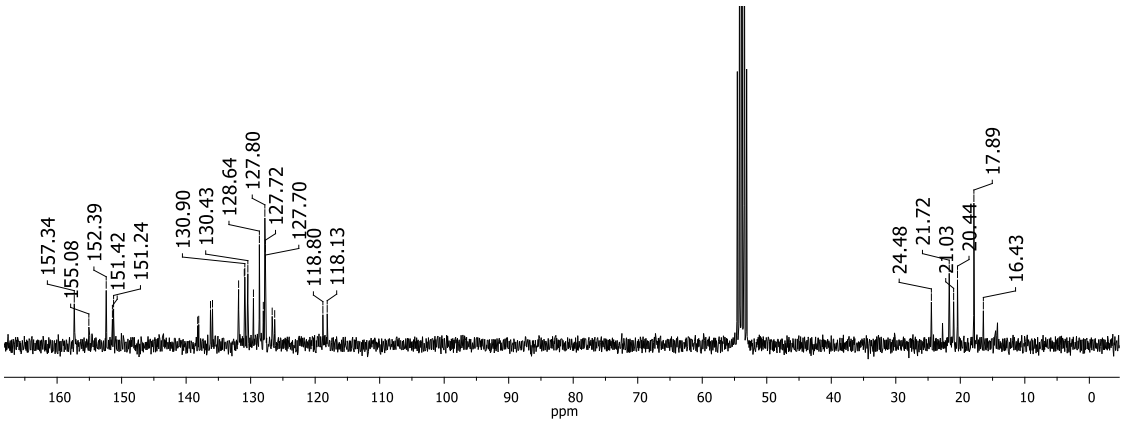

Figure 4.22 $^{13}C\{^{1}H\}$ NMR spectrum of **405** in CD_2Cl_2 at 23 °C measured on a 300-MHz Varian iNova.

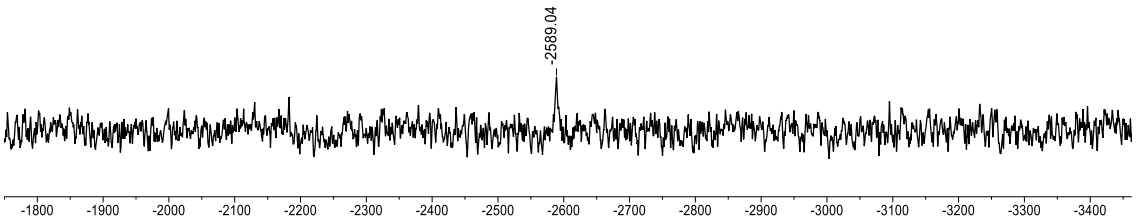

Figure 4.23 $^{195}Pt\{^{1}H\}$ NMR spectrum of **405** in C_6D_6 at 23 °C measured on a 400-MHz Varian iNova.

4.5.2.2 Reactivity Studies

Attempt to Remove H_2O from 404. A sample of **404** as a yellow powder was transferred to a 25 mL Schlenk flask and heated at 130 °C under vacuum for 48 h. After 48 h, the discolored solid was redissolved in C_6D_6 forming a red solution. ^{1}H NMR analysis shows a mixture of 53% **403** and 47% **405** was formed (Figure 4.24).

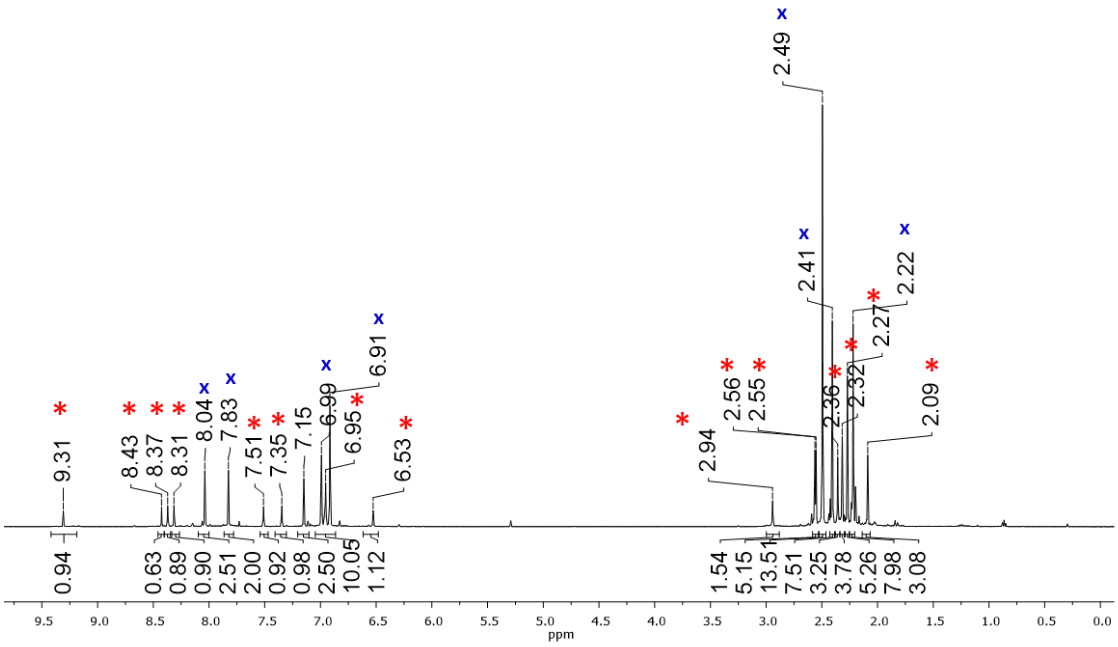

Figure 4.24 ^{1}H NMR spectrum measured on a 500-MHz Varian iNova of product mixture (**403**, x; **405**, *) in C_6D_6 after heating at 130 °C for 48 h under vacuum.

Reaction of 402 with 5 mol% 403. 402 (18 mg, 0.026 mmol) was dissolved in 1.8 mL of C_6D_6. **403** was then added (55 μL of 0.024 M soln in C_6D_6, 0.0013 mmol). The reaction was monitored by ^{1}H NMR spectroscopy (Table 4.1). After five minutes, free methane was observed in the ^{1}H NMR spectrum along with 15% conversion of **402** to **405**. After 18 h, 80% of the **402** was converted to the Pt(II) cyclometallated species. 5% of the **403** along with free methane were also observed in the ^{1}H NMR spectrum.

Table 4.1 Summary of relative ratios of Pt species in solution over time for reaction of **402** with 5 mol% **403** in C_6D_6.

Time	402	405	403
5 min	80%	15%	5%
1 h 45 min	71 %	24%	5%
3 h 15 min	57%	38%	5%
6 h	45%	50%	5%
18 h	15%	80%	5%

4.5.3 X-Ray Diffractometry Details

4.5.3.1 X-Ray Data Collection, Solution, and Refinement for 404·HOTf·½C_6H_5F[z]

Crystals were grown from fluorobenzene layered with pentane. An orange block of suitable size and quality (0.47 × 0.24 × 0.14 mm) was selected from a representative sample of crystals of the same habit using an optical microscope, mounted onto a nylon loop, and placed in a cold stream of nitrogen (150 K). Low-temperature X-ray data were obtained on a Bruker APEXII CCD based diffractometer (Mo sealed X-ray tube, K_α = 0.71073 Å). All diffractometer manipulations, including data collection, integration, and scaling were carried out using the Bruker APEX2 software.[142] An absorption correction was applied using SADABS.[143] The space group was determined on the basis of systematic absences and intensity statistics. The structure was solved by direct methods in

[z] X-ray data solution and refinement conducted by Billy McCulloch.

the monoclinic I2/a space group using SHELXS.[144] All non-hydrogen atoms were refined with anisotropic thermal parameters. Hydrogen atoms bound to carbon were placed in idealized positions and refined using a riding model. The hydrogen atoms on the metal-bound water were located in the difference map, and refined with restraints. The hydrogen atom on the triflic acid moiety was not observed in the difference map, but placed in an idealized position and refined using a riding model in order to obtain the correct charge balance. The structure was brought to convergence by weighted full-matrix least-squares refinement on $|F|^2$ using SHELXL.[144] A check for missed symmetry was run using the ADDSYM program within PLATON,[145] revealing no apparent higher symmetry. Disordered solvent was satisfactorily modeled using PLATON's SQUEEZE functionality – 4 voids were located in the unit cell, each containing 30 e^- with volume 175 $Å^3$.

4.5.3.2 X-Ray Data Collection, Solution, and Refinement for 404·C_6D_6[aa]

Crystals were grown from a solution of deuterobenzene/fluorobenzene layered with pentane. An orange block of suitable size and quality (0.15 × 0.07 × 0.04 mm) was selected from a representative sample of crystals of the same habit using an optical microscope, mounted onto a nylon loop, and placed in a cold stream of nitrogen (150 K). Low-temperature X-ray data were obtained on a Bruker APEXII CCD based diffractometer (Mo sealed X-ray tube, K_α = 0.71073 Å). All diffractometer manipulations, including data collection, integration, and scaling were carried out using the Bruker

[aa] X-ray data solution and refinement conducted by Billy McCulloch.

APEX2 software.[142] An absorption correction was applied using SADABS.[143] The space group was determined on the basis of systematic absences and intensity statistics. The structure was solved by direct methods in the monoclinic $P2_1/c$ space group using SHELXS.[144] All non-hydrogen atoms were refined with anisotropic thermal parameters. Hydrogen atoms bound to carbon were placed in idealized positions and refined using a riding model. The hydrogen atoms associated with the coordinated water molecule were not observed in the difference map and therefore not explicitly modeled, though ^{1}H NMR evidence supports our assertion that it is indeed coordinated water. The structure was brought to convergence by weighted full-matrix least-squares refinement on $|F|^2$. PLATON's ADDSYM and NEWSYM features were used to check for missed symmetry.[145] Structure manipulations were performed with the aid of shelXle.[146]

4.5.3.3 X-Ray Data Collection, Solution, and Refinement for 405[bb]

Crystals were grown from a solution of deuterobenzene/fluorobenzene layered with pentane. An orange block of suitable size and quality (0.11 × 0.09 × 0.03 mm) was selected from a representative sample of crystals of the same habit using an optical microscope, mounted onto a nylon loop, and placed in a cold stream of nitrogen (150 K). Low-temperature X-ray data were obtained on a Bruker APEXII CCD based diffractometer (Mo sealed X-ray tube, K_α = 0.71073 Å). All diffractometer manipulations, including data collection, integration, and scaling were carried out using the Bruker

[bb] X-ray data solution and refinement conducted by Billy McCulloch.

APEX2 software.[142] An absorption correction was applied using SADABS.[143] The space group was determined on the basis of systematic absences and intensity statistics. The structure was initially solved by direct methods in the triclinic P1 space group using SHELXS,[144] and converted into the centrosymmetric P–1 space group with PLATON's ADDSYM feature after locating all heavy atoms.[145] All non-hydrogen atoms were refined with anisotropic thermal parameters. Hydrogen atoms bound to carbon were placed in idealized positions and refined using a riding model. PLATON's SQUEEZE feature was utilized to account for partial occupancy and disorder of solvent in the crystal structure, which appeared to be benzene based on the difference map (total void volume 205 $Å^3$, 37 e^-). The structure was brought to convergence by weighted full-matrix least-squares refinement on $|F|^2$. Structure manipulations were performed with the aid of shelXle.[146]

*4.5.4 Cyclic Voltagmmogram for Compound **401***

A BAS-100A electroanalyzer utilizing a three-electrode system with glassy carbon working electrode, platinum wire counter electrode, and a vycor-tipped $Ag/AgNO_3$ reference electrode was used for electrochemical measurements. Cyclic voltammogram (Figure 4.25) was obtained from 2 mM solution of compound **401** in CH_2Cl_2, using 10 mM $[Bu_4N][PF_6]$ supporting electrolyte at a scan rate of 200 mV/s. Solutions were degassed by a purge of Ar, and a blanket of Ar was maintained over the solution while the measurement was made. Cyclic voltammogram was referenced to Fc/Fc^+ ($E_{½}$ = 0 V). Data was collected with the assistance of Allen Lunsford.

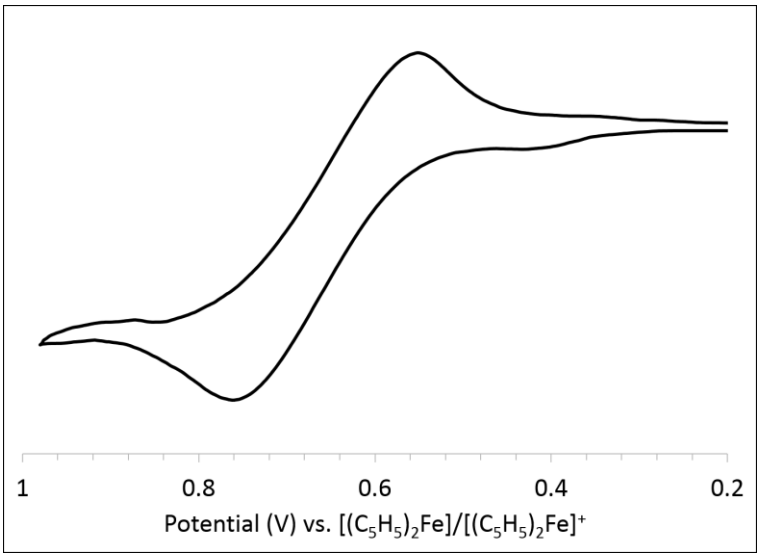

Figure 4.25 Cyclic voltammogram of **401** in CH_2Cl_2 at 23 °C. The scan rate was 200 mV/s in the positive direction. The cyclic voltammogram was obtained with 2 mM solution of Compound **401** in CH_2Cl_2 and 10 mM $[Bu_4N][PF_6]$ as the supporting electrolyte and resulted in a measured potential ($E_{½}$) equal to 0.65 V (vs Fc/Fc^+).

4.5.5 Synthesis and Reactivity of Pt(IV) NNN Complexes

4.5.5.1 Synthesis of Pt(IV) NNN Complexes

Cyclometallated (NNN)Pt(IV)(Me) (406). 402 (40. mg, 0.057 mmol) was transferred to a J. Young NMR tube and 0.6 mL of C_6D_6 was added. The solution became red but not all of the solid dissolved. MeOTf (7 μL, 0.06 mmol) was added and the NMR tube was inverted several times to mix the reagents. Some orange precipitate was observed after 15 min. The contents of the NMR tube were mixed on an NMR tube rotator for an additional 2 h and a significant amount of orange precipitate was observed. The contents of the NMR tube were transferred to a 5 mL vial and the solvent was decanted off. The supernatant was found to contain Pt(IV)cyclometallated species **406** and some unreacted

402 as observed by ^{1}H NMR spectroscopy. The orange solid was washed 3 × 2 mL pentane then dried under vacuum. Yield: 26 mg, 54%. The compound decomposes in dichloromethane within 16 h to form **401**. ^{1}H NMR (500 MHz, CD_2Cl_2, Figure 4.26): δ 9.20 (s, 1H, $J_{Pt\text{-}H}$ = 89 Hz, N=C*H*), 8.55 (s, 1H, Ar-*H*), 8.51 (s, 2H, $J_{Pt\text{-}H}$ = 80 Hz, N=C*H*), 7.88 (s, 1H, Ar-*H*), 7.75 (s, 1H, Ar-*H*), 7.09 (s, 1H, Ar-*H*), 7.04 (s, 2H, Ar-*H*), 6.90 (s, 1H, Ar-*H*), 3.77 (d, $J_{H\text{-}H}$ = 15 Hz, $J_{Pt\text{-}H}$ = 90 Hz, 1H, Pt-CH_2), 2.84 (s, 3H, Ar-CH_3), 2.75 (s, 3H, Ar-CH_3), 2.72 (s, 3H, Ar-CH_3), 2.54 (d, $J_{H\text{-}H}$ = 15 Hz, $J_{Pt\text{-}H}$ is obscured by other signals, 1H, Pt-CH_2), 2.43 (s, 3H, Ar-CH_3), 2.33 (s, 6H, Ar-CH_3), 2.16 (s, 3H, Ar-CH_3), 1.09 (s, $J_{Pt\text{-}H}$ = 81 Hz, 3H, Pt-CH_3). ^{13}C{^{1}H} NMR (125.7 MHz, CD_2Cl_2, Figure 4.27): δ 164.9, 156.8, 150.8, 149.0, 139.1, 138.6, 137.8, 137.6, 133.8, 133.6, 133.1, 132.5, 131.1, 130.6, 130.4, 130.1, 129.5, 129.2, 129.1, 129.0, 128.6, 128.3, 126.4, 126.0, 117.8, 116.0, 29.1, 24.0, 21.6, 20.9, 20.6, 19.8, 19.3, 19.2, 0.2, -*C*F_3 signal not resolved. ^{19}F NMR (282.2 MHz, CD_2Cl_2, Figure 4.28): δ –80.15. ^{195}Pt NMR (85.7 MHz, C_6H_5F, Figure 4.29): δ –1277. Elem. An. Found (Calculated) for $C_{36}H_{36}F_3N_3O_3SPt$: C, 51.16 (51.30); H, 4.21 (4.31)%.

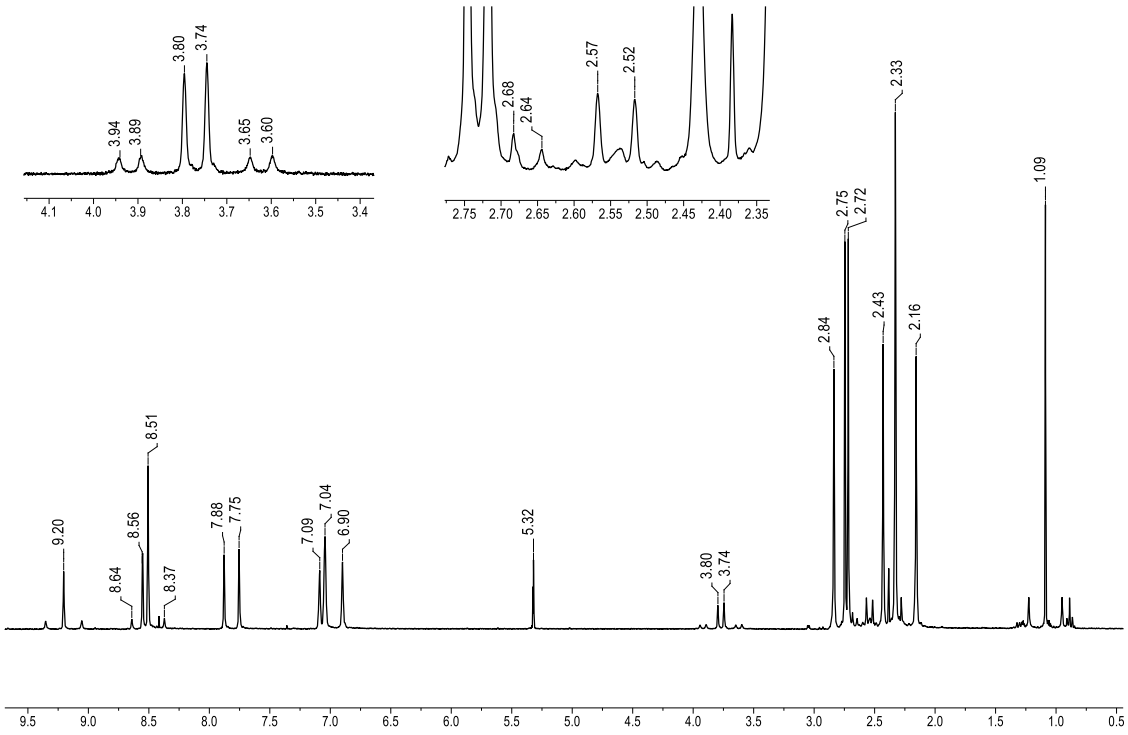

Figure 4.26 ^{1}H NMR spectrum of **406** in CD_2Cl_2 at 23 °C measured on a 300-MHz Varian iNova with insets showing methylene CH_2 signals with Pt coupling.

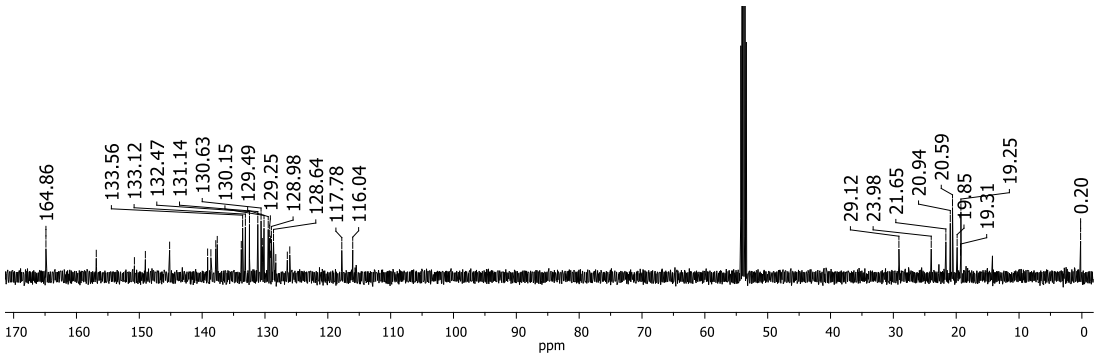

Figure 4.27 $^{13}C\{^{1}H\}$ NMR spectrum of **406** in CD_2Cl_2 at 23 °C measured on a 500-MHz Varian iNova.

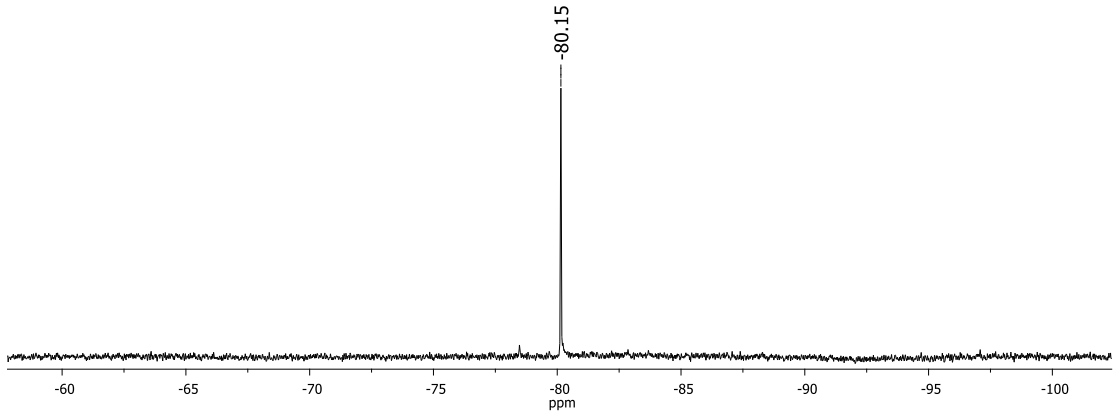

Figure 4.28 In situ ^{19}F NMR spectrum of **406** in CD_2Cl_2 at 23 °C measured on a 300-MHz Varian iNova.

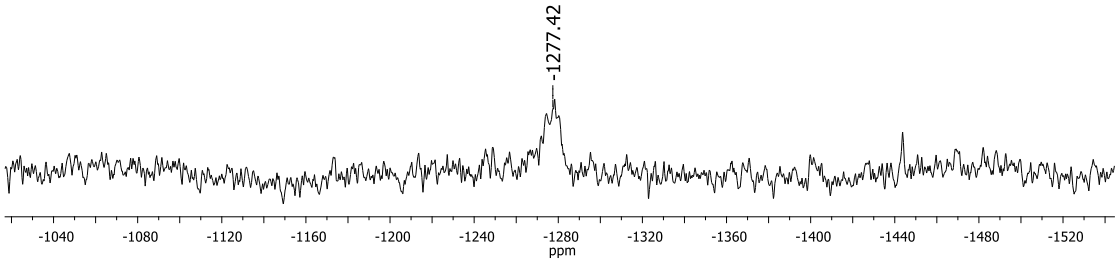

Figure 4.29 $^{195}Pt\{^1H\}$ NMR spectrum of **406** in C_6D_6 at 23 °C measured on a 400-MHz Varian iNova.

Cyclometallated (NNN)Pt(IV)(Ethyl) (407). 402 (25 mg, 0.035 mmol) was transferred to a J. Young NMR tube and 0.6 mL of C_6D_6 was added. The solution became red but not all of the solid dissolved. EtOTf (5 μL, 0.04 mmol) was added and the NMR tube was inverted several times to mix the reagents. Some orange-red precipitate was observed after 15 min. The NMR tube was mixed for an additional 16 h and a significant amount of orange-red precipitate was observed. The contents of the NMR tube were

transferred to a 5 mL vial and the supernatant was decanted off. The supernatant was found to contain Pt(II)cyclometallated species **405** as observed by ^{1}H NMR spectroscopy. The orange solid was washed 3 × 2 mL pentane then dried under vacuum. Yield: 11 mg, 36%. The compound decomposes in dichloromethane within 16 h to form **401**. ^{1}H NMR (400 MHz, CD_2Cl_2, Figure 4.30): δ 9.32 (s, 1H, $J_{Pt\text{-}H}$ = 88 Hz, N=C*H*), 8.62 (s, 1H, $J_{Pt\text{-}H}$ = 84 Hz), 8.59 (s, 1H, Ar-*H*), 8.55 (s, 1H, Ar-*H*), 7.95 (s, 1H, Ar-*H*), 7.81 (s, 1H, Ar-*H*), 7.10 (s, 2H, Ar-*H*), 7.05 (s, 1H, Ar-*H*), 6.92 (s, 1H, Ar-H), 4.04 (d, $J_{H\text{-}H}$ = 16 Hz, $J_{Pt\text{-}H}$ = 92 Hz, 1H, Pt-CH_2), 2.85 (s, 3H, Ar-CH_3), 2.76 (s, 3H, Ar-CH_3), 2.73 (s, 3H, Ar-CH_3), 2.73 (coupling obscured by other signals, 1H, Pt-CH_2CH$_3$), 2.43 (s, 3H, Ar-CH_3), 2.35 (d, $J_{H\text{-}H}$ = 16 Hz, 1H, Pt-CH_2), 2.33 (s, 3H, Ar-CH_3), 2.27 (s, 3H, Ar-CH_3), 2.24 (s, 3H, Ar-CH_3), 2.08 (dq, $J_{H\text{-}H}$ = 8 Hz, $J_{H\text{-}H}$ = 8 Hz, 1H, Pt-CH_2CH$_3$), –0.59 (t, $J_{H\text{-}H}$ = 8 Hz, $J_{Pt\text{-}H}$ = 64 Hz). ^{13}C{^{1}H} NMR (100.5 MHz, CD_2Cl_2): δ 164.7, 157.4, 150.5, 148.8, 145.5, 139.1, 138.8, 137.9, 137.8, 133.7, 133.7, 133.2, 132.6, 131.3, 130.8, 130.2, 130.1, 129.7, 129.7, 129.5, 129.3, 128.8, 126.5, 126.0, 120.3 (q, $J_{F\text{-}C}$ = 319 Hz, -CF_3), 118.0, 116.3, 30.4, 27.5, 25.1, 24.1, 21.7, 21.0, 20.6, 19.5, 19.2, 17.1. ^{19}F NMR (282.2 MHz, CD_2Cl_2): δ –80.09. Elem. An. Found (Calculated) for $C_{37}H_{38}F_3N_3O_3SPt$: C, 51.96 (51.86); H, 4.61 (4.47)%.

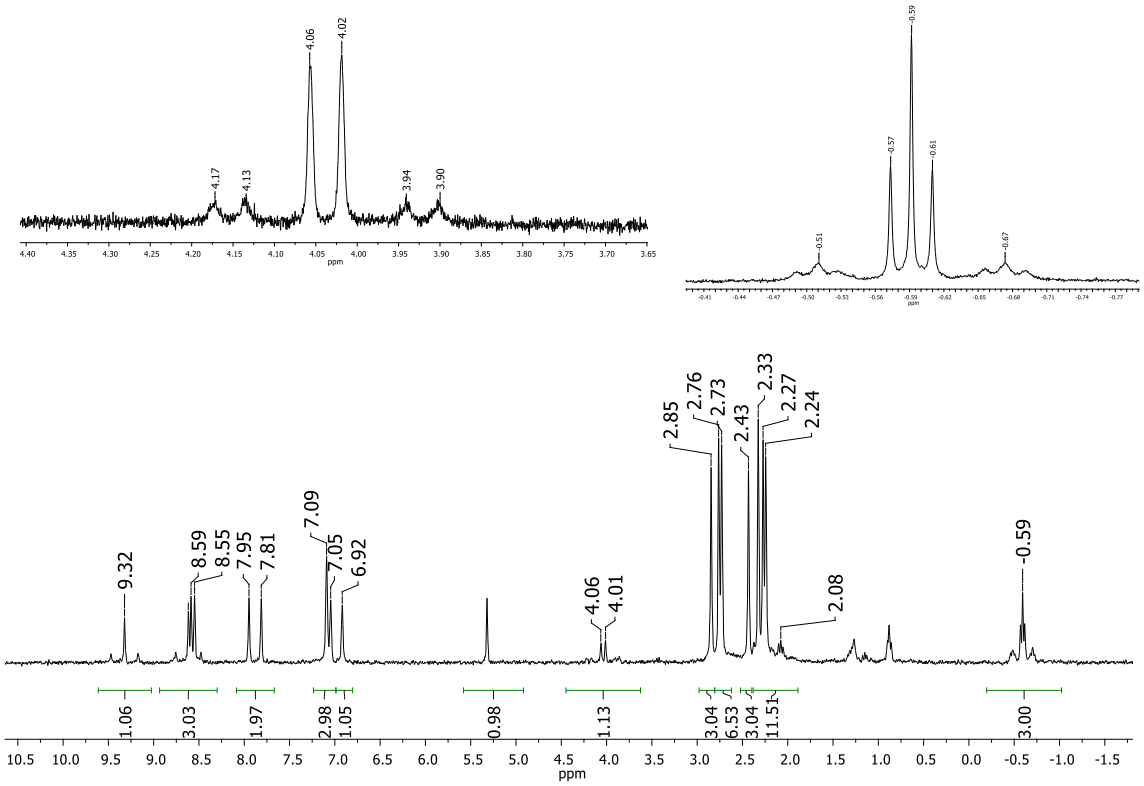

Figure 4.30 ^{1}H NMR spectrum of **407** in CD_2Cl_2 at 23 °C measured on a 300-MHz Varian iNova with insets showing methylene CH_2 signals with Pt coupling.

4.5.5.2 Reactivity of Pt(IV) NNN Complexes

Reaction of 402 with DOTf. Triflic anhydride (9 μL, 0.05 mmol) was added to 0.7 mL of C_6D_6. Degassed D_2O (1 μL, 0.05 mmol) was added and the solution was placed in an oil bath at 90 °C for 19 h. ^{19}F NMR spectroscopy showed 90% conversion to DOTf and 10% triflic anhydride remained. Two ^{19}F NMR signals were observed for DOTf at –77.6 ppm and –80.1 ppm (broad), matching literature values for the observation of DOTf in an organic phase and droplet phase, respectively. The solution was transferred into a

vial and the total volume was brought to 2 mL. Using C_6H_5F as an internal standard for ^{19}F NMR spectroscopy, the resulting solution was found to contain 0.09 mmol DOTf and 0.01 mmol triflic anhydride. Separately, **402** (16 mg, 0.023 mmol) was mixed with 0.5 mL C_6D_6 in a J. Young NMR tube to form a red-orange solution with some undissolved **402**. DOTf (500 μL of 0.045 M soln in C_6D_6, 0.023 mmol) was added and the NMR tube was inverted several times. The solution immediately become orange-yellow. Examination of the resulting solution by ^1H NMR spectroscopy after 10 min showed 80% conversion to **403** and 20% conversion to **405**. CH_3D and CH_4 were observed in a 1:4 molar ratio. Integration of the *ortho* methyl signal of the mesityl ring was found to integrate slightly low (11.4 versus 12). ^2H NMR spectroscopy in C_6H_6 was used to confirm the incorporation of deuterium into the *ortho* methyl of the mesityl sidearm with a signal observed at 2.45 ppm versus 2.5 ppm in C_6D_6 for the fully protio species.

Monitoring Cyclometallated 406 Synthesis in the Presence of 2,6-di-*tert*-butylpyridine. MeOTf (2.2 μL, 0.020 mmol) and 2,6-di-*tert*-butylpyridine (4.5 μL, 0.020 mmol) were added to 1 mL of C_6D_6 in a J. Young NMR tube. **402** (14 mg, 0.020 mmol) was then transferred to a J. Young NMR tube. The solution became red and homogeneous. A ^1H NMR spectrum taken after 12 min showed 22% conversion to **[(NNN)PtMe$_2$]OTf (408)** and 78% starting material **402** (see Table 4.2). After 45 min some orange-red precipitate was observed. The ratio of Pt species in solution as indicated by ^1H NMR spectroscopy was 55% starting material, 43% **408**, and less than 2% **405**. Ethane and Pyr-H+ were also observed in solution at this point. In addition to ethane, some methane was apparent after 1 h 15 min. After 3 h 10 min, the ratio of Pt species in solution was 36%

402, 42% **408**, 21% **406**, and 1% **405**. The molar ratio of ethane to methane was 9:1 based on relative integrations in the ^{1}H NMR spectrum. After 21 h, a significant amount of orange-red precipitate was apparent. The breakdown of Pt species in solution was 37% **402**, 23% **405**, and 40% **406**. After 38 h, no **402** starting material was observed in the ^{1}H NMR spectrum. The Pt species remaining in solution were **405** (30%), **401** (35%; believed to form via reaction with CH_2Cl_2 impurity in C_6D_6), and **403** (35%). The molar ratio of ethane to methane based on relative integrations in the ^{1}H NMR spectrum was 2:1. A large amount of orange-red precipitate was present in solution. NMR characterization for **[(NNN)PtMe$_2$]OTf (408)**: ^{1}H NMR (400 MHz MHz, C_6D_6): δ 8.13 (s, $J_{195Pt-H}$ = 92 Hz, 2H, N=C*H*), 7.85 (s, 2H, Ar-*H*), 7.08 (s, 2H, Ar-*H*), 6.69 (s, 4H, Ar-*H*), 2.52 (s, 6H, -CH_3), 2.22 (s, 12H, -CH_3), 2.06 (s, 6H, -CH_3), 1.12 (s, $J_{195Pt-H}$ = 72 Hz, 6H, -Pt(CH_3)$_2$).

Table 4.2 Summary of relative ratios of Pt species in solution over time for **406** synthesis with 2,6-di-tert-butylpyridine.

	12 min	**45 min**	**54 min**	**1 h 15 min**	**3 h 10 min**	**15 h 50 min**	**16 h 14 min**	**20 h 41 min**	**38 h**
Ethane: Methane	-	ethane	ethane	3:1	9:1	9:1	9:1	2:1	2:1
402	78%	55%	49%	47%	36%	45%	46%	37%	-
408	22%	43%	49%	50%	42%	15%	-	-	-
403	-	-	-	-	-	-	-	-	35%
405	-	2%	1%	1%	1%	1%	1%	23%	35%
406	-	-	1%	2%	21%	40%	43%	40%	-
401	-	-	-	-	-	-	-	-	30%

Monitoring Cyclometallated 406 Synthesis without Base. MeOTf (2.2 μL, 0.020 mmol) was added to 1 mL of C_6D_6 in a J. Young NMR tube. **402** (14 mg, 0.020 mmol) was then transferred to a J. Young NMR tube. The solution became red and homogeneous. The ^{1}H NMR spectrum (see Table 4.3) taken after 18 min showed 52% conversion to **408** and 48% starting material (**402**). After 39 min, some orange-red precipitate was observed. In addition to some ethane formation, the ratio of Pt species in solution as indicated by ^{1}H NMR spectroscopy was 38% **402**, 60% **408**, and less than 2% **405**. Some methane was observed by ^{1}H NMR spectroscopy after 59 min and the molar ratio of ethane to methane based on relative integrations in the ^{1}H NMR spectrum was 1:22. After 3 h 10 min, the ratio of Pt species in solution was 1% **402**, 42% **403**, 59% **406**, and 3% **405**. The molar ratio of ethane to methane was 1:33 based on relative integrations in the ^{1}H NMR spectrum. After 20 h 15 min, a significant amount of orange-red precipitate had formed. The ratio of Pt species in solution was 1% **402**, 91% **403**, and 8% **406**. The molar ratio of ethane to methane was 1:14 based on relative integrations in the ^{1}H NMR spectrum.

Table 4.3 Summary of relative ratios of Pt species in solution over time for **402** synthesis without base.

	18 min	**39 min**	**59 min**	**1 h 4 min**	**3 h 9 min**	**15 h 52 min**	**16 h 25 min**	**20 h 51 min**
Ethane: Methane	-	-	1:22	1:33	1:33	1:18	1:12	1:14
402	48%	38%	21%	18%	1%	1%	1%	1%
408	52%	60%	13%	2%	-	-	-	-
403	-	-	11%	12%	42%	66%	70%	91%
405	-	2%	-	5%	3%	-	-	-
406	-	-	55%	63%	59%	33%	29%	8%

Monitoring Cyclometallated (407) Synthesis in the Presence of 2,6-di-*tert*-butylpyridine. EtOTf (2 μL, 0.015 mmol) and 2,6-di-*tert*-butylpyridine (3 μL, 0.013 mmol) were added to 1 mL of C_6D_6 in a J. Young NMR tube. **402** (10 mg, 0.014 mmol) was then transferred to a J. Young NMR tube. The solution became red and homogeneous. A ^{1}H NMR spectrum (see Table 4.4) taken after 15 min showed starting material (**402**). After 3 h 31 min, the relative amounts of the Pt species in solution was 90% **402** and 10% **405** as observed by ^{1}H NMR spectroscopy. Some methane was observed after 19 h 30 min and the ratio of Pt-Me had decreased to 75% with **405** increasing to 25%. No propane signals were apparent by ^{1}H NMR spectroscopy, but they may have been obscured by residual pentane in the NMR solvent. After 36 h 16 min, the ratio of Pt species in solution

was 62% **402** and 38% **405** with a small amount of orange-red precipitate observed on the walls of the NMR tube.

Table 4.4 Summary of relative ratios of Pt species in solution over time for **407** synthesis with 2,6-di-tert-butylpyridine.

	15 min	**3 h 31 min**	**19 h 30 min**	**36 h 16 min**
Gas observed by NMR	-	-	methane	methane
402	100%	90%	75%	62%
405	-	10%	25%	38%

Monitoring Cyclometallated (407) Synthesis without Base. EtOTf (2 μL, 0.015 mmol) was added to 1 mL of C_6D_6 in a J. Young NMR tube. **402** (10 mg, 0.014 mmol) was then transferred to a J. Young NMR tube. The solution became red and homogeneous. A ^{1}H NMR spectrum taken after 15 min showed the ratio of Pt species in solution to be 80% **402** and 20% **405** (see Table 4.5). Some methane was observed after 15 h 14 min and the relative percent of **402** in solution had decreased to 56% with **405** increasing to 44%. No propane signals were apparent by ^{1}H NMR spectroscopy, but they may have been obscured by residual pentane in the NMR solvent. After 37 h 7 min, some orange-red precipitate was observed on the walls of the NMR tube. Of the species remaining in solution, 94% was observed to be **405** and 6% **402**.

Table 4.5 Summary of relative ratios of Pt species in solution over time for **407** synthesis without base.

	15 min	**3 h 56 min**	**15 h 14 min**	**20 h 30 min**	**37 h 7 min**
Gas observed by NMR	-	-	methane	methane	methane
402	80%	63%	56%	36%	6%
405	20%	37%	44%	64%	94%

Monitoring Decomposition of isolated Solution of 70% 408. 402 (10 mg, 0.014 mmol) was dissolved in 1 mL C_6D_6. MeOTf was added (30 μL, 0.27 mmol). After 30 min at RT, 70% of the **402** was converted to **408**. The volatiles were removed yielding an orange solid. The solid was redissolved in 1 mL of C_6D_6 and transferred to a J. Young NMR tube. The solution was monitored by ^{1}H NMR spectroscopy. After six minutes, the solution was composed of 23% **402**, 70% **408**, and 7% **406**. Free ethane and free methane were both observed in solution at this point in approximately 1:3 molar ratio. After 16 h 20 min, no **402** or **408** was observed by ^{1}H NMR spectroscopy. The product mixture was composed of 20% **403**, 47% **405**, and 33% **406**. At this time, the ethane:methane molar ratio was approximately 3:4.

V. SUMMARY

This dissertation examined several pincer ligand scaffolds and assessed their ability to stabilize three-coordinate Pt centers. In attempts to work toward isolating a stable methane σ-complex we identified several components that needed to be optimized. This work presents the modular adjustment of the *trans*-influence of the central pincer donor, the basicity of the central N donor, the oxidation potential of the ligand backbone, and the steric profile of the neutral donor substituents. Future work will need to address the solubility issues associated with generating unsaturated mono- and dicationic Pt centers as well as continuing to avoid solvent activation or ligand non-innocence.

The use of silylene pincer ligands demonstrated the tendency of a Pt bound substituent to undergo a 1,2-migration to the silylium-like Si central donor atom. Silyl ligands have a strong *trans*-influence and can help stabilize unsaturation at a *trans*-coordination site of a metal center. This was demonstrated by the isolation of three unsaturated Pt species, including a siloxane bridged Pt dimer, where the distances between the Pt center and a chloro group on the carborane anion are among the longest Pt⋯Cl distances. The use of a silylene precursor to access these unsaturated Pt centers introduces not only a novel silylene based pincer ligand but also the unexpected protodesilylation of mesitylene. This reactivity is believed to be induced by adventitious water and, interestingly, water coordination to the unsaturated Pt center was not observed.

Our initial attempts to make a methane σ-complex involved the use of a weaker *trans*-influence central donor, N, in bis(phosphino)diarylamido platinum(II) cationic

complexes ([(PNP)Pt]$^+$). While we were unable to isolate a methane σ-complex of (PNP)Pt, reactivity studies showed the unsaturated Pt(II) center to be highly electrophilic. In arene solvents, [(PNP)Pt]$^+$ was shown to undergo rapid C-H activation of the arene across the N-Pt bond to give [(PN(H)P)Pt-aryl]$^+$ species. Additionally, because of the non-innocent nature of the (PNP) ligand, (PNP)Pt was shown to take part in metalloradical chemistry, abstracting a halogen atom from halogenated solvents with weak C-X bonds to give [(PNP)PtX] cations.

Although the reactivity of (PNP)Pt was really interesting, it seemed ill-suited as a candidate to bind methane. In seeking to discourage electrophilic C-H activation of the solvent across the N-Pt bond, we targeted a pincer ligand scaffold with reduced basicity at the N. The use of a pincer ligand with a lower oxidation potential was also targeted in order to avoid metalloradical pathways made available by ligand oxidation. This inspired the use of bis(imino)carbazolyl (NNN) pincer ligand backbone determined to have a lower oxidation potential relative to the PNP system. However, this ligand was observed to undergo intramolecular C-H activation reactions. Facile intramolecular C-H activation of a methyl group on the pendant mesityl sidearms of the ligand led to the isolation of cyclometallated Pt complexes. The displacement of a triflate group from the Pt metal center by water is consistent with a binding pocket that prefers smaller molecules. This system holds promise for targeting a methane σ-complex, provided that future modifications prevent intramolecular ligand activation.

Future modifications of the pincer ligand backbone, may require the use of central pincer donors with even weaker trans-influence relative to N. Increasing the solubility of

the unsaturated Pt species will allow less polar and more inert solvents to be explored as media for the generation of stable methane σ-complexes. Extending the steric bulk of the ligand sidearms may help to create a hydrophobic binding pocket conducive to alkane coordination with secondary ligand stabilization. Preliminary syntheses of some next generation ligand scaffolds are presented in the Appendix.

REFERENCES

(1) Neumann, A.; von Hirschhausen, C. *Rev. Environ. Econ. Pol.* **2015**, *9*, 64.

(2) Caballero, A.; Perez, P. J. *Chem. Soc. Rev.* **2013**, *42*, 8809.

(3) Weissermel, K.; Arpe, H. J. *Industrial Organic Chemistry*; Wiley-VCH: Weinhem, Germany, 2008.

(4) Häussinger, P.; Lohmüller, R.; Watson, A. M. In *Hydrogen, 2. Production. Ullmann's Encyclopedia of Industrial Chemistry*; Wiley-VCH Verlag GmbH & Co. KGaA: 2000.

(5) Ott, J.; Gronemann, V.; Pontzen, F.; Fiedler, E.; Grossmann, G.; Kersebohm, D. B.; Weiss, G.; Witte, C. In *Methanol. Ullmann's Encyclopedia of Industrial Chemistry*; Wiley-VCH Verlag GmbH & Co. KGaA: Weinheim, Germany, 2012.

(6) Luo, Y.-R. *Comprehensive Handbook of Chemical Bond Energies*; 1st ed.; CRC Press: Boca Raton, Florida, 2007.

(7) Otsuka, K.; Wang, Y. *Appl. Catal. A Gen.* **2001**, *222*, 145.

(8) Lyons, J. E.; Ellis Jr, P. E.; Durante, V. A. In *Stud. Surf. Sci. Catal.*; Grasselli, R. K., Sleight, A. W., Eds.; Elsevier: 1991; Vol. Volume 67, p 99.

(9) Alayon, E. M. C.; Nachtegaal, M.; Ranocchiari, M.; van Bokhoven, J. A. *CHIMIA* **2012**, *66*, 668.

(10) Olah, G. A. *Angew. Chem. Int. Ed.* **2005**, *44*, 2636.

(11) Goldman, A. S.; Goldberg, K. I. *Activation and Functionalization of C-H Bonds*; ACS Symposium Series 885; American Chemical Society: Washington, DC, 2004.

(12) Arndtsen, B. A.; Bergman, R. G.; Mobley, T. A.; Peterson, T. H. *Acc. Chem. Res.* **1995**, *28*, 154.

(13) Tang, P.; Zhu, Q.; Wu, Z.; Ma, D. *Energ. Environ. Sci.* **2014**, *7*, 2580.

(14) Leeuwen, P. W. N. M. v. *Homogeneous Catalysis-Understanding the Art*; Kluwer Academic Publishers: Dordrecht, Netherlands, 2004.

(15) Gol'dshleger, N. F.; Tyabin, M. B.; Shilov, A. E.; Shteinman, A. A. *Russ. J. Phys. Chem.* **1969**, *43*, 1222.

(16) Goldshleger, N. F.; Eskova, V. V.; Shilov, A. E.; Shteinman, A. A. *Zh. Fiz. Khim.* **1972**, *46*, 1353.

(17) Shilov, A. E.; Shul'pin, G. B. *Chem. Rev.* **1997**, *97*, 2879.

(18) Labinger, J. A.; Bercaw, J. E. *Nature* **2002**, *417*, 507.

(19) Periana, R. A.; Taube, D. J.; Evitt, E. R.; Löffler, D. G.; Wentrcek, P. R.; Voss, G.; Masuda, T. *Science* **1993**, *259*, 340.

(20) Periana, R. A.; Taube, D. J.; Gamble, S.; Taube, H.; Satoh, T.; Fujii, H. *Science* **1998**, *280*, 560.

(21) Hashiguchi, B. G.; Konnick, M. M.; Bischof, S. M.; Gustafson, S. J.; Devarajan, D.; Gunsalus, N.; Ess, D. H.; Periana, R. A. *Science* **2014**, *343*, 1232.

(22) Jones, C. J.; Taube, D.; Ziatdinov, V. R.; Periana, R. A.; Nielsen, R. J.; Oxgaard, J.; Goddard, W. A. *Angew. Chem. Int. Ed.* **2004**, *43*, 4626.

(23) Crabtree, R. H. *Chem. Rev.* **2010**, *110*, 575.

(24) Murai, S. *Activation of Unreactive Bonds and Organic Synthesis*; Springer: New York, 2003; Vol. 3.

(25) Jones, W. D. *Science* **2000**, *287*, 1942.

(26) Ryabov, A. D. *Chem. Rev.* **1990**, *90*, 403.

(27) Crabtree, R. H. *Chem. Rev.* **1985**, *85*, 245.

(28) Hall, C.; Perutz, R. N. *Chem. Rev.* **1996**, *96*, 3125.

(29) Lersch, M.; Tilset, M. *Chem. Rev.* **2005**, *105*, 2471.

(30) Young, R. D. *Chem. Eur. J.* **2014**, *20*, 12704.

(31) Jones, W. In *Activation of Unreactive Bonds and Organic Synthesis*; Murai, S., Alper, H., Gossage, R. A., Grushin, V. V., Hidai, M., Ito, Y., Jones, W. D., Kakiuchi, F., van Koten, G., Lin, Y. S., Mizobe, Y., Murai, S., Murakami, M., Richmond, T. G., Sen, A., Suginome, M., Yamamoto, A., Eds.; Springer Berlin Heidelberg: 1999; Vol. 3, p 9.

(32) Green, J. C.; Green, M. L. H.; Parkin, G. *Chem. Commun.* **2012**, *48*, 11481.

(33) Hartwig, J. F. *Organotransition Metal Chemistry: From Bonding to Catalysis*; University Science Books: Mill Valley, California, 2010.

(34) He, J.; Li, S.; Deng, Y.; Fu, H.; Laforteza, B. N.; Spangler, J. E.; Homs, A.; Yu, J.-Q. *Science* **2014**, *343*, 1216.

(35) He, J.; Shigenari, T.; Yu, J.-Q. *Angew. Chem. Int. Ed.* **2015**, *54*, 6545.

(36) Daugulis, O.; Roane, J.; Tran, L. D. *Acc. Chem. Res.* **2015**, *48*, 1053.

(37) Dick, A. R.; Sanford, M. S. *Tetrahedron* **2006**, *62*, 2439.

(38) Kubas, G. J. *Metal Dihydrogen and σ-Bond Complexes*; Kluwer Academic/Plenum Publishers: New York, 2001.

(39) Kubas, G. J.; Ryan, R. R.; Swanson, B. I.; Vergamini, P. J.; Wasserman, H. J. *J. Am. Chem. Soc.* **1984**, *106*, 451.

(40) Kubas, G. J. *J. Organomet. Chem.* **2001**, *635*, 37.

(41) Power, P. P. *Nature* **2010**, *463*, 171.

(42) Jetz, W.; Graham, W. A. G. *J. Am. Chem. Soc.* **1969**, *91*, 3375.

(43) Hoyano, J.; Elder, M.; Graham, W. A. G. *J. Am. Chem. Soc.* **1969**, *91*, 4568.

(44) Graham, W. A. G.; Jetz, W. *Inorg. Chem.* **1971**, *10*, 4.

(45) Lachaize, S.; Sabo-Etienne, S. *Eur. J. Inorg. Chem.* **2006**, *2006*, 2115.

(46) Hartwig, J. F.; Muhoro, C. N.; He, X.; Eisenstein, O.; Bosque, R.; Maseras, F. *J. Am. Chem. Soc.* **1996**, *118*, 10936.

(47) Muhoro, C. N.; He, X.; Hartwig, J. F. *J. Am. Chem. Soc.* **1999**, *121*, 5033.

(48) Lin, Z. In *Contemporary Metal Boron Chemistry I*; Marder, T., Lin, Z., Eds.; Springer Berlin Heidelberg: 2008; Vol. 130, p 123.

(49) Lam, W. H.; Lin, Z. *Organometallics* **2000**, *19*, 2625.

(50) Schlecht, S.; Hartwig, J. F. *J. Am. Chem. Soc.* **2000**, *122*, 9435.

(51) Pandey, K. K. *Coord. Chem. Rev.* **2009**, *253*, 37.

(52) Muhoro, C. N.; Hartwig, J. F. *Angew. Chem. Int. Ed.* **1997**, *36*, 1510.

(53) Kubas Gregory, J. *Acc. Chem. Res.* **1988**, *21*, 120.

(54) Blanksby, S. J.; Ellison, G. B. *Acc. Chem. Res.* **2003**, *36*, 255.

(55) Maltby, P. A.; Schlaf, M.; Steinbeck, M.; Lough, A. J.; Morris, R. H.; Klooster, W. T.; Koetzle, T. F.; Srivastava, R. C. *J. Am. Chem. Soc.* **1996**, *118*, 5396.

(56) Gründemann, S.; Limbach, H.-H.; Buntkowsky, G.; Sabo-Etienne, S.; Chaudret, B. *J. Phys. Chem. A* **1999**, *103*, 4752.

(57) Chinn, M. S.; Heinekey, D. M.; Payne, N. G.; Sofield, C. D. *Organometallics* **1989**, *8*, 1824.

(58) Klooster, W. T.; Koetzle, T. F.; Jia, G.; Fong, T. P.; Morris, R. H.; Albinati, A. *J. Am. Chem. Soc.* **1994**, *116*, 7677.

(59) Pike, S. D.; Chadwick, F. M.; Rees, N. H.; Scott, M. P.; Weller, A. S.; Krämer, T.; Macgregor, S. A. *J. Am. Chem. Soc.* **2015**, *137*, 820.

(60) Brookhart, M.; Green, M. L. H.; Parkin, G. *Proc. Natl. Acad. Sci.* **2007**, *104*, 6908.

(61) Brookhart, M.; Green, M. L. H. *J. Organomet. Chem.* **1983**, *250*, 395.

(62) Dawoodi, Z.; Green, M. L. H.; Mtetwa, V. S. B.; Prout, K.; Schultz, A. J.; Williams, J. M.; Koetzle, T. F. *J. Chem. Soc., Dalton Trans.* **1986**, 1629.

(63) Dawoodi, Z.; Green, M. L. H.; Mtetwa, V. S. B.; Prout, K. *J. Chem. Soc., Chem. Commun.* **1982**, 802.

(64) Buchanan, J. M.; Stryker, J. M.; Bergman, R. G. *J. Am. Chem. Soc.* **1986**, *108*, 1537.

(65) Jones, W. D. *Acc. Chem. Res.* **2003**, *36*, 140.

(66) Stolz, I. W.; Dobson, G. R.; Sheline, R. K. *J. Am. Chem. Soc.* **1962**, *84*, 3589.

(67) Stolz, I. W.; Dobson, G. R.; Sheline, R. K. *J. Am. Chem. Soc.* **1963**, *85*, 1013.

(68) Perutz, R. N.; Turner, J. J. *J. Am. Chem. Soc.* **1975**, *97*, 4791.

(69) Poliakoff, M.; Turner, J. J. *J. Chem. Soc., Dalton Trans.* **1974**, 2276.

(70) Joly, A. G.; Nelson, K. A. *Chem. Phys.* **1991**, *152*, 69.

(71) Joly, A. G.; Nelson, K. A. *J. Phys. Chem.* **1989**, *93*, 2876.

(72) Simon, J. D.; Xie, X. *J. Phys. Chem.* **1986**, *90*, 6751.

(73) Simon, J. D.; Xie, X. *J. Phys. Chem.* **1987**, *91*, 5538.

(74) Nasielski, J.; Kirsch, P.; Wilputte-Steinert, L. *J. Organomet. Chem.* **1971**, *29*, 269.

(75) Cowan, A. J.; George, M. W. *Coord. Chem. Rev.* **2008**, *252*, 2504.

(76) Lawes, D. J.; Geftakis, S.; Ball, G. E. *J. Am. Chem. Soc.* **2005**, *127*, 4134.

(77) Lawes, D. J.; Darwish, T. A.; Clark, T.; Harper, J. B.; Ball, G. E. *Angew. Chem. Int. Ed.* **2006**, *45*, 4486.

(78) Calladine, J. A.; Torres, O.; Anstey, M.; Ball, G. E.; Bergman, R. G.; Curley, J.; Duckett, S. B.; George, M. W.; Gilson, A. I.; Lawes, D. J.; Perutz, R. N.; Sun, X.-Z.; Vollhardt, K. P. C. *Chem. Sci.* **2010**, *1*, 622.

(79) Ball, G. E.; Brookes, C. M.; Cowan, A. J.; Darwish, T. A.; George, M. W.; Kawanami, H. K.; Portius, P.; Rourke, J. P. *Proc. Natl. Acad. Sci.* **2007**, *104*, 6927.

(80) Geftakis, S.; Ball, G. E. *J. Am. Chem. Soc.* **1998**, *120*, 9953.

(81) Lawes, D. J. *NMR Spectroscopic Studies of Binding and Exchange in Rhenium Alkane Complexes.* PhD Thesis, University of New South Wales, 2008.

(82) Sun, X.-Z.; Grills, D. C.; Nikiforov, S. M.; Poliakoff, M.; George, M. W. *J. Am. Chem. Soc.* **1997**, *119*, 7521.

(83) Schultz, R. H.; Bengali, A. A.; Tauber, M. J.; Weiller, B. H.; Wasserman, E. P.; Kyle, K. R.; Moore, C. B.; Bergman, R. G. *J. Am. Chem. Soc.* **1994**, *116*, 7369.

(84) Duckett, S. B.; George, M. W.; Jina, O. S.; Matthews, S. L.; Perutz, R. N.; Sun, X.-Z.; Vuong, K. Q. *Chem. Commun.* **2009**, 1401.

(85) Young, R. D.; Hill, A. F.; Hillier, W.; Ball, G. E. *J. Am. Chem. Soc.* **2011**, *133*, 13806.

(86) Calladine, J. A.; Duckett, S. B.; George, M. W.; Matthews, S. L.; Perutz, R. N.; Torres, O.; Vuong, K. Q. *J. Am. Chem. Soc.* **2011**, *133*, 2303.

(87) Young, R. D.; Lawes, D. J.; Hill, A. F.; Ball, G. E. *J. Am. Chem. Soc.* **2012**, *134*, 8294.

(88) Bernskoetter, W. H.; Schauer, C. K.; Goldberg, K. I.; Brookhart, M. *Science* **2009**, *326*, 553.

(89) Walter, M. D.; White, P. S.; Schauer, C. K.; Brookhart, M. *J. Am. Chem. Soc.* **2013**, *135*, 15933.

(90) Evans, D. R.; Drovetskaya, T.; Bau, R.; Reed, C. A.; Boyd, P. D. W. *J. Am. Chem. Soc.* **1997**, *119*, 3633.

(91) Castro-Rodriguez, I.; Nakai, H.; Gantzel, P.; Zakharov, L. N.; Rheingold, A. L.; Meyer, K. *J. Am. Chem. Soc.* **2003**, *125*, 15734.

(92) Pike, S. D.; Thompson, A. L.; Algarra, A. G.; Apperley, D. C.; Macgregor, S. A.; Weller, A. S. *Science* **2012**, *337*, 1648.

(93) Castro-Rodriguez, I.; Olsen, K.; Gantzel, P.; Meyer, K. *J. Am. Chem. Soc.* **2003**, *125*, 4565.

(94) Castro-Rodriguez, I.; Olsen, K.; Gantzel, P.; Meyer, K. *Chem. Commun.* **2002**, 2764.

(95) Bloch, E. D.; Queen, W. L.; Krishna, R.; Zadrozny, J. M.; Brown, C. M.; Long, J. R. *Science* **2012**, *335*, 1606.

(96) Wu, H.; Simmons, J. M.; Liu, Y.; Brown, C. M.; Wang, X.-S.; Ma, S.; Peterson, V. K.; Southon, P. D.; Kepert, C. J.; Zhou, H.-C.; Yildirim, T.; Zhou, W. *Chem. Eur. J.* **2010**, *16*, 5205.

(97) Andreychuk, N. R.; Emslie, D. J. H. *Angew. Chem. Int. Ed.* **2013**, *52*, 1696.

(98) Walter, M. D.; White, P. S.; Schauer, C. K.; Brookhart, M. *New J. Chem.* **2011**, *35*, 2884.

(99) Ortuño, M. A.; Conejero, S.; Lledós, A. *Beilstein J. Org. Chem.* **2013**, *9*, 1352.

(100) Braunschweig, H.; Radacki, K.; Rais, D.; Scheschkewitz, D. *Angew. Chem. Int. Ed.* **2005**, *44*, 5651.

(101) Braunschweig, H.; Brenner, P.; Dewhurst, R. D.; Jimenez-Halla, J. O. C.; Kupfer, T.; Rais, D.; Uttinger, K. *Angew. Chem. Int. Ed.* **2013**, *52*, 2981.

(102) Dorta, R.; Stevens, E. D.; Hoff, C. D.; Nolan, S. P. *J. Am. Chem. Soc.* **2003**, *125*, 10490.

(103) Lavallo, V.; Canac, Y.; DeHope, A.; Donnadieu, B.; Bertrand, G. *Angew. Chem. Int. Ed.* **2005**, *44*, 7236.

(104) Clavier, H.; Nolan, S. P. *Chem. Commun.* **2010**, *46*, 841.

(105) Rivada-Wheelaghan, O.; Ortuno, M. A.; Diez, J.; Lledos, A.; Conejero, S. *Angew. Chem. Int. Ed.* **2012**, *51*, 3936.

(106) Morales Morales, D.; Jensen, C. M. *The Chemistry of Pincer Compounds*; Elsevier: Amsterdam, Netherlands, 2007.

(107) van Koten, G.; Milstein, D. *Organometallic Pincer Chemistry*; Springer: Heidelberg, 2013.

(108) Szabó, K. J.; Wendt, O. F. *Pincer and Pincer-Type Complexes: Applications in Organic Synthesis and Catalysis*; Wiley-VCH Verlag GmbH & Co. KGaA: Weinheim, Germany, 2014.

(109) Brück, A.; Gallego, D.; Wang, W.; Irran, E.; Driess, M.; Hartwig, J. F. *Angew. Chem. Int. Ed.* **2012**, *51*, 11478.

(110) Wang, W.; Inoue, S.; Irran, E.; Driess, M. *Angew. Chem. Int. Ed.* **2012**, *51*, 3691.

(111) Gallego, D.; Brück, A.; Irran, E.; Meier, F.; Kaupp, M.; Driess, M.; Hartwig, J. F. *J. Am. Chem. Soc.* **2013**, *135*, 15617.

(112) Handwerker, H.; Paul, M.; Blümel, J.; Zybill, C. *Angew. Chem. Int. Ed.* **1993**, *32*, 1313.

(113) Burford, R. J.; Piers, W. E.; Ess, D. H.; Parvez, M. *J. Am. Chem. Soc.* **2014**, *136*, 3256.

(114) Davidson, J. J.; DeMott, J. C.; Douvris, C.; Fafard, C. M.; Bhuvanesh, N.; Chen, C.-H.; Herbert, D. E.; Lee, C.-I.; McCulloch, B. J.; Foxman, B. M.; Ozerov, O. V. *Inorg. Chem.* **2015**, *54*, 2916.

(115) Haibach, M. C.; Wang, D. Y.; Emge, T. J.; Krogh-Jespersen, K.; Goldman, A. S. *Chem. Sci.* **2013**, *4*, 3683.

(116) Mankad, N. P.; Rivard, E.; Harkins, S. B.; Peters, J. C. *J. Am. Chem. Soc.* **2005**, *127*, 16032.

(117) Yang, H.; Gabbaï, F. P. *J. Am. Chem. Soc.* **2014**, *136*, 10866.

(118) Korshin, E. E.; Leitus, G.; Shimon, L. J. W.; Konstantinovski, L.; Milstein, D. *Inorg. Chem.* **2008**, *47*, 7177.

(119) MacInnis, M. C.; MacLean, D. F.; Lundgren, R. J.; McDonald, R.; Turculet, L. *Organometallics* **2007**, *26*, 6522.

(120) Mitton, S. J.; McDonald, R.; Turculet, L. *Organometallics* **2009**, *28*, 5122.

(121) Takaya, J.; Iwasawa, N. *J. Am. Chem. Soc.* **2008**, *130*, 15254.

(122) Whited, M. T.; Deetz, A. M.; Boerma, J. W.; DeRosha, D. E.; Janzen, D. E. *Organometallics* **2014**, *33*, 5070.

(123) Weng, W.; Chen, C.-H.; Foxman, B. M.; Ozerov, O. V. *Organometallics* **2007**, *26*, 3315.

(124) Waterman, R.; Hayes, P. G.; Tilley, T. D. *Acc. Chem. Res.* **2007**, *40*, 712.

(125) Calimano, E.; Tilley, T. D. *J. Am. Chem. Soc.* **2009**, *131*, 11161.

(126) Ramirez-Contreras, R.; Ozerov, O. V. *Dalton Trans.* **2012**, *41*, 7842.

(127) Douvris, C.; Michl, J. *Chem. Rev.* **2013**, *113*, PR179.

(128) Grumbine, S. D.; Tilley, T. D.; Arnold, F. P.; Rheingold, A. L. *J. Am. Chem. Soc.* **1993**, *115*, 7884.

(129) Mitchell, G. P.; Tilley, T. D. *Angew. Chem. Int. Ed.* **1998**, *37*, 2524.

(130) Feldman, J. D.; Mitchell, G. P.; Nolte, J.-O.; Tilley, T. D. *Can. J. Chem.* **2003**, *81*, 1127.

(131) Watanabe, C.; Inagawa, Y.; Iwamoto, T.; Kira, M. *Dalton Trans.* **2010**, *39*, 9414.

(132) Agou, T.; Sasamori, T.; Tokitoh, N. *Organometallics* **2012**, *31*, 1150.

(133) Hayes, P. G.; Beddie, C.; Hall, M. B.; Waterman, R.; Tilley, T. D. *J. Am. Chem. Soc.* **2006**, *128*, 428.

(134) Allemann, O.; Duttwyler, S.; Romanato, P.; Baldridge, K. K.; Siegel, J. S. *Science* **2011**, *332*, 574.

(135) Crosby, S. H.; Deeth, R. J.; Clarkson, G. J.; Rourke, J. P. *Dalton Trans.* **2011**, *40*, 1227.

(136) Butts, M. D.; Scott, B. L.; Kubas, G. J. *J. Am. Chem. Soc.* **1996**, *118*, 11831.

(137) Tsay, C.; Mankad, N. P.; Peters, J. C. *J. Am. Chem. Soc.* **2010**, *132*, 13975.

(138) Gu, W.; McCulloch, B. J.; Reibenspies, J. H.; Ozerov, O. V. *Chem. Commun.* **2010**, *46*, 2820.

(139) Drew, D.; Doyle, J. R.; Shaver, A. G. In *Inorg. Synth.*; John Wiley & Sons, Inc.: 2007, p 346.

(140) Tamm, M.; Dreßel, B.; Baum, K.; Lügger, T.; Pape, T. *J. Organomet. Chem.* **2003**, *677*, 1.

(141) Knotter, D. M.; Grove, D. M.; Smeets, W. J. J.; Spek, A. L.; Van Koten, G. *J. Am. Chem. Soc.* **1992**, *114*, 3400.

(142) *APEX2*; Version 2013.2-0; Bruker AXS Inc.: Madison, WI, 2013.

(143) Sheldrick, G. M. *SADABS*; Version 2008/1; Bruker AXS Inc: Madison, WI, 2008.

(144) Sheldrick, G. M. *Acta Crystallogr. Sect. A* **2008**, *64*, 112.

(145) Spek, A. L. *J. Appl. Crystallogr.* **2003**, *36*, 7.

(146) Hubschle, C. B.; Sheldrick, G. M.; Dittrich, B. *J. Appl. Crystallogr.* **2011**, *44*, 1281.

(147) Gaussian 09, Revision B.01, Frisch, M. J.; Trucks, G. W.; Schlegel, H. B.; Scuseria, G. E.; Robb, M. A.; Cheeseman, J. R.; Scalmani, G.; Barone, V.; Mennucci, B.; Petersson, G. A.; Nakatsuji, H.; Caricato, M.; Li, X.; Hratchian, H. P.; Izmaylov, A. F.; Bloino, J.; Zheng, G.; Sonnenberg, J. L.; Hada, M.; Ehara, M.; Toyota, K.; Fukuda, R.; Hasegawa, J.; Ishida, M.; Nakajima, T.; Honda, Y.; Kitao, O.; Nakai, H.; Vreven, T.; Montgomery Jr., J. A.; Peralta, J. E.; Ogliaro, F.; Bearpark, M. J.; Heyd, J.; Brothers, E. N.; Kudin, K. N.; Staroverov, V. N.; Kobayashi, R.; Normand, J.; Raghavachari, K.; Rendell, A. P.; Burant, J. C.; Iyengar, S. S.; Tomasi, J.; Cossi, M.; Rega, N.; Millam, N. J.; Klene, M.; Knox, J. E.; Cross, J. B.; Bakken, V.; Adamo, C.; Jaramillo, J.; Gomperts, R.; Stratmann, R. E.; Yazyev, O.; Austin, A. J.; Cammi, R.; Pomelli, C.; Ochterski, J. W.; Martin, R. L.; Morokuma, K.; Zakrzewski, V. G.; Voth, G. A.; Salvador, P.; Dannenberg, J. J.; Dapprich, S.; Daniels, A. D.; Farkas, Ö.; Foresman, J. B.; Ortiz, J. V.; Cioslowski, J.; Fox, D. J.; Gaussian, Inc.: Wallingford, CT, 2009.

(148) Stephens, P. J.; Devlin, F. J.; Chabalowski, C. F.; Frisch, M. J. *J. Phys. Chem.* **1994**, *98*, 11623.

(149) Becke, A. D. *J. Chem. Phys.* **1993**, *98*, 5648.

(150) Lee, C.; Yang, W.; Parr, R. G. *Phys. Rev. B* **1988**, *37*, 785.

(151) Küchle, W.; Dolg, M.; Stoll, H.; Preuss, H. *J. Phys. Chem.* **1994**, *100*, 7535.

(152) Hariharan, P. C.; Pople, J. A. *Theoret. Chim. Acta* **1973**, *28*, 213.

(153) Francl, M. M.; Pietro, W. J.; Hehre, W. J.; Binkley, J. S.; Gordon, M. S.; DeFrees, D. J.; Pople, J. A. *J. Chem. Phys.* **1982**, *77*, 3654.

(154) Zhao, Y.; Truhlar, D. G. *J. Chem. Phys.* **2006**, *125*.

(155) Lersch, M.; Tilset, M. *Chem. Rev.* **2005**, *105*, 2471.

(156) Fekl, U.; Goldberg, K. I. In *Adv. Inorg. Chem.: Including Bioinorganic Studies, Vol 54* 2003; Vol. 54, p 259.

(157) Shilov, A. E.; Shul'pin, G. B. *Russ. Chem. Rev.* **1987**, *56*, 442.

(158) Shilov, A. E.; Shul'pin, G. B. *Activation and Catalytic Reactions of Saturated Hydrocarbons in the Presence of Metal Complexes*; Kluwer Academic Publishers: Dordrecht, Netherlands, 2000.

(159) Goldman, A. S.; Roy, A. H.; Huang, Z.; Ahuja, R.; Schinski, W.; Brookhart, M. *Science* **2006**, *312*, 257.

(160) Lyons, T. W.; Sanford, M. S. *Chem. Rev.* **2010**, *110*, 1147.

(161) Bercaw, J. E.; Labinger, J. A. *Proc. Natl. Acad. Sci.* **2007**, *104*, 6899.

(162) Jones, W. D. *Acc. Chem. Res.* **2003**, *36*, 140.

(163) Jones, W. D. *Inorg. Chem.* **2005**, *44*, 4475.

(164) Balcells, D.; Clot, E.; Eisenstein, O. *Chem. Rev.* **2010**, *110*, 749.

(165) van der Boom, M. E.; Milstein, D. *Chem. Rev.* **2003**, *103*, 1759.

(166) Choi, J.; MacArthur, A. H. R.; Brookhart, M.; Goldman, A. S. *Chem. Rev.* **2011**, *111*, 1761.

(167) Harkins, S. B.; Peters, J. C. *Organometallics* **2002**, *21*, 1753.

(168) Liang, L. C.; Lin, J. M.; Lee, W. Y. *Chem. Commun.* **2005**, 2462.

(169) Johansson, L.; Tilset, M.; Labinger, J. A.; Bercaw, J. E. *J. Am. Chem. Soc.* **2000**, *122*, 10846.

(170) Reinartz, S.; White, P. S.; Brookhart, M.; Templeton, J. L. *J. Am. Chem. Soc.* **2001**, *123*, 12724.

(171) Parmene, J.; Ivanovic-Burmazovic, I.; Tilset, M.; van Eldik, R. *Inorg. Chem.* **2009**, *48*, 9092.

(172) Hasegawa, M.; Segawa, Y.; Yamashita, M.; Nozaki, K. *Angew. Chem. Int. Ed.* **2012**, *51*, 6956.

(173) Liang, L. C.; Lin, J. M.; Hung, C. H. *Organometallics* **2003**, *22*, 3007.

(174) Winter, A. M.; Eichele, K.; Mack, H. G.; Potuznik, S.; Mayer, H. A.; Kaska, W. C. *J. Organomet. Chem.* **2003**, *682*, 149.

(175) Fan, L.; Foxman, B. M.; Ozerov, O. V. *Organometallics* **2004**, *23*, 326.

(176) Liang, L. C. *Coord. Chem. Rev.* **2006**, *250*, 1152.

(177) Mindiola, D. J. *Acc. Chem. Res.* **2006**, *39*, 813.

(178) Zhu, Y. J.; Smith, D. A.; Herbert, D. E.; Gatard, S.; Ozerov, O. V. *Chem. Commun.* **2012**, *48*, 218.

(179) Fan, L.; Parkin, S.; Ozerov, O. V. *J. Am. Chem. Soc.* **2005**, *127*, 16772.

(180) Gregor, L. C.; Chen, C. H.; Fafard, C. M.; Fan, L.; Guo, C. Y.; Foxman, B. M.; Gusev, D. G.; Ozerov, O. V. *Dalton Trans.* **2010**, *39*, 3195.

(181) Zhu, Y.; Chen, C. H.; Fafard, C. M.; Foxman, B. M.; Ozerov, O. V. *Inorg. Chem.* **2011**, *50*, 7980.

(182) Fan, L.; Ozerov, O. V. *Chem. Commun.* **2005**, 4450.

(183) Fan, L.; Yang, L.; Guo, C. Y.; Foxman, B. M.; Ozerov, O. V. *Organometallics* **2004**, *23*, 4778.

(184) Weng, W.; Guo, C. Y.; Celenligil-Cetin, R.; Foxman, B. M.; Ozerov, O. V. *Chem. Commun.* **2006**, 197.

(185) Huacuja, R.; Herbert, D. E.; Fafard, C. M.; Ozerov, O. V. *J. Fluorine Chem.* **2010**, *131*, 1257.

(186) Stephan, D. W.; Erker, G. *Angew. Chem. Int. Ed.* **2010**, *49*, 46.

(187) Heyduk, A. F.; Driver, T. G.; Labinger, J. A.; Bercaw, J. E. *J. Am. Chem. Soc.* **2004**, *126*, 15034.

(188) Ben-Ari, E.; Gandelman, M.; Rozenberg, H.; Shimon, L. J. W.; Milstein, D. *J. Am. Chem. Soc.* **2003**, *125*, 4714.

(189) Ben-Ari, E.; Cohen, R.; Gandelman, M.; Shimon, L. J. W.; Martin, J. M. L.; Milstein, D. *Organometallics* **2006**, *25*, 3190.

(190) Renkema, K. B.; Bosque, R.; Streib, W. E.; Maseras, F.; Eisenstein, O.; Caulton, K. G. *J. Am. Chem. Soc.* **1999**, *121*, 10895.

(191) Lu, S.-F.; Du, D.-M.; Zhang, S.-W.; Xu, J. *Tetrahedron-Asymmetr.* **2004**, *15*, 3433.

(192) Puri, M.; Gatard, S.; Smith, D. A.; Ozerov, O. V. *Organometallics* **2011**, *30*, 2472.

(193) Timpa, S. D.; Fafard, C. M.; Herbert, D. E.; Ozerov, O. V. *Dalton Trans.* **2011**, *40*, 5426.

(194) Clot, E.; Eisenstein, O.; Jasim, N.; Macgregor, S. A.; McGrady, J. E.; Perutz, R. N. *Acc. Chem. Res.* **2011**, *44*, 333.

(195) Parkin, G. *Acc. Chem. Res.* **2009**, *42*, 315.

(196) Adhikari, D.; Mossin, S.; Basuli, F.; Huffman, J. C.; Szilagyi, R. K.; Meyer, K.; Mindiola, D. J. *J. Am. Chem. Soc.* **2008**, *130*, 3676.

(197) Radosevich, A. T.; Melnick, J. G.; Stoian, S. A.; Bacciu, D.; Chen, C. H.; Foxman, B. M.; Ozerov, O. V.; Nocera, D. G. *Inorg. Chem.* **2009**, *48*, 9214.

(198) Qian, Y. Y.; Chan, K. S. *Organometallics* **2012**, *31*, 5452.

(199) Cheung, C. W.; Chan, K. S. *Organometallics* **2011**, *30*, 4269.

(200) Kimmich, B. F. M.; Bullock, R. M. *Organometallics* **2002**, *21*, 1504.

(201) Adamo, C.; Barone, V. *J. Chem. Phys.* **1999**, *110*, 6158.

(202) Reed, C. A.; Fackler, N. L. P.; Kim, K.-C.; Stasko, D.; Evans, D. R.; Boyd, P. D. W.; Rickard, C. E. F. *J. Am. Chem. Soc.* **1999**, *121*, 6314.

(203) Reed, C. A.; Kim, K.-C.; Stoyanov, E. S.; Stasko, D.; Tham, F. S.; Mueller, L. J.; Boyd, P. D. W. *J. Am. Chem. Soc.* **2003**, *125*, 1796.

(204) Juhasz, M.; Hoffmann, S.; Stoyanov, E.; Kim, K.-C.; Reed, C. A. *Angew. Chem. Int. Ed.* **2004**, *43*, 5352.

(205) Brookhart, M.; Grant, B.; Volpe, A. F. *Organometallics* **1992**, *11*, 3920.

(206) Weigend, F.; Ahlrichs, R. *Phys. Chem. Chem. Phys.* **2005**, *7*, 3297.

(207) Martin, R. L.; Hay, P. J.; Pratt, L. R. *J. Phys. Chem. A* **1998**, *102*, 3565.

(208) Sieffert, N.; Bühl, M. *Inorg. Chem.* **2009**, *48*, 4622.

(209) Kundu, S.; Brennessel, W. W.; Jones, W. D. *Inorg. Chim. Acta* **2011**, *379*, 109.

(210) Ozerov, O. V. In *The Chemistry of Pincer Compounds*; Jensen, C. M., Morales-Morales, D., Eds.; Elsevier Science B.V.: Amsterdam, 2007, p 287.

(211) Mindiola, D. J.; Bailey, B. C.; Basuli, F. *Eur. J. Inorg. Chem.* **2006**, 3135.

(212) Harkins, S. B.; Peters, J. C. *J. Am. Chem. Soc.* **2005**, *127*, 2030.

(213) Whited, M. T.; Grubbs, R. H. *Acc. Chem. Res.* **2009**, *42*, 1607.

(214) Cantat, T.; Graves, C. R.; Scott, B. L.; Kiplinger, J. L. *Angew. Chem. Int. Ed.* **2009**, *48*, 3681.

(215) Harkins, S. B.; Peters, J. C. *J. Am. Chem. Soc.* **2004**, *126*, 2885.

(216) Csok, Z.; Vechorkin, O.; Harkins, S. B.; Scopelliti, R.; Hu, X. *J. Am. Chem. Soc.* **2008**, *130*, 8156.

(217) Madhira, V. N.; Ren, P.; Vechorkin, O.; Hu, X.; Vicic, D. A. *Dalton Trans.* **2012**, *41*, 7915.

(218) DeMott, J. C.; Bhuvanesh, N.; Ozerov, O. V. *Chem. Sci.* **2013**, *4*, 642.

(219) Kieltsch, I.; Dubinina, G. G.; Hamacher, C.; Kaiser, A.; Torres-Nieto, J.; Hutchison, J. M.; Klein, A.; Budnikova, Y.; Vicic, D. A. *Organometallics* **2010**, *29*, 1451.

(220) Inagaki, T.; Phong, L. T.; Furuta, A.; Ito, J.-i.; Nishiyama, H. *Chem. Eur. J.* **2010**, *16*, 3090.

(221) Wanniarachchi, S.; Liddle, B. J.; Toussaint, J.; Lindeman, S. V.; Bennett, B.; Gardinier, J. R. *Dalton Trans.* **2010**, *39*, 3167.

(222) Mudadu, M. S.; Singh, A. N.; Thummel, R. P. *J. Org. Chem.* **2008**, *73*, 6513.

(223) Hollas, A. M.; Gu, W.; Bhuvanesh, N.; Ozerov, O. V. *Inorg. Chem.* **2011**, *50*, 3673.

(224) Gaunt, J. A.; Gibson, V. C.; Haynes, A.; Spitzmesser, S. K.; White, A. J. P.; Williams, D. J. *Organometallics* **2004**, *23*, 1015.

(225) Britovsek, G. J. P.; Gibson, V. C.; Hoarau, O. D.; Spitzmesser, S. K.; White, A. J. P.; Williams, D. J. *Inorg. Chem.* **2003**, *42*, 3454.

(226) Barbe, J.-M.; Habermeyer, B.; Khoury, T.; Gros, C. P.; Richard, P.; Chen, P.; Kadish, K. M. *Inorg. Chem.* **2010**, *49*, 8929.

(227) Priqueler, J. R. L.; Butler, I. S.; Rochon, F. D. *Appl. Spectrosc. Rev.* **2006**, *41*, 185.

(228) Conroy, K. D.; Piers, W. E.; Parvez, M. *J. Organomet. Chem.* **2008**, *693*, 834.

(229) Oulié, P.; Freund, C.; Saffon, N.; Martin-Vaca, B.; Maron, L.; Bourissou, D. *Organometallics* **2007**, *26*, 6793.

(230) Spencer, L. P.; Fryzuk, M. D. *J. Organomet. Chem.* **2005**, *690*, 5788.

(231) Schrodi, Y.; Schrock, R. R.; Bonitatebus, P. J. *Organometallics* **2001**, *20*, 3560.

(232) Hamidi, S.; Jende, L. N.; Martin Dietrich, H.; Maichle-Mössmer, C.; Törnroos, K. W.; Deacon, G. B.; Junk, P. C.; Anwander, R. *Organometallics* **2013**, *32*, 1209.

(233) Horchler, S.; Parisini, E.; Roesky, H. W.; Schmidt, H.-G.; Noltemeyer, M. *J. Chem. Soc., Dalton Trans.* **1997**, 2761.

(234) Schulz, S.; Häming, L.; Herbst-Irmer, R.; Roesky, H. W.; Sheldrick, G. M. *Angew. Chem. Int. Ed.* **1994**, *33*, 969.

(235) Waggoner, K. M.; Power, P. P. *J. Am. Chem. Soc.* **1991**, *113*, 3385.

(236) Marquard, S. L.; Bezpalko, M. W.; Foxman, B. M.; Thomas, C. M. *J. Am. Chem. Soc.* **2013**, *135*, 6018.

(237) Kwan Huang, E.; Cheung, W.-M.; Sung, H. H. Y.; Williams, I. D.; Leung, W.-H. *Organometallics* **2013**, *32*, 733.

(238) King, E. R.; Sazama, G. T.; Betley, T. A. *J. Am. Chem. Soc.* **2012**, *134*, 17858.

(239) Newman, C. P.; Casey-Green, K.; Clarkson, G. J.; Cave, G. W. V.; Errington, W.; Rourke, J. P. *Dalton Trans.* **2007**, 3170.

(240) Shul'pin, G. B.; Shilov, A. E.; Kitaigorodskii, A. N.; Zeile Krevor, J. V. *J. Organomet. Chem.* **1980**, *201*, 319.

(241) Shul'pin, G. B. *J. Organomet. Chem.* **1981**, *212*, 267.

(242) Shul'pin, G. B.; Kitaigorodskii, A. N. *J. Organomet. Chem.* **1981**, *212*, 275.

(243) Shul'pin, G. B.; Nizova, G. V.; Shilov, A. E. *J. Chem. Soc., Chem. Commun.* **1983**, 671.

(244) Scott, V. J.; Labinger, J. A.; Bercaw, J. E. *Organometallics* **2011**, *30*, 4374.

(245) Falvello, L. R.; Garde, R.; Miqueleiz, E. M.; Tomás, M.; Urriolabeitia, E. P. *Inorg. Chim. Acta* **1997**, *264*, 297.

(246) Yang, W.; Zhang, Z.; Han, C.; Zhang, Z.; Xu, H.; Yan, P.; Zhao, Y.; Liu, S. *Chem. Commun.* **2013**, *49*, 2822.

APPENDIX

A.1 Synthesis of (NNN) ligand derivatives

*A.1.1 1,8-diformyl-3,6-di-tert-butyl-9-methyl-carbazole (**A01**)*

1,8-dibromo-3,6-di-*tert*-butyl-9-methyl-carbazole[246] (1.60 g, 3.55 mmol) was dissolved in diethyl ether (~ 100 mL) in a 250-mL Schlenk flask in Ar-filled glovebox. Flask was placed in a freezer at –35 °C for 1 h then *n*-BuLi (3.5 mL of 2.5 M soln in diethyl ether, 8.8 mmol) was added and the solution was stirred for 1.5 h. Dimethylformamide (2.0 mL, 0.026 mmol) was then added and the reaction was stirred for 16 h. Volatiles were reduced to approximately 50 mL and flask was removed from glovebox. 10 mL of 2% HCl soln was added to the solution and the remaining diethyl ether was removed under vacuum. The solid was collected and washed with water then dissolved in CH_2Cl_2 and dried over $MgSO_4$. The solution was filtered over a pad of Celite and silica gel. Pale yellow solid was collected after recrystallization from a CH_2Cl_2 solution layered with pentane at –35 °C. Yield: 745 mg, 60%. ^{1}H NMR (500 MHz, $CDCl_3$, Figure A.1): δ 10.47 (s, 2H, -C*H*O), 8.34 (d, J_{HH} = 2 Hz, 2H, Ar-*H*), 8.04 (d, J_{HH} = 2 Hz, 2H, Ar-*H*), 4.13 (s, 3H, N-C*H*$_3$), 1.50 (s, 18H, -C(C*H*$_3$)$_3$).

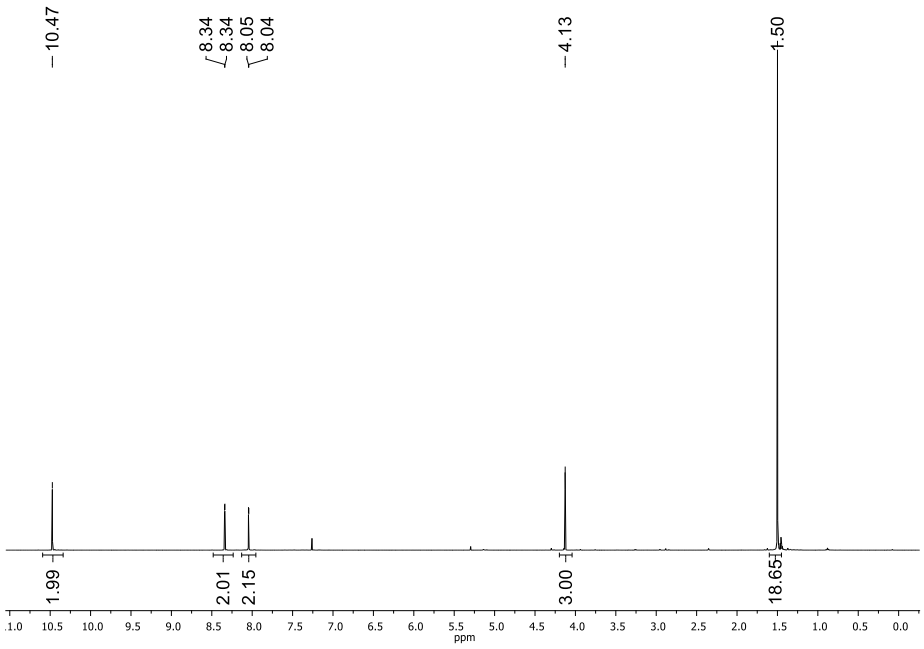

Figure A.1 ^{1}H NMR spectrum of **A01** in $CDCl_3$ at 23 °C measured on a 500-MHz Varian iNova.

*A.1.2 ^{tBu}(NNN)^{tBu}Me (**A02**)*

A01 (110.7 mg, 0.3168 mmol) was dissolved in 20 mL of mesitylene followed by 3,5-di-*tert*-butylaniline (155 mg, 0.755 mmol), two drops HOAc, and molecular sieves. The solution was placed in an oil bath at 150 °C (Scheme A.1). After 16 h, the bright yellow solution was filtered through Celite and silica gel. The volatiles were removed under vacuum yielding a yellow oily residue. The residue was triturated with a minimal amount of pentane giving a yellow solid, the supernatant was removed, and then the solid was dried under vacuum. Yield: 125 mg, 54%. ^{1}H NMR ($CDCl_3$, Figure A.2): δ 9.20 (s, 2H, N=C*H*), 8.25 (s, 2H, Ar-*H*), 8.18 (s, 2H, Ar-*H*), 7.38 (s, 2H, Ar-*H*), 7.18 (s, 4H, Ar-*H*), 4.15 (s, 3H, N-CH_3), 1.55 (s, 18H, -C(CH_3)$_3$), 1.41 (s, 36H, -C(CH_3)$_3$).^{13}C{^{1}H} NMR

($CDCl_3$, Figure A.3): δ 158.0, 152.0, 143.5, 141.9, 125.9, 125.6, 121.0, 120.2, 119.6, 115.4, 41.86, 35.2, 35.0, 32.1, 31.7.

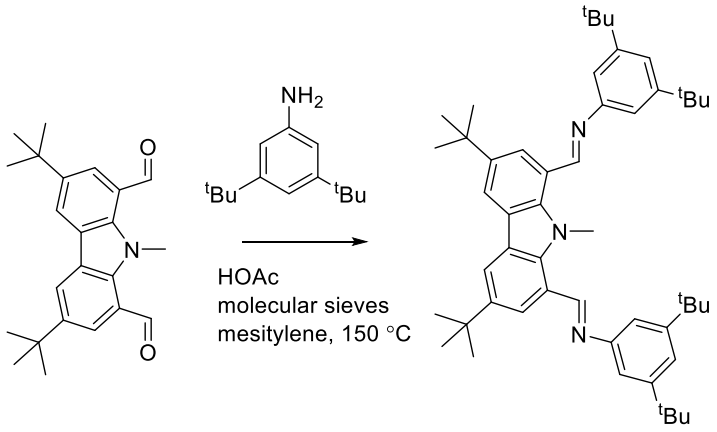

Scheme A.1 Synthesis of **A02**.

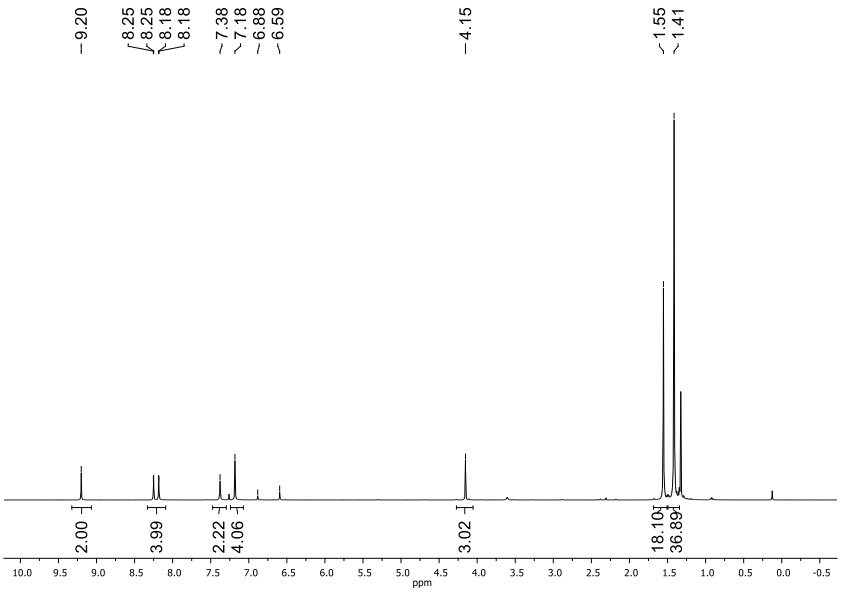

Figure A.2 ^{1}H NMR spectrum of **A02** in $CDCl_3$ at 23 °C measured on a 500-MHz Varian iNova.

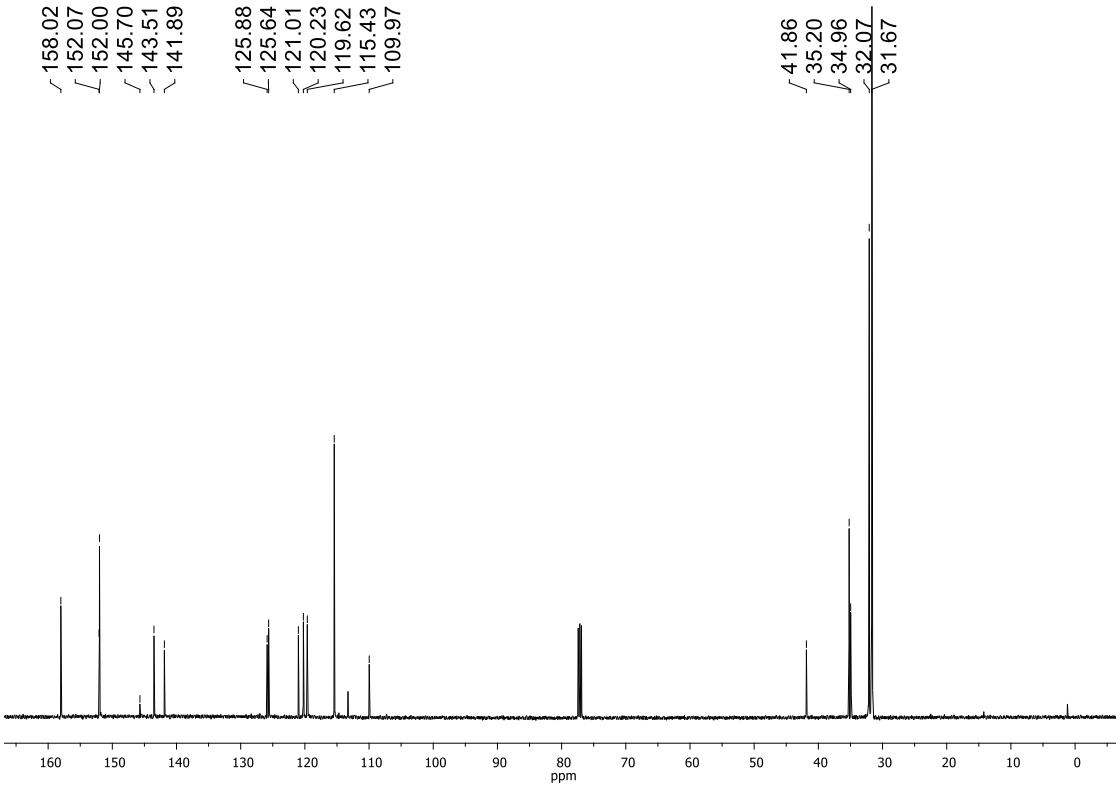

Figure A.3 $^{13}C\{^{1}H\}$ NMR spectrum of **A02** in $CDCl_3$ at 23 °C measured on a 500-MHz Varian iNova.

*A.1.3 ^{Me}(NNN)^{C6F5}Me (**A03**)*

A01 (29.8 mg, 0.112 mmol) was dissolved in 0.5 mL of mesitylene in a screw cap NMR tube. Pentafluoroaniline (156.1 mg, 0.755 mmol), 2 drops of HOAc, and molecular sieves were then added (Scheme A.2). The pale yellow solution was placed in an oil bath at 150 °C for 3 days. The orange precipitate was collected and washed with pentane. Yield: 40.6 mg, 61%. ^{1}H NMR ($CDCl_3$, Figure A.4): δ 9.19 (s, 2H, N=C*H*), 8.02 (s, 2H, Ar-*H*), 7.96 (s, 2H, Ar-*H*), 4.08 (s, 3H, N-CH_3), 2.59 (s, 6H, Ar-CH_3). $^{19}F\{^{1}H\}$ NMR (282.211

MHz, $CDCl_3$): δ 154.4 (dd, J_{F-F} = 20 Hz, J_{F-F} = 6 Hz), 161.4 (t, J_{F-F} = 17 Hz), 163.8 (ddd, J_{F-F} = 20 Hz, J_{F-F} = 20 Hz, J_{F-F} = 6 Hz).

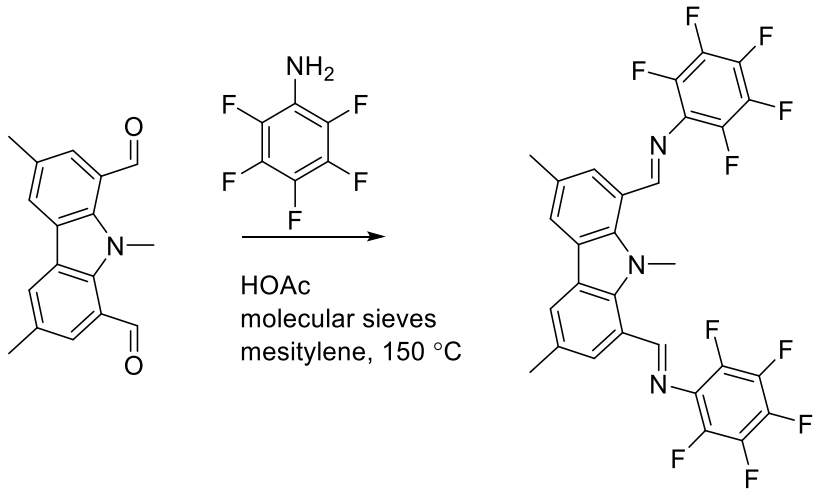

Scheme A.2 Synthesis of **A03**.

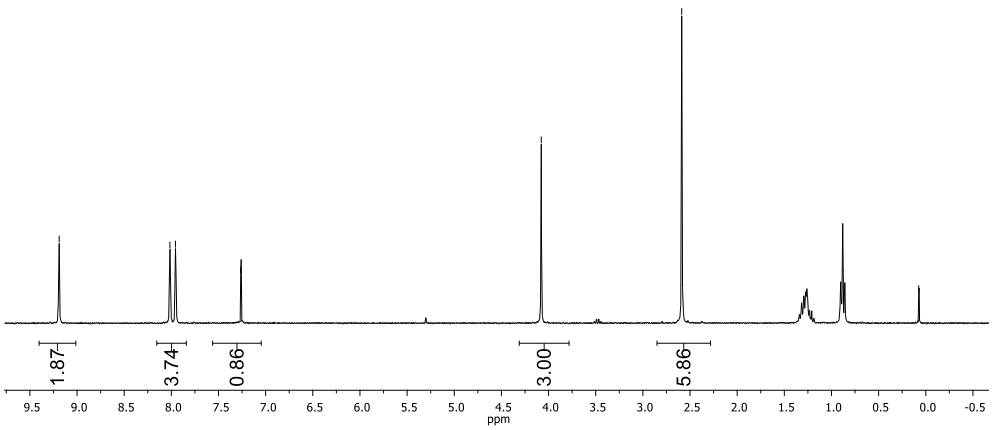

Figure A.4 ^{1}H NMR spectrum of **A03** in $CDCl_3$ at 23 °C measured on a 300-MHz Varian iNova.

A.2 ^{tBu}(POP)^{tBu} ligand synthesis

*A.2.1 ^{tBu}(POP)^{tBu} (**A04**)*

4,5-dibromo-2,7-di-tert-butyl-9,9-dimethylxanthene (1.03 g, 2.13 mmol) was mixed with 30 mL of Et_2O to form a suspension. This mixture was placed in a freezer at –35 °C for 1 h to cool. *n*BuLi (1.9 mL, 4.8 mmol) was then added dropwise. After ten minutes, the solution was a clear pale yellow. The solution was left to warm to RT for 1 h then volatiles were removed giving a pale yellow residue. The residue was redissolved in THF and ClP^tBu_2 (0.97 mL, 5.1 mmol) was then added dropwise and the solution became bright orange (Scheme A.3). The reaction flask was placed in an oil bath at 60 °C overnight. After 24 h, the solution had faded to a pale yellow. Volatiles were removed to give a beige oily solid and the product was extracted with CH_2Cl_2 and filtered over Celite. Volatiles were removed to give a beige solid. The solid was washed with cold diethyl ether (3 × 2 mL) and volatiles were removed again to give a white solid. The product was recrystallized from CH_2Cl_2 layered with diethyl ether at –35 °C. Yield: 673 mg, 52%. ^{1}H NMR (299.958 MHz, C_6D_6, Figure A.5): δ 7.63 (d, J = 3 Hz, Ar-*H*), 7.37 (d, J = 5 Hz, Ar-*H*), 1.60 (s, 6H, C(CH_3)$_2$), 1.36 (s, 18H, -C(CH_3)$_3$), 1.27–1.25 (br m, 36H, P(C(CH_3)$_3$)$_2$). ^{13}C{^{1}H} NMR (125.670 MHz, C_6D_6, Figure A.6): δ 154.1 (t, $J_{P\text{-}C}$ = 12 Hz, C_{Ar}), 143.6 (C_{Ar}), 131.5 (t, $J_{P\text{-}C}$ = 1 Hz), 130.3 (t, $J_{P\text{-}C}$ = 1 Hz), 125.8 (m), 122.6, 35.7 (t, $J_{P\text{-}C}$ = 2 Hz), 34.6, 32.9 (m), 31.8, 31.5, 31.2 (t, $J_{P\text{-}C}$ = 9 Hz). ^{31}P{^{1}H} NMR (202.265, C_6D_6): δ 12.2.

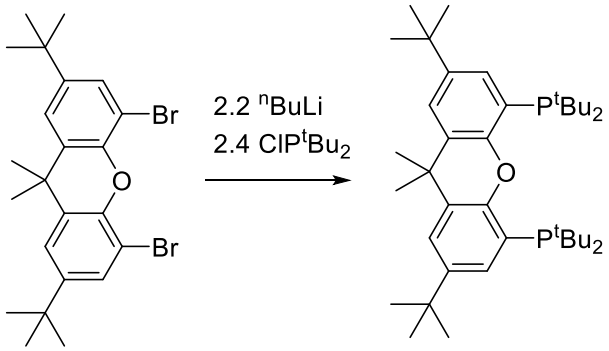

Scheme A.3 Synthesis of **A04** ligand.

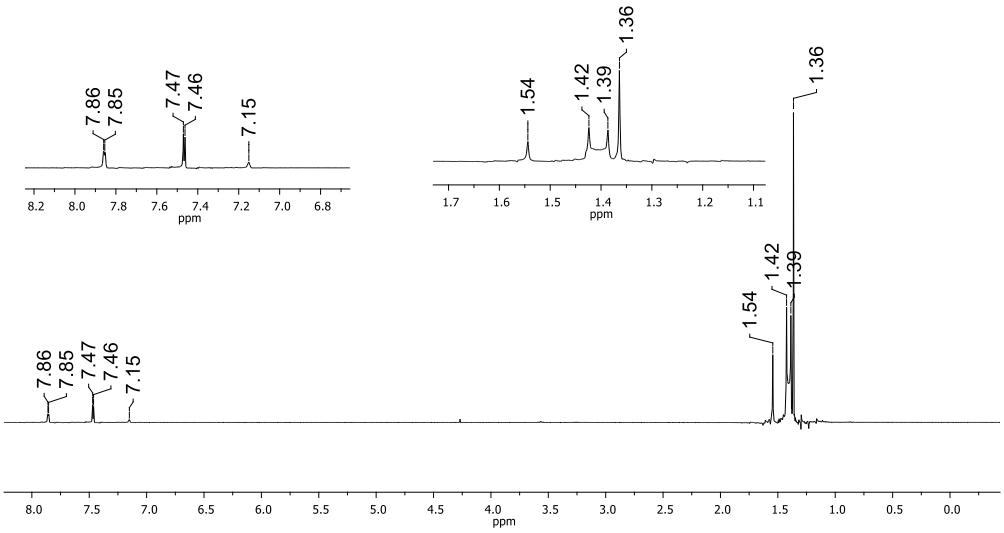

Figure A.5 ^{1}H NMR spectrum of **A03** in C_6D_6 at 23 °C measured on a 300-MHz Varian iNova.

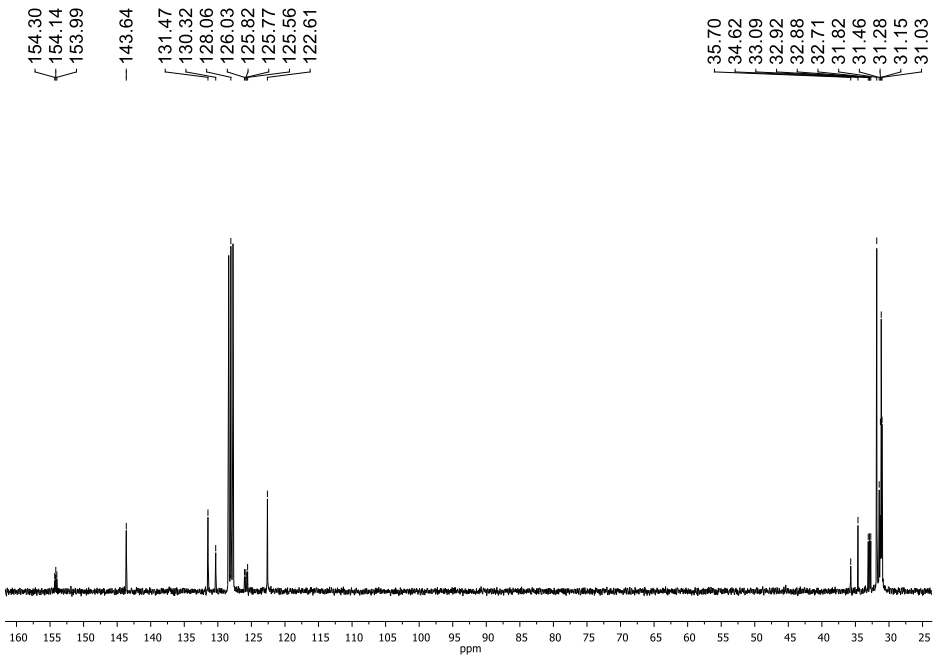

Figure A.6 $^{13}C\{^{1}H\}$ NMR spectrum of **A03** in C_6D_6 at 23 °C measured on a 300-MHz Varian iNova.